

**VISCOELASTIC FLOWS IN COMPLEX GEOMETRIES:
AN ANALYSIS OF THE FILLING STAGE OF THE
INJECTION MOLDING OF THERMOPLASTICS**

by

Thanasis D. Papathanasiou

**A Thesis submitted to the Faculty of Graduate Studies
and Research in partial fulfilment of the
requirements for the Degree of
Doctor of Philosophy**

**Department of Chemical Engineering
McGill University
Montreal, Quebec, Canada**

© T.Papathanasiou, January 1991.

ABSTRACT

Prediction of flow and stress patterns in viscoelastic fluids flowing through channels of complex shape is of theoretical interest in non-Newtonian fluid mechanics but also of large practical interest in the materials processing industry. The first part of this work presents a finite difference computational analysis of the flow of an Upper Convected Maxwell fluid through various geometrically complex channels. The method of Boundary Fitted Curvilinear Coordinates is used to remove the problem of boundary complexity from the finite difference solution of flow problems on arbitrary domains. Several elastic effects, such as vortex growth in contractions and vortex suppression in expanding sections are predicted. The second part of this Thesis is concerned with the modelling of the filling stage of injection molding in a cavity of complex shape with an insert. Non-isothermality, viscoelasticity and the presence of an advancing interface are dealt with in this section. Solution adaptive curvilinear meshes are used for the numerical solution of the model equations on a time-dependent domain. Stress, temperature, pressure, velocity and shear rate profiles within the cavity have been obtained by this analysis. Parametric studies have revealed the effect of key process characteristics on the pressure and thermal gradients during filling. Model predictions are compared to experimental results obtained on an injection molding machine. The model is able to predict with satisfactory accuracy the pressure evolution as well as the pressure gradients developing in the cavity during filling. Finally, a three-dimensional solution of the energy equation revealed the strong spatial and temporal variation of temperature within the mold in both the planar and the thickness directions, and allowed for an evaluation of the crystallinity development in the solidified material during filling.

RESUME

La prédiction des profils d'écoulement et de tension pour les fluides viscoélastiques s'écoulant à travers des conduits de forme complexe est d'intérêt théorique en mécanique des fluides non-Newtoniens, mais aussi d'intérêt pratique dans l'industrie de transformation des matériaux. La première partie de ce travail présente une analyse par différences finies de l'écoulement d'un fluide de Maxwell à travers plusieurs conduits de géométries complexes. La méthode des coordonnées curvilignes fixées aux limites est utilisée pour éliminer le problème des limites de domaine de la solution par différences finies de problèmes d'écoulement avec des domaines arbitraires. Plusieurs effets élastiques, dont la croissance des vortex dans les expansions sont prédits. La deuxième partie de cette Thèse est consacrée à la modélisation de l'étape de remplissage du moulage par injection dans un moule de forme complexe avec une obstruction. Les conditions non-isotherme., la viscoélasticité et la présence d'une interface mobile sont traitées dans cette section. Des réseaux curvilinéaires s'adaptant à la solution sont utilisés pour la solution numérique des équations dans un domaine qui est fonction du temps. Les profils de température, pression et vitesse à l'intérieur de la cavité ont été obtenus par cette méthode. Des études paramétriques ont révélé l'effet de caractéristiques importantes du procédé sur les gradients de pression et de température durant le remplissage. Les prédictions du modèle sont comparées à des résultats expérimentaux obtenus sur une machine de moulage par injection. Le modèle est capable de prédire, avec une précision satisfaisante, l'évolution de la pression ainsi que les gradients de pression qui se développent dans la cavité durant le remplissage. Enfin, une solution tridimensionnelle de l'équation d'énergie a révélé la forte variation spatiale et temporelle de la température à l'intérieur du moule dans la direction du plan et de l'épaisseur. Les profils de cristallinité ont été obtenus en utilisant la modèle d'Avrami.

ACKNOWLEDGEMENTS

I wish to express my sincere gratitude and appreciation to my supervisor Dr. M.R. Kamal for his guidance, support and encouragement during the course of this study. He supplied the means that made this work possible, gave me the academic freedom to pursue my ideas and always was a source of motivation and wise advice in difficult moments.

Several of my colleagues with the Polymer Group at McGill helped in various ways. I wish to thank in particular Mr. Furong Gao for his help in the injection molding experiments, Mr. Savvas Hatzikiriakos for his help in the rheological characterization of the resin and for many helpful discussions and Dr. Peter Singh for his help with the APPLICON graphics. Also Mark Weber and Mazen Samara for helpful suggestions on the manuscript and Mr. Dimitri Kolovos for his advice regarding the RMS experiments.

The financial assistance of the Faculty of Graduate Studies at McGill University and that of the Department of Chemical Engineering at McGill University is highly appreciated. This work was also made possible thanks to the excellent computer and graphics facilities of the Polymer Group, Department of Chemical Engineering, McGill University.

TABLE OF CONTENTS

ABSTRACT	i1
RESUME	i2
ACKNOWLEDGEMENTS	i3
TABLE OF CONTENTS	i4
LIST OF FIGURES	i8
LIST OF TABLES	i18
LIST OF APPENDICES	i19
INTRODUCTION	0
(I): NUMERICAL GRID GENERATION	1
(I.1) PRELIMINARIES	1
(I.2) RECENT ADVANCES IN NUMERICAL GRID GENERATION	3
(I.3) RECENT APPLICATIONS OF CURVILINEAR COORDINATE SYSTEMS	4
(I.4) METHODS FOR NUMERICAL GRID GENERATION	6
(I.4.1) Elliptic Grid Generation	6
(I.4.2) The Biharmonic System	8
(I.4.3) Other PDE-based Grid Generation Methods	9
(I.4.4) Algebraic Grid Generation	10
(I.4.5) Mixed Grid Generation Methods	11
(I.5) ORTHOGONAL AND NON-ORTHOGONAL GRIDS	12
(I.6) STRUCTURED - UNSTRUCTURED MESHES	16
(I.7) GRID GENERATION ON MULTIPLY CONNECTED DOMAINS	17
(I.8) VALIDATION OF THE TRANSFORMATION ROUTINES AND OF THE LAPLACE SOLVER	19
(I.9) SUMMARY	20
(II) SIMULATION OF VISCOELASTIC FLOW	22
(II.1) PRELIMINARIES	22
(II.2) FORMULATION OF THE PROBLEM	25

		i5
(II.3)	NUMERICAL SOLUTION	28
(II.3.1)	Numerical Treatment of the Constitutive Equation	28
(II.3.2)	Transformation of the Model Equations in Curvilinear Coordinates	31
(II.3.3)	Discretization of the Transformed Equations	34
(II.3.4)	Stability of Finite Difference Approximations and Upwind Differencing	35
(II.3.4.1)	The QUICK Upwinding Scheme	38
(II.3.5)	Transformation and Discretization of the non-Newtonian Source Function $D(S)$.	39
(II.3.6)	Solution of the Discrete Equations	42
(II.3.7)	The Numerical Algorithm	46
(II.4)	VALIDATION OF THE NUMERICAL ALGORITHM	49
(II.4.1)	Comparisons With Numerical and Experimental Results from the Literature.	49
(II.4.2)	Quantitative Comparison with Standard Software	53
(II.4.3)	Grid Refinement Studies	57
(II.5)	CASE STUDIES	59
(II.5.1)	The 4:1 Sudden Contraction	59
(II.5.1.1)	Stress Patterns	62
(II.5.1.2)	Flow Patterns	68
(II.5.2)	Smooth 4:1 Contractions	68
(II.5.3)	Flow in a 20:1 Tapered Contraction	81
(II.5.4)	Flow in a non-Symmetric Channel	81
(II.5.5)	The Contraction/Expansion Problem	88
(II.5.6)	Flow in a Bend	96
(II.6)	CONCLUSIONS	105
(III)	INJECTION MOLDING	107
(III.1)	PRELIMINARIES	107
(III.2)	MATHEMATICAL ANALYSIS OF THE FILLING STAGE	109
(III.2.1)	Fluid Dynamics	109

(III.2.2)	The Energy Equation	113
(III.2.3)	The Constitutive Model	115
(III.2.4)	Viscosity Modelling	118
(III.2.5)	Pressure Calculation	119
(III.2.6)	Previous Modelling Work on Filling	121
(III.3)	EXPERIMENTAL	125
(III.3.1)	Objectives	125
(III.3.2)	Material	125
(III.3.2.1)	Rheological Characterization	127
(III.3.3)	Equipment	131
(III.3.3.1)	Injection Molding Machine	131
(III.3.3.2)	Instrumentation	131
(III.3.4)	Experimental Conditions and Procedure	133
(III.3.5)	Certain Experimental Observations	133
(III.3.5.1)	Pressure Variation	133
(III.3.5.2)	Progression of the Melt Front	135
(III.3.5.3)	Shape of the Advancing Front	135
(III.4)	SIMULATION RESULTS	140
(III.4.1)	Progression of the Melt Front	140
(III.4.2)	Variation of Cavity Pressure with Time	143
(III.4.2.1)	Effect of Ram Velocity	143
(III.4.2.2)	Effect of the Geometry of the Cavity	143
(III.4.2.3)	Effect of Melt Temperature at the Gate	149
(III.4.2.4)	Effect of Material Properties	149
(III.4.3)	Pressure Drop in the Cavity During Filling	149
(III.4.3.1)	Effect of Ram Velocity	149
(III.4.3.2)	Effect of the Geometry of the Cavity	152
(III.4.3.3)	Effect of Melt Temperature	152
(III.4.3.4)	Effect of Material Properties	152
(III.4.4)	Temperature Drops in the Cavity During Filling	157

(III.4.4.1)	Effect of Ram Velocity	157
(III.4.4.2)	Effect of Geometry	157
(III.4.4.3)	Effect of Material Properties	160
(III.4.5)	Spatial Variation of Certain Characteristic Parameters	160
(III.4.6)	Three Dimensional Thermal Analysis	163
(III.4.6.1)	Rectangular Cavity - Thermal Profiles	163
(III.4.6.2)	Complex cavity - Microstructure Development During Filling	171
(III.5)	COMPARISON OF MODEL PREDICTIONS WITH EXPERIMENTAL DATA	179
(III.6)	SUMMARY	197
(IV)	CONCLUSION	199
(IV.1)	Conclusions	199
(IV.2)	Recommendations	200
(IV.3)	Novel Contributions	202
(V)	LIST OF SYMBOLS	204
(VI)	REFERENCES	207
	APPENDIX A.1	
	APPENDIX A.2	
	APPENDIX A.3	
	APPENDIX A.4	
	APPENDIX A.5	
	APPENDIX A.6	
	APPENDIX A.7	

LIST OF FIGURES

I.4.5.1	Flow diagram for interactive grid generation.	13
I.7.1	Methods for transforming multiply connected physical domains into simple computational domains; (a) slab configuration, (b) slit configuration, (c) reduction of connectivity using a cut.	18
I.8.1	Curvilinear grid used for the numerical solution of the Laplace equation in the annular region between two cylinders.	21
II.3.5.1	Computational molecules associated with the discretization of the non-Newtonian source function $D(S)$; (a) in cartesian and (b) in curvilinear coordinates with QUICK upwinding.	41
II.3.5.2	(a): Computational molecule used in the solution of the Poisson equation in Cartesian Coordinates, and (b), the corresponding molecule in general curvilinear coordinates. (c-e): Computational molecules associated with the numerical solution of the constitutive equation: (c); central differencing, (d) first order upwinding, (e) QUICK scheme.	45
II.4.1	Comparison between the present solution (solid lines) and the solution of Kawaguti (markers) for Newtonian flow in a bend. Contours are values of the stream function.	50
II.4.2	Comparison between the present solution (broken lines) and the solution of Cochrane et.al. (broken lines) for flow in a bend (contours are vorticity levels).	51
II.4.3	Comparison between simulation results (solid lines) and experimental velocity measurements (broken lines) from Cochrane et al. U and V are velocities in the horizontal and transverse directions respectively.	52
II.4.4	Predicted YY-normal stress patterns; solid lines from Song & Yoo (1987), broken lines from present study. Contour levels are: (A):-0.85, (B):-0.55, (C):-0.25, (D):-0.10, (E):0.1, (F):0.9. Dimensionless quantities.	54

II.4.2.1	Curvilinear grid on the complete 4:1 sudden contraction, used for comparison of the proposed numerical solution with standard software.	55
II.4.3.1	Meshes used for grid refinement studies in a 4:1 contraction with smooth edge.	58
II.5.1.1	Grids constructed on a 4:1 sudden contraction; (A) $P=Q=0$, (B): attraction to the upper boundary, (C) high concentration of grid lines near the reentrant corner.	63
II.5.1.1.1	Dimensionless shear stress $ T^y $ distribution in a 4:1 contraction. Solid line: $We=0.7$, broken line: $We=0.01$	65
II.5.1.1.2	Dimensionless stress contours on a planar 4:1 contraction at $We=0.32$ and $Re=2.3$	66
II.5.1.1.3	Effect of kinematics used in the integration of the constitutive model on the xx -normal stress along the $i=11$ coordinate line. Solid line: viscoelastic kinematics; dotted line: Newtonian kinematics. Grid (A) of figure (II.5.1.1).	67
II.5.1.2.1	Streamlines of a Newtonian fluid in a 4:1 abrupt contraction at various levels of the Reynolds number.	69
II.5.1.2.2	Streamlines of a Maxwell fluid ($We=0.7$) in a 4:1 abrupt contraction at various levels of the Reynolds number.	70
II.5.2.1	The rounded corner geometry and part of the computational grid used in the simulations.	72
II.5.2.2	Streamlines of a Maxwell fluid in the R1 rounded-corner contraction at two elasticity levels.	73
II.5.2.3	Streamlines of a Maxwell fluid in the R3 rounded corner contraction at two elasticity levels.	74
II.5.2.4	Effect of fluid elasticity ($De=\lambda \cdot \dot{\gamma}_{max}$) on vortex strength in various meshes for the rounded corner geometries R1 and R3. The vortex strength is defined as the (%) ratio of the circulation in the vortex to the total flowrate through the contraction.	75

II.5.2.5	Effect of fluid elasticity ($De=\lambda \cdot \gamma_{max}$) on vortex size in various meshes for the rounded corner geometries R1 and R3.	76
II.5.2.6	Dimensionless xx-normal stresses along the wall in a 21*42 and 21*45 meshes in the geometries R1 and R3. (a): Solid line corresponds to geometry R1, dotted line to R3. (b): Geometry R1.	78
II.5.2.7	Dimensionless xx-normal stresses along the $i=20$ coordinate line (closest to the wall) in a 21*42 mesh in the geometry R3.	79
II.5.2.8	Dimensionless xx- and yy-normal stresses along the $i=2$ coordinate line (near the centreline) for various values of the relaxation time in the geometry R3.	80
II.5.2.9	Stress contours on the contraction R1. $Re=0.1$ and $\lambda=0.675$. Contour values are (in alphabetical order): For T^{xx} ; 10, 3, 2, 1, 0.5, 0.3, 0.2, 0.1, 0, -0.15, -0.2. For T^{yy} ; 0.7, 0.6, 0.45, 0.3, 0.15, 0, -0.15, -0.3, -0.4, -0.6. For T^{xy} ; 3, 1.5, 1, 0.75, 0.55, 0.45, 0.35, 0.2. For $(T^{xx}-T^{yy})$; 10, 4, 2.5, 2, 1, 0.5, 0.1, 0, -0.2, -0.4.	82
II.5.2.10	Effect of elasticity on the xx-normal stress in the contraction R1. $Re=0.1$	83
II.5.2.11	Centerline velocity in the rounded corner contraction R1 at various elasticity levels	84
II.5.3.1	The geometry and the curvilinear mesh used in the study of the 20:1 tapered contraction	85
II.5.3.2	Dimensionless xx- and yy-normal stresses in a 20:1 tapered contraction at $We=0.15$	86
II.5.3.3	Vorticity distributions in the 20:1 tapered contraction at $We=0.1$. (B): Corner detail.	87
II.5.4.1	The geometry and the curvilinear mesh used in the study of the 4:1 sudden contraction with asymmetric entrance region.	89

II.5.4.2	Streamlines (A) and shear stress (B) patterns for a Maxwell fluid flowing through a 4:1 non-symmetric contraction	90
II.5.4.3	Dimensionless principal stress difference ($T^x - T^y$) in a non symmetric 4:1 planar contraction	91
II.5.5.1	The geometry and the curvilinear mesh used in the study of the contraction/expansion flow	93
II.5.5.2	Secondary flow in the contraction/expansion problem at various elasticity levels. $Re=12.0$	94
II.5.5.3	Vortex size and strength at various relaxation times in the contraction - expansion geometry. $Re=12$.	95
II.5.5.4	Dimensionless xx - and yy -normal stresses along the axis of symmetry in the contraction/expansion geometry for a range of the fluid elasticity at $Re=12$.	97
II.5.5.5	Wall values of the dimensionless xx -normal stress (A) and of the vorticity (B) at a range of the fluid relaxation time. $Re=12$.	98
II.5.5.6	Effect of inertia on flow patterns in a contracting/expanding flow of a Newtonian fluid. Part (C) shows the actual length of the computational domain used in the simulations.	99
II.5.5.7	Effect of inertia on vorticity distributions in a contracting/expanding flow of a Newtonian fluid.	100
II.5.6.1	The geometry and the curvilinear grid used to study the flow in a bend. The grid lines are normal to the upper boundary of the bend.	101
II.5.6.2	Vorticity distributions in a bend at $Re=48$ (A) and $Re=16$ (B). Newtonian flow.	102
II.5.6.3	Corner detail of the secondary flows in a bend at $Re=48$. Newtonian fluid	103
II.5.6.4	Corner detail of vorticity contours in a bend. Maxwell fluid; $Re=16$ and $We=0.14$	104

		i12
II.5.6.5	Dimensionless stress contours in a Maxwell fluid ($We=0.24$) flowing through a bend at $Re=4.0$.	106
III.3.1.1	Complex shaped cavity used in the injection molding experiments (A) and the location of temperature (T_1, T_2, T_3) and pressure (P_1, P_2, P_3) transducers (B).	126
III.3.2.1.1	Shear viscosity data obtained for the resin Sclair 2908 (INSTRON capillary measurements) and the associated power law parameters.	128
III.3.2.1.2	Dynamic viscosity data for resin Sclair 2908. RMS experiments.	129
III.3.2.1.3	Dynamic storage (G') and loss moduli (G'') for the resin Sclair 2908.	130
III.3.5.1.1	(A) Typical variation of cavity and nozzle pressure during an injection molding cycle; (B) Typical variation of cavity pressure at the gate (cavity CR1).	135
III.3.5.2.1	Response of the surface cavity thermocouples during an injection molding cycle at two temperatures showing the effect of melt temperature on melt progression speed and filling times; experimental.	136
III.3.5.3.1	Experimental short shots showing the evolution of the shape and location of the free surface during filling.	137
III.3.5.3.2	Experimental short shots showing the evolution of the shape and location of the free surface during filling.	138
III.3.5.3.3	Experimental shorts shots showing the detailed evolution of the shape of the free surface in the wake of the obstacle and the formation of weld line.	139
III.4.1.1	Predicted filling patterns for the complex cavity TE9 (Table III.4.2.2.1) at various melt flowrates.	141
III.4.1.2	Predicted filling patterns in a rectangular cavity of constant thickness.	142
III.4.1.3	Computational grids constructed automatically at various instances during filling of mold CR1.	144

III.4.1.4	Computational grids constructed automatically at various instances during filling of mold CR1.	145
III.4.2.1	Effect of ram velocity on pressure-time profiles at two locations in the cavity CR1 (corresponding to the locations of transducers P1 and P2). $T_{melt}=200^{\circ}$ C.	146
III.4.2.2	Effect of the geometry of the mold on pressure-time profiles at two locations in the cavity CR1 (corresponding to the locations of transducers P1 and P2). $T_{melt}=200^{\circ}$ C.	147
III.4.2.3	Effect of melt temperature at the gate on pressure-time profiles at two locations in the cavity TE9 (corresponding to the locations of transducers P1 and P2).	150
III.4.2.4	Effect of power law parameters on the pressure-time profile at the gate; (A) parameters as reported by Lafleur(1983),(B) parameters determined in this study. Cavity CR1.	151
III.4.3.1	Effect of ram velocity on pressure drop in the cavity CR1 at two instances during filling. $T_{melt}=200^{\circ}$ C.	153
III.4.3.2	Effect of mold geometry on pressure drop at an instant during filling. $T_{melt}=200^{\circ}$ C. Solid line : cavity TE15; dotted line: cavity TE2; broken line: cavity TE9 (refer to Table III.4.2.2.1).	154
III.4.3.3	Effect of melt temperature at the gate on pressure drop in the cavity TE9 at an instant during filling along the $i=16$ coordinate line.	155
III.4.3.4	Effect of power law parameters on pressure drop in the cavity CR1 at $t=1.34s$. (A) parameters reported by Lafleur (1983); (B) parameters determined in this study.	156
III.4.4.1	Effect of ram velocity on temperature drop in the cavity CR1 at two instances during filling. $T_{melt}=200^{\circ}$ C.	158
III.4.4.2	Effect of mold geometry on temperature drops at various instances during filling. $T_{melt}=200^{\circ}$ C. Solid line : cavity TE15; dotted line: cavity TE2; broken line: cavity TE9 (refer to Table III.4.2.2.1).	159

		i14
III.4.4.3	Effect of power law parameters on temperature profile in the cavity CR1 at $t=1.34s$ and $t=0.91s$. (A) parameters reported by Lafleur (1983); (B) parameters determined in this study.	161
III.4.5.1	Spatial variation of temperature at an instant towards the end of filling ($t=1.6s$). Cooling Rate: $482 (W/m^2/K)$; Ram velocity 1.0 cm/s ; $T_{\text{mold}}=235^{\circ} \text{ C}$. Mold TE9 (A) and CR1 (B).	162
III.4.5.2	Spatial variation of viscosity (a) and rate of deformation (expressed by II, (b)) in cavity CR1. Heat transfer coef. = $482 (W/m^2/K)$; Ram velocity 1.0 cm/s ; $T_{\text{mold}}=235^{\circ} \text{ C}$.	164
III.4.5.3	Predicted spatial variation of shear stresses in the thickness direction (T^x and T^y). Cavity CR1. Heat transfer coef. = $482 (W/m^2/K)$; Ram velocity 1.0 cm/s ; $T_{\text{mold}}=235^{\circ} \text{ C}$.	165
III.4.5.4	Predicted planar distribution of longitudinal (A) and transverse (B) velocities in cavity C1. Heat transfer coef. = $482 (W/m^2/K)$; Ram velocity 1.0 cm/s ; $T_{\text{mold}}=235^{\circ} \text{ C}$.	166
III.4.5.5	Predicted distribution of T^x (A) and longitudinal velocity (A) in cavity CR1. Heat transfer coef. = $482 (W/m^2/K)$; Ram velocity 1.0 cm/s ; $T_{\text{mold}}=235^{\circ} \text{ C}$.	167
III.4.6.1	Predicted distribution of temperature at the end of filling of a rectangular cavity, at two planes in distance DZ from the wall of the mold.	169
III.4.6.2	Predicted distribution of temperature at the end of filling of a rectangular cavity, at planes in distance $DZ=0.0378'$ from the wall of the mold and along the centerplane of the mold.	170
III.4.6.3	Gap-wise distribution of temperature at the end of filling of a rectangular cavity along the line $i=2$. The thickness of the cavity has been multiplied by 10 for the purpose of illustration.	172

		i15
III.4.6.4	Gap-wise distribution of temperature at the end of filling of a rectangular cavity along the line $i=6$. The thickness of the cavity has been multiplied by 10 for the purpose of illustration.	173
III.4.6.5	Gap-wise distribution of temperature at the end of filling of a rectangular cavity along the centerline. The thickness of the cavity has been multiplied by 10 for the purpose of illustration.	174
III.4.6.6	Crystallinity profile along the logical plane $k=2$ towards the of filling of cavity CR1. Heat transfer coefficient is $538 \text{ W/m}^2\text{K}$.	177
III.4.6.7	Temperature profiles on the logical plane $k=2$ and on the centerplane ($k=6$) towards the of filling of cavity CR1. Heat transfer coefficient is $538 \text{ W/m}^2\text{K}$.	178
III.5.1	Experimental ram velocity profile during the filling stage corresponding to experiment HP6.	180
III.5.2	Comparison between experimental and computed pressure-time profiles. Experiment HP6.	181
III.5.3	Comparison between computed and experimental pressure drops in the cavity. Experiment HP6.	182
III.5.4	Computed temperature drops in the cavity CR1 for conditions corresponding to those of experiment HP6.	184
III.5.5	Experimental ram velocity profile during the filling stage corresponding to experiments HP8 and HP9.	187
III.5.6	Comparison between experimental and computed pressure-time profiles. (A): Experiment HP8; (B): Experiment HP9.	188
III.5.7	Comparison between computed and experimental pressure drops in the cavity. (A): Experiment HP8; (B): Experiment HP9	190

		i16
III.5.8	Computed temperature drops in the cavity CR1 for conditions corresponding to those of (a): Experiment HP8; (b): Experiment HP9.	191
III.5.9	Comparison between computed and experimental pressure-time profiles at the locations of the three pressure transducers in cavity CR1. Experiment HP9.	192
III.5.10	Experimental ram velocity profile during the filling stage corresponding to experiment HP7.	193
III.5.11	Comparison between experimental and computed pressure-time profiles. Experiment HP7.	194
III.5.12	Comparison between computed and experimental pressure drops in the cavity. Experiment HP7.	195
III.5.13	Computed temperature drops in the cavity CR1 for conditions corresponding to those of experiment HP7.	196
A.1.1	Some of the problems associated with unreasonable values of the distortion functions in Poisson-type elliptic grid generation.	1.3
A.4.1	Situations arising during mold filling that necessitate rearrangement of free surface nodes for successful continuation of the computations.	4.12
A.4.2	Other situations where rearrangement of the grid nodes on the free surface might be necessary.	4.14
A.4.3	Computational advancement of the free surface in the case of flow between two parallel planes, displaying the rolling motion of the free surface. No-slip conditions are imposed on the walls.	4.15
A.5.1	Spatial variation of T^x and $(T^x - T^y)$ at $t=0.8s$. Cooling Rate: $482 \text{ (W/m}^2\text{/K)}$; Ram velocity 1.0 cm/s ; $T_{\text{melt}}=235^\circ \text{ C}$. Mold TE9.	5.2
A.5.2	Spatial variation of the second invariant of the rate of deformation tensor (a) and of viscosity during the filling of cavity TE9 at $t=1.2s$. Predicted values. Cooling Rate: $482 \text{ (W/m}^2\text{/K)}$; Ram velocity 1.0 cm/s ; $T_{\text{melt}}=235^\circ \text{ C}$.	5.3

- A.5.3 Spatial variation of T^x and T^y stresses during the filling of cavity TE9 at $t=1.2s$. Predicted values. Cooling Rate: 482 ($W/m^2/K$); Ram velocity 1.0 cm/s; $T_{melt}=235^\circ C$. 5.4
- A.5.4 Spatial variation of T^y (a) and transverse planar velocity (b, in in/s) during the filling of cavity TE9 at $t=1.2s$. Predicted values. Cooling Rate: 482 ($W/m^2/K$); Ram velocity 1.0 cm/s; $T_{melt}=235^\circ C$. 5.5
- A.5.5 Spatial variation of longitudinal (U) and transverse (V) planar velocities at $t=0.8s$. Cavity TE9. Cooling Rate: 482 ($W/m^2/K$); Ram velocity 1.0 cm/s; $T_{melt}=235^\circ C$. 5.6
- A.5.6 Spatial variation of the second invariant of the rate of deformation tensor (a) and of viscosity during the filling of cavity TE9 at $t=0.8s$. Predicted values. Cooling Rate: 482 ($W/m^2/K$); Ram velocity 1.0 cm/s; $T_{melt}=235^\circ C$. 5.7
- A.5.7 Spatial variation of the second invariant of the rate of deformation tensor (A) and of viscosity (B) during the filling of cavity TE9 at $t=1.6s$. Predicted values. Cooling Rate: 482 ($W/m^2/K$); Ram velocity 1.0 cm/s; $T_{melt}=235^\circ C$. 5.8
- A.5.8 Spatial variation of T^x and (T^x-T^y) at $t=1.6s$ during the filling of mold TE9. Cooling Rate: 482 ($W/m^2/K$); Ram velocity 1.0 cm/s; $T_{melt}=235^\circ C$. 5.9
- A.5.9 Spatial variation of T^x and T^y stresses during the filling of cavity TE9 at $t=1.6s$. Predicted values. Cooling Rate:482 ($W/m^2/K$); Ram velocity 1.0 cm/s; $T_{melt}=235^\circ C$. 5.10

LIST OF TABLES

Table (II.1):	Difference (%) between the two numerical solutions along the axis of symmetry in an abrupt 4:1 contraction	56
Table (II.2):	Influence of grid refinement on computational results. (a): Newtonian fluid, (b): Maxwell fluid ($De=1.7$). Geometry R360	
Table (III.3.3.1):	Specifications of the injection molding machine	132
Table (III.4.2.2.1):	Dimensions of cavities used in simulation studies.	148
Table (III.5.2):	Comparison between predicted and experimental time required for the melt front to reach the temperature transducers T1, T2 and T3 in cavity CR1.	186

LIST OF APPENDICES

- Appendix A.1:** Numerical Implementation of Elliptic Grid Generator.
- Appendix A.2:** Coordinate Invariance of Partial Differential Equations.
- Appendix A.3:** Review of Transformation Relations.
- Appendix A.4:** The Boundary Conditions.
- Appendix A.5:** Further Results on the Spatial Variation of Key Process Parameters During Injection Mold Filling.
- Appendix A.6:** Dimensions of the Complex-Shaped Cavity Used in the Simulations.
- Appendix A.7:** Boundary Conditions in Injection Mold Filling.

INTRODUCTION

As the title indicates, this study is concerned with the numerical simulation of viscoelastic flows in complex geometries. The ultimate objective, is to model the filling of a cold mold of complex shape with a molten viscoelastic, crystallisable material such as polyethylene.

This Thesis evolves in three largely independent steps, each with its separate introduction, literature survey and summary sections. In part (I), the main ideas behind the concept of boundary-fitted curvilinear coordinates (BFCCs) and numerical grid generation are presented. This is a fairly new field that has seen extensive use in computational fluid dynamics but only limited use in the materials processing field (even though commercial software such as Phoenics are based on this concept). In part (II), BFCCs are used for the numerical simulation of steady state, isothermal flows of a Maxwell fluid in various complex geometries.

Part (III) is concerned with the modelling of the filling stage of injection molding of a material obeying the White-Metzner constitutive model. Non-isothermal free surface flows are computed as the melt fills the cavity. In the first approach of this subject, the model equations are solved in a "gap-averaged" sense, ignoring thermal gradients in the thickness direction and evaluating the state variables on a "representative average plane". In section (III.4.6) a three dimensional solution of the energy equation during filling is presented, which, coupled with the non-isothermal crystallization kinetics model of Nakamura (1972,1973) allows for a complete representation of the thermal fields during filling, an evaluation of crystallinity development, as well as for an estimation of the thickness of the solidified layer and its effect on the pressure build-up during filling. All the computer programs developed in the course of this work can be obtained upon request from the Author and/or Professor M.R. Kamal, Dept. of Chemical Engineering, McGill University.

(I) NUMERICAL GRID GENERATION

(I.1) PRELIMINARIES

Numerical grid generation has now become a common and often necessary link in the chain of events that lead to the numerical solution of partial differential equations (PDEs) on regions of arbitrary shape. This is especially true in computational fluid dynamics, from whence much of the impetus for the development of numerical grid generation, but the approach is equally applicable to all physical problems that involve solution of partial differential equations on arbitrary domains. Numerically generated boundary conforming curvilinear meshes have provided the key to removing the problem of the boundary shape from finite difference solutions, and the same grids can be equally well used in conjunction with finite element codes. With such meshes, all numerical algorithms are implemented on a uniform square grid in the logical domain, regardless of the shape of the physical region. The method is equally applicable to steady state as well as transient problems, with rigid or deforming boundaries.

In the earlier years of computational fluid dynamics, most of the emphasis was placed on the development of stable, fast and accurate finite difference algorithms for the solution of the discrete forms of the governing PDEs. As a result, a large body of knowledge has accumulated in this area. On the other side, since most of the finite difference algorithms are based on rectangular computational grids, their application to flow (or in general field) problems with a complex boundary requires the introduction of new nodes at the intersections of the grid lines with the domain boundaries. Unavoidably, this causes some boundary grid cells to be smaller than the interior ones, and, consequently, difference formulae on these grids can produce large and irregular truncation errors which contaminate the solution. Given that in most flow situations large gradients of the field variables exist near the boundaries, the

above-mentioned approach will give inaccurate solutions in the region where the highest accuracy is needed.

For the above reason, solution of the model equations in a coordinate system, with the property that the boundary of the physical system coincides with coordinate lines, is highly desirable. Spherical or cylindrical coordinates are examples of boundary conforming coordinate systems and have been used extensively to facilitate the solution of certain types of flow problems. A relatively recent development is the use of general curvilinear coordinate systems, so that the boundaries of the physical system, no matter how complex, coincide with coordinate lines (or surfaces in 3D). Two of the major advantages of such an approach are:

- (a) The boundary conditions can be applied accurately without any need for interpolation. Inversely, when the location of the boundary is to be determined (eg, in free surface problems) this can be done more accurately in curvilinear boundary conforming coordinates than in Cartesian coordinates.
- (b) Since a general boundary conforming curvilinear coordinate system can always be constructed, so that, for any shape of flow geometry the computational domain will be a uniform rectangular grid, all the existing knowledge on the finite difference solution of PDEs can be directly applied for the solution of the transformed flow equations.

Even though finite elements are by far the dominant simulation method in solid mechanics and the most commonly used method for the simulation of viscoelastic flow in complex geometries, last decade has seen a virtual explosion in the use of general curvilinear boundary-fitted coordinate systems for the solution of field problems in complex geometries, using the finite difference method. Problems treated by the method vary from aero- and general fluid dynamics to heat transfer, electric

fields, marine and environmental engineering and structure analysis. The field of numerical generation of curvilinear coordinate grids is, itself, developing as an independent research area, as evidenced by conferences and publications devoted entirely to this subject. It holds a great promise as a key element in the solution of realistic flow problems, particularly with the development of 3D grids, adaptive grids and multiblock grids.

(L2) RECENT ADVANCES IN NUMERICAL GRID GENERATION

A large number of papers has appeared in recent years concerning new ideas and methods in numerical grid generation. Among the subjects that seem to be of major interest is the use of multiblock configurations for the solution of field problems in very complex domains, where the connectivity between subregions is very important for a smooth solution (Ohring (1983), Eiseman (1982, 1982), Steinhoff (1986), Thompson (1987)). The use of higher than second order systems, namely the fourth order biharmonic system, is also a subject that draws attention because it is promising higher flexibility in controlling the smoothness as well as the orthogonality of the grid (Bell et al. (1982), Sparis (1985)).

Orthogonal grid generation in two dimensional domains is an active research area as well (Ryskin and Leal (1983), Mobley and Stewart (1980), Haussling and Coleman (1981), Ascoli et al. (1987), Davies (1981), Potter and Tuttle (1973)). It seems however, that higher order systems will eventually substitute the second order systems for the construction of orthogonal grids because of their higher flexibility.

Conformal mapping-based and algebraic grid generation methods have advanced in recent years (Eiseman (1982,1982,1985,1988), Floryan (1985,1986), Inoue (1983, 1985), Yang and Shih (1986). Finally, the increased need for 3D simulation, which approaches the feasibility point following the ever increasing use of supercomputers, has stimulated research in 3D curvilinear grid generation (Takagi et al. (1985), Marshall et al. (1986), Saltzman (1986), Kim and Thompson (1988)). In spite of that, much remains to be done in the theoretical treatment of 3D curvilinear grid genera-

tion. It seems that, at this stage, the best approach is the use of multiple contiguous block structures, which will divide the complex region in simpler subregions (Miki and Takagi (1986)).

(L3) RECENT APPLICATIONS OF CURVILINEAR COORDINATE SYSTEMS

It is out of the scope of this work to discuss in length publications concerning the applications of curvilinear coordinate systems in computational fluid dynamics. An excellent review article on this subject with 341 references, covering the progress made up to 1981 is that of Thompson et al. (1982). In the following the advances made in recent years will be summarized and new trends and new areas of application will be identified.

In the general area of computational fluid dynamics a large number of recent publications concerns the simulation of more realistic flow problems in complex two- or three-dimensional geometries, using boundary fitted curvilinear coordinate systems. A good example of the impact of numerically generated curvilinear coordinate systems in computational fluid dynamics is a series of two papers by Miyata and Nishimura (1985) and Miyata et al. (1987). In the first paper, they solved the 3D incompressible Navier-Stokes equations for the flow around a ship with free waves, using a traditional marker-and-cell finite difference algorithm. As the authors comment, "...although the agreement in wave geometry is satisfactory, the viscous flow is not solved due to the use of a rectangular inflexible mesh system ...". In the second paper, a general 3D boundary conforming curvilinear grid and higher accuracy finite difference expressions was used and better results were obtained, even though the contribution of the grid itself has not been explicitly evaluated by the authors.

Further applications of curvilinear coordinate systems in flow problems, always in the area of newtonian fluids, include analysis of flow in 2D channels of arbitrary shape (Aubert and Deville (1983), Hung and Brown (1977), Pope (1978), Rangwalla and

Munson (1987), Garg and Maji (1988), Rapley (1988), Loeffler (1988), Shyy (1988), Fodemski et al. (1987), Yang and Shih (1986). Applications in the solution of the Navier Stokes equations in 3D include the work of Miyata and Nishimura (1987), Shyy and Braaten (1986) and Yang and Camarero (1986), while a simulation of free surface flows using a boundary conforming curvilinear grid has been reported by Asaithambi (1987).

Since much of the impetus for the development of boundary conforming curvilinear grids has traditionally come from the field of computational aerodynamics, a number of recent applications concerns, naturally, the analysis of flow around moving or stationary solid bodies (Thames et al. (1977), Thompson et al. (1974), Ohring (1983), Ogawa and Ishiguro (1987), Rapley (1988), Lapworth (1988), Olling and Dulikravich (1987), Tzaribas et al. (1986)). Finally, the application of adaptive grids has been evaluated by Shyy (1988) and Eiseman (1987), who found that, for certain complex flows, the use of an adaptive grid smoothed the solution and dampened out instabilities, thus leading to a faster convergence (also Thompson, (1985)).

Solutions of field problems using general curvilinear coordinate systems have found applications in other areas, besides traditional fluid computations. Miki and Takagi (1986) used a 3D curvilinear grid generator in the solution of the 3D Poisson equation of electrostatics which simulates the field in the electron gun of a colour picture tube. Dvinsky and Popel (1986) used a boundary fitted curvilinear coordinate system to simulate the motion of a particle of arbitrary shape moving in a channel of arbitrary shape. Glakpe et al. (1987) solved the 3D convection problem in a study applicable to nuclear reactor spent fuel shipping casks. In the field of marine engineering, Li and Lu (1987) used a curvilinear grid to calculate the forces exerted by waves on large coastal and/or offshore structures, while Hauser et al. (1986, 1986) studied a part of the Hamburg harbour area by solving the shallow water equations in a curvilinear boundary fitted grid. Hsu and Tu (1987) used a self-adaptive curvilinear grid to predict the aerodynamic drag in a transonic projectile, while

Glekas et al. (1987) used general curvilinear coordinates to solve a problem of importance in environmental engineering, namely the transport of a passive contaminant in a hilly terrain. Finally, Baba et al. (1987) obtained spectacular results regarding the viscous boundary layer development, flow separation and vortex shedding around an oscillatory cylinder, solving the Navier Stokes equations in a general boundary fitted curvilinear grid.

(I.4) METHODS FOR NUMERICAL GRID GENERATION

It can be said, that the "modern era" of numerical grid generation started with the 1974 paper by Thompson et. al. where they described what is now known as "elliptic grid generator" and used it to solve potential flow around Joukowski and Karman-Trefftz airfoils. Because of its versatility, ease of implementation and smoothness of the resulting grids, elliptic grid generation is now widely used for numerical grid generation, its major disadvantage being the need for iterative solution of the generating equations and, in general, the non-orthogonality of the resulting meshes.

(I.4.1) Elliptic Grid Generation

In an elliptic grid generation system, the physical (x,y) and computational (ξ,η) coordinates are related through the following Poisson equations:

$$\nabla^2 \xi = P(\xi,\eta) \quad (I.1)$$

$$\nabla^2 \eta = Q(\xi,\eta) \quad (I.2)$$

In practice, we first define the rectangular (ξ,η) domain and from this and the boundary correspondence we determine the coordinates of the interior nodes. Therefore, the following set of equations is normally used:

$$\alpha \cdot x_{\xi\xi} - 2 \cdot \beta \cdot x_{\xi\eta} + \gamma \cdot x_{\eta\eta} = -(P \cdot x_{\xi} + Q \cdot x_{\eta}) \cdot J^2 \quad (I.3)$$

$$\alpha \cdot y_{\xi\xi} - 2 \cdot \beta \cdot y_{\xi\eta} + \gamma \cdot y_{\eta\eta} = -(P \cdot y_{\xi} + Q \cdot y_{\eta}) \cdot J^2 \quad (I.4)$$

where α, β, γ are functions of the transformation, given by:

$$\alpha = (x_{\eta})^2 + (y_{\eta})^2 \quad (I.5)$$

$$\beta = x_{\xi} \cdot x_{\eta} + y_{\xi} \cdot y_{\eta} \quad (I.6)$$

$$\gamma = (x_{\xi})^2 + (y_{\xi})^2 \quad (I.7)$$

J is the Jacobian of the transformation, given by

$$J = x_{\xi} \cdot y_{\eta} - y_{\xi} \cdot x_{\eta} \quad (I.8)$$

The functions P and Q are control (or distortion) functions used to control the distribution of the coordinate (grid) lines in the physical domain. According to Thompson et al. (1980, 1985), these functions can take the form of summations of decaying exponentials:

$$P = \sum e_i \cdot \text{sign}(\xi - \xi_i) \cdot \exp(-c_i \cdot |\xi - \xi_i|) - \sum b_i \text{sign}(\xi - \xi_i) \cdot \exp\{-d_i \cdot |(\xi - \xi_i)^2 + (\eta - \eta_i)^2|^{0.5}\} \quad (I.9)$$

$$Q = \sum e_i \cdot \text{sign}(\eta - \eta_i) \cdot \exp(-c_i \cdot |\eta - \eta_i|) - \sum b_i \text{sign}(\eta - \eta_i) \cdot \exp\{-d_i \cdot |(\xi - \xi_i)^2 + (\eta - \eta_i)^2|^{0.5}\} \quad (I.10)$$

In the first expression, the effect of a_i is to attract ξ -lines to a specific ξ_i -line, whereas the effect of b_i is to attract ξ -lines towards the point (ξ_i, η_i) . The intensity of the attraction is further determined by the coefficients c_i and d_i , which dictate how fast

the attraction decays with distance (note that $(\xi - \xi_0)$ is the distance between the lines ξ and ξ_0 , whereas $|(\xi - \xi_0)^2 + (\eta - \eta_0)^2|^{0.5}$ is the distance between points on a ξ -line and the point (ξ_0, η_0) .) If $P=Q=0$, the Laplace equation is recovered. In this case, no attraction to coordinate lines is imposed, and the form of the grid will be determined only by the distribution of the boundary nodes. In the absence of boundary curvature, the coordinate lines will tend to be equally spaced (smoothing effect of the Laplacian), but will become more closely spaced over convex boundaries and less so over concave ones. One of the attractive features of the Laplace system is that it produces the elliptic grid with the maximum possible smoothness. Further details on the form and functions of P and Q are given by Thompson et al. (1980, 1985).

It is interesting to note that, while a Laplace system (Equations (I.1) and (I.2), with $P=Q=0$) gives, theoretically, a one-to-one mapping since it exhibits an extremum principle (guaranteeing that the maximum values of the curvilinear coordinates occur on the boundary of the physical region), in the corresponding Poisson system ($P, Q \neq 0$), the extremum principle may be lost. Therefore, a Poisson elliptic system cannot guarantee the construction of an one-to-one mapping for arbitrary values of the P and Q . Nevertheless, the existence of an extremum principle is a sufficient but not necessary condition for that; thus, a Poisson system may give an one-to-one mapping, provided that some care has been taken for the selection of the control function P and Q . Some theoretical considerations on the uniqueness of the solutions of grid-generating PDE systems of second order have been recently discussed by Giannakopoulos et al. (1988). This subject is further discussed in Appendix A.1.

(I.4.2) The Biharmonic System

The elliptic system discussed previously, is by no means the only available elliptic grid generator. Thompson et al. (1985), Bell et al. (1982) and Sparis (1985) discuss other alternative elliptic systems. Of potential interest is a fourth order system, generated by the biharmonic equation:

$$\nabla^4 \xi = P(\xi, \eta) \quad (I.11)$$

$$\nabla^4 \eta = Q(\xi, \eta) \quad (I.12)$$

This system has the attractive properties of allowing specification of more boundary conditions than the second order Poisson system. Namely, it allows specification of both, the location of the boundary points and the intersection angles between the coordinate lines and the boundary. This is not possible with second order systems (Laplace or Poisson), which allow only Dirichlet or Neumann boundary conditions on the boundary. So when a grid orthogonal on the boundary is desired, the angle of the coordinate lines at the boundaries must be specified at 90° , and this deprives us from the choice of mesh spacing. In that case, the grid lines will concentrate near convex corners and disperse near concave ones. Therefore, a fourth order system is a good candidate for the construction of orthogonal grids in cases where complete boundary correspondence is required.

(I.4.3) Other PDE-based Grid Generation Methods

Beside the elliptic grid generator, parabolic and hyperbolic grid generation systems are also based on the solution of PDEs. In each of these cases, the grid is generated by numerical solution of a parabolic or hyperbolic set of PDEs, marching in the direction of one curvilinear coordinate between two boundary curves. In neither case can the complete boundary of the region be specified, the latter being a property only of elliptic generation systems. Because of the marching nature of these generating systems, both parabolic and hyperbolic grid generation are computationally faster than their elliptic counterpart which normally requires iterative solution. The parabolic system can be applied to generate the grid between the boundaries of a doubly connected region (eg, the annular region between two cylinders), whereas the hyperbolic system allows only one boundary to be specified, and is therefore of interest only in cases where the exact location of one boundary is not important (eg,

computational grid for flow around a sphere, cylinder, airfoil etc.). Hyperbolic systems can also be used to generate grids that are orthogonal to the boundary, and are particularly suitable for the simulation of external flows; a disadvantage is that mesh non-uniformities, originating from geometric discontinuities at the boundary will propagate into the field (characteristic property of hyperbolic systems). Similar effects are not present when elliptic generators are used, because of the smoothing effect of the Laplacian or Poisson operators.

(1.4.4) Algebraic Grid Generation

A class of grid generation methods that are not based on solution of PDEs is the algebraic grid generation methods. These are interpolation or approximation procedures that relate a computational domain which is a rectangular parallelepiped (square in 2D, box in 3D) to an arbitrarily shaped physical domain with corresponding sides. Traditionally, such transformations have been globally defined by analytic functions of a complex variable. In this case, the transformation yields conformal coordinates which are inherently non-singular and over which the equations of fluid dynamics assume their simplest possible form. The fundamental limitations, however, are a loss of control over the boundary point distribution and a practical restriction to two dimensions. According to Eiseman (1988), a successful way to define the interpolations is by means of univariate functions of the individual coordinates in the logical space, which are combined in a Boolean sum to create the complete transformation. In general, however, it is obvious that there are as many ways to generate algebraic grids as are interpolation methods (Langrange, Hermite and splines being some of the most popular ones). It is impossible to cover all these methods in this review. Further details can be found in Thompson (1985) and Eiseman (1988).

A recent development is the control point formulation (CPF) proposed by Eiseman (1988). In a CPF context, a set of control points is established within the grid in such

a way that the best features of a Boolean sum and tensor product are incorporated. The CPF has the capacity to conform precisely to prescribed boundaries, while being able to manipulate the configuration of the computational mesh through a rather sparse net of control points. The CPF has been used for the construction of interactively adaptive grids and a computer code (CFGRID) is available (Eiseman (1988)). Algebraic grid generation is computationally efficient and as such, ideally suited for interactive and/or adaptive grids.

(I.4.5) Mixed Grid Generation Methods

Since elliptic grid generation is computationally expensive, it is customary, in commercial grid generators designed to work on PCs and workstations, to combine elliptic and algebraic grid generation techniques. Usually, an algebraic method is used for the construction of the initial mesh, while an elliptic generator smoothens the algebraic grid.

In the context of this work, transfinite bilinear interpolation was used to supply a good initial guess for the coordinates of the interior nodes. This consisted of two linear Lagrange interpolations, each acting independently in each coordinate direction, therefore creating a multi-directional interpolation. The general form of the transfinite interpolation is:

$$\mathbf{r}(\xi, \eta) = \sum \phi_n(\xi/I) \cdot \mathbf{r}(\xi_n, \eta) + \sum \phi_m(\eta/J) \cdot \mathbf{r}(\xi, \eta_m) - \sum \phi_n(\xi/I) \cdot \phi_m(\eta/J) \cdot \mathbf{r}(\xi_n, \eta_m) \quad (\text{I.13})$$

In Equation (I.13), ϕ are Lagrange polynomials and \mathbf{r} is a position vector.

Using the result of the algebraic interpolation as initial guess, the final grid was constructed by solving the elliptic generating equations. Details of the numerical solution are given in APPENDIX (A.1). A general procedure for the generation of a computational mesh, where interactive refinement is included, is described in Figure

(I.4.5.1).

(I.5) ORTHOGONAL AND NON-ORTHOGONAL GRIDS

The following discussion concerns only elliptic grid generation systems. An orthogonal curvilinear coordinate system is one where the grid lines intersect at 90° . Analytically, this is equivalent to the condition that the non-diagonal components of the metric tensor vanish, since in 2D,

$$\cos(\theta) = \delta / (\alpha \cdot \gamma)^{0.5} \quad (\text{I.14})$$

where (θ) is the angle of intersection between coordinate lines and α, β and γ are defined by Equations (I.5) to (I.7).

In general, a curvilinear coordinate system for the solution of a PDE or a set of PDEs on an arbitrary domain does not have to be orthogonal. Nevertheless, there are some advantages associated with the use of an orthogonal grid:

- (a) In orthogonal grids, the transformed equations will include fewer terms; namely, the mixed derivatives will disappear.
- (b) The application of Neumann boundary conditions is more straightforward in an orthogonal grid.
- (c) Severe departure from orthogonality may introduce large truncation errors in the numerical solution.

There are basically two approaches in the construction of an orthogonal curvilinear coordinate system. Those based on the construction of the orthogonal grid starting from a non-orthogonal one (Davies, (1981), Potter and Tuttle (1973)), and those

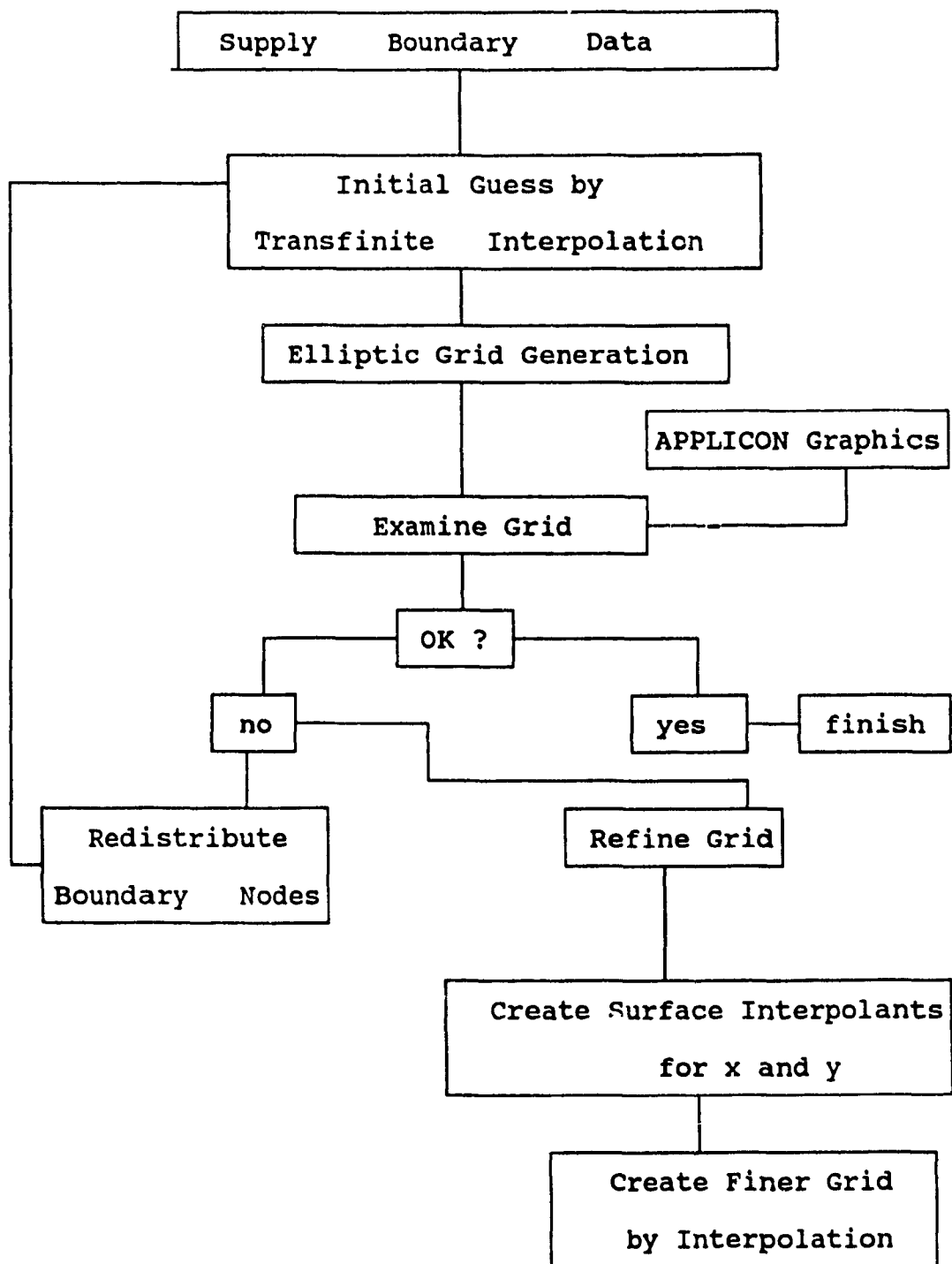


Figure (I.4.5.1): Flow diagram for interactive grid generation

based on solutions of PDEs. In the former case, a set of coordinate lines of the non-orthogonal system is retained, while the other set is replaced by lines emanating from the boundary and crossing the first set orthogonally. According to this method the line spacing can be controlled as in a non-orthogonal system using control functions, or by the distribution of the boundary points from which one set of lines emanates. This method permits specification of nodes on only 3 out of the 4 boundaries of the system, which can be a problem in cases where the boundary values are taken as solution of another problem (eg; in a non-isothermal flow situation where the temperatures on the wall are obtained as a solution of a separate heat transfer problem, or in the study of an interface between two immiscible fluids). In such a case, complete correspondence on certain boundaries is necessary, so that the coordinate lines on both sides emanate from the same boundary points- otherwise the application of matching conditions can be greatly complicated.

In construction methods based on solutions of PDEs, best described in the paper by Ryskin and Leal (1983) as the strong and weak constraint method, the orthogonal grid is constructed as the solution of an elliptic system. This method yields conformal mapping as the limiting case when the distortion function is 1. The method is considered superior to conformal mapping, since in conformal mapping the requirement that the distortion function be 1 can lead to grids unsuitable for numerical computations. In summary, the strong constraint method can be used to generate orthogonal grids in regions with a free surface, whereas the weak constraint method has to be used when the complete boundary correspondence is prescribed. In the last case, whose practical importance was explained above, the distortion function cannot be determined a priori but has to be updated iteratively as part of the solution (Thompson, (1985)). It has been shown by Ascoli et al. (1987), that separability of the distortion function is a sufficient condition for orthogonality of the grid constructed by the strong constraint method. Nevertheless, no such theoretical tool is available for the weak constraint method, and Chikhliwala and Yortsos (1985), who

have tested that method, found that it failed to give orthogonal grids of acceptable quality under conditions of complete boundary correspondence in regions without an axis of symmetry.

It has been indicated (Ryskin and Leal (1983) , Rangwalla and Munson (1987)) that the elliptic grid generation method of Thompson has the severe drawback of not giving generally orthogonal grids. This is not considered such a serious problem. In any case, a satisfactory degree of orthogonality can be achieved by proper selection of the boundary points, and this can be sufficient for computational purposes (Ferziger, (1987)). Furthermore, given the experience of Chikhliwala and Yortsos (1985) who found that there is always a deviation from perfect orthogonality (due to either the method of construction, the method of solution of the generating PDEs, an improper selection of the distortion function, the geometry of the domain of solution or simply numerical errors), it does not seem to be advisable to use the simplified forms of the transformed equations (that is, drop the mixed derivative terms). It is rather preferable to use the complete form of the transformed equations, in grids sufficiently close to orthogonal, so that truncation errors are kept at a minimum (Thompson, (1982)). Moreover, since it seems unlikely that orthogonal grids can be constructed in three dimensional problems (Ryskin and Leal, (1983)), it would be beneficial to gain as much experience as possible with the general non-orthogonal grids in the 2D case before proceeding to more complicated 3D problems. Of course, care should be exercised that the deviation from orthogonality is not too severe, or else problems might arise.

In this work, the general second order elliptic grid generation method of Thompson (1974) is followed. However, it was found necessary in the solution of the pressure equation with Newmann boundary conditions (see part III on injection molding) that the grid be normal to the boundary of the flow channel. Boundary orthogonality is easier to implement and less restrictive on the grid than complete orthogonality. The construction of grids orthogonal to the boundary will be discussed in APPENDIX

(A.1).

(L6) STRUCTURED - UNSTRUCTURED MESHES

In the classification of computational meshes one distinguishes between structured and unstructured meshes. A structured mesh is one where some relation, imposed by the generation technique, exists between the grid points. Structured meshes are created by various mappings (conformal, algebraic, PDEs), while an unstructured mesh is created in point-by-point fashion. In unstructured meshes, one has to define its connectivity to surrounding nodes besides the coordinates of each node. All known methods for solution of PDEs (finite differences, finite volume and finite elements) can be used in conjunction with structured meshes. Only integral methods (finite volume and finite elements) can be used on unstructured ones. Structured meshes are very attractive because of their simplicity, both in their generation as well as for the solution of the flow equations. However, for the solution of flow problems in increasingly complex domains using structured grids, it is most often necessary to break up the domain into many simpler blocks. In this case, the connectivity between these blocks must be specified, i.e. an explicit table must be generated which denotes the connectivity of the blocks as well as the coordinates of the grid points at the block interfaces. When the number of structured blocks becomes very large, as is the case of very complex domains, then the major advantage of structured meshes, i.e. their simplicity, is lost.

Construction of unstructured meshes is independent of the complexity of the physical domain; this makes them natural candidates for very complex problems. However, multiblock structured meshes have been successfully used in very complex domains, such as on and around complex airplanes, propellers, submarines etc. Given the inability of the unstructured meshes to support finite difference flow solvers, it is believed that structured meshes will continue to be widely used well into the next decade. However, as more numerical methods shift to integral techniques (this is a

fact already in aerodynamics) and the required geometrical complexity increases, it is likely that more and more emphasis will be placed on the use of unstructured meshes and/or hybrid meshes.

(I.7) GRID GENERATION ON MULTIPLY CONNECTED DOMAINS

The application of the grid generation ideas presented in the previous sections is straightforward when the physical domain is simply connected. Some special care should however be exercised when transforming multiply connected domains, such as domains with inserts. In the context of this study, it was necessary to generate grids in multiply connected domains during the simulation of injection molding in a cavity with an insert.

Three of the most popular methods for treating multiply connected domains are depicted in Figure (I.7.1). The slab configuration (I.7.1.A) simply excludes from the calculations all the interior points that fall on the insert; in this case, an insert of arbitrary shape is transformed into a rectangle in logical space. The slit configuration, shown schematically in Figure (I.7.1.B), transforms an insert into a horizontal or vertical line. Special care should be exercised when using this configuration, since all variables are double valued on the slit. In this case, no grid points are excluded from the calculations. A third way that reduces the connectivity of the physical space is shown in Figure (I.7.1.C). A cut is introduced, which opens the field; upon deformation of the opened domain one recovers the familiar rectangular computational domain. In this configuration, care should be exercised so that points on the two sides of the rectangular domain that correspond to the cut be assigned the same values of independent variables. Regions of higher connectivity can be treated similarly. For example, three inserts can be represented by three slits or three rectangles. Reduction of the connectivity of a highly complex domain by means of branch cuts can, however, result in extremely complex configurations. In this work the slit configuration was used. Examples of grids generated by this method are given in

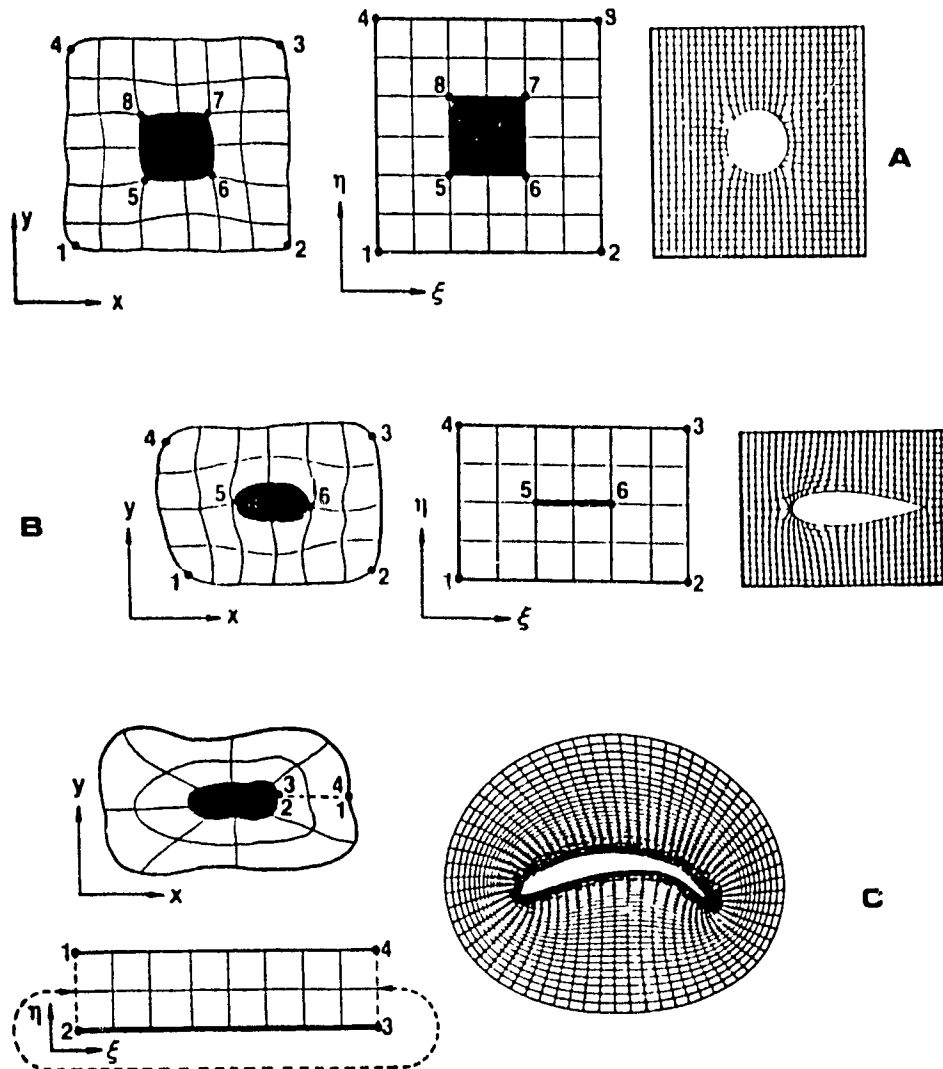


Figure (I.7.1): Methods for transforming multiply connected physical domains into simple computational domains; (A) slab configuration, (B) slit configuration, (C) reduction of connectivity using a cut.

Part (III).

(L8) VALIDATION OF THE TRANSFORMATION ROUTINES AND OF THE LAPLACE SOLVER

The purpose of this section is to test the accuracy of the transformation routines as well as the accuracy of the Laplace solver - the routine that solves the transformed form of the Laplace equation. In general curvilinear coordinates, this is given by Equation (I.15).

$$\nabla^2 f = (\alpha \cdot f_{\xi\xi} - 2 \cdot \beta \cdot f_{\eta\xi} + \gamma \cdot f_{\eta\eta})/J^2 + (\nabla^2 \xi) \cdot f_{\xi} + (\nabla^2 \eta) \cdot f_{\eta} \quad (\text{I.15})$$

The Laplace solver is a key routine for the calculation of stream function, vorticity, pressure and temperature (section (III) on injection molding and (II) on viscoelastic flow); it is therefore essential to establish the correctness of this subroutine. Furthermore, since the coefficients α , β , γ , $(\nabla^2 \xi)$ and $(\nabla^2 \eta)$ are functions of the coordinate transformation, it is also essential to establish that the transformation itself does not introduce errors that contaminate the results of the Laplace solver.

For this purpose it was decided to solve the Laplace equation in the annular region between two cylinders with $R_1=1$ and $R_2=10$, subject to Dirichlet boundary conditions:

$$f(R_1) = 2x \quad \text{and} \quad f(R_2) = 1.01x \quad (\text{I.16})$$

An analytical solution for the Laplace equation under these boundary conditions is:

$$f(x,y) = x(1 + 1/(x^2 + y^2)) \quad (\text{I.17})$$

This was the only case in this study that the "cut" configuration was used for grid generation. The cut was introduced along the line $(1,0) - (10,0)$. To ensure continuity of derivatives along the cut, it was specified that the ξ -coordinate lines are normal on the $\eta=1$ and $\eta=j_{\max}$ lines. The resulting grid is given in Figure (I.8.1). The maximum difference between analytical and numerical solution for the 19×31 grid of Figure (I.8.1) and a convergence tolerance of 10^{-5} was 1.4 %. The average error was 0.8%. Use of a 31×31 grid reduced the maximum and average errors to 0.9 and 0.5% respectively.

(I.9) SUMMARY

- The method of Numerical Grid Generation based on an elliptic generating system was chosen for the construction of structured curvilinear meshes on two-dimensional domains.
- The method was used successfully in simply and multiply connected regions.
- The correctness of the transformation routines and of the Laplace solver was successfully tested against available analytical solutions.

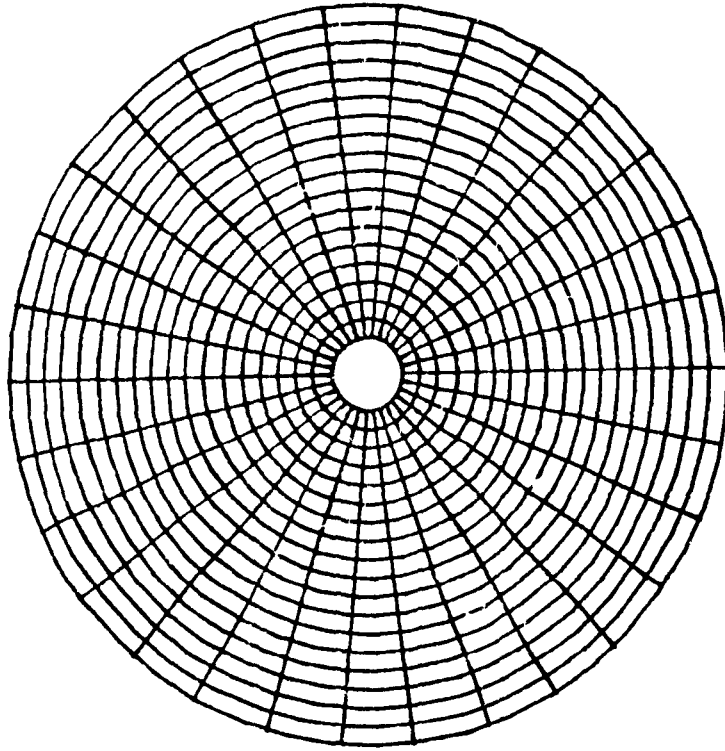


Figure (I.8.1): Curvilinear grid used for the numerical solution of the Laplace equation in the annular region between two cylinders.

(II) SIMULATION OF VISCOELASTIC FLOW

(II.1) PRELIMINARIES

Elastic fluids, such as polymeric solutions or melts, exhibit a substantially different flow behaviour compared with Newtonian or variable viscosity non-elastic fluids. Certain elastic effects, such as rod climbing, the hole pressure effect, the development of vortices in some entry flows, the die swell effect etc., can be attributed to non-zero normal stress differences that are characteristic of elastic materials. Others, such as stress relaxation, strain recovery and stress overshoot are manifestations of the memory of previous deformation that characterizes elastic fluids. It has been observed that the deviation from Newtonian behaviour is strongest in flow through channels involving abrupt changes in geometry.

Understanding and predicting complex viscoelastic flows is essential for the proper design and optimization of key polymer processing operations. However, the theoretical analysis of viscoelastic flows poses many challenges. These include the need for development of realistic constitutive equations, the development of proper numerical methods for the solution of the model equations, which have been shown to be more complex than their Newtonian counterpart, and the need for appropriate discretization techniques that will be both flexible and accurate in mapping complex flow fields. As of today, not all of the above subjects have been developed satisfactorily.

One of the major complications arises from the inadequacy of the well-documented Navier-Stokes equations of the Newtonian fluid mechanics to describe viscoelastic flows. The complex molecular structure of viscoelastic fluids gives rise to stress fields that cannot be predicted by the simple Newtonian viscosity. Therefore, the need has emerged for development of constitutive equations that will be suitable for these materials. Based on molecular theories, a number of such constitutive equations has

emerged in recent years (Bird et al. (1987)). These equations can be of the integral (explicit) or differential (implicit) type and relate the stresses with the kinematics of the flow field. None of the equations proposed this far can claim success in predicting all aspects of viscoelastic behaviour, especially in flowing polymer melts. The situation is better in dilute polymeric solutions, but still much remains to be done before completely reliable quantitative predictions for complex viscoelastic flows can be made. Comparisons of the predictions of various constitutive models in different flow situations still occupies a substantial part of the research in non-Newtonian fluid mechanics (Armstrong et al. (1985)). In this work the Upper Convected Maxwell Model (UCMM) was used. This choice is not justified because of its success in describing real polymer melt behaviour, but mostly because it has been widely used in previous simulations - thus giving some common ground with previous research.

Viscoelastic phenomena appearing in simple rheometrical experiments are now well understood and their theoretical prediction does not require sophisticated numerical analysis. Therefore, and since the most interesting, theoretically and industrially, non-Newtonian effects are observed in flows through channels of complex shape, the major effort in computational non-Newtonian fluid mechanics has been directed towards the prediction of viscoelastic effects in industrially important non-elementary geometrical configurations, such as flow over a slot, through contractions and expansions, flow between cylinders, around obstacles, corners etc.. In certain cases, this introduces geometrical singularities which represent the second major difficulty in the numerical solution of complex viscoelastic flows.

The third major problem in the simulation of viscoelastic flows is the fact that the numerical solutions tend to break down when the elasticity of the material, usually expressed by the Weissenberg or Deborah number, exceeds some critical value. The problem, termed as the High Weissenberg Number Problem (HWNP) in the literature, appears regardless of the discretization technique (finite differences or finite elements, (Davies et al. (1984))), or the choice of constitutive equation, even

though constitutive models which incorporate a retardation time have been found to be computationally more stable than purely elastic models. Reported critical Weissenberg numbers vary from study to study, but the symptoms behind the failure are more or less common: spurious, field-wide oscillations of the field variables, especially of the stresses, whose intensity increases as the elasticity parameter increases. Josse and Finlayson (1984) linked this failure to the inadequacy of the Galerkin formulation (in finite element solutions) to solve hyperbolic problems, especially in non-smooth geometries (see also King et al. (1988), Marchall and Crochet (1987)), Debbaut et al. (1988), Debbaut and Crochet (1986)). This of course would not answer why finite difference solutions showed the same unstable behaviour, and therefore a large amount of work has been devoted in relating the failure of viscoelastic simulations to approximation errors, (Mendelson et al. (1982), Dupret et al. (1985)), and to the change of type of the governing equations (Joseph et al. (1985), Ahrens et al. (1987), Yoo and Joseph (1985)). Because of this change, standard numerical techniques used in Newtonian fluid mechanics have been proven inadequate for the solution of the mixed-type non-Newtonian problem. Recent advances in this area include either switching algorithms that treat differently the elliptic and hyperbolic regions of the flow regime (Song and Yoo, (1987), Choi et al. (1988)) or the use of derived forms of the momentum equation that are explicitly elliptic (King et al. (1988)). Other researchers (Lipscomb et al. (1987) and Apelian et al. (1988)) have proposed the use of more realistic constitutive equations and relaxation of the non-slip boundary condition as means of handling viscoelastic flow problems with stress singularities (such as the stick-slip problem and the abrupt contraction problem). A review of the state of the art on the origins and cures of the HWNP has been given by Keunings (1986,1987).

Even though the problem is not settled yet, significant advances have been reported recently by Crochet and coworkers (1986, 1987, 1988) and King et al.(1988), both groups working with finite elements. Crochet and co-workers have focused on the use of sub-elements to account for the very steep stress gradients appearing in many

viscoelastic flows and on the use of streamline upwinding to take into account the hyperbolic nature of the constitutive equation; they obtained convergent solutions for very high values of the elasticity parameter in various contraction flows. King and co-workers employed an explicitly elliptic form of the momentum equation and obtained convergent results for high values of the elasticity parameter in stick-slip flows as well as in flows between eccentric cylinders. From the above, it becomes evident most of the advances in numerical simulation of viscoelastic flows have been reported in the context of finite elements. This is not surprising, since traditional finite difference techniques have difficulties dealing with complex shapes. However, successful use of finite differences for the simulation of viscoelastic flows has been reported by Perera and Walters (1977, 1977), Cochrane et al. (1981, 1982), Song and Yoo (1987), Choi et al. (1988).

(II.2) FORMULATION OF THE PROBLEM

We are interested in the simulation of steady-state, isothermal flows of an upper convected Maxwell fluid in channels of complex shape. Adopting the stream function/vorticity (ψ, ω) formulation of the equations of motion, we have to solve the elliptic stream function equation:

$$\nabla^2 \psi = -\omega \quad (\text{II.1})$$

and the elliptic vorticity equation

$$\nabla^2 \omega = \text{Re} \cdot (\psi_y \cdot \omega_x - \psi_x \cdot \omega_y) + D(\mathbf{S}) \quad (\text{II.2})$$

In (II.2), Re is the Reynolds number of the flow ($\text{Re} = \rho UL/\mu$), ρ and μ are the fluid density and viscosity respectively and $D(\mathbf{S})$ is a non-Newtonian source function, given by equation (II.3):

$$D(\mathbf{S}) = (\mathbf{S}^x - \mathbf{S}^y)_{,y} + (\mathbf{S}^y)_{,x} - (\mathbf{S}^y)_{,x} \quad (\text{II.3})$$

and $\mathbf{S}^x, \mathbf{S}^y, \mathbf{S}^z$, are the non-Newtonian contributions to the stress tensor (\mathbf{T}). The stream function (ψ) and vorticity (ω) are related to the kinematics of the flow as follows:

$$u = \partial\psi/\partial y, \quad v = -\partial\psi/\partial x, \quad \omega = \partial v/\partial x - \partial u/\partial y \quad (\text{II.3.a})$$

where (u) and (v) are the velocities in the x (longitudinal) and y (transverse) directions, respectively. Throughout this Thesis, subscripts indicate partial differentiation, whereas superscripts are reserved for tensor components.

The boundary conditions for stream function and vorticity at the inlet can be obtained from a proper velocity profile. On the axis of symmetry, $\omega=0$, and $\psi=\text{constant}$. On solid walls, $\psi=\text{constant}$ and (ω) will be obtained by:

$$\omega_{\text{wall}} = -(\nabla^2\psi)_{\text{wall}} \quad (\text{II.4})$$

More details on the boundary conditions and their finite-difference implementation can be found in standard books on Newtonian and non-Newtonian fluid mechanics (Roache, (1976), Crochet et al. (1984), Crochet and Walters (1983)) as well as in Appendix (A.3) of this Thesis.

To model the relation between stress and kinematics in the fluid, a constitutive equation is needed. The Upper Convected Maxwell model used in this work consists, in dimensionless form, of the following set of partial differential equations:

$$\mathbf{T}^x(1-2 \cdot \text{We} \cdot u_x) + \text{We} \cdot (u \cdot (\mathbf{T}^x)_x + v \cdot (\mathbf{T}^x)_y) - 2\text{We} \cdot \mathbf{T}^x \cdot u_x = 2 \cdot u_x \quad (\text{II.5})$$

$$\mathbf{T}^y(1-2 \cdot \text{We} \cdot v_y) + \text{We} \cdot (u \cdot (\mathbf{T}^y)_x + v \cdot (\mathbf{T}^y)_y) - 2\text{We} \cdot \mathbf{T}^y \cdot v_x = 2 \cdot v_y \quad (\text{II.6})$$

$$\mathbf{T}^* + \text{We} \cdot (\mathbf{u} \cdot (\mathbf{T}^*)_{,i} + \mathbf{v} \cdot (\mathbf{T}^*)_{,j}) - \text{We} \cdot \mathbf{T}^* \cdot \mathbf{v}_x - \text{We} \cdot \mathbf{T}^* \cdot \mathbf{u}_y = \mathbf{v}_x + \mathbf{u}_y \quad (\text{II.7})$$

The pertinent dimensionless quantities are:

$$x=x'/L, y=y'/L, u=u'/U, v=v'/U, \mathbf{T}=\mathbf{T}'L/U\mu \quad (\text{II.7.a})$$

where starred quantities are dimensional quantities. In (ii.5)-(II.7), We is the Weissenberg number, defined as $\text{We}=\lambda U/L$, where (λ) is a relaxation time of the fluid and U, L are a characteristic velocity and a characteristic length respectively. The discussion is limited to a single relaxation time. However, extension to a spectrum of relaxation times is straightforward in the context of differential constitutive models, by writing

$$\mathbf{T} = \sum \mathbf{T}_k \quad (\text{II.8})$$

where the contribution of each node \mathbf{T}_k obeys equations (II.5) to (II.7) with material parameters λ_k and μ_k . The Upper Convected Maxwell model is a member of the general family of differential constitutive models described by the generic equation:

$$\mathbf{A}(\mathbf{T}) \cdot \mathbf{T} + \lambda(\delta\mathbf{T}/\delta t) = \mu \cdot \boldsymbol{\gamma} \quad (\text{II.9})$$

$\delta\mathbf{T}/\delta t$ is an objective time derivative that is defined as a linear combination of lower ($\mathbf{T}^{(l)}$) and upper ($\mathbf{T}^{(u)}$) convected derivatives:

$$\delta\mathbf{T}/\delta t = \alpha \cdot \mathbf{T}^{(l)} + (1-\alpha) \cdot \mathbf{T}^{(u)} \quad (\text{II.10})$$

$$\mathbf{T}^{(l)} = \mathbf{D}\mathbf{T}/\mathbf{D}t + \mathbf{T} \cdot \nabla\mathbf{u}^T + \nabla\mathbf{u} \cdot \mathbf{T} \quad (\text{II.10.a})$$

$$\mathbf{T}^{(u)} = \mathbf{D}\mathbf{T}/\mathbf{D}t - \mathbf{T} \cdot \nabla\mathbf{u} - \nabla\mathbf{u}^T \cdot \mathbf{T} \quad (\text{II.10.b})$$

D/Dt is the material time derivative

$$D/Dt = \partial/\partial t + \mathbf{u} \cdot \nabla \quad (\text{II.10.c})$$

The Maxwell model is obtained as the limiting case of equation (II.9) when $\mathbf{A} = \mathbf{I}$, \mathbf{I} being the unit tensor. For $\alpha=0.0$, 0.5 and 1.0 we obtain the upper convected, corrotational and lower-convected Maxwell models. Viscometric data indicate that suitable values for (α) are usually between 0 and 0.1; therefore the upper-convected Maxwell model is preferably used in viscoelastic computations. When the model-dependent tensor \mathbf{A} is taken as a function of the stress tensor, other viscoelastic models can be obtained from equation (II.9), including the models of Phan-Thien & Tanner when $\mathbf{A} = \exp(\epsilon \lambda \text{tr}(\mathbf{T})/\mu) \cdot \mathbf{I}$, and the Giesekus model when $\mathbf{A} = \mathbf{I} + \beta \lambda \mathbf{T}/\mu$ (Keunings, (1987)).

(II.3) NUMERICAL SOLUTION

(II.3.1) Numerical Treatment of the Constitutive Equation

The first basic choice to be made in the numerical solution of the constitutive model is how the elastic stress tensor \mathbf{S} , whose spatial derivatives appear in the vorticity equation (equation (II.2)), should be computed. We can either solve directly equations (II.5)-(II.7) for the components of the total stress tensor (\mathbf{T}) and then calculate the elastic contributions numerically using equation (II.11); alternatively we may substitute the transformation

$$\mathbf{T} = \mathbf{S} + 2\mathbf{d} \quad (\text{II.11})$$

directly into the constitutive model and then solve directly the resulting system of hyperbolic partial differential equations. It should be noted that even though both methods are mathematically equivalent, they are not necessarily numerically

equivalent because of the different discretization errors involved at each stage.

According to the first method, the stress equations can be written as follows:

$$A_1 T^x + We_L T^x = 2B T^y + F_1 \quad (II.12)$$

$$A_2 T^y + We_L T^y = C T^x + B T^y + F_2 \quad (II.13)$$

$$A_3 T^y + We_L T^y = 2C T^y + F_3 \quad (II.14)$$

where

$$L = \psi_y(\partial/\partial x) - \psi_x(\partial/\partial y) \quad (II.15)$$

and

$$A_1 = 1 - 2We(\partial^2\psi/\partial x\partial y) \quad (II.16)$$

$$A_2 = 1 \quad (II.17)$$

$$A_3 = 1 + 2We(\partial^2\psi/\partial x\partial y) \quad (II.18)$$

$$B = We(\partial^2\psi/\partial y^2) \quad (II.19)$$

$$C = -We(\partial^2\psi/\partial x^2) \quad (II.20)$$

$$F_1 = 2(\partial^2\psi/\partial x\partial y) \quad (II.21)$$

$$F_2 = (\partial^2\psi/\partial y^2) - (\partial^2\psi/\partial x^2) \quad (II.22)$$

$$F_3 = -2(\partial^2\psi/\partial x\partial y) \quad (\text{II.23})$$

According to the second alternative, the constitutive model may be written in terms of the components of the elastic stress tensor (**S**) as:

$$A_1 S^x + We_L S^x = 2BS^y + G_1 \quad (\text{II.24})$$

$$A_2 S^y + We_L S^y = CS^x + BS^y + G_2 \quad (\text{II.25})$$

$$A_3 S^y + We_L S^y = 2CS^y + G_3 \quad (\text{II.26})$$

where

$$G_1 = 2We(2(\partial^2\psi/\partial x\partial y)^2 - (\partial\psi/\partial y)(\partial^3\psi/\partial x^2\partial y) + (\partial\psi/\partial x)(\partial^3\psi/\partial x\partial y^2) + (\partial^2\psi/\partial y^2)((\partial^2\psi/\partial y^2) - (\partial^2\psi/\partial x^2))) \quad (\text{II.27})$$

$$G_2 = -We(2((\partial^2\psi/\partial x\partial y)((\partial^2\psi/\partial y^2) + (\partial^2\psi/\partial x^2)) + \epsilon((\partial^2\psi/\partial y^2) - (\partial^2\psi/\partial x^2))) \quad (\text{II.28})$$

$$G_3 = 2We(2(\partial^2\psi/\partial x\partial y)^2 + (\partial\psi/\partial y)(\partial^3\psi/\partial x^2\partial y) - (\partial\psi/\partial x)(\partial^3\psi/\partial x\partial y^2) - (\partial^2\psi/\partial x^2)((\partial^2\psi/\partial y^2) - (\partial^2\psi/\partial x^2))) \quad (\text{II.29})$$

The new complication introduced by the second method is the need for the evaluation of third derivatives of the stream function. On a uniform square grid, these derivatives can be evaluated using the following equations:

$$(\partial^3\psi/\partial x^3)_{ij} = (\psi_{i+2j} - 2\psi_{i+1j} + 2\psi_{ij} - \psi_{i-2j})/2h^3 \quad (\text{II.30})$$

$$(\partial^3\psi/\partial y^3)_{ij} = (\psi_{ij+2} - 2\psi_{ij+1} + 2\psi_{ij-1} - \psi_{ij-2})/2h^3 \quad (\text{II.31})$$

$$(\partial^3\psi/\partial x^2\partial y)_{ij} = (\psi_{i+1j+1} - 2\psi_{ij+1} + \psi_{i-1j+1} - 2\psi_{ij-1} - \psi_{i-1j-1})/2h^3 \quad (\text{II.32})$$

$$(\partial^3\psi/\partial y^2\partial x)_{ij} = (\psi_{i+1,j+1} - 2\psi_{i+1,j} + \psi_{i+1,j-1} - 2\psi_{i,j} + \psi_{i,j-1})/2h^3 \quad (\text{II.33})$$

Appropriate expressions are also available for boundary points. For example, on a stationary, non-slip boundary, the expression for the third derivative of the stream function will be (to $O(h^2)$):

$$(\partial^3\psi/\partial x^3)_w = (\psi_{w-1,j} - 2\psi_{w,j} + 2\psi_{w+2,j} - \psi_{w+3,j})/2h^3 \quad (\text{II.34})$$

The main advantage of the first method, that is of the evaluation of the total stress tensor from the constitutive model, is that only derivatives of order up to second need to be evaluated. On the other side, greater computer storage is required with that method, since both the total (**T**) and the elastic (**S**) stress tensors need to be computed and stored at all times. The work of Tiefenbruck and Leal (1982)) indicates that there seems little to choose between them from the standpoints of accuracy and time of computation. In the context of this work, the constitutive model was solved for the total stress tensor (**T**) and the elastic contributions were evaluated by means of equation (II.11).

(II.3.2) Transformation of the Model Equations in Curvilinear Coordinates

In order to be able to solve viscoelastic flow problems in channels of arbitrary geometry using finite differences, the model equations must be transformed in the new, curvilinear coordinate system (ξ, η) . Applying the general transformation relations presented in Appendix (A.3) in the two-dimensional case, we obtain the following transformation relations for the derivatives appearing in the transformed equations (in the following, f is a scalar and J is the Jacobian of the coordinate transformation):

$$f_x = (y_\eta f_\xi - y_\xi f_\eta)/J \quad (\text{II.35})$$

$$f_y = (x_\xi f_\eta - x_\eta f_\xi)/J \quad (\text{II.36})$$

$$f_{xx} = \frac{[(y_\eta)^2 \cdot f_{\xi\xi} - 2 \cdot y_\xi \cdot y_\eta \cdot f_{\eta\xi} + (y_\xi)^2 \cdot f_{\eta\eta}]/J^2 + [((y_\eta)^2 \cdot y_{\xi\xi} - 2 \cdot y_\xi \cdot y_\eta \cdot y_{\eta\xi} + (y_\xi)^2 \cdot y_{\eta\eta}) \cdot (x_\eta \cdot f_\xi - x_\xi \cdot f_\eta) + ((y_\eta)^2 \cdot x_{\xi\xi} - 2 \cdot y_\xi \cdot y_\eta \cdot x_{\eta\xi} + (y_\xi)^2 \cdot x_{\eta\eta}) \cdot (-y_\eta \cdot f_\xi + y_\xi \cdot f_\eta)]/J^3}{\quad} \quad (\text{II.37})$$

$$f_{yy} = \frac{[(x_\eta)^2 \cdot f_{\xi\xi} - 2 \cdot x_\xi \cdot x_\eta \cdot f_{\eta\xi} + (x_\xi)^2 \cdot f_{\eta\eta}]/J^2 + [((x_\eta)^2 \cdot y_{\xi\xi} - 2 \cdot x_\xi \cdot x_\eta \cdot y_{\eta\xi} + (x_\xi)^2 \cdot y_{\eta\eta}) \cdot (x_\eta \cdot f_\xi - x_\xi \cdot f_\eta) + ((x_\eta)^2 \cdot x_{\xi\xi} - 2 \cdot x_\xi \cdot x_\eta \cdot x_{\eta\xi} + (x_\xi)^2 \cdot x_{\eta\eta}) \cdot (-y_\eta \cdot f_\xi + y_\xi \cdot f_\eta)]/J^3}{\quad} \quad (\text{II.38})$$

$$f_{xy} = \frac{[(x_\xi \cdot y_\eta + x_\eta \cdot y_\xi) \cdot f_{\eta\xi} - x_\xi \cdot y_\xi \cdot f_{\eta\eta} - x_\eta \cdot y_\eta \cdot f_{\xi\xi}]/J^2 + [(x_\xi \cdot y_{\eta\eta} - x_\eta \cdot y_{\xi\eta})/J^2 + (x_\eta \cdot y_\eta \cdot J_\xi - x_\xi \cdot y_\eta \cdot J_\eta)/J^3] \cdot f_\xi + [(x_\eta \cdot y_{\xi\xi} - x_\xi \cdot y_{\xi\eta})/J^2 + (x_\xi \cdot y_\xi \cdot J_\eta - x_\eta \cdot y_\xi \cdot J_\xi)/J^3] \cdot f_\eta}{\quad} \quad (\text{II.39})$$

In the case that the grid is non-orthogonal, the transformed form of the Laplacian operator appearing in the stream function and vorticity equations will contain the two second derivatives, as well as first and mixed derivatives of the dependent variables. Namely, the transformed form of the Laplacian of a scalar (f) is:

$$\nabla^2 f = (\alpha \cdot f_{\xi\xi} - 2 \cdot \beta \cdot f_{\eta\xi} + \gamma \cdot f_{\eta\eta})/J^2 + (\nabla^2 \xi) \cdot f_\xi + (\nabla^2 \eta) \cdot f_\eta \quad (\text{II.40})$$

with

$$\alpha = (x_\eta)^2 + (y_\eta)^2 \quad (\text{II.40.a})$$

$$\beta = (x_\xi)(x_\eta) + (y_\eta)(y_\xi) \quad (\text{II.40.b})$$

$$\gamma = (x_\xi)^2 + (y_\xi)^2 \quad (\text{II.40.c})$$

Even though this adds to the complexity of the equations to be solved, it does not alter their elliptic form, since it can be proven that an elliptic equation will remain elliptic if transformed in another coordinate system, provided that the mapping is

non-singular, i.e., as long as the Jacobian of the transformation is not zero (Appendix (A.2)). The relative complexity of the transformed equations is a small price to pay for the versatility offered by non-orthogonal grids. The appearance of other than second derivatives in the transformed form of the Laplacian alters the 5-point computational molecule usually employed in the numerical solution of the Laplace equation. This is not the case in the transformed form of the constitutive equation, since first derivatives are always transformed into combinations of only first derivatives in curved space. However, implementation of the QUICK scheme requires the use of non-traditional computational molecules. More details of the discretized form of the model equations are given in the following section.

Use of the basic transformation relations between curvilinear (η, ξ) and cartesian (x, y) coordinates results in the following transformed form of the model equations:

$$[\alpha \cdot \psi_{\xi\xi} - 2\beta \cdot \psi_{\eta\xi} + \gamma \cdot \psi_{\eta\eta}] \cdot J^2 + (\nabla^2 \xi) \cdot \psi_{\xi} + (\nabla^2 \eta) \cdot \psi_{\eta} = -\omega \quad (\text{II.40.d})$$

$$[\alpha \cdot \omega_{\xi\xi} - 2\beta \cdot \omega_{\eta\xi} + \gamma \cdot \omega_{\eta\eta}] \cdot J^2 + (\nabla^2 \xi) \cdot \omega_{\eta} + (\nabla^2 \eta) \cdot \omega_{\xi} = \text{Re}(\omega_{\xi} \cdot \psi_{\eta} - \omega_{\eta} \cdot \psi_{\xi})/J + D(\mathbf{S}) \quad (\text{II.40.e})$$

$$T^x(1 - 2\text{We} \cdot u_x) + \text{We}[(u \cdot y_{\eta} - v \cdot x_{\eta})(T^x)_{\xi} + (v \cdot x_{\xi} - u \cdot y_{\xi})(T^x)_{\eta}]/J = 2\text{We}T^y \cdot u_y + 2u_x \quad (\text{II.40.f})$$

$$T^y(1 - 2\text{We} \cdot v_y) + \text{We}[(u \cdot y_{\eta} - v \cdot x_{\eta})(T^y)_{\xi} + (v \cdot x_{\xi} - u \cdot y_{\xi})(T^y)_{\eta}]/J = 2\text{We}T^x \cdot v_x + 2v_y \quad (\text{II.40.g})$$

$$T^x + \text{We}[(u \cdot y_{\eta} - v \cdot x_{\eta})(T^y)_{\xi} + (v \cdot x_{\xi} - u \cdot y_{\xi})(T^y)_{\eta}]/J = \text{We}[T^x \cdot v_x + T^y \cdot u_y] + v_x + u_y \quad (\text{II.40.h})$$

with

$$\partial u / \partial x = \partial^2 \psi / \partial y \partial x = -\partial v / \partial y \quad (\text{II.40.j})$$

$$\partial u / \partial y = \partial^2 \psi / \partial y^2 \quad (\text{II.40.k})$$

$$\partial v / \partial x = -\partial^2 \psi / \partial x^2 \quad (\text{II.40.l})$$

(II.3.3) Discretization of the Transformed Equations

The finite difference expressions for the first, second and mixed derivatives that have been used in the discretization of the transformed form of the equations of motion follow.

For the first derivatives, central differencing was used in the interior of the flow domain:

$$(\partial f / \partial \xi)_{ij} = (f_{i+1,j} - f_{i-1,j}) / 2h \quad (\text{II.41})$$

$$(\partial f / \partial \eta)_{ij} = (f_{i,j+1} - f_{i,j-1}) / 2h \quad (\text{II.42})$$

Central differencing was found to work well in the momentum equations. However, their application in the discretization of spatial stress derivatives resulted in an unstable algorithm. This was expected since the stress equations are hyperbolic in character. Appropriate discretization techniques that improve on stability and accuracy will be discussed in the next section.

In the interior of the flow domain, the second derivatives appearing in the partial differential equations for the stream function and the vorticity were discretized using the following formulae:

$$(\partial^2 f / \partial \xi^2)_{ij} = (f_{i+1,j} - 2f_{ij} + f_{i-1,j}) / h^2 \quad (\text{II.43})$$

$$(\partial^2 f / \partial \eta^2)_{ij} = (f_{i,j+1} - 2f_{ij} + f_{i,j-1}) / h^2 \quad (\text{II.44})$$

For the mixed partial derivatives, the following expressions can be used:

$$(\partial^2 f / \partial \xi \partial \eta)_{ij} = (f_{i+1,j+1} - f_{i-1,j+1} - f_{i+1,j-1} + f_{i-1,j-1}) / 4h^2 \quad (\text{II.45})$$

$$(\partial^2 f / \partial \xi \partial \eta)_{ij} = (f_{i+1,j+1} + 2f_{ij} - f_{i,j+1} - f_{i+1,j} + f_{i-1,j+1} - f_{i,j+1} - f_{i+1,j-1}) / 2h^2 \quad (\text{II.46})$$

$$(\partial^2 f / \partial \xi \partial \eta)_{ij} = (-f_{i-1,j+1} - 2f_{ij} + f_{i,j+1} + f_{i+1,j} - f_{i+1,j+1} + f_{i,j-1} + f_{i+1,j}) / 2h^2 \quad (\text{II.47})$$

On the boundaries, one-sided differences have to be used. These expressions for the first and second derivatives follow (Collatz, (1966)):

$$(\partial f / \partial \xi)_w = (-f_{w-2j} + 4f_{w-1j} - 3f_{wj}) / 2h \quad (\text{second order}) \quad (\text{II.48})$$

$$(\partial f / \partial \xi)_w = (f_{wj} - f_{w-1j}) / h \quad (\text{first order}) \quad (\text{II.49})$$

$$(\partial^2 f / \partial \xi^2)_w = (2f_{wj} - 5f_{w-1j} + 4f_{w-2j} - f_{w-3j}) / h^2 \quad (\text{II.50})$$

In Equations (II.48) - (II.50) the subscript (w) indicates boundary values.

(II.3.4) Stability of Finite Difference Approximations and Upwind Differencing.

The question of stability and accuracy is of major importance in the solution of partial differential equations, particularly in the case of equations containing convective terms. The simple one-dimensional convection-diffusion equation has been used extensively as a model for the study of such equations. This equation, in one dimension, is:

$$f_x - a(x)f f_x - b(x) = 0 \quad (\text{II.51})$$

The conventional approximation of equation (II.51) with central differences used in the approximation of the first derivative is:

$$(f_{i+1} - 2f_i + f_{i-1}) / h^2 = a(x)f_i (f_{i+1} - f_{i-1}) / 2h + b(x) \quad (\text{II.52})$$

This representation is stable when the local Grid Reynolds Number ($|\rho_1|$) satisfies $|\rho_1| < 1$, where $\rho_1 = 0.5ha(x)f_x$. By choosing the mesh size (h) sufficiently small, it is possible to always satisfy that stability condition. In practice however, mesh refinement is not always feasible because of the increased requirements in computer time and storage. This is especially true when we are solving systems of several PDEs in higher dimensions. Therefore, there is a strong need for stable alternatives to the central difference scheme.

The simplest alternative is to maintain the central difference approximation for the second derivative in equation (II.51) while using an one-sided approximation for the first derivative. Usually, backward differencing is used when $f > 0$ and forward when $f < 0$. The one sided difference is then always upstream or upwind of x_i , and the alternative scheme is:

$$f'_i(x_i) = (f_i - f_{i-1})/h, \quad f_i > 0 \quad (\text{II.53.a})$$

$$f'_i(x_i) = (f_{i+1} - f_i)/h, \quad f_i < 0 \quad (\text{II.53.b})$$

This upwind scheme, termed "first upwind scheme" by Roache (1976), is unconditionally stable for all values of the local grid Reynolds number. Its disadvantage is that it has only first order accuracy, with a truncation error

$$T_i(x) = 0.5ha(x_i)f(x_i)f''_x(x_i) + O(h^2) \quad (\text{II.54})$$

The first term in this expression, which is $O(h)$, is frequently referred to as "false diffusion" or "artificial viscosity". It is larger than the true diffusion term in (II.51) when $\rho_1 > 1$, and it results in a smearing of sharp gradients of the variable f . Another method (Spalding (1972)) uses a mixture of central and upwind differences. If $\rho_1 < 1$, the result is identical to central differencing, while if $\rho_1 > 1$ the convection term is approximated as in the upwind scheme. The advantage of this scheme is that it is

unconditionally stable, it has no artificial diffusion when $\rho_1 < 1$, whereas, when $\rho_1 > 1$ the false diffusion is proportional to the magnitude of $(\rho_1 - 1)$. A third method (Gentry et al. (1966)) displays something near the unconditional stability of the upwind differencing, while retaining the second order accuracy of central differencing when the spatial variation in the convective term (ff_x) is small. This method involves an averaging of velocities on either side of the mesh point, together with an upwind approximation of derivatives. With reference to equation (41), we write:

$$f \cdot f_x(x) = (ff)_x/2 \quad (\text{II.55})$$

with

$$(ff)_x(x) = (f_{r1}f_{r2} - f_{l1}f_{l2})/h \quad (\text{II.56})$$

$$\text{where, } f_{r1} = (f_i + f_{i+1})/2, f_{l1} = (f_i + f_{i-1})/2, \text{ and} \quad (\text{II.56.a})$$

$$\text{when } f_{r1} > 0, f_{r2} = f_i \quad (\text{II.56.b})$$

$$f_{r1} < 0, f_{r2} = f_{i+1} \quad (\text{II.56.c})$$

$$\text{when } f_{l1} > 0, f_{l2} = f_{i-1} \quad (\text{II.56.d})$$

$$f_{l1} < 0, f_{l2} = f_i \quad (\text{II.56.e})$$

Because of the false diffusion errors associated with first order upwinding and the inherent stability associated with second order central differencing, none of the methods described above are completely satisfactory for high values of the local grid Reynolds number. There is always a decision to be made regarding the amount of accuracy one is willing to sacrifice for stability and/or attainable computer times.

In the context of this work, the numerical approximation of first derivatives is crucial in the numerical solution of the constitutive equations. It was mentioned earlier, that the High Weissenberg Number Problem has been linked to the inadequacy of central differencing in the numerical solution of hyperbolic problems. Other studies have also

shown that the accumulation of approximation errors can lead to numerical breakdown. It seems, therefore, that we deal with a problem which requires both, accuracy and stability, features that most numerical schemes do not combine. The performance of central differences for the approximation of convected derivatives in the constitutive equation was evaluated at initial stages of this project and was found very poor as far as convergence was concerned. For a 4:1 planar contraction flow, the maximum attainable Weissenberg number was only around 0.1. First order upwinding extended the convergence up to 0.32 for the same problem. In an attempt to extend the range of convergence even further, it was decided to use a third-order upwinding difference scheme (QUICK) proposed by Leonard (1979). This scheme has not been previously used in numerical solutions of viscoelastic flows, but has performed well in the modelling of highly convective flows (Ferziger, (1987)). Overall, use of the QUICK scheme extended the range of convergence of the numerical algorithm up to $We=0.7$ for the 4:1 sudden contraction problem with a reentrant corner (section II.5.1). However, its performance was better in non-singular problems (section II.5.2) where the range of convergence was almost tripled (from $De=1.5$ to $De=4.2$ in the smooth 4:1 contraction R1 of figure II.5.2.1).

(II.3.4.1) The Quick Upwinding Scheme

According to the QUICK method, the stresses at cell boundaries are obtained by a third order asymmetric interpolation using one downstream and two upstream points. This is equivalent to correcting a linear approximation of the cell boundary value by a term proportional to the upstream curvature of the interpolated data. If f_R and f_L indicate approximations of a function (f) at the points $i+1/2$, $i-1/2$ (which are the right and left faces of the cell surrounding the point (i)), the QUICK scheme uses the following interpolation formulae:

$$f_R = (f_i + f_{i+1})/2 - (f_{i-1} + f_{i+1} - 2f_i)/8 \quad (II.57)$$

$$f_L = (f_i + f_{i+1})/2 - (f_{i+2} + f_i - 2f_{i+1})/8 \quad (\text{II.58})$$

As a result of equations (II.57) and (II.58), the derivative at the point (i) is approximated by:

$$f'_i(x_i) = (f_{i+1/2} - f_{i-1/2})/h = (3f_i + 3f_{i+1} - 7f_{i-1} + f_{i-2})/8h \quad (\text{II.59})$$

Equation (II.59) was used in the numerical discretization of the stress equations. In modelling boundary conditions with the QUICK algorithm, both the wall value and the wall gradient are needed at each end of the computational region. The boundary stress values are usually given by a physical boundary condition. The boundary gradient must be chosen to be consistent with quadratic interpolation between the boundary value and the values at the first two interior nodes (f_{w+1} , f_{w+2}). This requirement gives:

$$(f'_x)_w = (8f_w + 3f_{w+1} - f_{w+2})/3h \quad (\text{II.60})$$

Evidently, the extension of the QUICK method in two dimensions is straightforward. In that case, the appropriate discretization formulae in the (x) and (y) directions on a uniform mesh will be:

$$(f'_x)_{ij} = (3f_{ij} + 3f_{i+1j} - 7f_{i-1j} + f_{i-2j})/8h \quad (\text{II.60.a})$$

$$(f'_y)_{ij} = (3f_{ij} + 3f_{ij+1} - 7f_{ij-1} + f_{ij-2})/8h \quad (\text{II.60.b})$$

where the indices (i) and (j) correspond to the directions (x) and (y) respectively.

(II.3.5) Transformation and Discretization of the non-Newtonian Source Function D(S)

In traditional finite differences based on rectangular meshes in cartesian coordinates, the non-Newtonian source function $D(S)$ can be discretized based on the computational molecule of Figure (II.3.5.1.a). The corresponding formula for the point (i,j) would then be:

$$D_{ij} = \frac{(S_{i+1,j+1}^x - S_{i+1,j-1}^x - S_{i-1,j+1}^x + S_{i-1,j-1}^x - S_{i+1,j+1}^y + S_{i+1,j-1}^y + S_{i-1,j+1}^y - S_{i-1,j-1}^y)/4. - S_{i+1,j}^y - S_{i-1,j}^y - S_{i,j+1}^y - S_{i,j-1}^y}{S_{i,j+1}^y + S_{i,j-1}^y} \quad (II.61)$$

In the context of general curvilinear coordinates, first derivatives are the only new derivatives introduced by the transformation of $D(S)$. The computational molecule will therefore remain unchanged if central or forward/backward differences are being used for the evaluation of those first order derivatives. If the QUICK scheme is used, the computational molecule will further include some new upstream points as shown in Figure (II.3.5.1.b). The form of the function $D(S)$ in general curvilinear coordinates is, after considerable algebra:

$$D(S) = AS_{\xi\xi}^y + BS_{\eta\eta}^y + CS_{\eta\xi}^y + DS_{\eta}^y + FS_{\xi}^y + L_1(S^x - S^y)_{\eta\xi} + L_2(S^x - S^y)_{\eta\eta} + L_3(S^x - S^y)_{\xi\xi} + L_4(S^x - S^y)_{\xi} + L_5(S^x - S^y)_{\eta} \quad (II.62)$$

where

$$A = ((x_{\eta})^2 - (y_{\eta})^2)/J^2 \quad (II.63)$$

$$B = ((x_{\xi})^2 - (y_{\xi})^2)/J^2 \quad (II.64)$$

$$C = 2(y_{\eta}y_{\xi} - x_{\eta}x_{\xi})/J^2 \quad (II.65)$$

$$D = (-(x_{\xi})D_1 + (y_{\xi})D_2 + (x_{\eta})D_3 - (y_{\eta})D_4)/J^3 \quad (II.66)$$

$$F = (D_1(x_{\eta}) - (y_{\eta})D_2 - (x_{\eta})D_3 + (y_{\eta})D_4)/J^3 \quad (II.67)$$

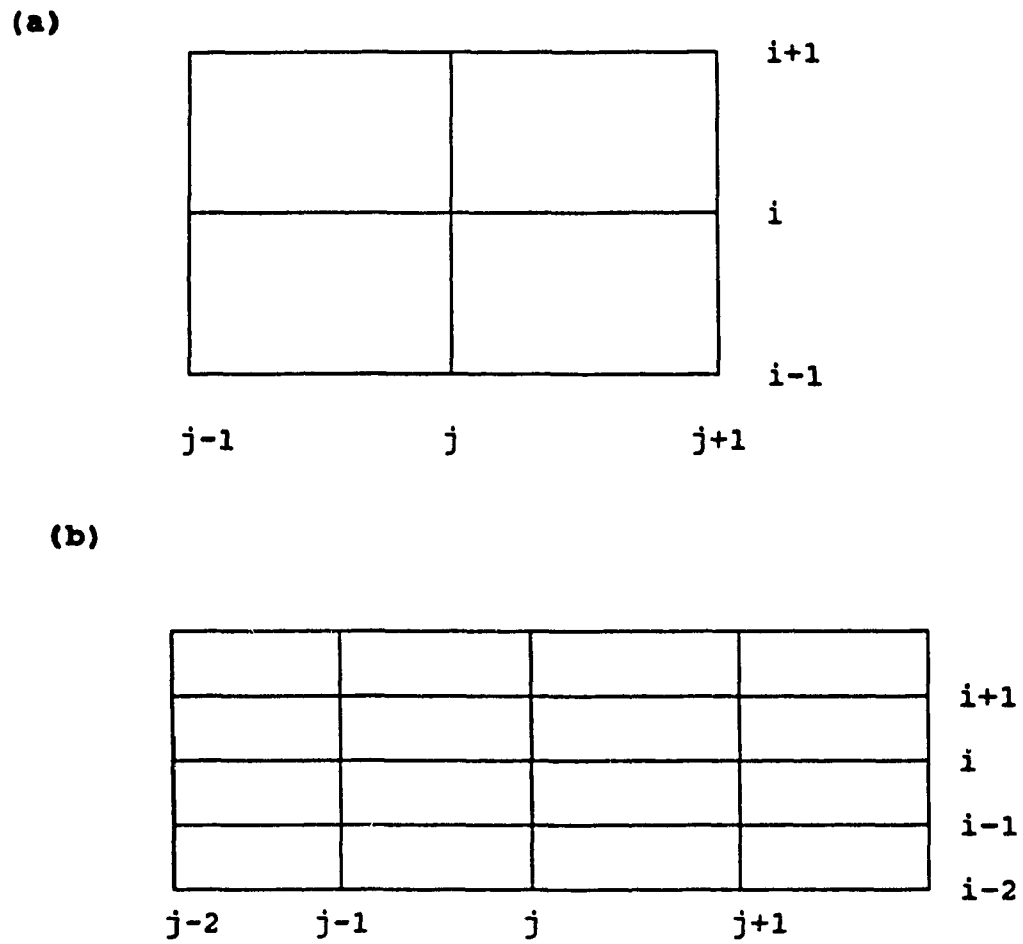


Figure (II.3.5.1): Computational molecules associated with the discretization of the non-Newtonian source function $D(S)$; (a) in cartesian coordinates, (b) in curvilinear coordinates with QUICK upwinding.

$$D_1 = (x_\eta)^2 \cdot y_{\xi\xi} - 2 \cdot x_\xi \cdot x_\eta \cdot y_{\eta\xi} + (x_\xi)^2 \cdot y_{\eta\eta} \quad (\text{II.68})$$

$$D_2 = (x_\eta)^2 \cdot x_{\xi\xi} - 2 \cdot x_\xi \cdot x_\eta \cdot x_{\eta\xi} + (y_\xi)^2 \cdot x_{\eta\eta} \quad (\text{II.69})$$

$$D_3 = ((y_\eta)^2 \cdot y_{\xi\xi} - 2 \cdot y_\xi \cdot y_\eta \cdot y_{\eta\xi} + (y_\xi)^2 \cdot y_{\eta\eta}) \quad (\text{II.70})$$

$$D_4 = (y_\eta)^2 \cdot x_{\xi\xi} - 2 \cdot y_\xi \cdot y_\eta \cdot x_{\eta\xi} + (y_\xi)^2 \cdot x_{\eta\eta} \quad (\text{II.71})$$

$$L_1 = (x_\xi \cdot y_\eta + x_\eta \cdot y_\xi) / J^2 \quad (\text{II.72})$$

$$L_2 = -x_\xi \cdot y_\xi / J^2 \quad (\text{II.73})$$

$$L_3 = -x_\eta \cdot y_\eta / J^2 \quad (\text{II.74})$$

$$L_4 = (x_\xi \cdot y_{\eta\eta} - x_\eta \cdot y_{\xi\eta}) / J^2 + (x_\eta \cdot y_\eta \cdot J_\xi - x_\xi \cdot y_\eta \cdot J_\eta) / J^3 \quad (\text{II.75})$$

$$L_5 = (x_\eta \cdot y_{\xi\xi} - x_\xi \cdot y_{\xi\eta}) / J^2 + (x_\xi \cdot y_\xi \cdot J_\eta - x_\eta \cdot y_\xi \cdot J_\xi) / J^3 \quad (\text{II.76})$$

(II.3.6) Solution of the Discrete Equations

There are essentially two distinct groups of methods for the solution of the system of algebraic equations resulting from the discretization of a partial differential equation: direct and iterative methods. Direct methods are usually variations of Gaussian elimination, making use of forward and backward substitutions. These correspond to the decomposition of the coefficient matrix (**A**) into lower and upper triangular parts (**L** and **U** respectively), so that:

$$\mathbf{A} = \mathbf{L} \cdot \mathbf{U} \quad (\text{II.77})$$

To be efficient, direct methods require very careful programming, especially when large sparse matrices are considered. On the other hand, iterative methods have been used extensively in the solution of the algebraic equations resulting from the finite

difference approximation of partial differential equations. In fact, for very large systems, they are the only feasible methods. Beside ease of programming, iterative methods make good use of sparsity and structure and it is not necessary to store the coefficient matrix but simply to generate the non-zero elements when they are needed. In the context of this work, the iterative method of successive relaxation (SR) was employed. For the solution of the linear system

$$\mathbf{A} \cdot \mathbf{x} = \mathbf{b} \quad (\text{II.78})$$

the successive relaxation method employs the following decomposition of the coefficient matrix:

$$\mathbf{A} = \mathbf{E} + \mathbf{F}, \text{ where} \quad (\text{II.78.a})$$

$$\mathbf{E} = \mathbf{D}/a - \mathbf{L}, \text{ and } \mathbf{F} = \mathbf{D}/a - (\mathbf{D} - \mathbf{U}) \quad (\text{II.79})$$

where \mathbf{D} , \mathbf{L} and \mathbf{U} are the diagonal, lower and upper triangular parts of \mathbf{A} respectively, and (a) is a relaxation parameter, $0 < a < 2$. If $0 < a < 1$ the method is called under-relaxation, whereas for $1 < a < 2$ the method is termed over-relaxation. Overall, the iterative process will then be:

$$(\mathbf{D} - a\mathbf{L}) \cdot \mathbf{x}^{k+1} = [(1-a)\mathbf{D} + a\mathbf{U}] \cdot \mathbf{x}^k + a\mathbf{b} \quad (\text{II.80})$$

The advantage of SR against the simple Gauss-Seidel iteration which utilizes the decomposition

$$\mathbf{A} = (\mathbf{D} - \mathbf{L}) - \mathbf{U} \quad (\text{II.81})$$

and the iterative algorithm

$$(\mathbf{D} - \mathbf{L}) \cdot \mathbf{x}^{[r+1]} = [\mathbf{U}] \cdot \mathbf{x}^{[r]} + \mathbf{b} \quad (\text{II.82})$$

is that convergence can be accelerated with optimum choice of the relaxation parameter (a). In the context of this work, both methods have been used with success.

The computational molecules associated with the constitutive model are shown in Figure (II.3.5.2). (a) is the molecule corresponding to the Poisson Equation in cartesian coordinates, while (b) is the computational molecule for the same equation in curvilinear coordinates. (c), (d) and (e) are computational molecules associated with the constitutive equation in curvilinear coordinates. In (c), central differencing is used for the discretization of the spatial derivatives of the stress. (d) corresponds to first order upwinding while (c) is obtained when the QUICK scheme is used.

For the solution of the stream function equation, and with reference to the computational molecules of Figure (II.3.5.2), the typical iteration will be:

$$\psi_{ij}^{[r+1]} = f(\psi_{i-1,j-1}^{[r+1]}, \psi_{i-1,j}^{[r+1]}, \psi_{i-1,j+1}^{[r+1]}, \psi_{i,j-1}^{[r+1]}, \psi_{i,j+1}^{[r]}, \psi_{i+1,j-1}^{[r]}, \psi_{i+1,j}^{[r]}, \psi_{i+1,j+1}^{[r]}, \omega_{ij}^{[r]}) \quad (\text{II.83})$$

where [r] is an iteration indicator.

Similarly, the iterative update for the vorticity at the grid-point (i,j) will be:

$$\omega_{ij}^{[r+1]} = g(\omega_{i-1,j-1}^{[r+1]}, \omega_{i-1,j}^{[r+1]}, \omega_{i-1,j+1}^{[r+1]}, \omega_{i,j-1}^{[r+1]}, \omega_{i,j+1}^{[r]}, \omega_{i+1,j-1}^{[r]}, \omega_{i+1,j}^{[r]}, \omega_{i+1,j+1}^{[r]}, D(\mathbf{S})_{ij}, \psi_{i,j+1}^{[r+1]}, \psi_{i,j-1}^{[r+1]}, \psi_{i+1,j}^{[r+1]}, \psi_{i-1,j}^{[r+1]}) \quad (\text{II.84})$$

The stress values at the grid points are updated after the iterative loop for the determination of the kinematics has converged. The iterative update for the stress components, with reference to the computational molecule corresponding to the QUICK scheme, will have the form:

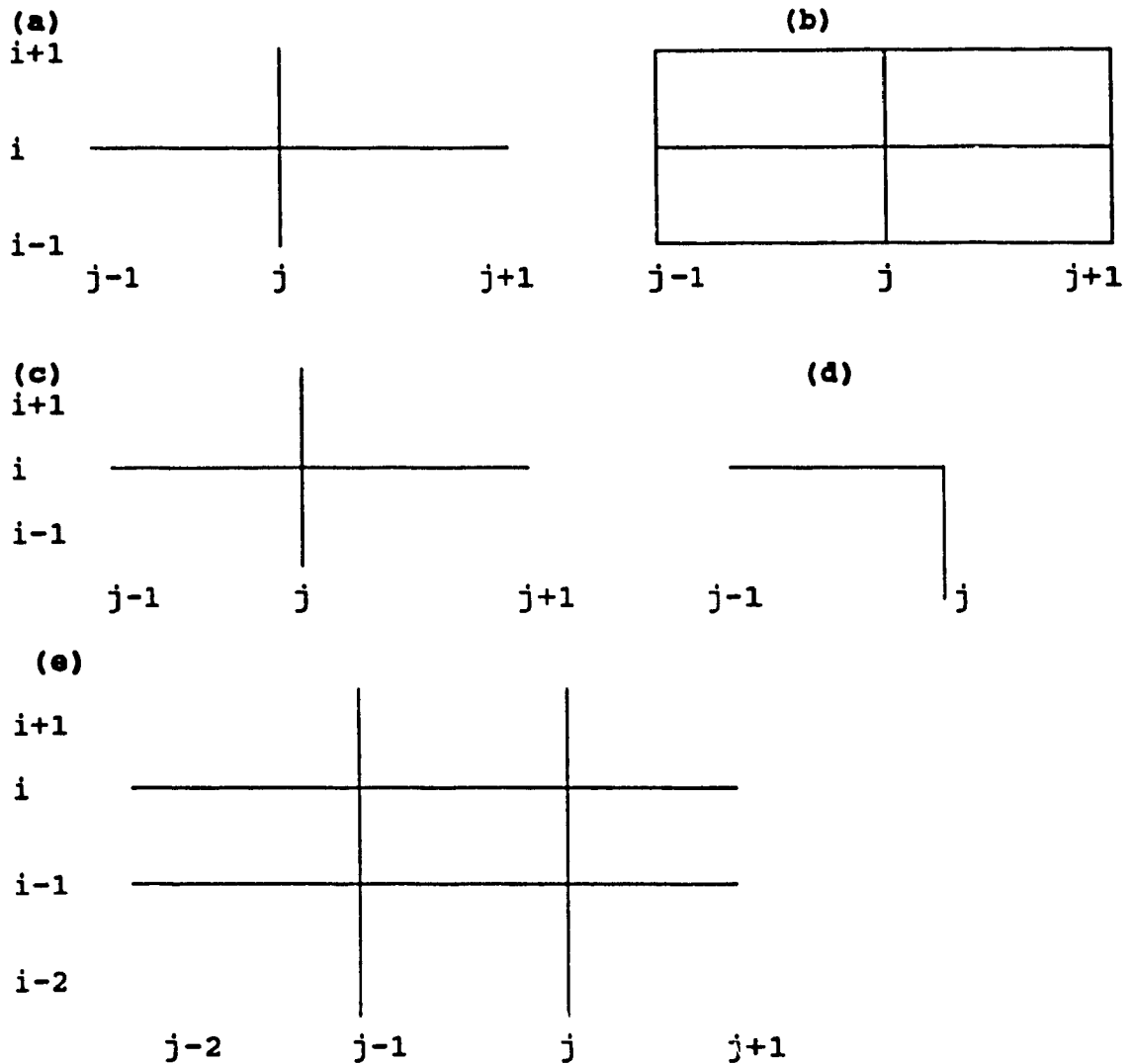


Figure (II.3.5.2): (a): Computational molecule used in the solution of the Poisson Equation in Cartesian Coordinates, and (b), the corresponding molecule in general curvilinear coordinates. (c-e): Computational molecules associated with the numerical solution of the constitutive equation: (c); Central Differencing, (d) First-order upwinding, (e) QUICK scheme.

$$\mathbf{T}_j^{[r+1]} = h(\mathbf{T}_{j-2}^{[r+1]}, \mathbf{T}_{j-1}^{[r+1]}, \mathbf{T}_{j+1}^{[r]}, \mathbf{T}_{i+j}^{[r]}, \mathbf{T}_{i,j}^{[r+1]}, \mathbf{T}_{i+2j}^{[r+1]}, \psi, \omega) \quad (\text{II.85})$$

where \mathbf{T} is the vector of the (unknown) stress nodal values:

$$\mathbf{T} = (\mathbf{T}^x, \mathbf{T}^y, \mathbf{T}^z)^T \quad (\text{II.86})$$

with $\mathbf{T}^x = \{\mathbf{T}_{ij}^x\}$, $\mathbf{T}^y = \{\mathbf{T}_{ij}^y\}$, $\mathbf{T}^z = \{\mathbf{T}_{ij}^z\}$

and ψ and ω being the vectors of the nodal values of vorticity and stream function obtained from the solution of the equations of motion.

(II.3.7) The Numerical Algorithm

The problem to be solved consists of a set of 5 non-linear, coupled partial differential equations. The kinematics (Equations (II.1) and (II.2)) form an elliptic system while the constitutive model (Equations (II.5) to (II.7)) forms a set of three hyperbolic equations. These equations are coupled through the kinematic coefficients in the stress equations and through the non-Newtonian source function in the equations of motion. This coupling is a major stumbling block in the numerical solution, mainly because of the different nature of the two sets of equations. Two major approaches have evolved in the literature for the solution of the problem: these are known as the **coupled** and the **decoupled** methods. In a coupled approach, the discretized equations are solved simultaneously for all dependent variables (ψ , ω and \mathbf{T}), usually by means of the Newton iterative scheme. In the decoupled approach, one solves separately for (ψ, ω) and \mathbf{T} . With known stress fields, the kinematics are updated and so on until convergence. The major advantage of a decoupled approach lies in the breakup of the total problem into an elliptic kinematic and a hyperbolic stress sub-problem. Appropriate numerical methods that take into account the nature of the two sub-problems can therefore be used. Both integral and differential constitutive models

can be treated in the context of decoupled methods, whereas coupled methods can only accommodate differential models. It has been stated (Keunings, (1987)) that the major disadvantage of decoupled methods is the slow convergence of the successive relaxation algorithms usually employed in the solution of the discrete systems and the lack of intermediate information regarding the qualitative behaviour of the numerical solution, usually obtainable from the Jacobian matrix in a coupled approach. Published results indicate that both, coupled and decoupled methods suffer from high computational requirements in CPU time. Study of the qualitative behaviour of the solution can only be accomplished using Newton-Raphson iteration, but this can be done in the context of both coupled and decoupled techniques.

In this work, the non-linear coupling between stresses and kinematics was accounted for by separate solution of the corresponding equations, therefore adopting the decoupled method. Each set of discretized equations was solved iteratively by a successive relaxation algorithm.

It has been suggested by several authors (Crochet et al. (1984)) that values of the unknown vectors be smoothed after each iteration by a formula of the form:

$$\mathbf{x}^{[r+1]} = (1-\beta) \cdot \mathbf{x}^{[r+1]} + \beta \cdot \mathbf{x}^{[r]} \quad , 0 < \beta < 1 \quad (\text{II.87})$$

However, apart from smoothing of iterative updates of the boundary vorticity which is some times essential for convergence, smoothing always reduces the speed of convergence of the iterative algorithm. It should therefore be employed only if convergence can not be achieved without it, as is the case when higher values of We and/or Re are used or in geometries involving abrupt changes in the shape of the boundary.

Another point of considerable importance is the choice of the initial guess vectors. For low values of the elasticity parameter, the quality of the initial guess will determine the number of outer iterations required for convergence, whereas for

relatively higher values of We the quality of the initial guess will determine whether the algorithm will converge at all. Continuation with respect to the elasticity parameter (We) is therefore advisable, even though continuation with respect to both We and Re has also been reported (Walters and Webster, (1982)). Given the small effect of the elasticity on the kinematics of a Maxwell fluid, at least for small increments of the elasticity parameter, the algorithm that was utilized in the present study employed a continuation approach, where the solution for a given We was used as an initial guess for the next We ($We_{(i+1)} = We_{(i)} + dWe$), starting from the Newtonian solution as the first guess. The computational algorithm can be outlined as follows:

- (a) Initialize by solving the Newtonian problem ($We=0.0$).
- (b) Update the Weissenberg number ($We_{i+1} = We_i + dWe$).
- (c) Solve the stress equations ((II.5) to (II.7)) for the new We .
- (d) Update kinematics (solve equations (II.1) and (II.2)), with stresses calculated at the step (c).
- (e) Continue with steps (c) and (d) until convergence.

At each of the steps (c) and (d), iteration was terminated when the norm of the iterative corrections, defined as:

$$\text{NORM} = [\sum_j (\mathbf{x}_j^{(n)} - \mathbf{x}_j^{(n-1)})^2]^{1/2} / N, \quad N = \text{number of grid points}$$

was less than 10^{-6} . For the outer iteration, a tolerance of 10^{-4} was usually employed. If, at some stage, divergence was detected (usually that occurred in the solution of Equations (II.5)-(II.7), step (c)), the increment of We was halved and the calculations repeated, until convergence was obtained or until the required dWe became smaller than a prescribed tolerance.

(II.4) VALIDATION OF THE NUMERICAL ALGORITHM

The objective of the following section is to compare numerical predictions of this work with available numerical and experimental results from the literature.

(II.4.1) Comparisons with Numerical and Experimental Results from Literature.

The flow of Newtonian and Maxwell fluids in a bend and in a 4:1 sudden contraction has been studied, amongst others, by Perrera and Walters (1977), Kawaguti (1969), Cochrane et al. (1982) and Song and Yoo (1987). In this section, numerical predictions of the present work are compared to numerical and experimental results reported in these references.

Figure (II.4.1) shows the streamlines in a bend at $Re = 48$. Continuous lines represent the present solutions, while (o) are results of Kawaguti (1969). It can be concluded that the agreement is quite satisfactory. Calculated vorticity contours are compared with simulations of Cochrane et al. (1982) in Figure (II.4.2). Solid lines represent the solution of Cochrane et al. while broken lines are results of the present work. Again the agreement is quite good.

Figure (II.4.3) is a comparison between computational results of the present work and experimental velocity measurements taken from Cochrane et al. (1982). The agreement is very good for the transverse velocity, but poorer for the longitudinal velocity. However, given the uncertainties involved in the experimental measurements, it is concluded that the numerical predictions are in reasonable agreement with those experiments.

Regarding the flow of a Maxwell fluid, the predictions of this work were compared to the simulations of Song and Yoo (1987). In general, very good agreement was

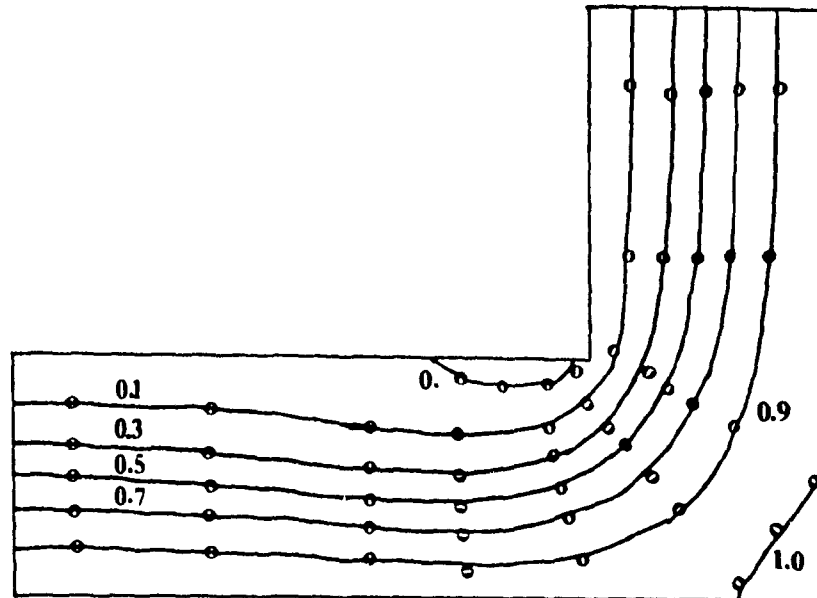


Figure (II.4.1): Comparison between the present solution (solid lines) and the solution of Kawaguti (markers) for Newtonian flow in a bend. Contours are values of the stream function.

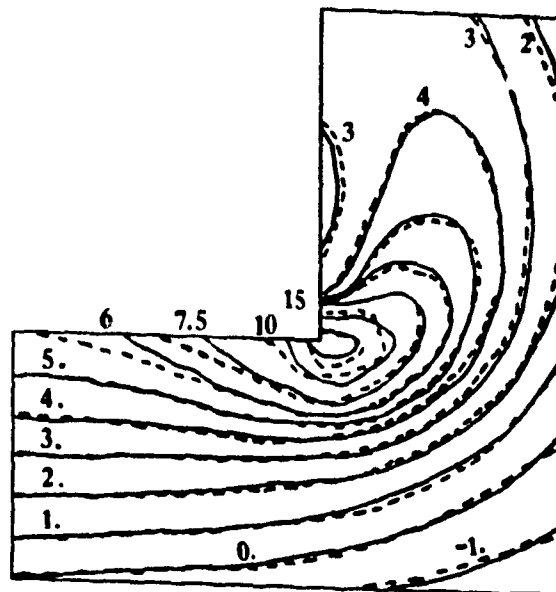


Figure (II.4.2): Comparison between the present solution (broken lines) and the solution of Cochrane et.al. (solid lines) for flow in a bend (contours are vorticity levels).

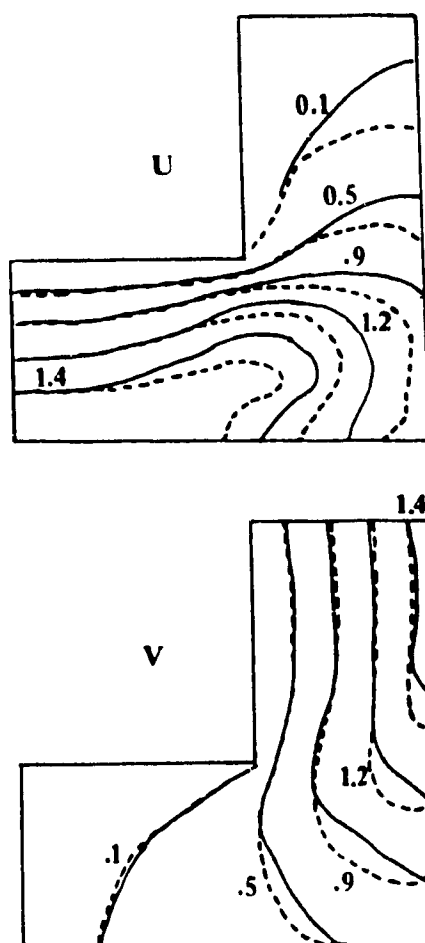


Figure (II.4.3): Comparison between simulation results (solid lines) and experimental velocity measurements from Cochrane et al. (broken lines). U and V are velocities in the horizontal and transverse directions respectively.

observed, even though the numerical technique employed in this study did not utilize a type switching algorithm. Sample comparisons are given in Figure (II.4.4). Further results for the flow in a bend and a sudden contraction, as well as qualitative comparisons with existing simulations are given in following section.

(II.4.2) Quantitative Comparisons with Standard Software

As of today, the combined shear and extensional flow of viscoelastic fluids in contractions and expansions has no known analytical solution. All the above comparisons have been made with reference to published numerical solutions of Newtonian or viscoelastic flows. Therefore, comparison of numerical results with exact solutions is bound to be incomplete. However, along an axis of symmetry, the flow is shear-free, and the constitutive model reduces to a set of two ordinary differential equations.

$$We \cdot u \cdot (dT^x/dx) + (1 - 2 \cdot We \cdot u_x) \cdot T^x = 2 \cdot u_x \quad (II.88)$$

$$We \cdot u \cdot (dT^y/dx) + (1 - 2 \cdot We \cdot v_y) \cdot T^y = 2 \cdot v_y \quad (II.89)$$

with $T^y = 0$.

In the following, the results of the proposed computational algorithm along the axis of symmetry (in this case the curvilinear grid covers the complete contraction (Figure (II.4.2.1)) and not only the upper half) are compared to the results obtained by integration of Equations (II.88) and (II.89) using a standard and reliable ODE solver, namely the IMSL routine IVPAG which utilizes Gear's algorithm for stiff systems. The velocities and velocity gradients appearing in the constitutive equation were calculated by the proposed numerical algorithm, with second order accurate central differences in the representation of $\partial u/\partial x$. As can be seen in Table (II.1) the

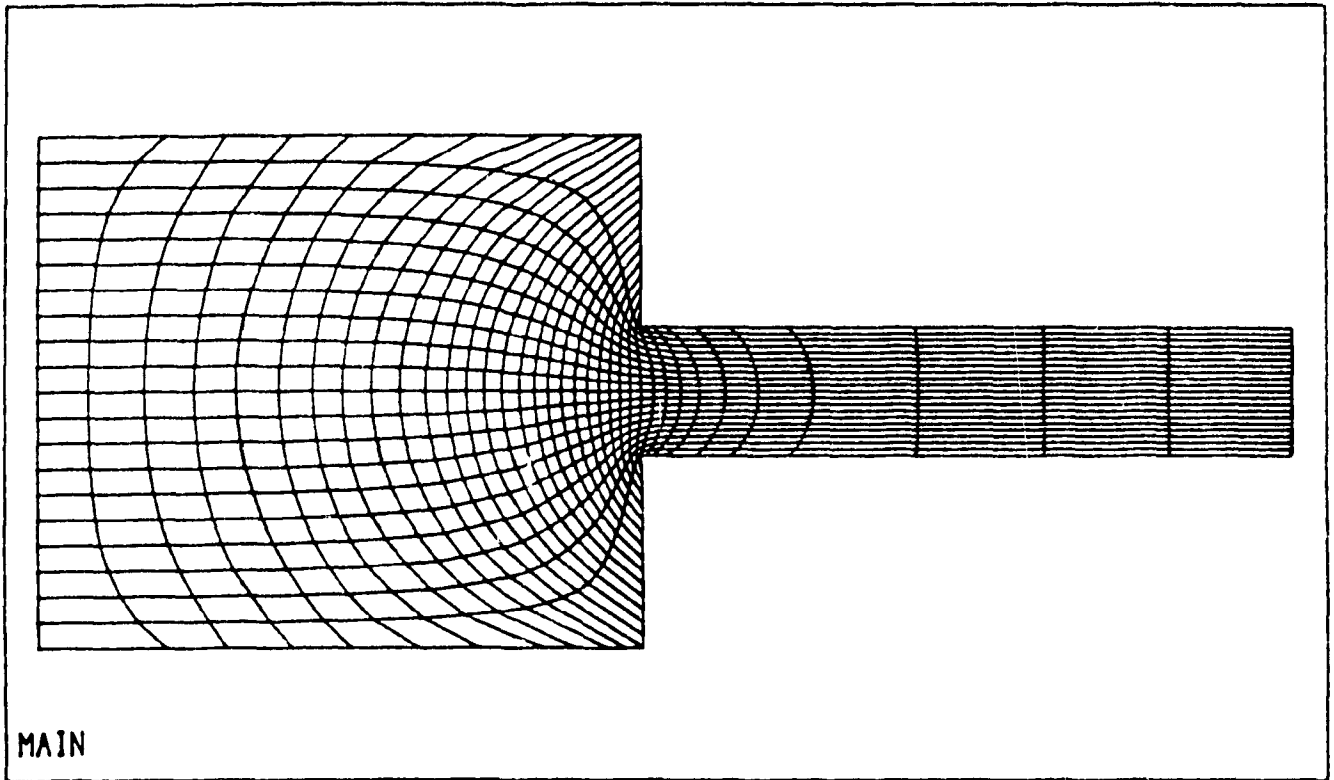


Figure (II.4.2.1):

Curvilinear grid on the complete 4:1 sudden contraction, used for comparison of the proposed numerical solution with standard software

(λ)	Maximum Difference (%)
0.0	0.5
0.3	0.6
0.5	1.1
0.7	0.8

Table (II.1) Difference (%) between the two numerical solutions along the axis of symmetry in an abrupt 4:1 contraction. The comparison is for the dimensionless xx-stress.

agreement is very good.

(II.4.3) Grid Refinement Studies

It is known that the quality of a numerical solution depends heavily, besides the numerical algorithm itself, on the finite difference or finite element mesh that has been employed. For non-singular problems, like the ones considered in this section, infinite grid refinement should lead to the correct solution of the problem - if such a solution exists. However, because of computer time considerations it is not always feasible to use highly refined meshes. The objective of this section is to examine how much the numerical predictions change with varying grid size and configuration, as well as whether these changes are localized or global. For this purpose the geometry of a 4:1 contraction with a rounded corner and two groups of computational grids have been employed. In the first, the grids have 11 horizontal lines and 42, 62 and 75 vertical lines (Figure (II.4.3.1)). The grids of the second group are the same as in Figure (II.4.3.1), but with 21 equidistant lines in the horizontal direction. The highest concentration of nodes is in the entrance region, in an attempt to refine the vorticity calculations in that area. Table (II.2) summarizes some results for the flow of a Newtonian and a Maxwell fluid at $Re=2.0$.

The maximum value of the vorticity occurred near the entrance of the narrow tube, at a horizontal distance of approximately, 4.85. The grid size did not appreciably affect the location of this maximum. As is further explained in APPENDIX (A.4) the wall vorticity is calculated by Equation (II.1) which requires numerical evaluation of one-sided second order derivatives of the stream function. This is an operation very sensitive to the grid size and shape near the wall, even more so near regions of strong boundary curvature. This reflects into maximum wall vorticities changing with grid size. It is interesting to notice that this difference is decreasing with increased resolution, a trend suggesting convergent solutions. The strength of the calculated

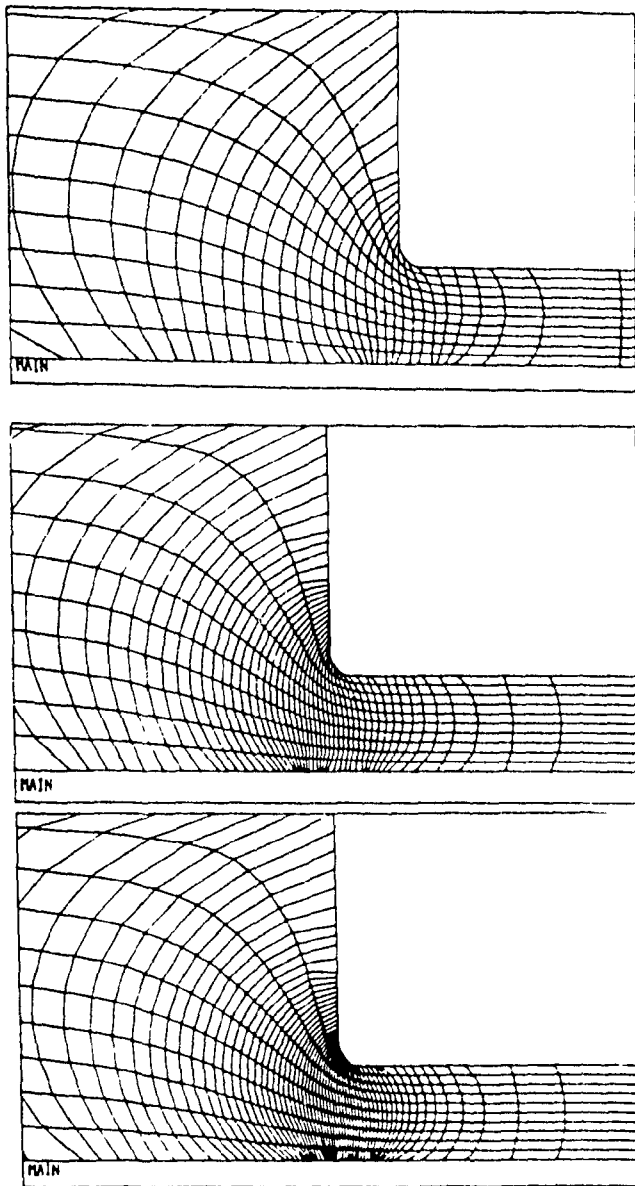


Figure (II.4.3.1):

Mesher used for grid refinement studies in a 4:1 contraction with smooth edge.

vortex decreases with grid refinement. Nevertheless, for the finer grids (d), (e), (f) (Table(II.2)), this change becomes progressively smaller, suggesting that the calculated vortex is not a numerical artifact (on this point further evidence is given in Section (II.5.2)).

The vorticities calculated in the vicinity of the corner along the $i=i_{\max}-1$ line were much less affected by the grid size - the maximum differences being less than 10%, and there was practically no difference at a distance further away from the wall. Since, on no-slip walls parallel to the x-axis, the xx-normal stress is proportional to ω^2 , it is understandable why published simulations show the wall stress to depend strongly on the grid size and shape (Marshall and Crochet, (1987)).

(II.5) CASE STUDIES

(II.5.1) The 4:1 Sudden Contraction

In the following the steady state isothermal flow of a Maxwell fluid through a 4:1 planar contraction is studied. This geometry has been the subject of extensive study, both computationally and experimentally (Cable and Boger (1978), Boger et al.(1986)). A review is given by White et al. (1987). For this reason it serves well as a starting point in testing the performance of the BFCC approach. The flow channel has the following characteristics:

Upstream Radius : 2.0

Downstream Radius: 0.5

Total Length : 10.0

The contraction was located at a distance 4.8 from the entrance. The inlet velocity profile was the one used by Song and Yoo (1987):

Grid	ω_{\max}		Vortex Strength (%)	
	(a)	(b)	(a)	(b)
(11*42) (a)	11.25	(12.02)	1.13	(2.05)
(11*62) (b)	14.02	(14.38)	1.04	(1.75)
(11*75) (c)	16.17	(16.43)	0.97	(1.54)
(21*42) (d)	10.99	(12.11)	0.48	(1.26)
(21*62) (e)	14.28	(14.51)	0.44	(1.22)
(21*75) (f)	14.93	(15.07)	0.42	(1.20)

Table (II.2) Influence of Grid Refinement on Computational Results (a): Newtonian Fluid, (b): Maxwell Fluid ($De=1.7$).

$$u=0.375 \cdot (1.0 - y^2/4), 0 < y < 2.0$$

Previous research regarding the simulation of elastic flows in abrupt contractions suggests the following:

- (a) The presence of singular stresses at the re-entrant corner renders the computations very demanding in its neighbourhood. Grid refinement has not solved the problem of numerical breakdown, and in certain cases it has an adverse effect on convergence (Keunings (1986), Lipscomb et al. (1987)). The treatment of the singularity at the re-entrant corner is a very important research topic by itself. At this point, it is only mentioned that the nature of this viscoelastic singularity has only been established for a second order fluid, and therefore, proper techniques for dealing with the stresses at the neighbourhood of singular points are, in general, not available.
- (b) The size and configuration of the computational grid have a remarkable effect on both, model predictions and stability of the numerical solution (Davies et al. (1984)).
- (c) Errors in the discrete (FD or FE) approximation of the stress gradients appearing near the re-entrant corner accumulate and lead to eventual breakdown (Mendelson et al. , Dupret et al. (1985)). These errors increase sharply as the Weissenberg number increases, since, in that case, the corresponding stress gradients become steeper. In an effort to deal with unrealistically high stresses, Apelian et al. (1988) proposed the introduction of a strain dependent relaxation time, that would allow the fluid to approach Newtonian behaviour as the stress levels increase. On the other side, Marshall and Crochet (1987) used stress sub-elements in order to obtain a more accurate representation of the stress field. It is interesting to notice that this partial grid refinement has resulted, in their work, in opposite results than a global (that is, for both $(\omega), (\psi)$ and (T)) grid refinement produced in previous publications. Whether this staggered discretization or the upwind

differentiation that was employed is the reason for the dramatic improvement in the convergence of the algorithm, is not clear.

- (d) Beside affecting the accuracy of the stress evaluation, numerical errors are further introduced in the model equations by the non-Newtonian source function ($D(S)$, Equation (3)), which includes second derivatives of the components of the elastic stress tensor. This is the apparent reason why integration of the constitutive equation with Newtonian kinematics gives convergent solutions for higher values of the elasticity parameter than the solution of the complete coupled problem. Davies (1984) has demonstrated how such approximation errors are responsible for the loss of convergence in Picard-type solutions of creeping flows of second order fluids.

Since the problem of treating a local singularity is out of the scope of this work, this presentation focuses on the global characteristics of the flow and stress fields, rather than on their specific values at the re-entrant corner. As expected at a singular point, the corner values of the stresses and vorticity are very much grid-dependent. Simulations with the various grids of Figure (II.5.1.1) gave corner vorticities between 18 and 43, for $Re=2.0$ and Newtonian flow. In following section, results in "rounded" 4:1 contractions are presented, in an attempt to investigate whether any features of the flow and stress fields are influenced by the presence of the sharp corner.

(II.5.1.1) Stress Patterns

The stress build-up and relaxation in an elastic fluid as it flows through a complex channel are of major importance in several polymer processing operations. Warpage can be the result of frozen-in stresses that were not give sufficient time to relax in injection molded parts, while very high wall stresses in extrusion dies can result in surface deficiencies of the extrudate. It is therefore very desirable for design and optimization purposes, to predict the spatial distribution of shear and normal stresses. The distribution of the shear stress in the 4:1 contraction is depicted in Figure

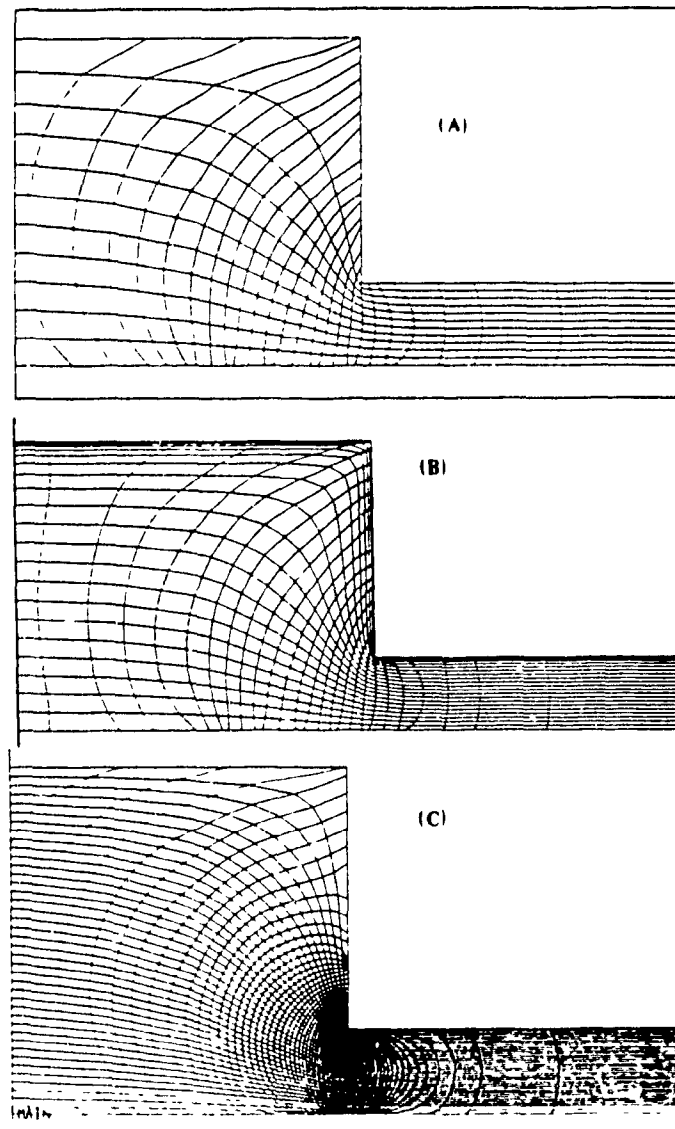


Figure (II.5.1.1):

Grids constructed on a 4:1 sudden contraction; (A): $P=Q=0$, (B): attraction to the upper boundary, (C) high concentration of grid lines near the reentrant corner.

(II.5.1.1.1) for two values of the relaxation time. The effect of the geometry is manifested by the presence of a low shear region at the upstream corner of the contraction. This region has been shown to decrease as the contraction becomes more streamlined, but is relatively unaffected by the elasticity of the fluid. However, as the elasticity of the material increases, the iso-stress contours shift slightly downstream. This is expected, since for higher relaxation times, the fluid stress adjusts more slowly to the changing velocity field. The shear and normal stress patterns in a contraction for $We=0.32$ are given in Figure (II.5.1.1.2). Overall, it has been observed, that increasing the fluid elasticity results in reduction of the size of the area of negative T^a . The yy -normal stresses near the center of the cavity also decrease in absolute value as the fluid elasticity increases. All these results are in general agreement with the simulations of Song and Yoo (1987), and Choi et al. (1988). The non-smooth contours observed in these figures are artifacts of the graphics package. No wiggles exist in the solution as evidenced by line graphs (Figure II.5.1.1.3, II.5.2.8).

The stress profiles along the axis of symmetry were practically unaffected by the type of kinematics used in the integration of the constitutive model. However, the stress profiles near the wall were found to be very sensitive to the kinematics of the flow. Figure (II.5.1.1.3) gives a comparison of the stress profiles obtained when the constitutive equation is integrated using Newtonian (dotted) and non-Newtonian kinematics (solid line). Specifically, the non-Newtonian kinematics were obtained by complete solution of the pertinent set of equations using the continuation approach described earlier, with a maximum step size in the Weissenberg number equal to 0.01. In the first case, the stress peak is much smaller and the stress undershoot disappears. This shows that stress over- and undershoot are not inherent properties of the constitutive model, but are rather induced by the specific kinematics and the specific geometry of the contraction. This is further supported by the simulation results of part (II.5.2) in rounded 4:1 contractions.

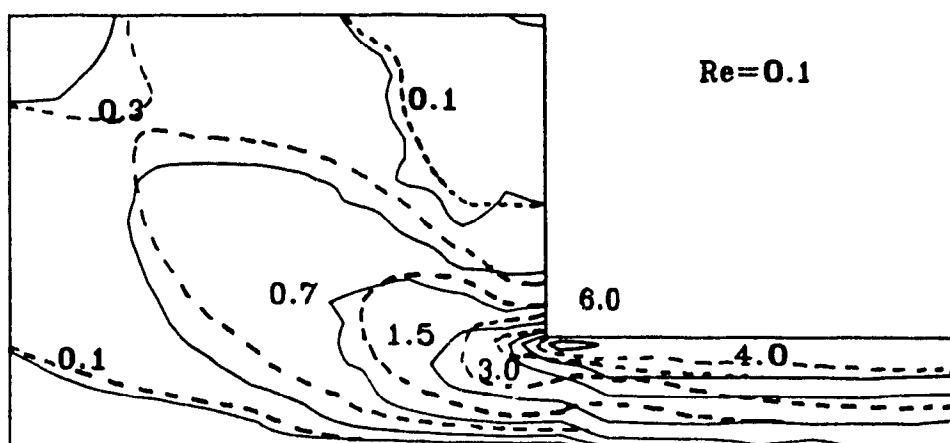


Figure (IL5.1.1.1): Dimensionless shear stress $|T^*|$ distribution in a 4:1 contraction. Solid line: $We=0.7$, broken line: $We=0.01$

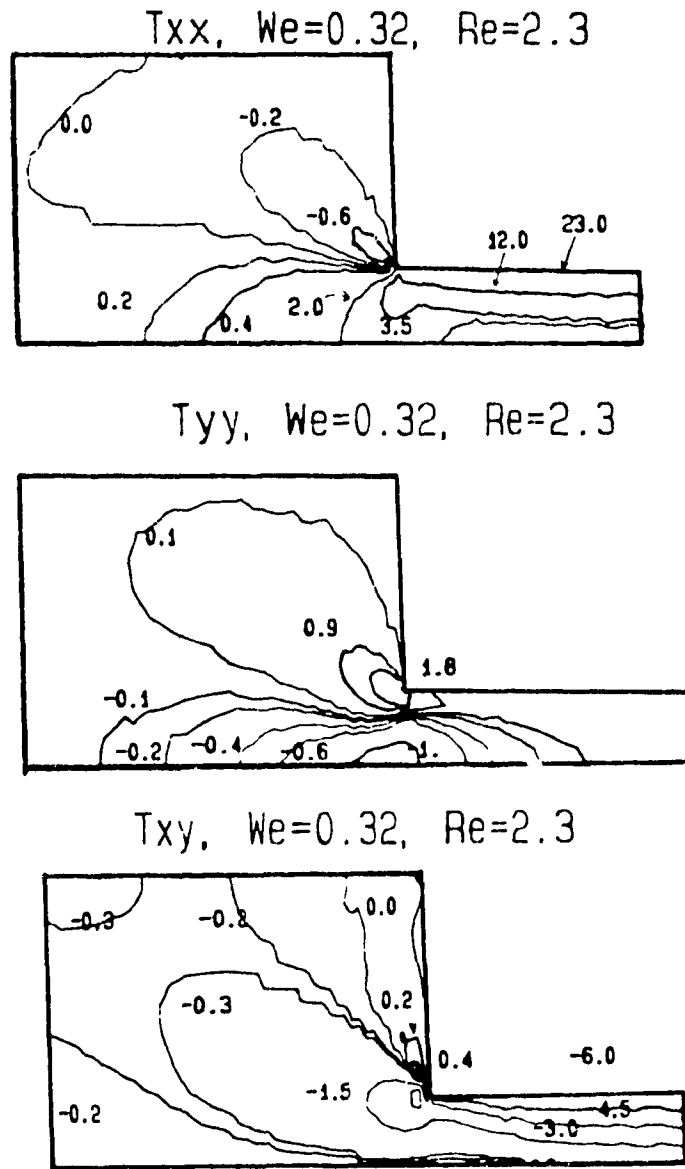


Figure (II.5.1.1.2): Dimensionless stress contours on a planar 4:1 contraction at $We=0.32$ and $Re=2.3$.

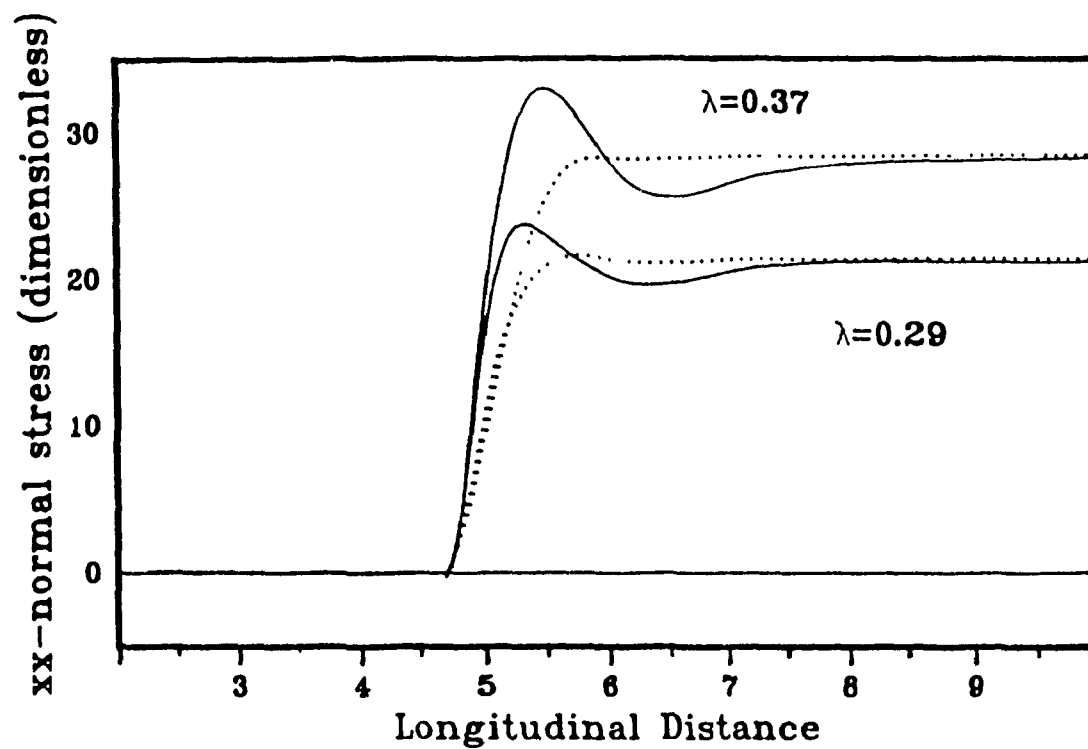


Figure (II.5.1.1.3): Effect of kinematics used in the integration of the UCM model on the dimensionless xx -normal stress along the $i=11$ coordinate line. Solid lines correspond to viscoelastic kinematics; dotted lines to Newtonian kinematics. Grid (A) of Figure (II.5.1.1).

(II.5.1.2) Flow Patterns

In a specific flow geometry, inertia and elasticity are the dominant factors that determine the form of the flow field. Keeping in mind that the effect of elasticity should never be dissociated from the Reynolds number (Pilate and Crochet, (1977)), the effect of the relaxation time on the form of the flow field at the entry section at various levels of inertia is examined. Experimental evidence suggests that the vortex activity in planar flows is rather weak compared to the axisymmetric flows. The maximum vortex activity appears at very low Reynolds number, and reduces as the inertia of the fluid increases.

Figure (II.5.1.2.1) gives the streamlines of a Newtonian fluid at three Reynolds numbers. The predicted recirculation region decreases in both size and intensity as the inertia of the fluid increases. There is practically no recirculation at $Re=6.0$, whereas at near creeping flow conditions ($Re=0.1$) the relative strength of the predicted vortex is 1.14 %. At $Re=2.0$ the relative strength of the vortex is reduced to 0.76%. The corresponding streamlines for a Maxwell fluid are given in Figure (II.5.1.2.2). It is interesting to observe that, in the viscoelastic case, a second vortex appears at the lip of the contraction (lip vortex), which seems to be less affected by the inertia of the fluid than the corner vortex. It has been suggested that this vortex is a numerical artifact associated with the ad-hoc approximation of the corner vorticity based on Kawaguti's method. This vortex disappears when the corner becomes streamlined (section II.5.2), and that is an indication that the lip vortex might indeed be a numerical artifact.

(II.5.2) Smooth 4:1 Contractions

In this section, the flow and stress patterns in 90° non-abrupt contractions are studied. Such configurations are of practical importance, since a perfectly sharp corner is a

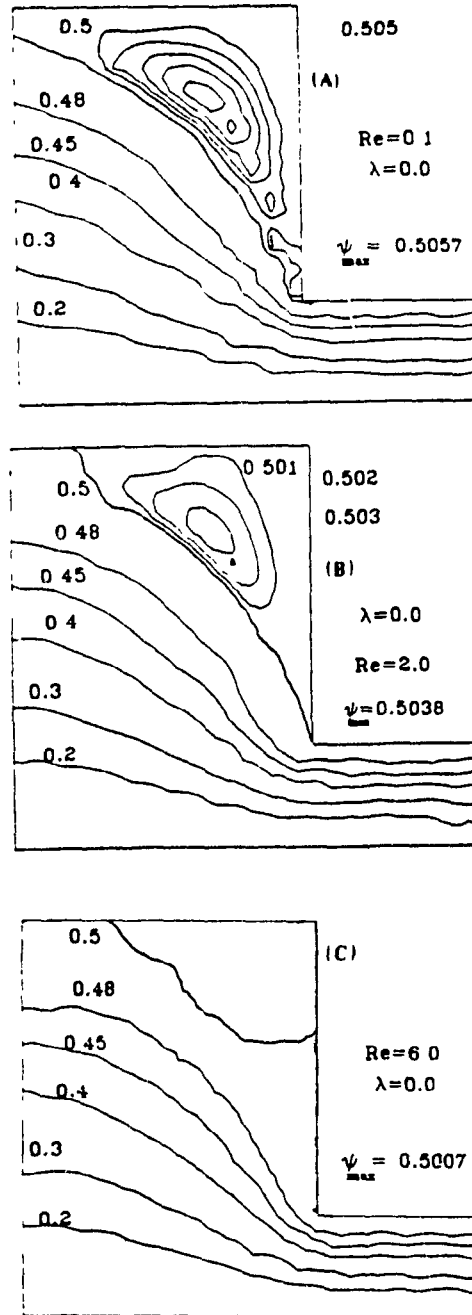


Figure (II.5.1.2.1): Streamlines of a Newtonian fluid in a 4:1 abrupt contraction at various levels of the Reynolds number.

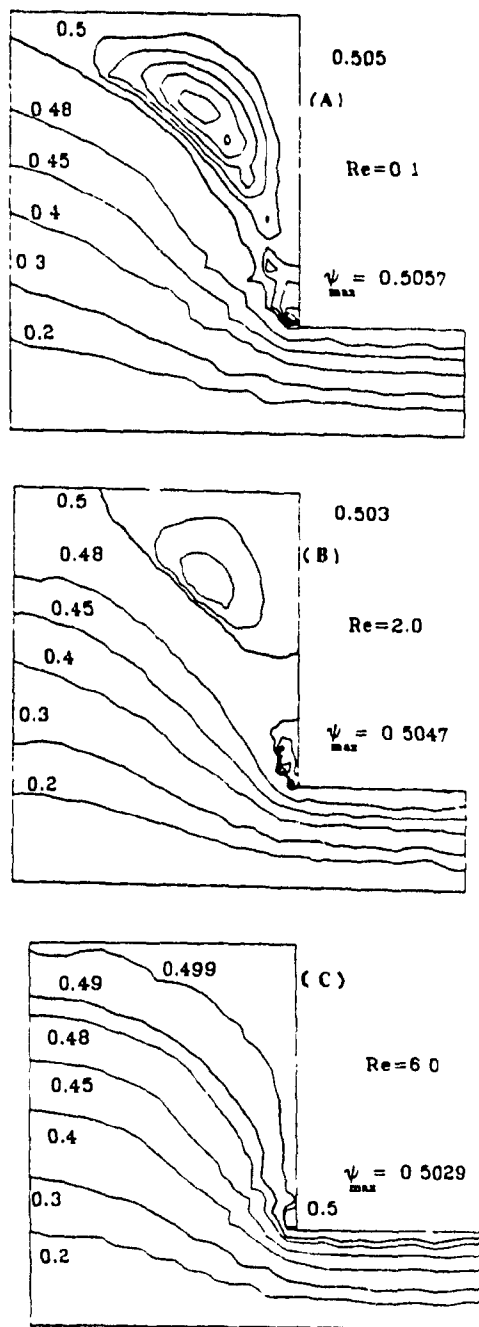


Figure (II.5.1.2.2): Streamlines of a Maxwell fluid (We=0.7) in a 4:1 abrupt contraction at various levels of the Reynolds number.

mathematical idealization, having no counterpart in the real world. The types of rounded corners studied along with the computational grids are shown in Figure (II.5.2.1). The treatment of curved boundaries like the ones introduced by the smooth edges of the contraction presents no difficulty in the context of boundary fitted curvilinear coordinates. This is a great advantage of the BFCC approach, since it allows a unified treatment of practically any kind of flow field, without the need to resort to sharp corners in order to accommodate a rectangular finite difference mesh or to tedious and often inaccurate boundary interpolations. In the following, the creeping flow ($Re=0.1$), of an upper convected Maxwell fluid is analyzed using various meshes. The problem of viscoelastic flows in planar contractions with smooth corner has not received large attention in the literature, even though it is an excellent candidate for meaningful grid refinement studies (Rosenberg and Keunings, (1988)).

Figures (II.5.2.2) and (II.5.2.3) show the streamlines in the two 4:1 contractions of Figure (II.5.2.1) at various elasticity levels. It is obvious that both the size and the strength of the corner vortex decrease as the re-entrant corner becomes more streamlined. This is true for Newtonian as well as for elastic fluids. The strength and size of the vortex increase with elasticity, a fact also observed experimentally in Boger fluids (Boger et.al. (1986)). The predicted vortex strength was found to decrease with grid refinement, as can be seen in Figures (II.5.2.4) and (II.5.2.5). However, when the grid refinement became too extensive, the reduction in the size and strength of the predicted vortex was proportionally smaller. Furthermore, the increase in strength of the secondary flow with elasticity was predicted in all meshes, regardless of mesh size; this leads to the conclusion that the predicted recirculation is not a numerical artifact, even though its specific strength is indeed grid dependent. In the smooth geometries examined here, grid refinement also led to significant increase in the range of convergence, contrary to what previous research has found for the sudden 4:1 contraction. This finding corroborates the assumption that the stress singularity at points of strong boundary discontinuity is, at least partially, responsible for the High

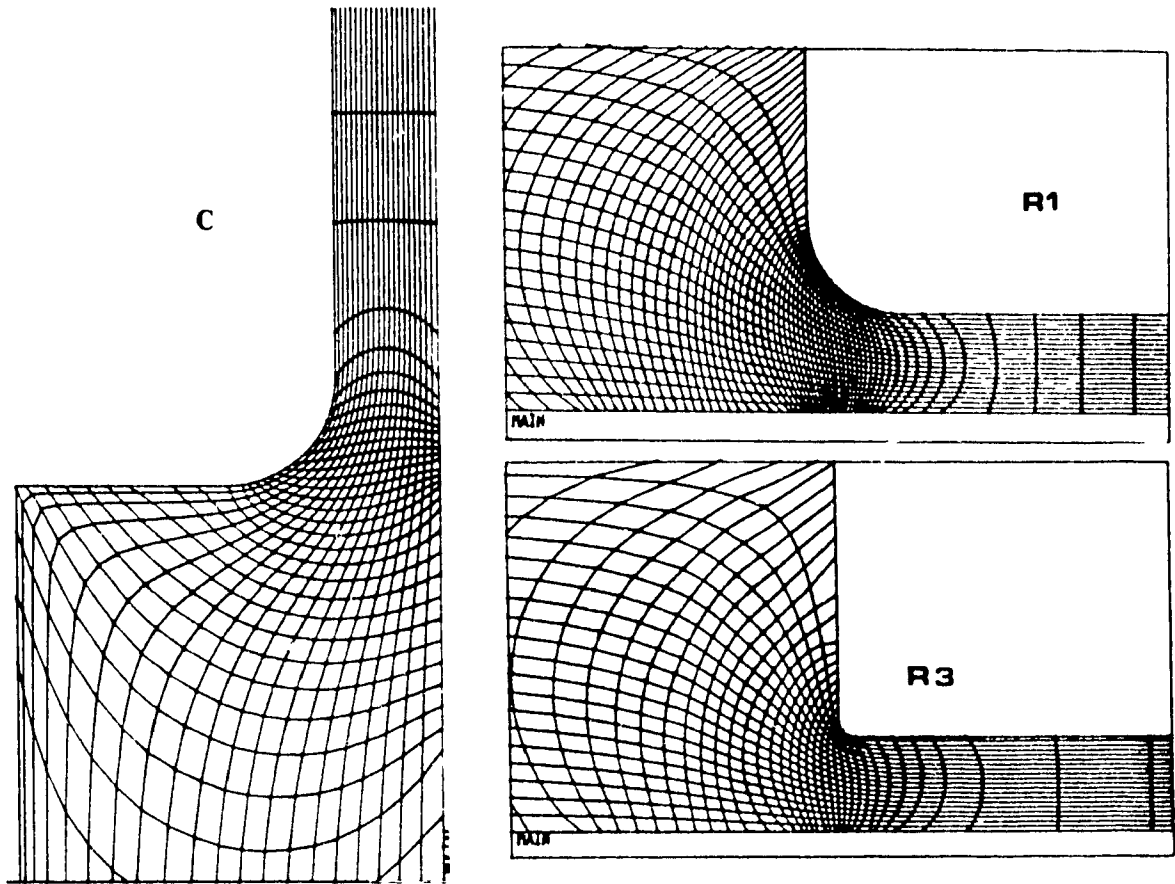
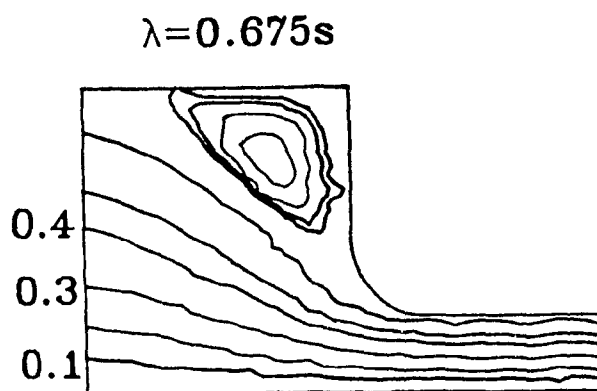
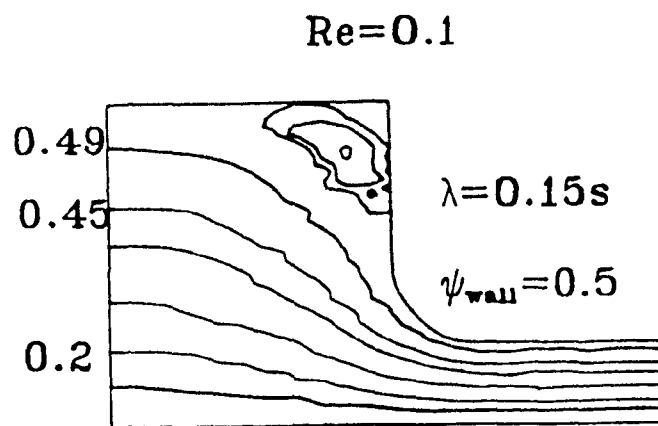


Figure (II.5.2.1): The rounded corner geometry and part of the computational grids used in the simulations



(in vortex: 0.5005,0.501,0.502,0.503)

Figure (II.5.2.2):

Streamlines of a Maxwell fluid in the R1 rounded-corner contraction at two elasticity levels

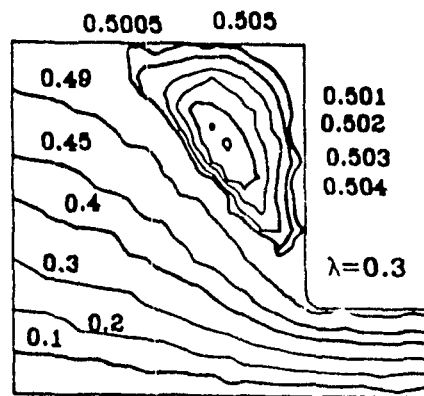
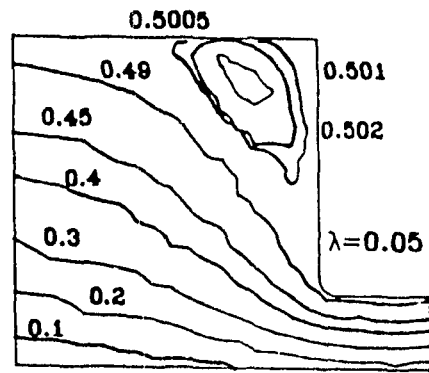


Figure (II.5.2.3):

Streamlines of a Maxwell fluid in the R3 rounded corner contraction at two elasticity levels

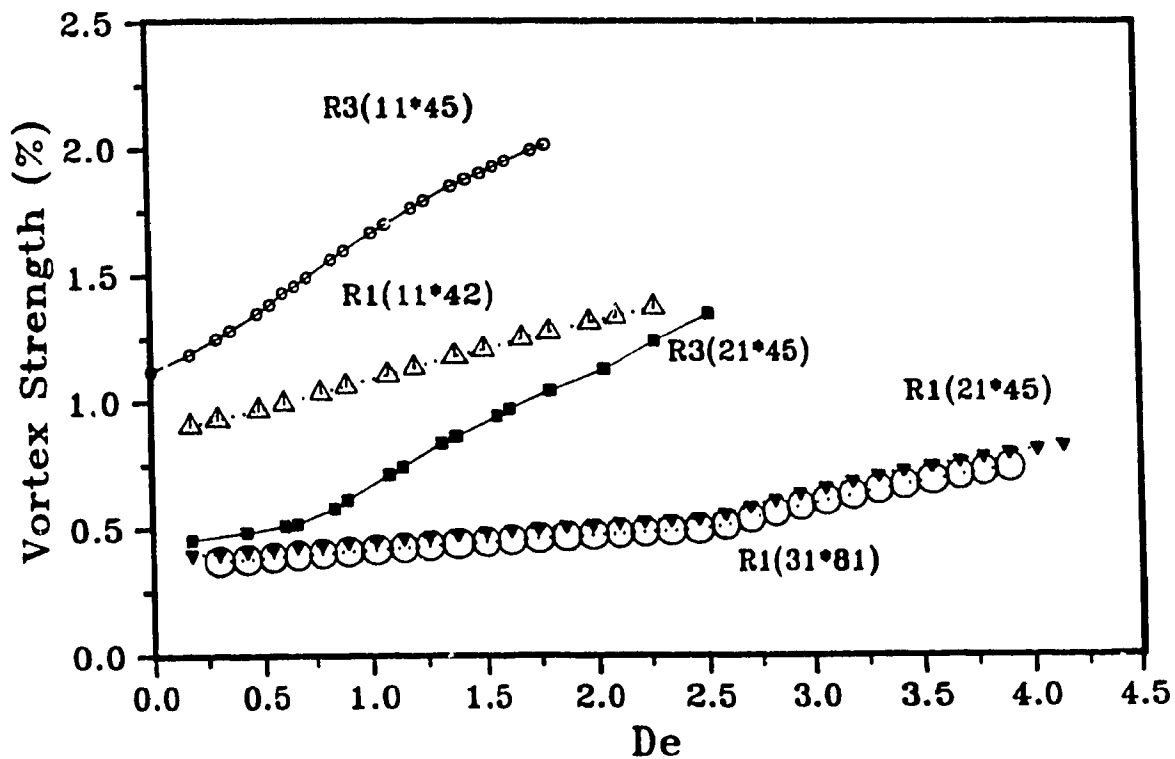


Figure (II.5.2.4):

Effect of fluid elasticity ($De = \lambda \cdot \gamma_{max}$) on vortex strength in various meshes for the rounded corner geometries R1 and R3. The vortex strength is defined as the (%) ratio of the circulation in the vortex to the total flowrate through the contraction.

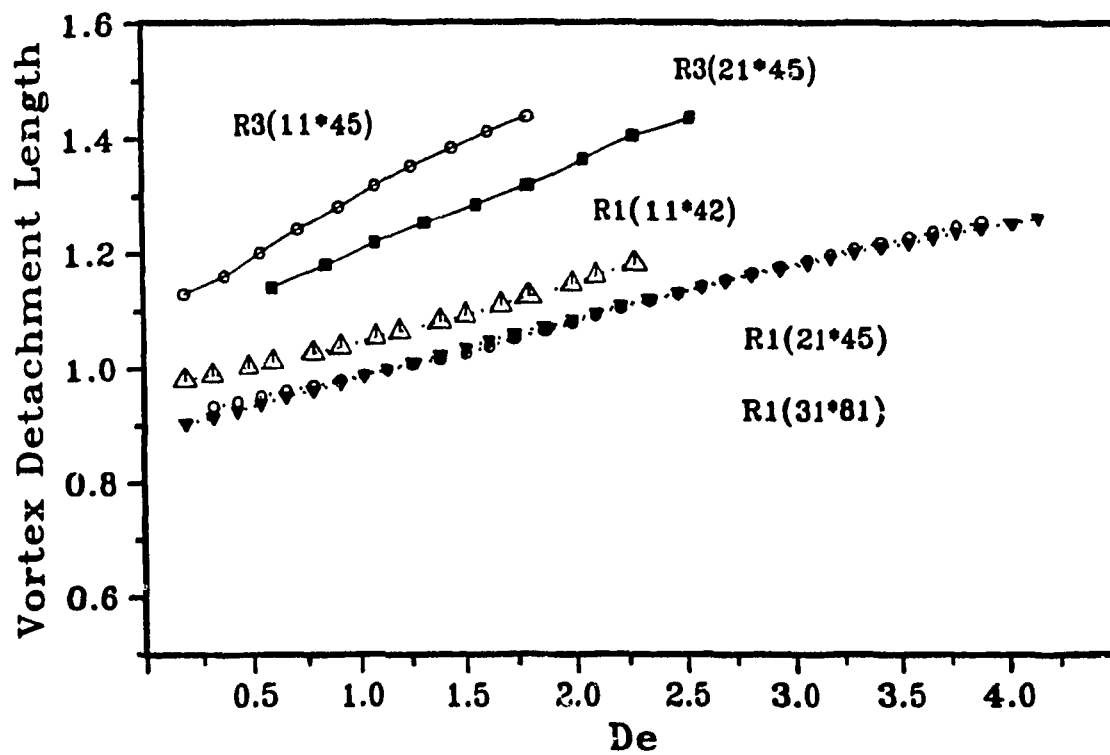


Figure (II.5.2.5):

Effect of fluid elasticity ($De = \lambda \cdot \dot{\gamma}_{max}$) on vortex size in various meshes for the rounded corner geometries R1 and R3.

Weissenberg Number Problem.

Figure (II.5.2.6.A) gives the xx -normal stress along the wall for the two smooth contractions at two levels of elasticity. 21×42 grids were used in these simulations. It is obvious that increasing (λ) increases substantially the stress level in both geometries. Furthermore, the sharper contraction (dotted line) is associated with much sharper stress gradients than the smoother one (solid lines); this partially explains the smaller limiting Deborah number in the sharper contraction (2.5 as compared to 4.2 in the smoother contraction R1). The stress along the wall in the smoother geometry R1 is further shown in figure (II.5.2.6.B) for a wider range of elasticity. Of interest is the transition from fairly smooth to substantially oscillatory response; this oscillatory behaviour signals the onset of numerical breakdown. The xx -normal stresses along the 20th coordinate line (the one closest to the wall) are shown in figure (II.5.2.7). Comparing to Figure (II.5.2.6), it can be seen that the stress response immediately near the wall is much smoother than that on the wall - still with a small amount of overshoot.

The stress build-up and relaxation in the vicinity of the re-entrant corner is of large practical interest, since this is an area of extreme conditions, where the fluid experiences combined shear and elongational flow. However, non-isothermal effects resulting from poor wall temperature control and/or viscous heating can influence the accuracy of measurements in that region. Aldhouse et al. (1986) found that the accuracy of birefringence measurements near the wall was severely affected by non-isothermality. On the other side, the behaviour of the stresses along and near the centerline is interesting, because this region is reasonably free of thermal gradients. Therefore, centerline stresses can be measured accurately and easily related to velocity data. Figure (II.5.2.8) presents the xx - and yy -normal stresses along a line very near to the axis of symmetry ($i=2$, 21×42 grid, distance from centerline at entry 0.1). The xx -stresses increase and the yy -normal stresses decrease in absolute value

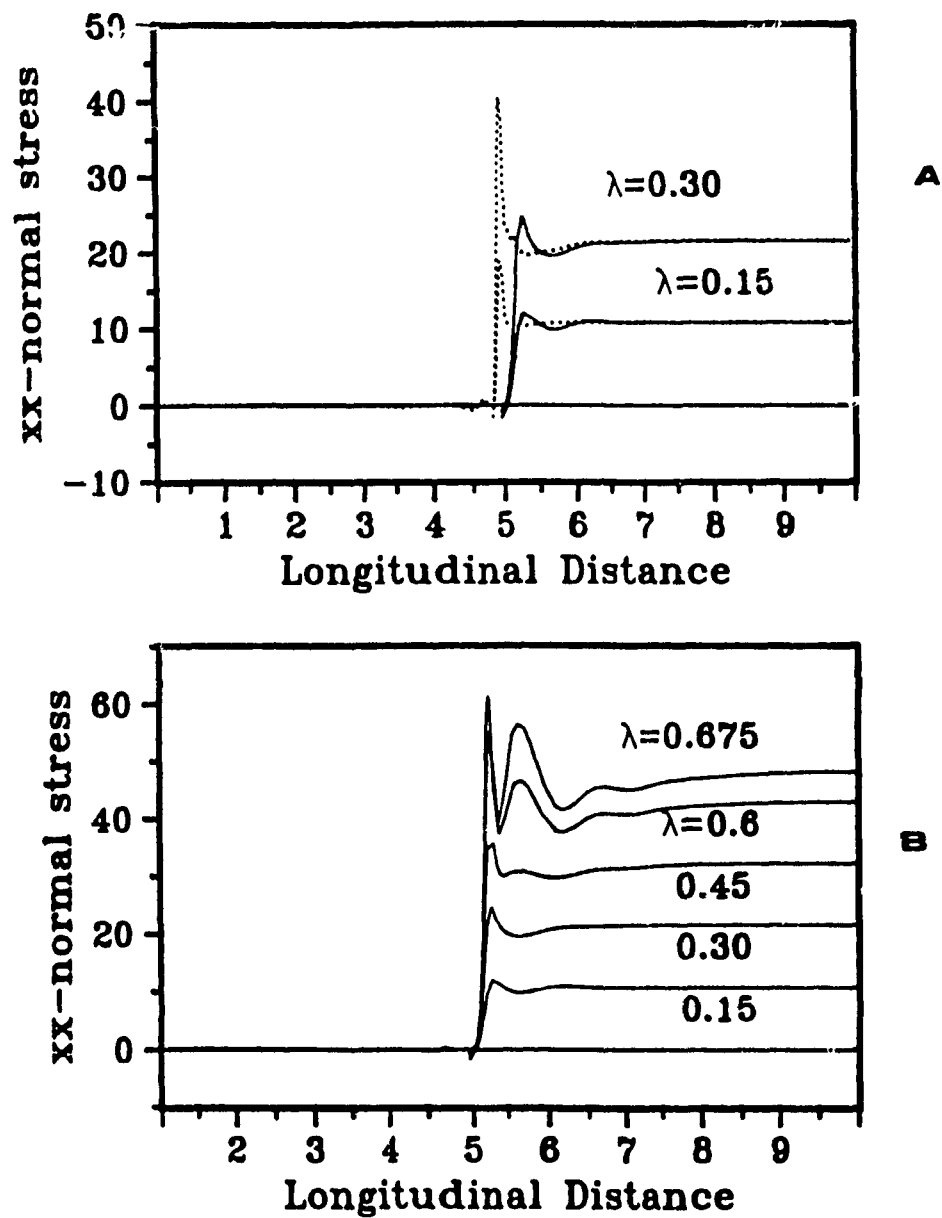


Figure (II.5.2.6): Dimensionless xx -normal stresses along the wall in a 21*42 and 21*45 meshes in the geometries R1 and R3. (A): Solid line corresponds to R1 and dotted line to R3; (B): Geometry R1.

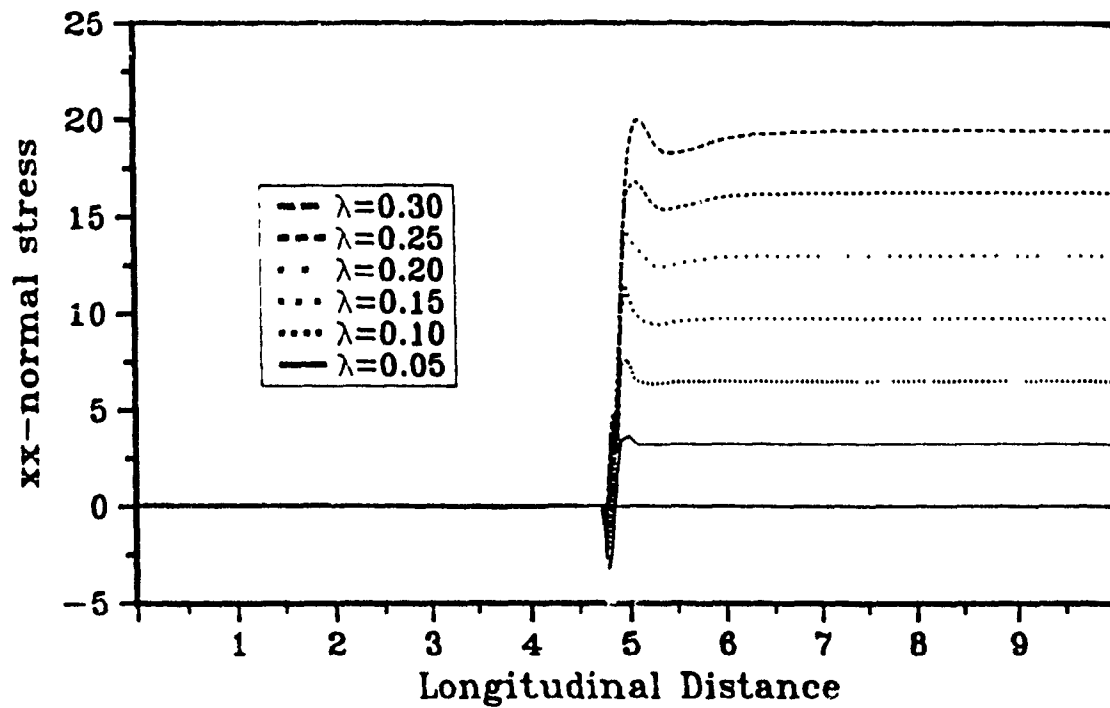


Figure (II.5.2.7):

Dimensionless xx -normal stresses along the $i=20$ coordinate line (closest to the wall) in a 21×42 mesh in the geometry R3.

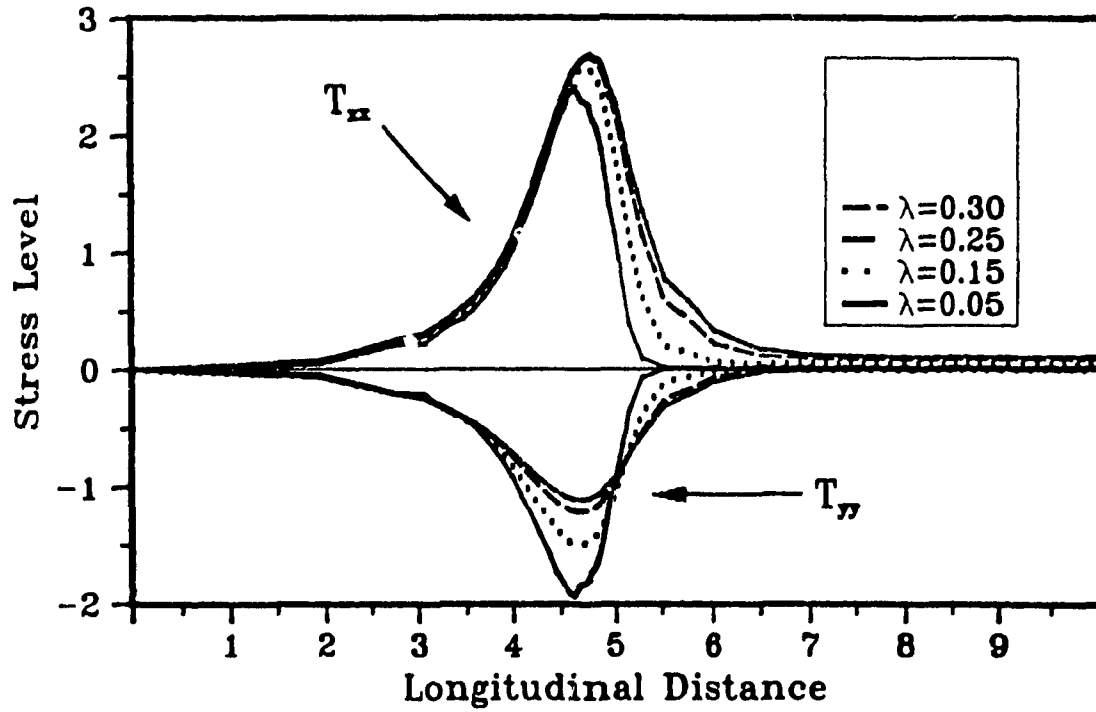


Figure (II.5.2.8):

Dimensionless xx - and yy -normal stresses along the $i=2$ coordinate line (near the centerline) for various values of the relaxation time in the geometry R3.

with increasing relaxation time. In both cases, the stress maximum is shifted downstream with increasing elasticity and the tube length required for the stresses to reach their downstream fully developed values also increases. This behaviour is in agreement with a theoretical analysis of the stress equations along the axis of symmetry and also with available experimental evidence (Aldhouse et al. (1986)). Stress contours in the contraction (R1) are shown in Figure (II.5.2.9). The effect of elasticity in the xx -stress patterns is further shown in figure (II.5.2.10). Clearly, the region of negative T_{xx} shrinks with increasing elasticity, while the stress level in the downstream tube increases. The velocity along the centerline for the smoother contraction (R1) is also shown in Figure (II.5.2.11) for a range of the relaxation times. Velocity overshoot, characteristic of elastic fluids, is present; its intensity increases with the relaxation time of the fluid.

(II.5.3) Flow in a 20:1 Tapered Contraction

In this section, the steady, isothermal flow of a Maxwell fluid in a 20:1 tapered contraction is considered. This type of geometry, with walls that are not lines of constant x or y in a Cartesian coordinate system, is rather very difficult to solve with traditional finite differences. On the other hand, it is a routine problem, at least from the discretization point of view, if one uses BFCCs. In the context of finite elements, this problem has been treated by Marshal and Crochet (1987), who presented certain features of the solution at very high Deborah numbers.

The geometry, along with the computational grid, are shown in Figure (II.5.3.1). Fully developed velocity profiles have been assumed at the inlet and outlet sections and no-slip walls. Sample results regarding the vorticity and stress distributions in this contraction are given in Figures (II.5.3.2) and (II.5.3.3).

(II.5.4) Flow in a non-Symmetric Channel

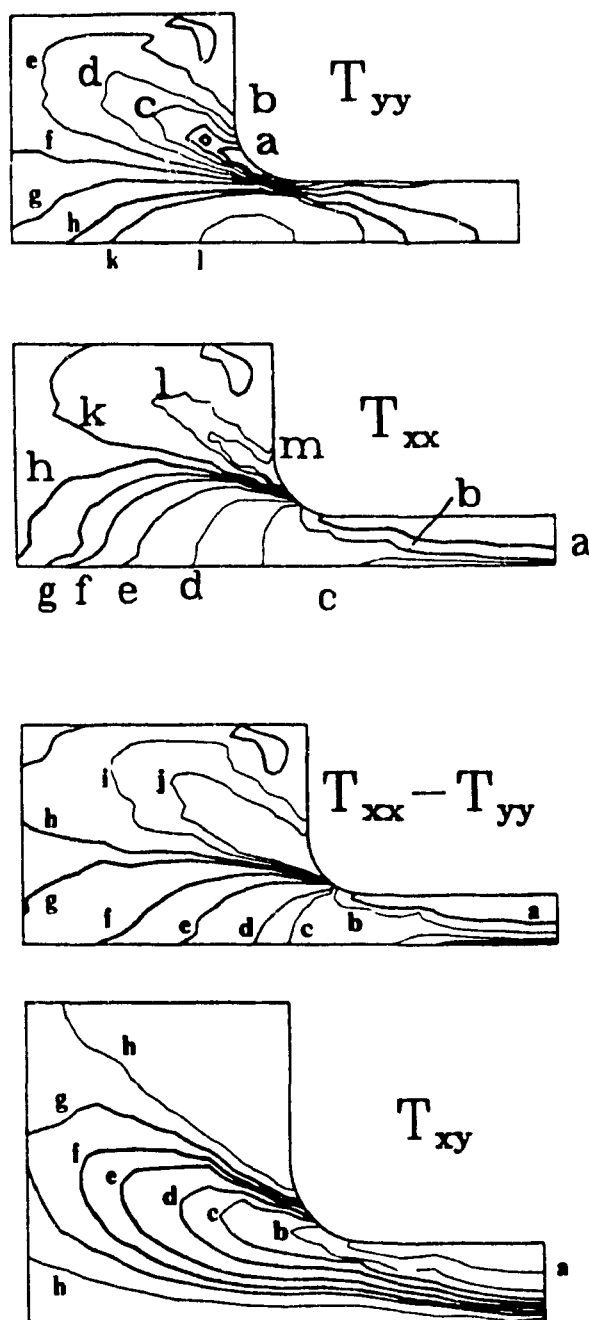


Figure (II.5.2.9): Dimensionless stress contours on the contraction R1. $Re=0.1$ and $\lambda=0.675$. Contour values are (in alphabetical order): For T^u ; 10, 3, 2, 1, 0.5, 0.3, 0.2, 0.1, 0, -0.15, -0.2. For T^v ; 0.7, 0.6, 0.45, 0.3, 0.15, 0, -0.15, -0.3, -0.4, -0.6. For T^w ; 3, 1.5, 1, 0.75, 0.55, 0.45, 0.35, 0.2. For $(T^u - T^v)$; 10, 4, 2.5, 2, 1, 0.5, 0.1, 0, -0.2, -0.4

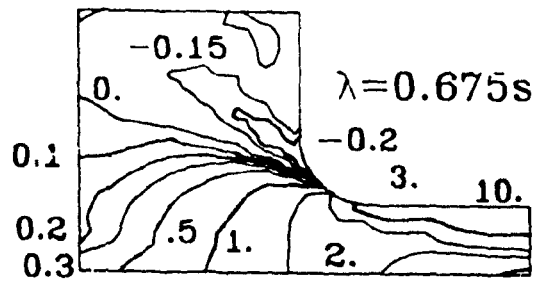
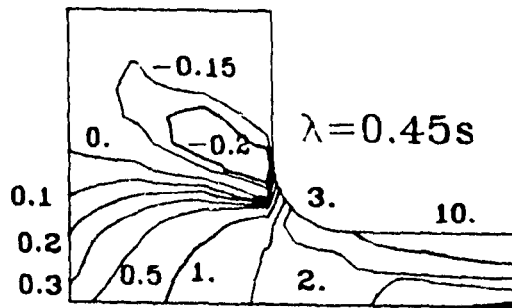
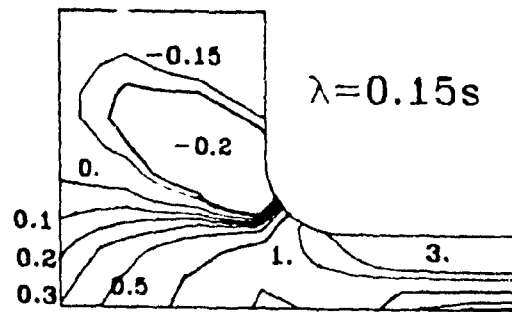


Figure (II.5.2.10): Effect of elasticity on the dimensionless xx -normal stress in the contraction R1. $Re=0.1$

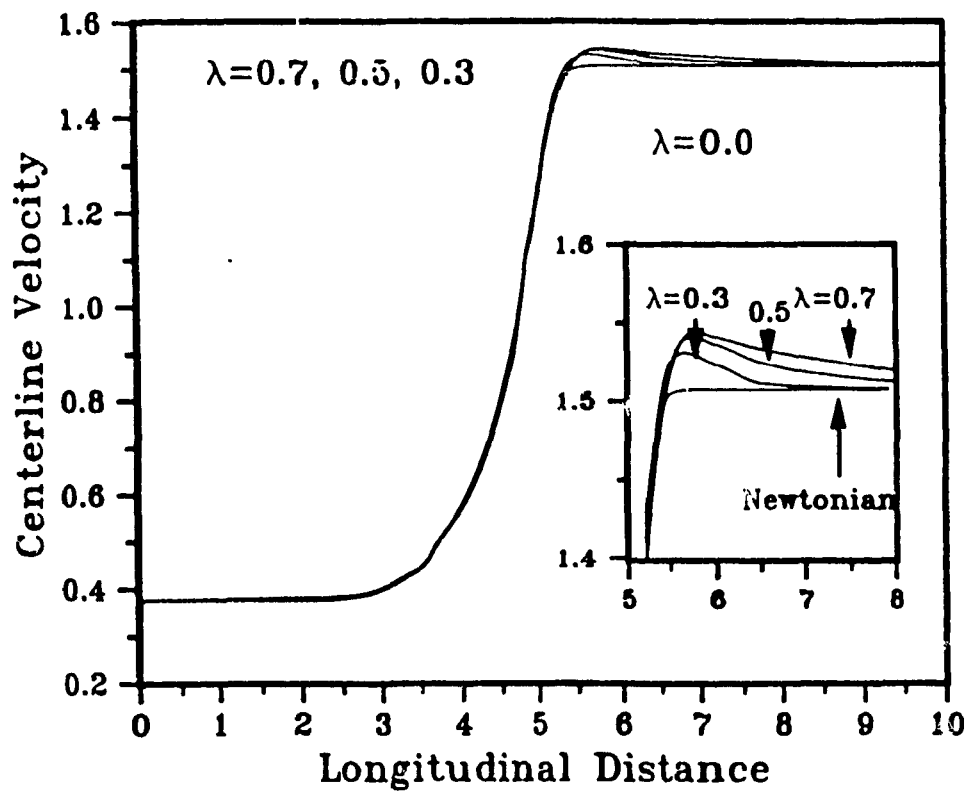


Figure (II.5.2.11): Centerline velocity in the rounded corner contraction R1 at various elasticity levels.

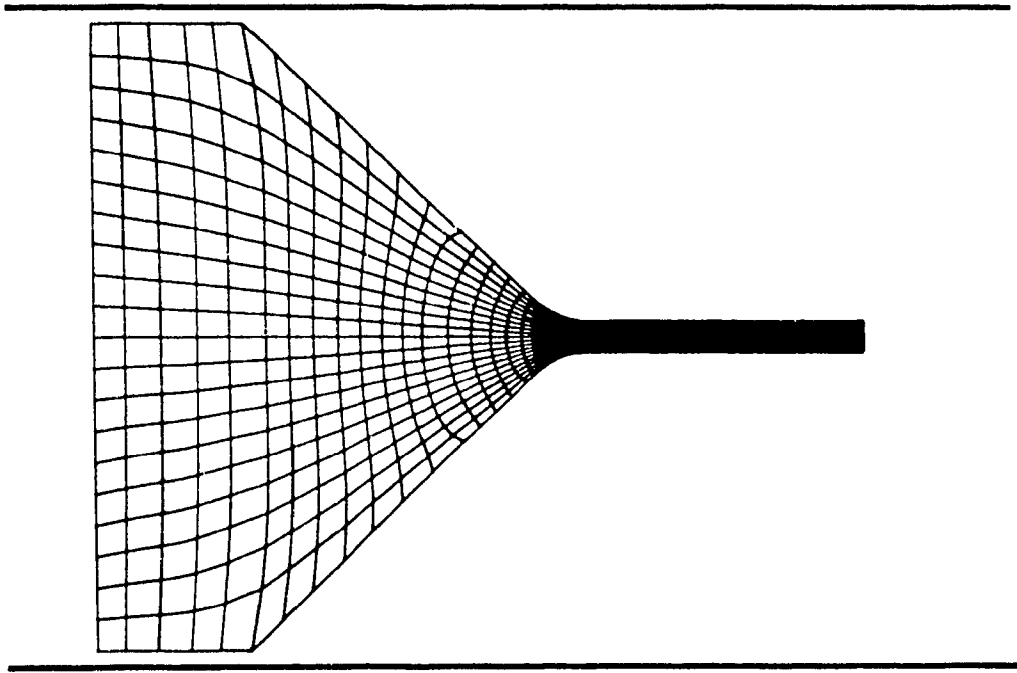
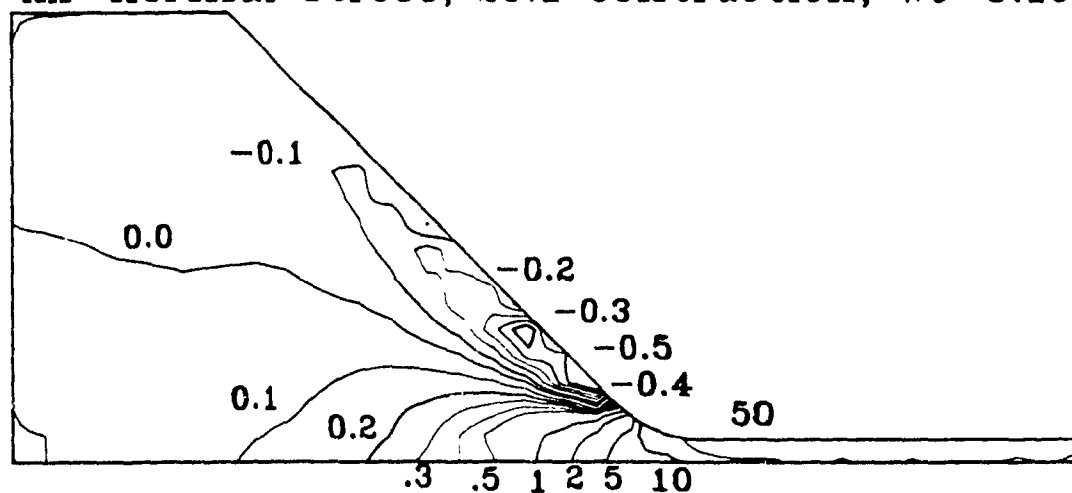


Figure (II.5.3.1):

The geometry and the curvilinear mesh used in the study of the 20:1 tapered contraction.

xx-normal stress, 20:1 Contraction, $We=0.15$



yy-normal stress, 20:1 Contraction, $We=0.15$

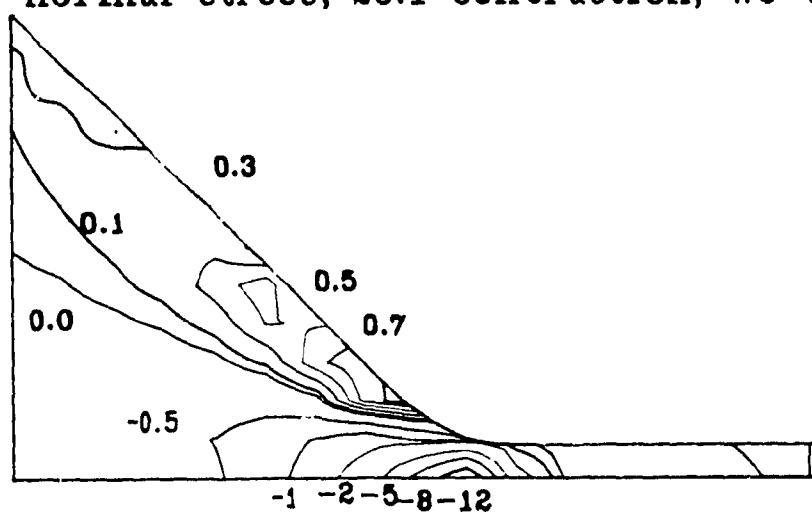


Figure (II.5.3.2): Dimensionless xx - and yy -normal stresses in a 20:1 tapered contraction at $We=0.15$

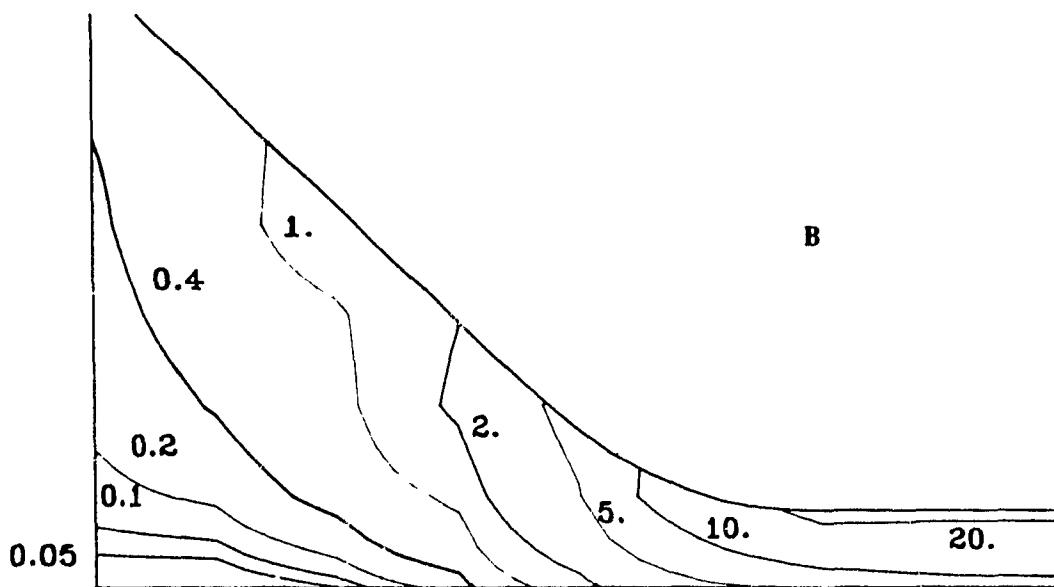
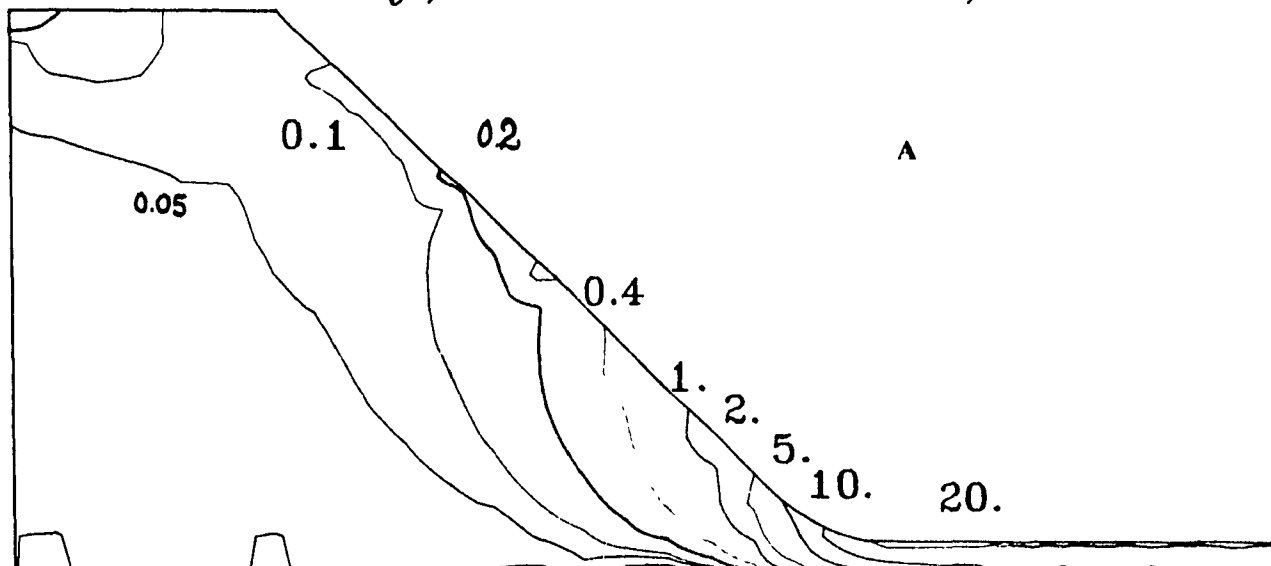
Vorticity, 20:1 Contraction, $We=0.1$ 

Figure (II.5.3.3):

Vorticity distributions in the 20:1 tapered contraction at $We=0.1$. (B): Corner detail.

It was argued earlier that the major incentive behind the use of BFCCs is the simulation of flow in channels of arbitrary geometry. Ability to analyze flow problems in arbitrary domains allows for the study of flow phenomena not only as functions of the material parameters but also as functions of the flow channel itself. In the following, the flow of a Maxwell fluid with $We=0.7$ through the non-symmetric contraction of Figure (II.5.4.1) is briefly analyzed. Since one corner of this contraction is sharp and the other is smooth, the resulting stress and flow patterns are significantly different from those in the symmetrical 4:1 contraction studied previously. The streamlines are given in Figure (II.5.4.2.A). Smoothing of the upper corner results in the disappearance of the upper recirculation vortex. The fluid is pushed upwards by the sharp corner and then converges into the downstream tube. This is evident by observing the flowpath of a particle injected at the center of the upstream tube (streamline with $\psi=0.75$). Qualitatively, this result is similar to experimental observations by Evans and Walters (1986). This geometry-induced redistribution of the velocity field affects significantly the stress patterns. Figure (II.5.4.2.B) shows the shear stress in the contraction. Evidently T_{xy} is not symmetrical, with higher shear present at the upper half of the flow channel.

The first normal stress difference (N_1) is shown in Figure (II.5.4.3). Again the pattern is asymmetric. Evidently, the lower part of the contraction is occupied by an extensive region of negative ($T_{xx}-T_{yy}$); the region of negative ($T_{xx}-T_{yy}$) in the upper part of the channel is considerably reduced. From the N_1 patterns, it is evident that the fluid experiences different deformation in the upper and lower half of the channel. In the upper half, stretching in the longitudinal direction is predominant, whereas at the lower half the fluid is mainly stretched in the transverse direction.

(II.5.5) The Contraction/Expansion Problem

In this section, a smooth 4:1 contraction/expansion problem is analyzed. This is an

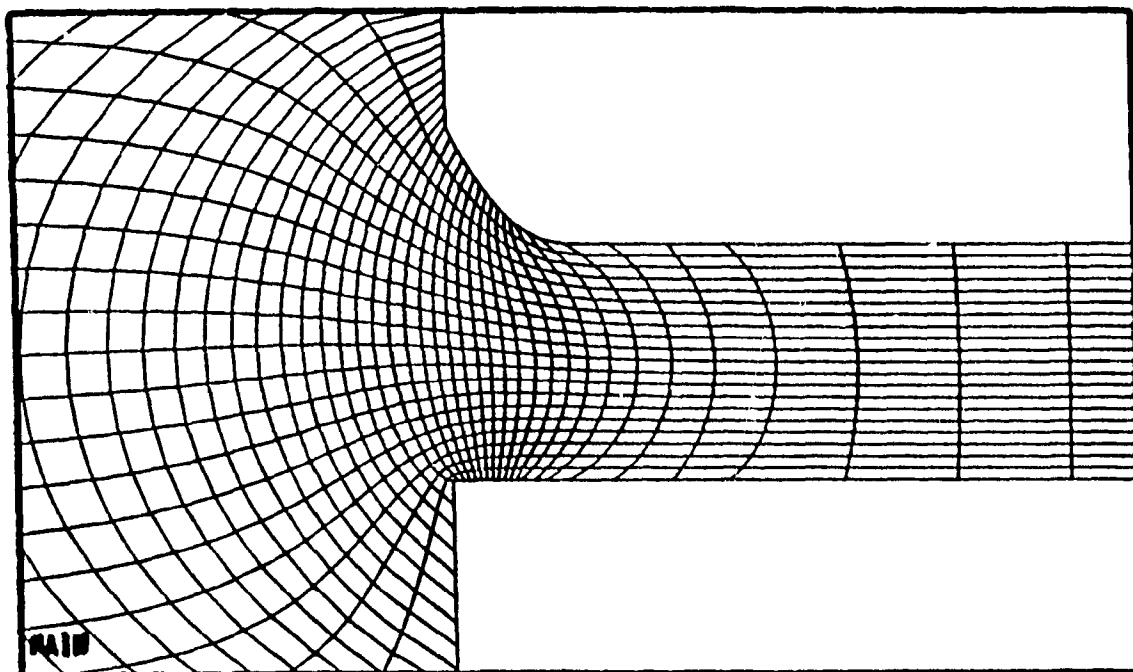


Figure (II.5.4.1):

The geometry and the curvilinear mesh used in the study of the 4:1 sudden contraction with asymmetric entrance region.

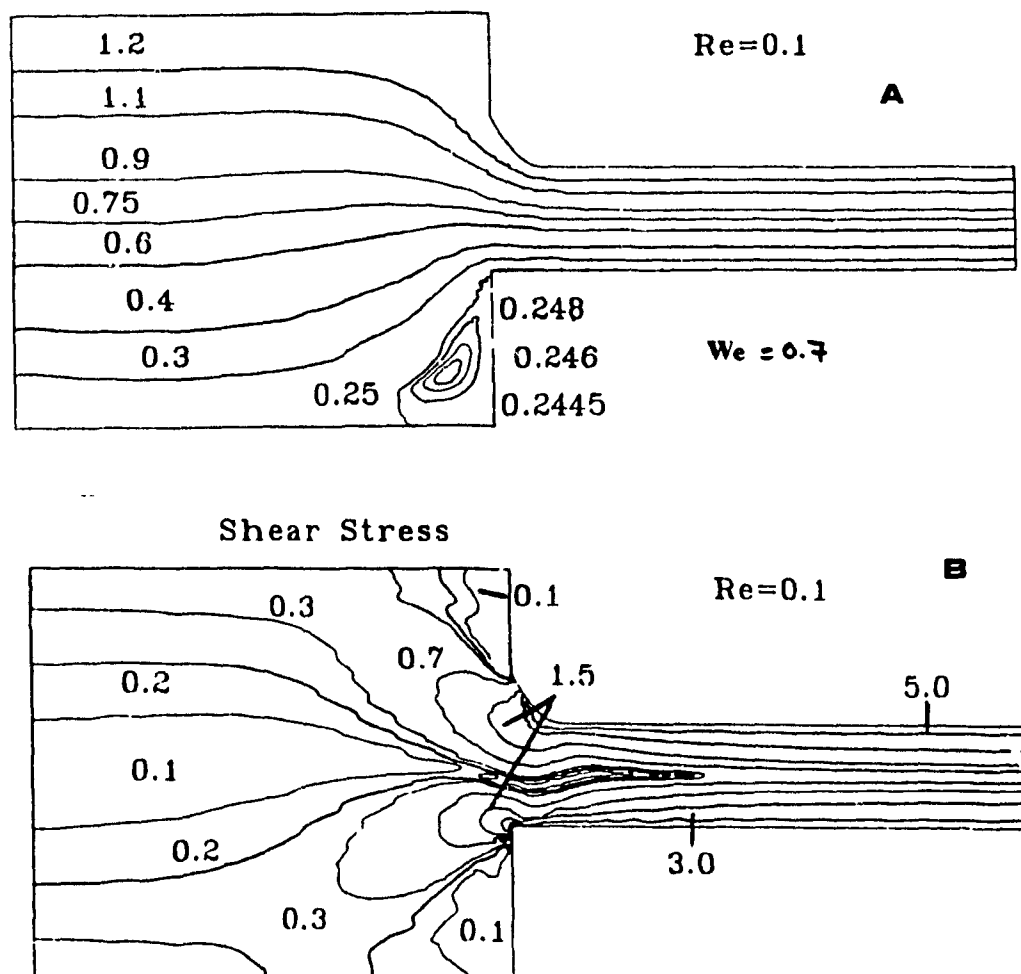


Figure (II.5.4.2): Streamlines (A) and dimensionless shear stress (B) patterns for a Maxwell fluid flowing through a 4:1 non-symmetric contraction.

Principal Stress Difference

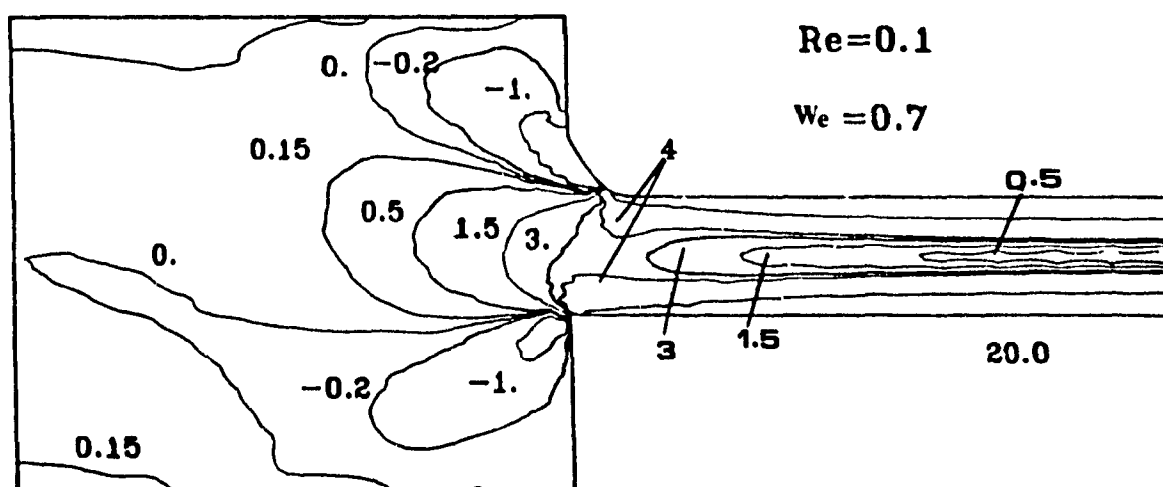


Figure (II.5.4.3): Dimensionless principal stress difference ($T^x - T^y$) in a non symmetric 4:1 planar contraction.

important problem in the polymer processing industry and has received considerable attention in the literature (Perera and Walters (1977)). The geometry and the computational grid are shown in Figure (II.5.5.1). Because of symmetry only the flow in the upper half of the flow channel is analyzed. The radius of the upstream and downstream parts is $R_1=4.0$, while at the tip of the contraction, the radius is $R_2=1.0$. A fully developed velocity profile is assumed at the inlet:

$$u(y) = u_0(1 - (0.25*y)^2), 0 < y < 4$$

The length of the outflow region was determined, iteratively, as the length required for stress and kinematics to reach the 99% of their theoretical fully developed values. The computational domain was then adjusted accordingly. In this contraction /expansion, the absence of a constant diameter section between the converging and diverging sections, as was the case in Perera and Walters (1977) complicates the problem, since the stresses which build up during the entry flow relax in an environment of rearranging velocity in the downstream diverging section.

An interesting elastic effect in expanding flows is the suppression of the secondary flow that is usually present in the expanding section at moderate and high values of the Reynolds number, with increased elasticity. Figure (II.5.5.2) shows the streamlines in the geometry of Figure (II.5.5.1) at $Re=12.0$ for a range of the elasticity parameter. Evidently, the intensity and size of the secondary flow is reduced as the elasticity of the material is increased. Figure (II.5.5.3) summarizes results regarding the size and strength of the secondary flow at various elasticity levels. In that figure, the vortex strength is defined as $100*(\psi_{max}-\psi_{val})/\psi_{val}$ and the vortex size (here, the relative detachment length) is defined as $100*(L_e/L_n)$, with L_n and L_e being the detachment lengths of the Newtonian and the elastic fluid. When the relaxation time increases from 0 to 0.22, the vortex detachment length is decreased to about 80% of the Newtonian value, while the strength of the secondary flow decreases from 3.8% to about 2.4%.

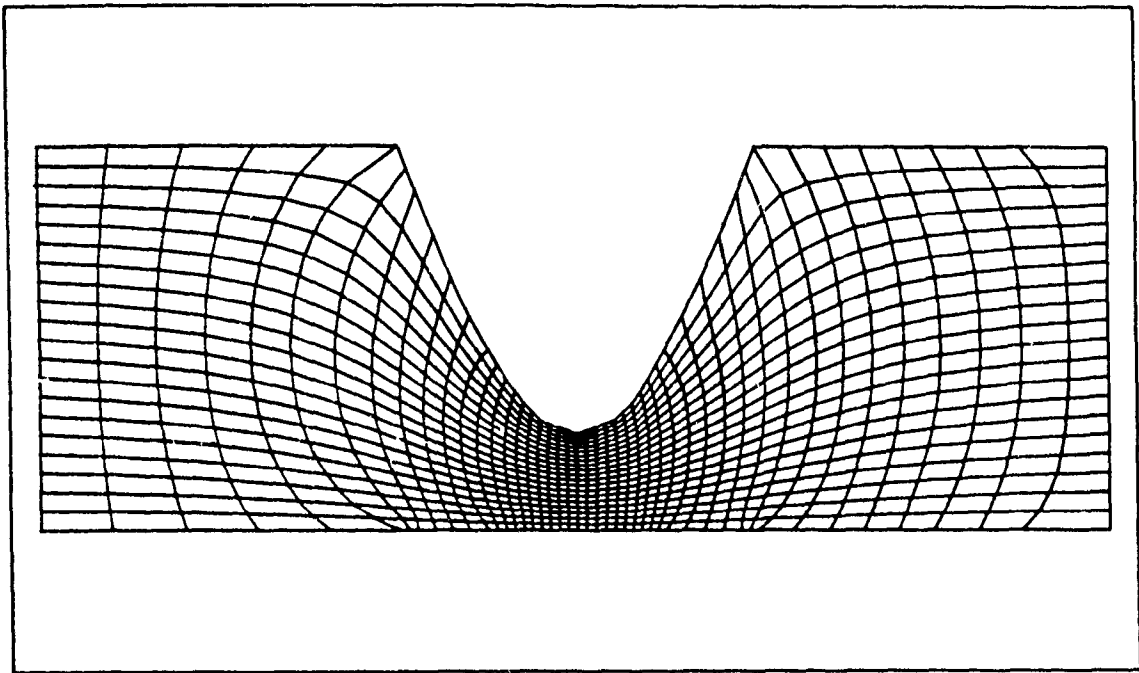


Figure (II.5.5.1):

The geometry and the curvilinear mesh used in the study of the contraction/expansion flow.

Elastic Vortex Reduction

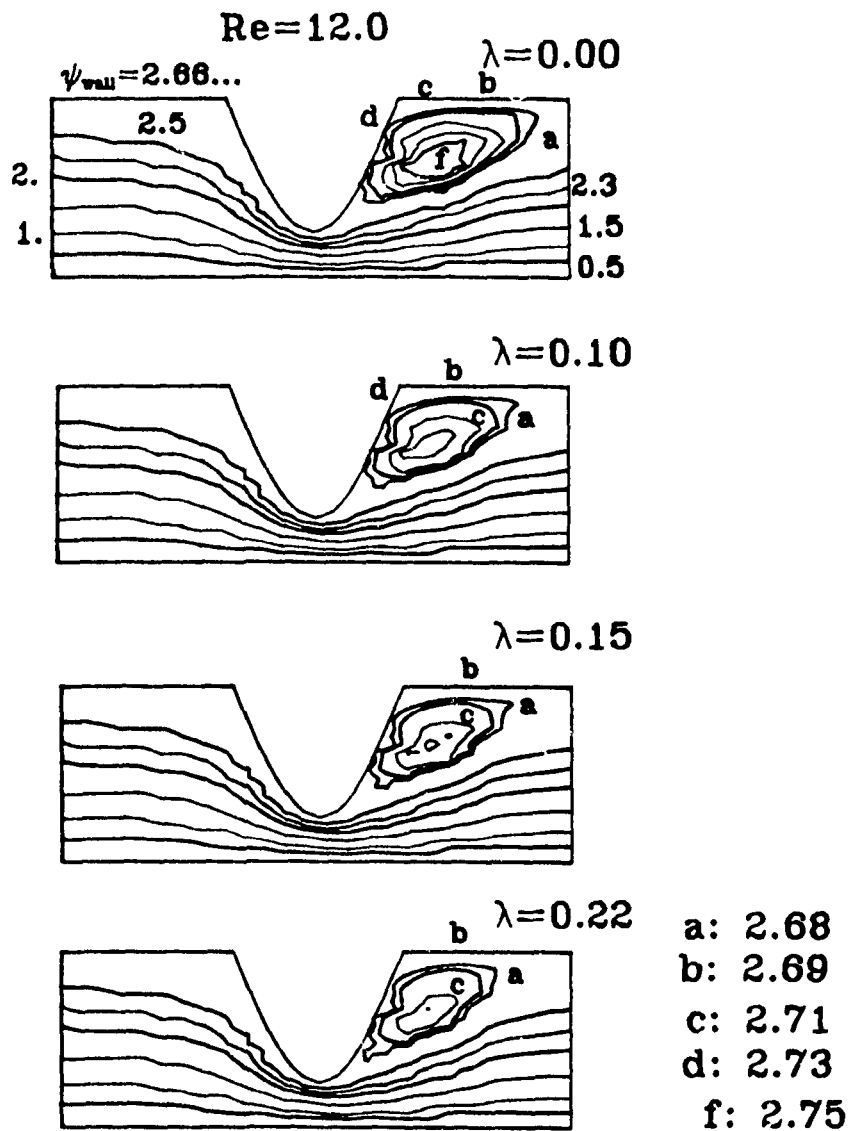


Figure (II.5.5.2):

Secondary flow in the contraction/expansion problem at various elasticity levels. $Re=12.0$.

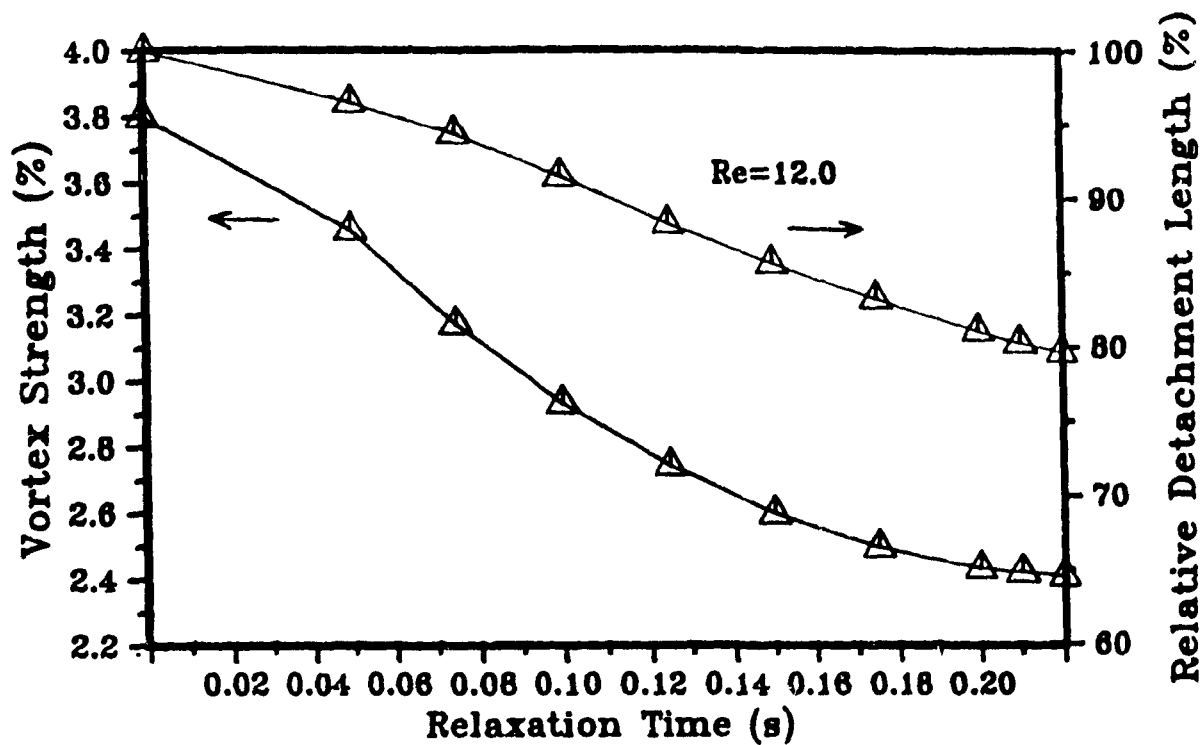


Figure (II.5.5.3):

Vortex size and strength at various relaxation times in the contraction - expansion geometry. $Re=12$.

The xx - and yy -normal stresses in the same geometry are shown in Figure (II.5.5.4). In both cases, the effect of elasticity can be seen in the slower stress decay to the fully developed values in the expanding section. The xx -normal stress along the wall as well as the wall vorticity are shown in Figure (II.5.5.5) for a range of relaxation times. Interestingly, the peak in xx -stress increases dramatically with elasticity; this increase is partially responsible for the numerical breakdown at higher elasticity levels. Similar, but less severe behaviour is also observed regarding the wall vorticity. Finally, the effect of inertia on flow patterns and vorticity distributions is shown in Figures (II.5.5.6) and (II.5.5.7).

(II.5.6) Flow in a Bend

In this section, the flow of Newtonian and Maxwell fluids in a bend is briefly analyzed. An extensive analysis of the flow of an Oldroyd - B fluid in this geometry has been given by Perera and Walters (1977).

The geometry and the computational grid, which was constructed with coordinate lines normal to the upper wall, are shown in Figure (II.5.6.1). The vorticity distributions in a Newtonian fluid at $Re=48$ and $Re=16$ are given in Figure (II.5.6.2). It can be seen that a region of high vorticity develops at the wall opposite of the corner of the bend, whose intensity increases with fluid inertia. This is in qualitative agreement with the work of Liou et al. (1984) in a curved bend. A detail of the two vortices that form at $Re=48$ is given in Figure (II.5.6.3). The distribution of vorticity in a Maxwell fluid at the neighbourhood of the re-entrant corner is shown in Figure (II.5.6.4). An elastic effect is a slight reduction of the vorticity near the wall downstream of the re-entrant corner (Perera and Walters (1977) and Cochrane et al. (1982)).

Some stress distributions in a Maxwell fluid flowing through a bend are given in

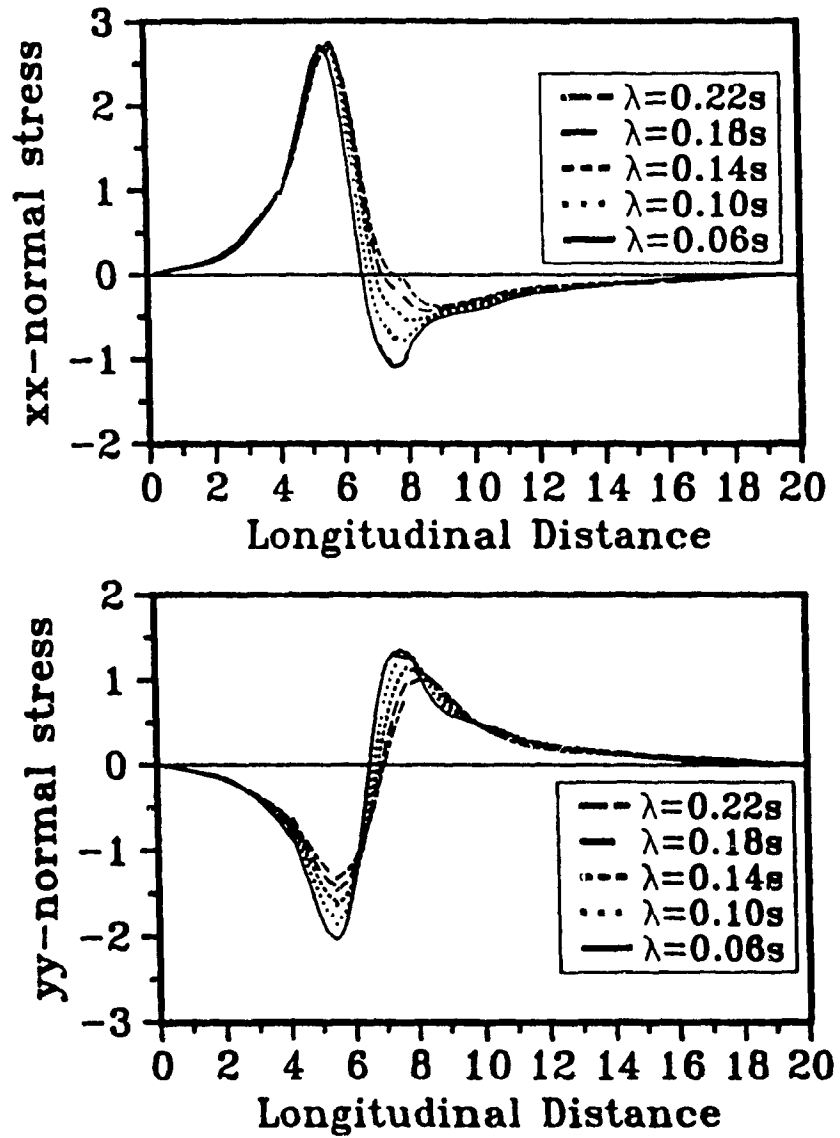


Figure (II.5.5.4):

Dimensionless xx - and yy -normal stresses along the axis of symmetry in the contraction/expansion geometry for a range of the fluid elasticity at $Re=12$.

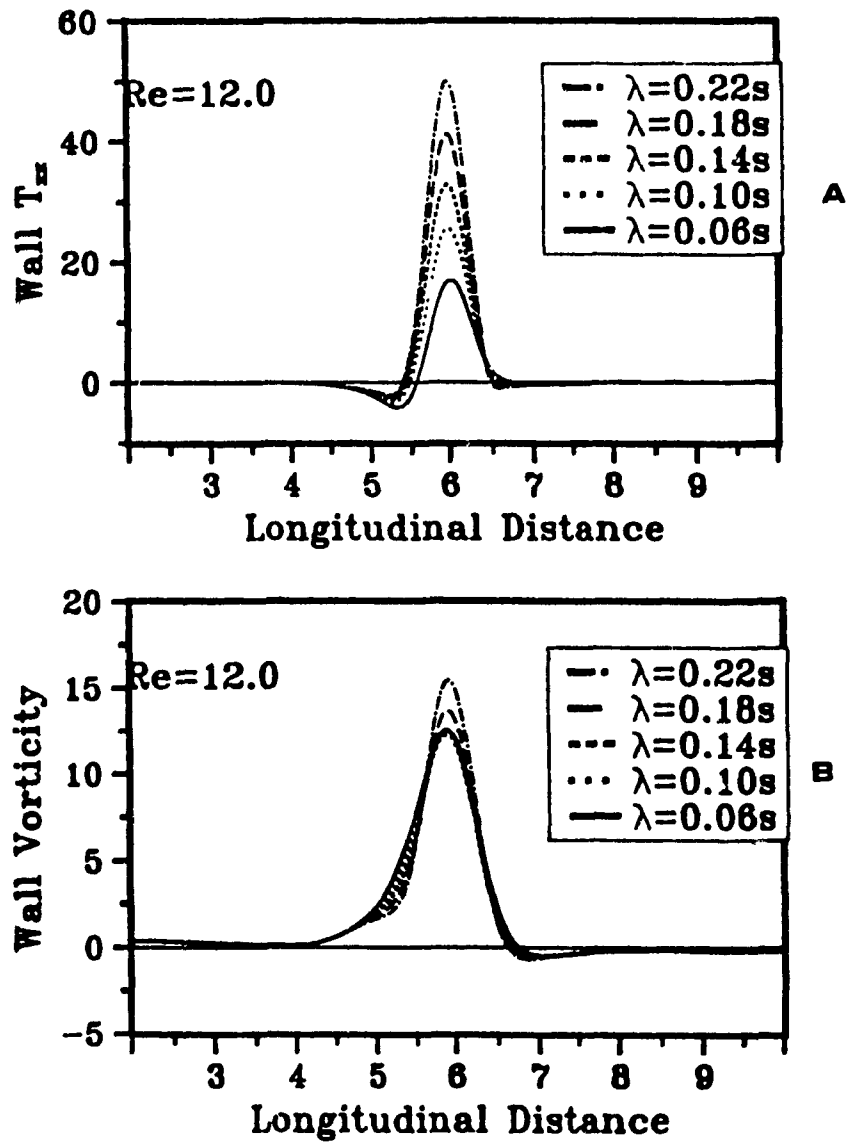


Figure (II.5.5.5):

Wall values of the dimensionless xx -normal stress (A) and of the vorticity (B) at a range of the fluid relaxation time. $Re=12$.

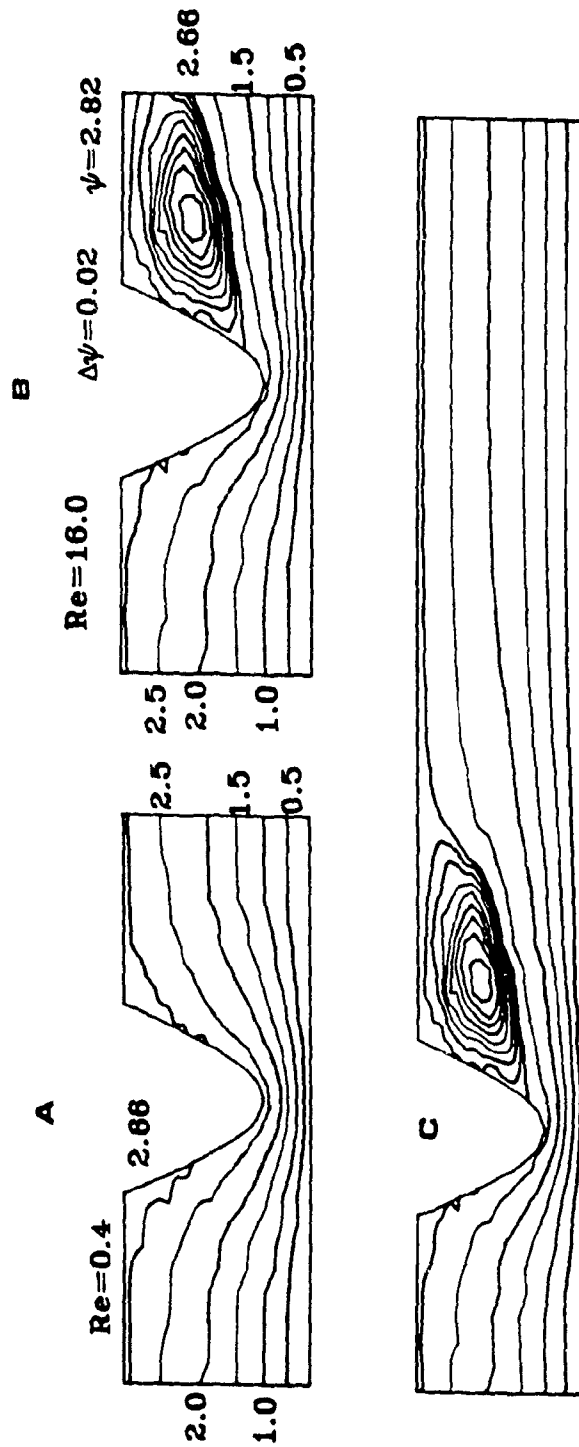


Figure (II.5.5.6):

Effect of inertia on flow patterns in a contracting/expanding flow of a Newtonian fluid. Part (C) shows the actual length of the computational domain used in the simulations.

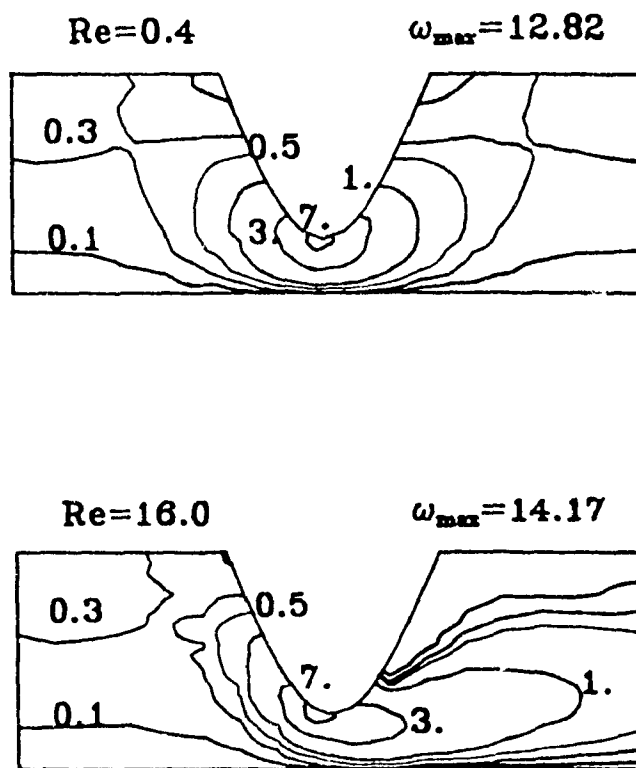


Figure (II.5.5.7): Effect of inertia on vorticity distributions in a contracting/expanding flow of a Newtonian fluid.

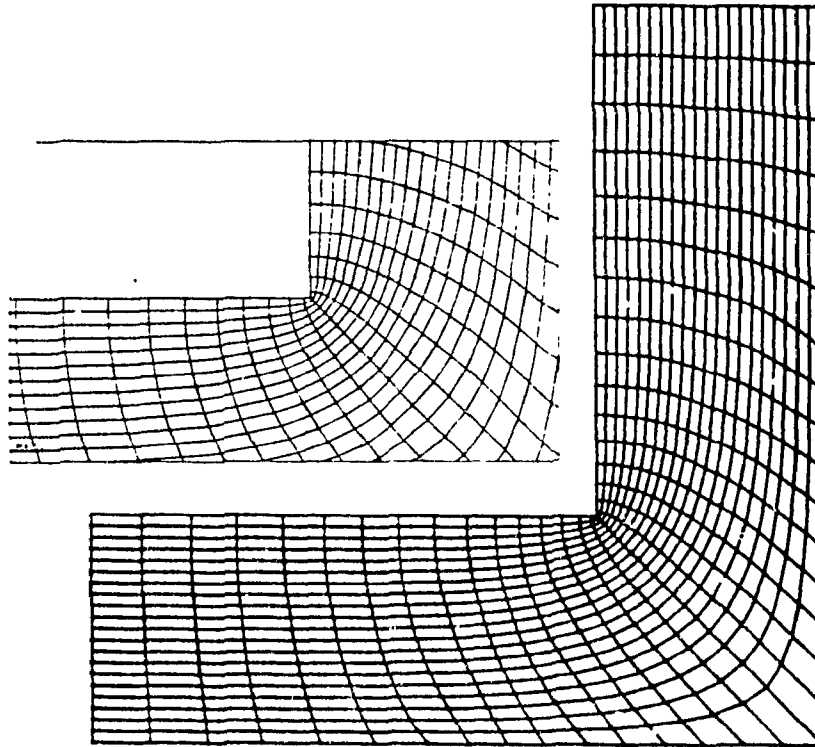


Figure (II.5.6.1):

The geometry and the curvilinear grid used to study the flow in a bend. The grid lines are normal to the upper boundary of the bend.

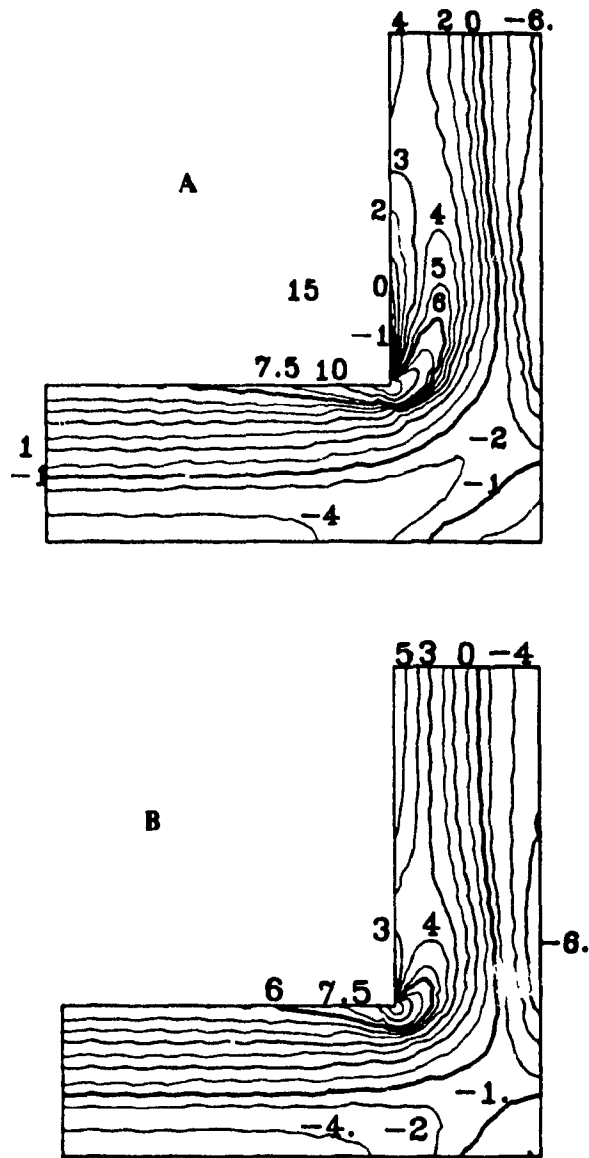


Figure (II.5.6.2):

Vorticity distributions in a bend at $Re=48$ (A) and $Re=16$; (B) Newtonian flow.

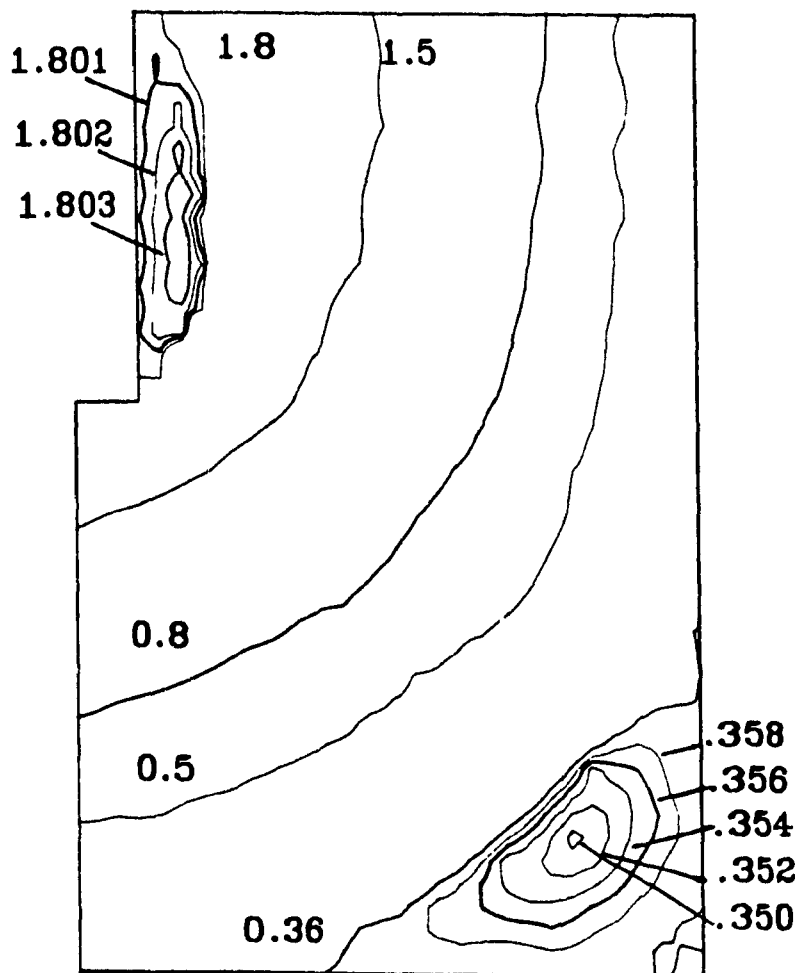


Figure (II.5.6.3):

Corner detail of the secondary flows in a bend at $Re=48$; Newtonian fluid.

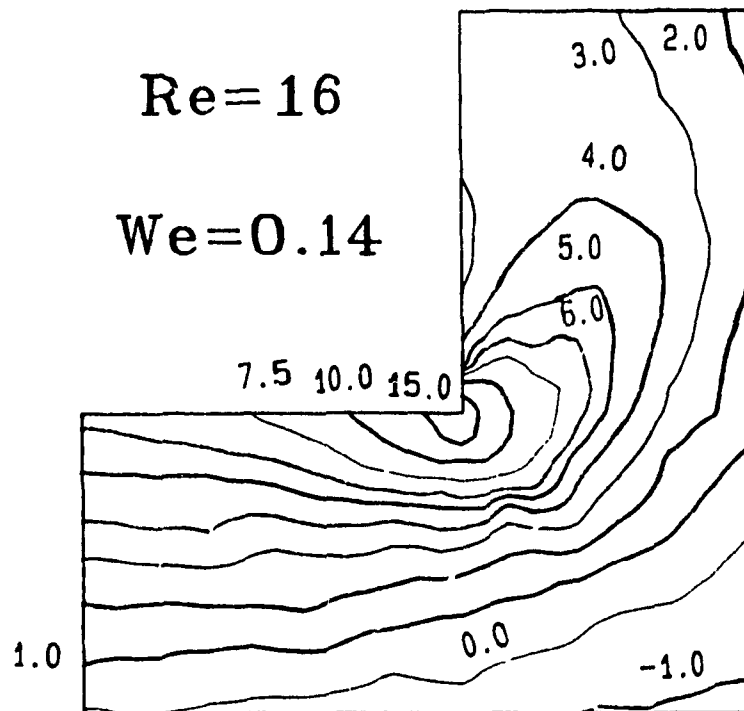


Figure (II.5.6.4):

Corner detail of vorticity contours in a bend. Maxwell fluid; $Re=16$ and $We=0.14$.

Figure (II.5.6.5). An elastic effect in this case is the distortion of the symmetry of the shear stress patterns around the re-entrant corner (see also Perera and Walters (1977)).

(II.6) CONCLUSIONS

An analysis of viscoelastic flows in complex geometries using the method of boundary-fitted curvilinear coordinates and finite differences has been presented. Use of BFCCs allows great flexibility in the accurate discretization of complex flow fields, therefore making the treatment of realistic flow channels straightforward. Simulation studies in various 4:1 planar contractions using the upper-convected Maxwell model revealed the effect of the fluid inertia and fluid elasticity, as well as the effect of the form of the entrance section on the flow and stress patterns. The lip vortex, usually present in the numerical simulation of viscoelastic fluids in sudden contractions containing a point of boundary discontinuity such as a re-entrant corner, seems to disappear when the corner is rounded. This corroborates the assumption that this vortex might be a numerical artifact related to the use of ad-hoc methods for the evaluation of the vorticity at a singular corner. Increased fluid inertia was found to reduce the size of the corner vortex, but had a smaller effect on the lip vortex. The computations were found to be reasonably convergent with grid refinement. The growth of the corner vortex with elasticity in contractions with smooth edges was found to be largely independent of grid size, being at the same time a strong function of geometry. This indicates that the corner vortex is not a numerical artifact but a characteristic property of the set of equations that model the flow of the Maxwell fluid. Finally, the stress patterns at the entrance section depend heavily on both the elasticity of the fluid and the specific form of the re-entrant corner.

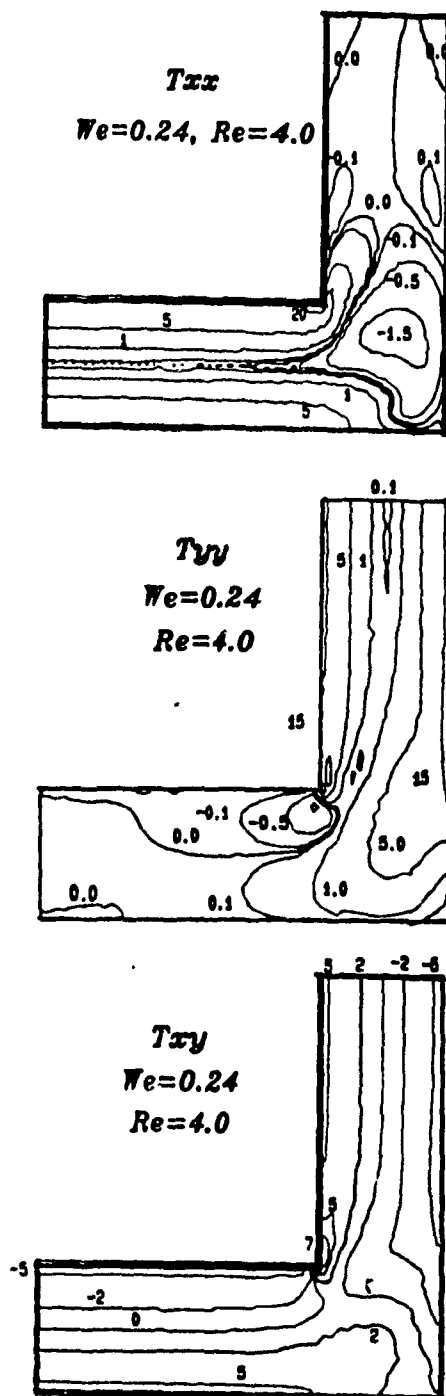


Figure (II.5.6.5):

Dimensionless stress contours in a Maxwell fluid ($We=0.24$) flowing through a bend at $Re=4.0$.

(III) INJECTION MOLDING

(III.1) PRELIMINARIES

Injection molding is an intermittent cyclic process used to produce uniform articles in a mold. It is a widely used plastics processing operation, particularly for articles involving a high degree of geometrical complexity. Injection molding products range from large automobile, aerospace and computer parts to tiny gears or paper clips. Inherent advantages of the process are its high degree of reproducibility and its utility in producing a wide range of products, usually of very complex shape, economically. Most polymers can be injection molded, including fiber reinforced engineering plastics, thermosetting polymers and liquid crystal polymers.

The process consists of three steps. During the filling stage, the molten polymer is forced into a cavity whose walls are maintained at a low temperature. When the cavity is full, more material is packed into the mold to account for the shrinkage usually occurring during solidification. After packing is completed, the material cools and solidifies. The cooling process continues until the article is solid enough to be ejected without damage. The cooling stage takes about 70-80% of the cycle time, which makes it very important economically. On the other side, the thermomechanical history experienced by the material during filling and packing is a major factor that determines the ultimate properties of the molded article.

The introduction of injection molding as a method for the processing of polymeric materials goes back to 1872, when J.W. Hyatt obtained a patent on a piston driven injection molding machine. Since then, improvements in the process, discovery of new materials with desirable properties, advances in automation and an ever expanding market for uniform finished articles have made injection molding a mature technology with product applications scanning practically every sector of modern life.

Unfortunately, our understanding of the injection molding process is rather sketchy. A large part of the problem is the limited knowledge of the rheological behaviour of molten polymers during the various stages of the injection molding process. Existing constitutive equations cannot always yield reliable estimates of the stress fields developing in a flowing polymer melt. Apart from that, the process itself combines characteristics that make its analysis extremely difficult. It includes non-isothermal transient flow with density variations, complex flow channels, free surfaces, structuring and solidification coupled with flow and heat transfer. No analytical solutions for such flow problems are known - or expected to be developed in the foreseeable future - and thus numerical solution of the governing equations is the only way to deal with the problem. This task becomes even more complicated by the extremely high flow and cooling rates occurring during the injection molding process. Since a major advantage of polymer injection molding is the ability to reproduce very complex shapes, computational treatment of complex geometries is necessary for practical applications of any modelling work.

In the absence of reliable design tools, trial and error methods have become the dominant practice in the design of molds. To start with, this approach seems inadequate in a time when everything moves towards higher efficiency and automation. Furthermore, there are several practical problems associated with a trial-and-error empirical mold design. Firstly, it can lead to significant capital losses and long delays for the delivery of a certain product. Specialized knowledge that has accumulated by mold designers over many years of service tends to be lost after the specialist retires. Theoretical understanding of the process is seen as a means to keep corporate experience continuous within the company and also speed up the process of transferring that experience to new designers, beside being the only rational way to ensure product quality and process efficiency. It should be realized that material cost is the major contributor to the final cost of an injection molded product (typically 50% of the total cost). This means that improvements in the processing conditions are not expected to contribute dramatically to the economics of a product - the

process is material and not labour or energy intensive. The element of time (from product conception to production), the need to maintain the continuity of the corporate experience, and the increasing demand for quality control are the factors that make the theoretical analysis and understanding of injection molding so desirable.

Research done in the field of non-Newtonian fluid mechanics and rheology has led to significant advances regarding our understanding of the behaviour of polymeric materials during processing. As a result, a number of commercially available software packages for the injection molding process has emerged. However, most of these packages provide only rough approximations of the actual flow behaviour, as might be expected if one considers the complexity of the processes involved. Much remains to be done before simulation takes its place as a reliable desktop tool of the plastics engineer.

(III.2) MATHEMATICAL ANALYSIS OF THE FILLING STAGE

(III.2.1) Fluid Dynamics

Analysis of the filling stage of injection molding is of high practical importance since the flow and thermal conditions during filling will determine several properties of the product such as the formation of weld lines, the distribution of crystallinity and orientation within the article, the pressure requirements etc. The moldability of a certain plastic, the required filling time, occurrence of short shots, jetting and sinkspots, the optimum location of the gate(s) and other process characteristics can also be assessed by a careful filling analysis (White and Dietz, (1979)). It is thus justifiable that a very large portion of the theoretical work concerning injection molding has been directed towards the filling stage.

In this work, the filling stage is treated as a fluid dynamics problem. Determination

of the state variables is sought by numerical solution of the corresponding conservation laws, coupled with a viscoelastic constitutive model. The equations modelling incompressible flow in 3 dimensions and cartesian coordinates are as follows.

Continuity:

$$u_x + v_y + w_z = 0 \quad (\text{III.1})$$

x-momentum:

$$\rho(u_t + uu_x + vv_x + ww_x) = -P_x + F^x + (T^x)_x + (T^y)_y + (T^z)_z \quad (\text{III.2})$$

y-momentum

$$\rho(v_t + uv_x + vv_y + ww_y) = -P_y + F^y + (T^x)_x + (T^y)_y + (T^z)_z \quad (\text{III.3})$$

z-momentum

$$\rho(w_t + uw_x + vw_y + ww_z) = -P_z + F^z + (T^x)_x + (T^y)_y + (T^z)_z \quad (\text{III.4})$$

In equations (III.1) to (III.4) u, v and w are the velocities in the x, y, z directions, respectively. F^x, F^y, F^z are the body forces in the three dimensions. The thickness of the mold is defined by the z coordinate, whereas x and y define the plane of the flow. The stress tensor (T) is the total stress tensor which includes viscous and elastic contributions. These stresses need to be determined by means of a suitable constitutive model as will be explained later. In the following analysis, the effect of the body forces will be neglected. Furthermore, the fluid velocity in the thickness direction will be ignored, since its value is very small compared to the velocities in the $(x-y)$ plane, and hardly affects the total kinematics of filling. This is equivalent to ignoring the fountain flow effect in the thickness direction, and is an assumption introduced by the need to keep the flow computations two-dimensional. The fountain flow, even though it is localized in a small area behind the advancing flow front and does not affect, macroscopically, the filling of the mold, has been found to be one of

the most important fluid dynamics features of the filling stage, influencing the orientation and crystallinity distributions of the finished articles. This problem has been treated extensively by Lafleur (1983) and Kamal et.al (1988). Complete analysis of the filling stage that takes into account simultaneously the spreading flow into the cavity and the fountain flow in the thickness direction can only be performed on a three-dimensional basis. In the case of complex molds with thick sections, this has to await advances in the generation of computational grids in three dimensional domains, not to mention the computer time requirements. The present work is confined to solutions of partial differential equations in two dimensional regions of arbitrary geometry, and most of the simplifications introduced in this section are results of this limitation. Only the energy equation has been solved in three dimensions, still assuming two-dimensional kinematics.

After the above assumptions, the flow equations simplify to the following set of partial differential equations:

$$\rho(u_t + uu_x + vu_y) = -P_x + (T^x)_x + (T^y)_y + (T^z)_z \quad (\text{III.5})$$

$$\rho(v_t + uv_x + vv_y) = -P_y + (T^y)_x + (T^y)_y + (T^z)_z \quad (\text{III.6})$$

$$u_x + v_y = 0 \quad (\text{III.7})$$

In these equations, the shear stresses in the z-direction (thickness) have been retained since they greatly contribute to the dynamics of the process.

The pressure can be eliminated from equations (III.5) and (III.6) by cross-differentiation and subtraction. Introducing the vorticity (ω) and stream function (ψ) as:

$$\omega = v_x - u_y \quad (\text{III.8})$$

$$u = \partial\psi/\partial y \quad , \quad v = -\partial\psi/\partial x \quad (III.9)$$

one obtains the following equivalent set of equations:

$$\nabla^2\psi = -\omega \quad (III.10)$$

$$\rho(\omega_t + \psi_x \omega_y - \psi_y \omega_x) = -F(T) \quad (III.11)$$

where $F(T)$ is given by

$$F(T) = (T^y - T^x)_{yy} + (T^y)_{xx} - (T^y)_{yy} + (T^x)_{xx} - (T^x)_{yy} \quad (III.12)$$

The left hand side of equation (III.11) contains only convected vorticity terms. It is generally accepted that partial differential equations with strong convective character are more difficult to solve than equations with a strong diffusive character. This means that the stability and accuracy of the discrete representation is more readily assured in diffusion, rather than convection-dominated equations. Even though equation (III.11) has been successfully solved as it stands (Gatski and Ramley, (1978)), in this work an approach first used by Perera and Walters (1977) will be used. The objective is to introduce a diffusive term in the vorticity equation. This can be accomplished by decomposing the stress tensor (T) into an elastic (S) and a purely viscous (D) part as follows:

$$T = S + \mu D \quad (III.13)$$

Following this decomposition, the vorticity equation can be recast in the following quasilinear elliptic form:

$$\mu(x,y) \cdot \nabla^2\omega + \rho \cdot (\omega_t + \psi_x \omega_y - \psi_y \omega_x) = F(S) \quad (III.14)$$

where $F(S)$ is still given by equation (III.12), but instead of the total stress (T) one uses the elastic contributions (S). In deriving Equation (III.14), the viscosity has been treated as a constant in the differentiations involved in (III.12); however, (μ) in (III.14) is in reality a function of temperature and shear rate, and therefore location dependent. Equations (III.10) and (III.14) constitute the final set of working equations for the modelling of the flow in the cavity. The boundary conditions for stream function and vorticity, as well as for the rest of the state variables in injection molding are summarized in Appendix A7.

(III.2.2) The Energy Equation

One of the most important characteristics of the filling stage in injection molding is the interaction between flow, heat generation due to flow, heat transfer from the hot melt to the cold walls of the mold and heat transferred to the cavity by the entering hot melt. This interaction determines not only the dynamics of the flow but also some important product properties, such as the distribution of crystallinity and orientation as well as the formation of weld lines.

Neglecting the heat of crystallization and assuming temperature independent thermal conductivity and incompressible flow, the energy equation in three dimensions takes the following form:

$$\rho \cdot C_p \cdot (T_t + u \cdot T_x + v \cdot T_y + w \cdot T_z) = \phi + \kappa \cdot \nabla^2 T \quad (III.15)$$

In the above equation, (ϕ) is a heat generation term, given by the following expression:

$$\phi = T : \nabla u = T^{xx} \cdot u_x + T^{yy} \cdot v_y + T^{yz} \cdot (u_y + v_z) + T^{zx} \cdot u_x + T^{xy} \cdot v_x \quad (III.16)$$

For power law fluids, the dissipation function is given by

$$\phi = \mu(T, \gamma) \cdot ((u_x)^2 + (v_x)^2) \quad (\text{III.17})$$

This expression, used by Kuo and Kamal (1976) and Shen (1984) makes use of the assumption that the velocity gradients in the (x-y) plane are negligible compared to the gradients in the thickness direction. In this work, the more general form of equation (III.16) was used. This takes into account the velocity gradients in the (x-y) plane as well as the gradients in the thickness direction and is also valid for a visco-elastic fluid. Velocity gradients in the plane of the flow (x-y) might be important in a mold with contracting and/or expanding sections.

In the light of the very high heat capacity of polymeric melts and their relatively low thermal conductivity, equation (III.15) is convection rather than diffusion dominated. In other words, this is a high Peclet number problem. For this reason, the quasi-steady state approach widely used for the description of the flow during filling (justifiable, considering that polymeric flows are practically inertialess flows) is not applicable for the solution of the energy equation. In this case, the problem is indeed transient, and if the solution is performed on a moving grid (as is the case in any approach that uses a solution dependent mesh), this requires transformation of the temporal, as well as of the spatial derivatives. This transformation is given in Appendix A.3.

After the assumption of zero velocity in the thickness direction, the energy equation reduces to the form:

$$\rho \cdot C_p \cdot (T_t + u \cdot T_x + v \cdot T_y) = \phi + \kappa \cdot \nabla^2 T \quad (\text{III.18})$$

Equation (III.18) is still a three-dimensional equation. To solve it in a two-dimensional context, some approximation has to be made. Specifically, equation (III.18) can be rendered two-dimensional by ignoring the thermal gradient in the z-direction, assuming a uniform bulk melt temperature in the thickness direction and

substituting the term (κT_x) with a heat loss term of the form $\kappa(T_x)_{z=b}$. This is equivalent to assuming the presence of a thin thermal layer adjacent to the mold walls and the existence of a bulk melt with a uniform temperature. This is a justifiable assumption, since there indeed exists a thin layer of solidified material on the mold wall. Its small thermal conductivity and the small duration of the filling stage, along with the associated high dissipation and thermal convection also contribute to the validity of such an assumption. Therefore, the final working form of the energy equation, utilizing gap-averaged temperatures, is (Shen (1984)):

$$\rho \cdot C_p \cdot (T_t + u \cdot T_x + v \cdot T_y) = \dot{\Phi} + \kappa \cdot (T_x)_{z=b} / b + \kappa \cdot \nabla^2 T \quad (\text{III.19})$$

In the above equation (∇^2) is the Laplace operator in the x-y plane and all quantities are average quantities in the thickness direction.

(III.2.3) The Constitutive Model

To model the relationship between flow kinematics, fluid properties and stresses, the White-Metzner modification of the Maxwell model has been used. This is a quasi-linear constitutive model and allows the viscosity as well as the relaxation time to be functions of the second invariant of the rate of deformation tensor and temperature (Middleman, (1979)). In compact tensorial form, the White-Metzner model is:

$$\mathbf{T} + \lambda(\mathbf{T}_t + (\mathbf{u}\nabla)\mathbf{T} - \mathbf{T}\nabla\mathbf{u} - \nabla\mathbf{u}^T\mathbf{T}) = \mu\mathbf{D} \quad (\text{III.20})$$

The components of the velocity gradient tensor $(\nabla\mathbf{u})$, say a_{ij} , are:

$$a_{ij} = \partial u_i / \partial x_j \quad (\text{III.21})$$

whereas those of the rate of deformation tensor (\mathbf{D}) are:

$$d_y = \partial u / \partial x_i + \partial u / \partial x_j \quad (\text{III.22})$$

The relaxation time and the viscosity are usually connected through a modulus (G) (Middleman (1979), Deiber and Schowalter (1981), Lafleur (1983)), so that

$$\lambda = \mu / G \quad (\text{III.22.a})$$

Performing the tensor operations involved in (III.20), the following partial differential equations are obtained for the components of (T).

$$\begin{aligned} \lambda((T^x)_i + u(T^x)_i + v(T^x)_j) + T^x = \mu(u_x + v_x) + \lambda((T^x)u_x \\ + (T^y)u_y + (T^z)v_x + (T^z)u_x) \end{aligned} \quad (\text{III.23})$$

$$\begin{aligned} \lambda((T^x)_i + u(T^x)_i + v(T^x)_j) + T^x(1-2\lambda u_x) = 2\mu(u_x) + \\ + 2\lambda((T^y)u_y + (T^z)u_x) \end{aligned} \quad (\text{III.24})$$

$$\begin{aligned} \lambda((T^y)_i + u(T^y)_i + v(T^y)_j) + T^y(1-2\lambda v_y) = 2\mu(v_y) + \\ + 2\lambda((T^y)v_x + (T^z)v_x) \end{aligned} \quad (\text{III.25})$$

$$\lambda((T^z)_i + u(T^z)_i + v(T^z)_j) + T^z(1-\lambda u_x) = \mu(u_x) + \lambda(T^z)u_y \quad (\text{III.26})$$

$$\lambda((T^z)_i + u(T^z)_i + v(T^z)_j) + T^z(1-\lambda v_y) = \mu(v_x) + \lambda(T^z)v_x \quad (\text{III.27})$$

In the derivation of the above equations, use was made of the assumption that $w=0$ and $T_{zz} = 0$. Again, x- and y-axes correspond to the plane of the flow and (z) is the thickness direction. As a result of this assumption the equations for the components of the stress tensor in the thickness direction are independent of the stresses in the (x-y) plane and can therefore be solved separately. As with the energy equation, the stress equations are completely time dependent and have to be solved on a moving grid. Even though this is a complication, the major problem in dealing with the stress

equations arises from the fact that we cannot render them completely two-dimensional, since we cannot ignore the shear stresses and velocity gradients in the thickness direction. For this reason, gap-averaged values for the planar velocities (u) and (v) are used. These average velocities are defined as follows:

$$\langle u \rangle = 2b^{-1} \cdot \int_0^{b/2} u(x,y,z) dz \quad (\text{III.28})$$

$$\langle v \rangle = 2b^{-1} \cdot \int_0^{b/2} v(x,y,z) dz \quad (\text{III.29})$$

It is furthermore assumed that, in the gapwise direction, the velocities (u) and (v) are fully developed:

$$u(x,y,z) = u_0(x,y) \cdot (1.0 - (2z/b)^{s+1}) \quad (\text{III.30})$$

$$v(x,y,z) = v_0(x,y) \cdot (1.0 - (2z/b)^{s+1}) \quad (\text{III.31})$$

In the above equations, (b) is the thickness of the cavity and $s=1/n$, n being the power law index of the fluid. The fully developed profile assumption is a reasonable assumption for the part of the flow field a few times the cavity thickness behind the melt front. Again, the fountain flow effect in the thickness direction is ignored in this analysis. The relation between u_0 , v_0 and the average velocities $\langle u \rangle$, $\langle v \rangle$ is:

$$\langle u \rangle = u_0(s+1)/(s+2) \quad (\text{III.32})$$

$$\langle v \rangle = v_0(s+1)/(s+2) \quad (\text{III.33})$$

Based on the assumed fully-developed profiles, the gradients of u and v in the thickness direction can be evaluated as:

$$u_z = -2^{s+1} u_0(s+1) z^s / b^{s+1} \quad (\text{III.34})$$

$$v_z = -2^{s+1} v_x (s+1) z^s / b^{s+1} \quad (\text{III.35})$$

Again, gap-averaged values for these gradients have to be used, in order to render the problem two-dimensional.

$$\langle u_z \rangle = 2 \langle u \rangle (s+2) / (s+1) b \quad (\text{III.36})$$

$$\langle v_z \rangle = 2 \langle v \rangle (s+2) / (s+1) b \quad (\text{III.37})$$

By means of the approximations introduced in equations (III.28) to (III.37), the stress equations can be solved in a two-dimensional sense, still taking into account the presence of shearing in the thickness direction. The equations to be solved are still equations (III.23) to (III.27), where $\langle u \rangle$ and $\langle v \rangle$ are used instead of u and v , and $\langle u_z \rangle$, $\langle v_z \rangle$ instead of u_z , v_z . Naturally, mean velocities $\langle u \rangle$ and $\langle v \rangle$ are used in the energy and momentum equations, where the notation $\langle \rangle$ was dropped for the ease of presentation.

(III.2.4) Viscosity Modelling

The shear viscosity is undoubtedly the single most important property in the modelling of the flow dynamics in injection molding. In a non-Newtonian fluid the viscosity is function of both the temperature and the shear rate. During the filling stage, the shear rates vary from very high near the gate to relatively low at regions of slow flow. Therefore, the power-law expression is not adequate to describe the shear viscosity at all locations within the cavity. One way to account for that is simply to consider constant viscosity at regions of low shear and a power law at regions of higher shear rates. This was done in this Thesis. At high shear rates (above 1.0 s^{-1}) the following functional form for the viscosity has been used:

$$\mu(T, \gamma) = K(T) (\dot{\gamma}/2)^{(1-n)/2} \quad (\text{III.39})$$

where (II) is the second invariant of the rate of deformation tensor and $K(T)$ is a temperature dependent consistence index. In the case that 5 components of this tensor are retained, as is the case in this work, (II) takes the following form:

$$II = 4(u_x)^2 + 4(v_y)^2 + (u_x + v_x)^2 + (u_x)^2 + (v_x)^2 \quad (III.40)$$

For the temperature dependence of viscosity, an Arrhenius-type expression was used:

$$K(T) = A \cdot \exp(\Delta E/RT) \quad (III.41)$$

For polyethylene Sclair 2908, which was used in the experimental part of this study, values for the parameters of this model have been determined experimentally. The results are reported in following section.

(III.2.5) Pressure Calculation

The major advantage of using the vorticity/stream function instead of the velocity/pressure formulation of the Navier-Stokes equations is that the pressure is removed as an independent variable. Furthermore, use of the stream function guarantees that the obtained velocity field will be divergence free, subject of course to numerical differentiation errors. In the following, it is described how the pressure can be recovered after the (ψ, ω) and the stress fields have been computed.

It has been shown that evaluation of pressure by direct integration of equations (III.5) and (III.6) in the x and y -directions, respectively, gives results that are dependent on the integration path, and therefore unacceptable (Roache (1976), Crochet et. al. (1984)). However, an elliptic Poisson equation for the pressure can be obtained by differentiation of equations (III.5) and (III.6) with respect to x and y , respectively, and addition. The resulting partial differential equation for pressure is:

$$\nabla^2 P = 2\rho \cdot (u_x \cdot v_y - v_x \cdot u_y) + L(T) \quad (\text{III.42})$$

where $L(T)$ is given by the following equation:

$$L(T) = (T^{\alpha})_{xx} + (T^{\beta})_{yy} + 2 \cdot (T^{\alpha\beta})_{xy} + (T^{\alpha})_{yy} + (T^{\beta})_{xx} \quad (\text{III.43})$$

The form of this equation is the same as that of the vorticity equation at steady state, the only difference being in the boundary conditions, as will be explained later. Crochet et. al.(1984), point out that the existence of pure Neumann boundary conditions for equation (III.42) makes it a much less well-conditioned problem than the corresponding Dirichlet elliptic problem. This reflects in iterative solutions requiring excessively long CPU times to converge. Shen (1984) points out that the solution of the pressure equation was the slowest part of their computational algorithm for an approximate analysis of filling and stresses the need for a more efficient solver of Neumann elliptic systems. Manero (1981) has shown that the problem of slow convergence does not appear if the method of preconditioned conjugate gradients is used to solve the discretized systems. In this work, the pressure equation was solved by means of a successive relaxation algorithm. This computation was by far the most CPU - intensive part of the computational algorithm, requiring more than half of the total CPU time.

Beside its very slow convergence, equation (III.42) is further complicated by the presence of derivatives of T^{α} and T^{β} in the thickness direction. The same derivatives appear in equation (III.12). Again, as with the derivatives of the velocities in the z -direction, we need to resort to simplifications in order to keep the problem two-dimensional.

Assuming that the power law behaviour is dominant over the elastic one, at least as far as T^{α} and T^{β} are concerned, and using the results of equations (III.32) to (III.41), we can obtain gap-averaged values for the gradients of T^{α} and T^{β} in the thickness

direction.

$$\langle (T^x)_x \rangle = -4\mu \cdot (s+2) \cdot \langle u \rangle / b^2 \quad (\text{III.44})$$

$$\langle (T^x)_y \rangle = -4\mu \cdot (s+2) \cdot \langle v \rangle / b^2 \quad (\text{III.45})$$

Therefore, the mixed derivatives of T^x and T^y at the RHS of equation (III.43) can be evaluated as:

$$(T^x)_{xx} = -4(s+2)b^{-2} \cdot (\partial(\mu \cdot \langle u \rangle) / \partial x) \quad (\text{III.46})$$

$$(T^x)_{yz} = -4(s+2)b^{-2} \cdot (\partial(\mu \cdot \langle v \rangle) / \partial y) \quad (\text{III.47})$$

This approximation, by which the effect of the elastic part of T^x and T^y in the development of the pressure profile has been ignored, is confined only to the pressure evaluation. The xz - and yz -stresses reported elsewhere in this thesis have been calculated by means of the viscoelastic defining equations (III.26) and (III.27).

(III.2.6) Previous Modelling Work on Filling

In past years, the thin cavity approximation has been used extensively to simplify the analysis of the flow during filling of a mold. The resulting Hele-Shaw flow (isothermal or non-isothermal) has been the subject of many studies. The assumptions underlying the Hele-Shaw flow can be summarized as follows:

- (a) Inertial forces are negligible compared to the viscous forces (the Reynolds number is of the order of 0). This is reasonable in the light of the high viscosity of polymer melts and has the attractive property of removing time as an independent variable, thus making the numerical treatment of the momentum equations easier.

- (b) Surface tension and normal stress effects on the profile of the free surface are negligible.
- (c) Viscosity, temperature, velocity and extra stresses vary strongly in the thickness direction but only weakly in the flow directions.
- (d) The variation of pressure and transverse velocity in the thickness direction is negligible.

Under these assumptions, the following set of equations for the pressure in the cavity results (Kuo and Kamal, (1976)):

$$P_x = \partial(\mu \cdot u_x) / \partial z \quad (\text{III.50})$$

$$P_y = \partial(\mu \cdot v_x) / \partial z \quad (\text{III.51})$$

If it is assumed that the only mechanism of heat transfer is conduction in the thickness direction, the energy equation simplifies to the following form (Kuo and Kamal (1976)):

$$\rho \cdot C_p \cdot T_t = \Phi + \kappa \cdot T_{zz} \quad (\text{III.52})$$

If heat transfer by convection in the (x-y) plane is also included, the energy equation becomes (Hieber and Shen, (1980)):

$$\rho \cdot C_p \cdot (T_t + u \cdot T_x + v \cdot T_y) = \Phi + \kappa \cdot T_{zz} \quad (\text{III.53})$$

Of special interest in the context of simplified flow fields is the work of Kuo and Kamal (1976) who obtained analytical solutions for the advancement of the flow front and the development of pressure and temperature profiles during the filling of a

rectangular cavity with a small gate. In a similar problem of a Hele-Shaw non-isothermal filling stage flow, Ryan and Chung (1980) used the method of conformal mapping to obtain solutions of the model equations. They reported results that compare well with the earlier work of Kuo and Kamal (1976).

Nevertheless, analytical solutions can, at this time, only be obtained for certain simple flows and simple geometries. Therefore, most of the simulation effort has been directed towards numerical solution of the governing equations; an approach that makes use of the computational power of the digital computer and allows great flexibility in the degree of rigor of the model, the shape of the flow field and the type of boundary conditions used. Numerical simulation of the filling stage, with various degrees of physical detail has been done, amongst others, by Kamal and Kenig (1972), Shen (1984), Hieber and Shen (1980) (inelastic Hele-Shaw flow), Kamal and Lafleur (1982),(1986),(1986), Wang et al. (1987, 1988). Recently, Kamal et al. (1988) presented a two-dimensional finite difference solution of a model for flow in the thickness direction during injection molding of a cavity with a uniform rectangular cross-section, including non-isothermal crystallization, fountain flow, elastic and inertia effects. The Marker-and-Cell method was used to track the advancement of the melt front. More complete reviews on the subject can be found in Kamal and Bata (1983, with 92 references) and White (1983, with 132 references).

In general, it has been observed that isothermal filling analysis can only give acceptable results regarding the pressure distributions and filling times when the cavity is thick, without sections where extensive wall solidification and viscous heating during filling might occur. In any other case, the interaction between flow and temperature fields will significantly affect the results of the analysis. The elasticity of the melt does not seem to affect substantially the model predictions either. Nevertheless, prediction of the microstructure of the product and consequently of its properties requires the use of a rigorous model; this seems to be a new challenge in the simulation of the filling stage of injection molding (Kamal, (1987)). A number

of commercially available software packages has appeared in the past years regarding the simulation of the filling stage (CADMOLD (IKV, Aachen, West Germany), MOLDFLOW (C. Austin, Australia), C-FLOW (Cornell University, USA)). These packages are mostly used for the prediction of filling times, pressure and stress distribution, short shots and weld lines, and for the balancing of the delivery channels.

(III.3) EXPERIMENTAL

(III.3.1) Objectives

The objective of this section is to present experimental results regarding the rheological characterization of the material used in the experimental part of this Thesis, as well as data obtained during the injection molding of polyethylene (Sclair 2908) in a mold of complex shape. Experimental results in the same complex mold have been used for validation of the computer simulation of the process. It was decided that the cavity used in the injection molding experiments should have the following characteristics:

- a: Variable thickness
- b: Converging and diverging sections
- c: At least one insert
- d: Walls composed of general curved segments

With these requirements in mind, the cavity of Figure (III.3.1.1) was designed, manufactured and used in a series of injection molding experiments. The upper part of that figure gives the dimensions of the cavity in the thickness direction in cm. The length of the cavity is 10.8 cm and its maximum width is 6.35 cm. The lower part (B) also shows the location of the transducers in the cavity. This mold will be referred to as "mold CR1" in the following. The rectangular cavity of constant thickness used by Lafleur (1983) will be referred to as "mold R1". Appendix A6 summarises the geometrical specifications of mold CR1.

(III.3.2) Material

The material used in the injection molding experiments is an injection molding grade high density polyethylene (Sclair 2908) supplied by DuPont Canada. A rheological

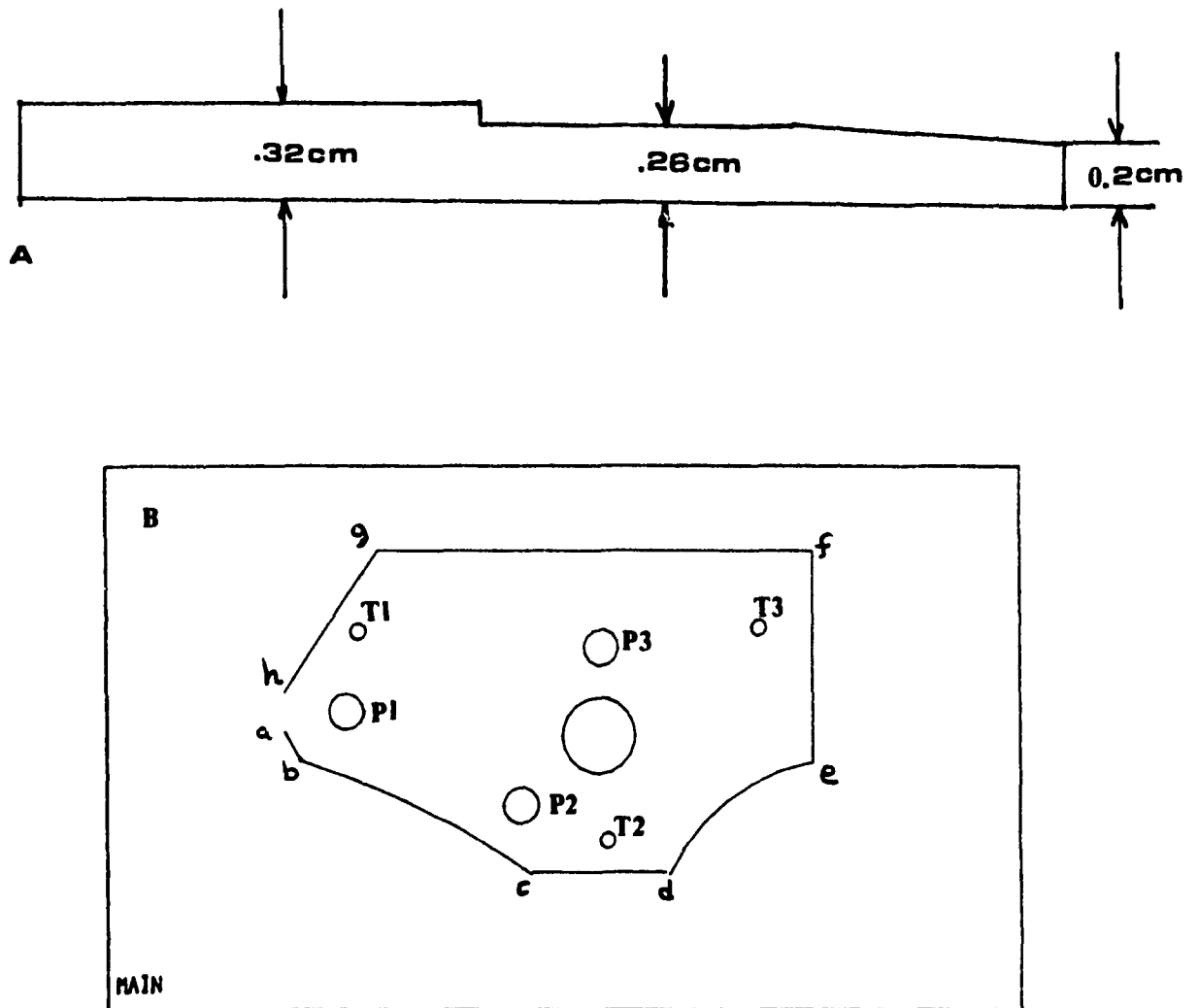


Figure (III.3.1.1): Complex shaped cavity used in the injection molding experiments (A) and the location of temperature (T1, T2, T3) and pressure (P1, P2, P3) transducers (B).

characterization of this resin was performed. In the computations performed in this Thesis, the heat capacity (C_p) and thermal conductivity (κ) are considered to be functions of temperature (Lafleur, (1983)).

(III.3.2.1) Rheological Characterization

The shear viscosity at a range of shear rates between 10^2 and 10^3 reciprocal seconds was measured in a Rheometrics Mechanical Spectrometer (RMS) operated at the cone-and-plate mode and an Instron Capillary Rheometer type MCR. In the latter, a capillary with $L/D=40$ and diameter 0.052 " ($1''=2.54$ cm) was used. Viscous heating and pressure effects can be minimized in such a capillary (Lafleur, (1983)). The true shear rate was calculated using the Rabinowitz correction.

The shear viscosity at high shear rates (typically above 1.0 s⁻¹) was modelled with a power law expression:

$$\mu = A \cdot \exp(\Delta E/RT) \cdot \dot{\gamma}^{(n-1)} \quad (\text{III.54})$$

The parameters A , $\Delta E/R$ and (n) were calculated from the viscosity data using standard regression analysis. Figure (III.3.2.1.1) shows viscosity data obtained for the polyethylene Sclair 2908 injection molding resin and the regression data used to calculate the flow activation energy (ΔE) and the coefficient A . The power-law coefficient was found to be slightly dependent on temperature. An average value of 0.755 was used in all simulations. Figure (III.3.2.1.2) gives the dynamic (complex) viscosity in the low shear rate region, as obtained from RMS experiments. The viscosity data from INSTRON and RMS measurements were in good agreement in the range of shear rates where the two methods overlapped. The storage and loss moduli at various temperatures were also obtained by RMS and are reported in Figure (III.3.2.1.3)

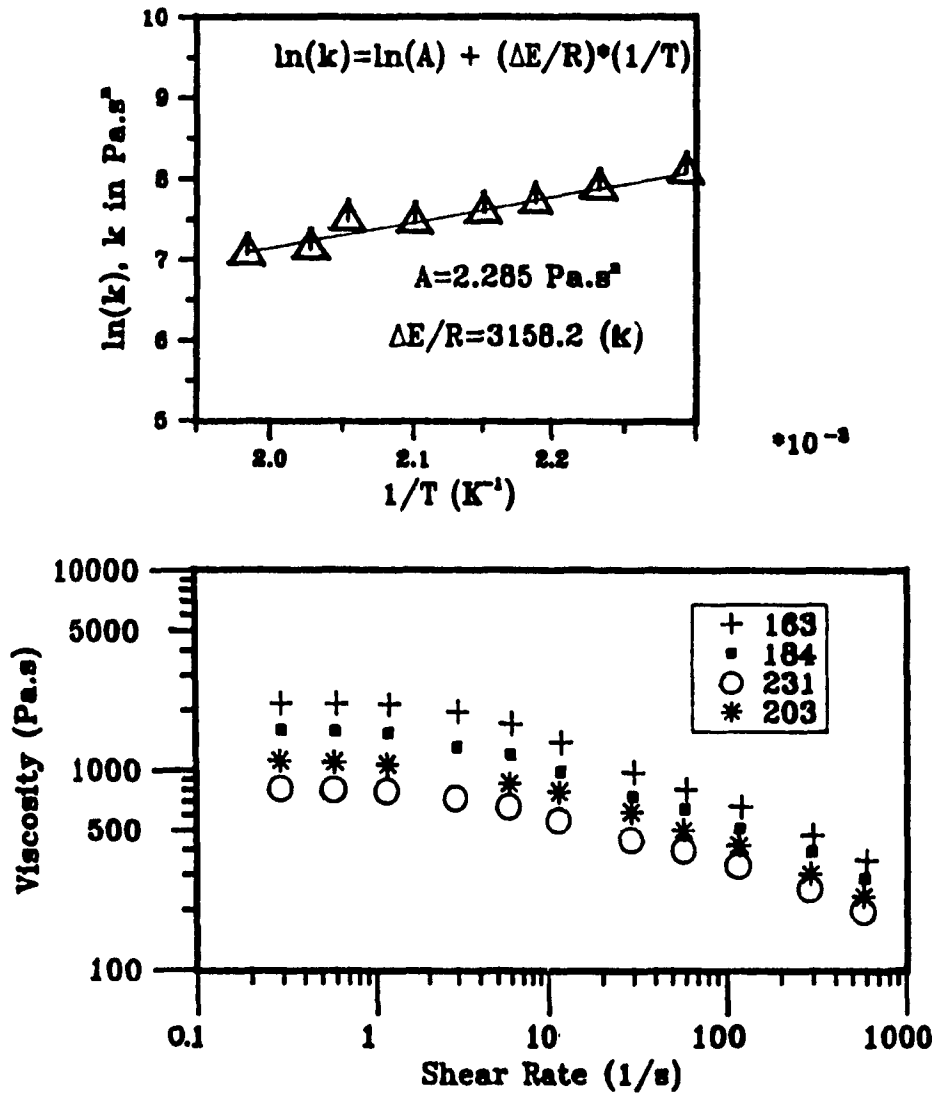


Figure (III.3.2.1.1): Shear viscosity data obtained for the resin Sclair 2908 (INSTRON capillary measurements) and the associated power law parameters.

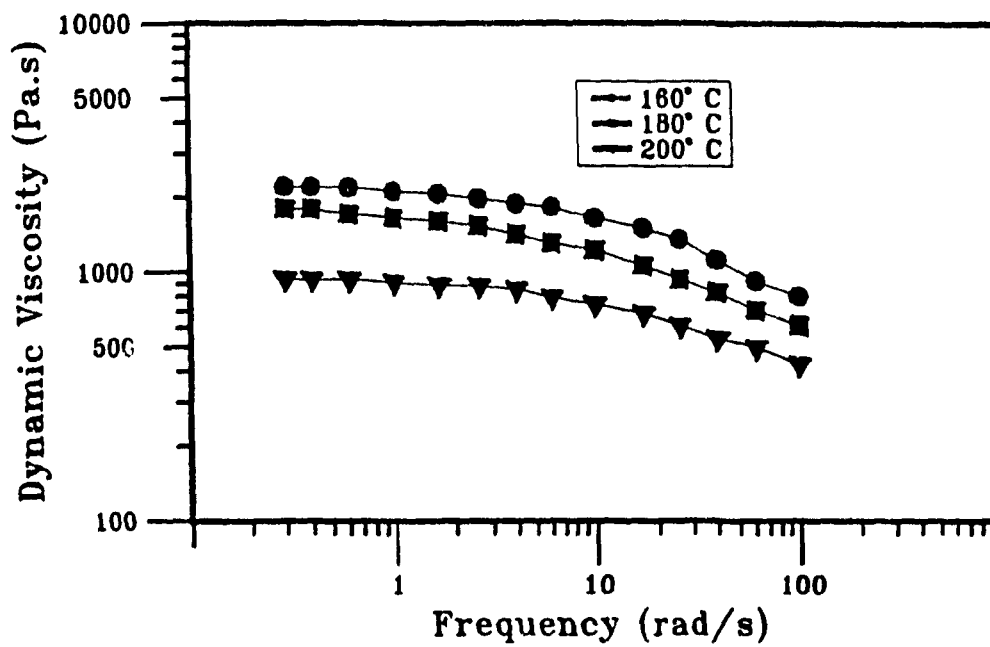


Figure (III.3.2.1.2): Dynamic viscosity data for resin Sclair 2908. RMS experiments.

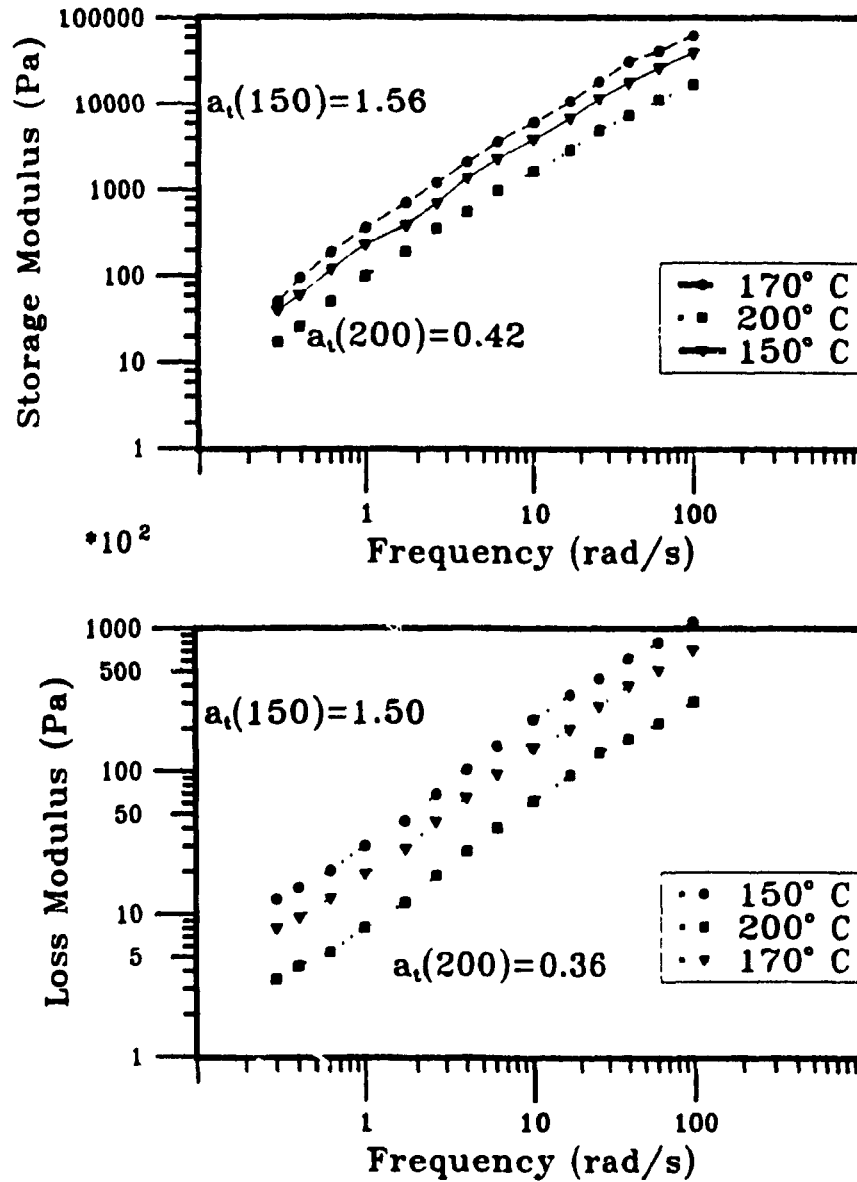


Figure (III.3.2.1.3):

Dynamic storage (G') and loss moduli (G'') for the resin Sclair 2908.

(III.3.3) Equipment

(III.3.3.1) Injection Molding Machine

The experimental work was carried out with a Danson-Metalmec reciprocating screw injection molding machine in the Department of Chemical Engineering at McGill University. The specifications of the machine are given in Table (III.3.3.1). The machine was operated in the semi-automatic mode, using the corresponding timers to specify the injection, holding and cooling times. The mold was cooled with tap water whose temperature varied seasonally between 18° and 23° C. The barrel temperatures in the front and rear sections were controlled by Gulton on-off controllers.

(III.3.3.2) Instrumentation

The pressure in the cavity was measured at three locations by Dynisco pressure transducers. One was located near the gate and the other two at intermediate positions in the cavity. The locations of the transducers are shown in Figure (III.3.1.1.B). Another pressure transducer was mounted at the nozzle to monitor the corresponding pressure. A linear velocity (TRANS-TEK, Model 112-001) and a linear displacement (Markite, Model 4709) transducers were used to monitor the motion of the ram, and, indirectly, measure the flowrate to the mold. A grounded junction thermocouple projecting into the polymer melt from the screw tip was used to measure the melt temperature at the nozzle. Three thermocouples flush mounted in the mold cavity were used to monitor the temperature at the mold surface; their locations are also shown in Figure (III.3.1.1.B). The calibration equations for these transducers follow:

$$\text{Cavity Pressure \#1:} \quad P(\text{Psi}) = 284.33*(\text{mV}) + 11.8 \quad (\text{III.54})$$

$$\text{Cavity Pressure \#2:} \quad P(\text{Psi}) = 88.65*(\text{mV}) - 196.4 \quad (\text{III.54.b})$$

Machine Model:	Danson Metalmec 60-SR
Capacity:	2 1/3 oz. (66.1 g)
Screw Diameter:	1.375 in (0.035 m)
Screw L/D Ratio:	15:1
Screw RPM:	40-150
Clamping Force:	60 T (53386 KN)
Hydraulic Pump:	Sperry-Vickers Vane Pump
Electric Motor:	20 HP (14.92 kW), 3 phase, 50 Hz
Servovalve:	Moog A076-103, 10 gpm (10 cu.m/hr) flow at 1000 psi (6.9 MPa)

Table (III.3.3.1): Specifications of the injection molding machine.

Cavity Pressure #3:	$P(\text{Psi}) = 434.86*(\text{mV}) - 103.2$	(III.54.c)
Nozzle Pressure:	$P(\text{Psi}) = 462.92*(\text{mV}) - 51.2$	(III.55)
Velocity Transducer:	$V(\text{cm/s}) = 0.209*(\text{mV}) - 0.004$	(III.56)
Displacement Transducer:	$L(\text{cm}) = 0.615*(\text{mV}) - 1.223$	(III.57)

(III.3.4) Experimental Conditions and Procedure.

Experiments were performed for a range of the process variables. For the purpose of illustration, four such experiments, designated as HP6, HP7, HP8 and HP9 are reported and will be used in later sections of this Thesis for comparison with model predictions. The melt entry temperatures (measured at the tip of the screw) were 200° C, 202° C, 235° C and 235° C, respectively. In order to simulate these experiments, the cooling rate was taken to be uniform throughout the faces of the mold, with an average heat transfer coefficient of 68 Btu/ft²/hr/F (386 W/m²K) in all experiments. (Gao, (1989), Mutel (1990)). This is a simplification of the actual situation in the mold, where the cooling rate can be fairly non-uniform, depending on the design of the cooling channels. In the absence of heat flux distribution data however, the assumption of uniform cooling rate is a reasonable approximation. Before injections were started, the injection molding machine was allowed to heat up and the barrel temperatures stabilize; that usually took 30-35 min. Then, 10-20 injections were performed without data acquisition, so that a thermal steady state was attained in the working machine. After that, data acquisition commenced.

(III.3.5) Certain Experimental Observations

The purpose of this section is to present selective experimental results of injection molding experiments of polyethylene in the complex-shaped mold, in an attempt to illustrate certain aspects of the filling stage.

(III.3.5.1) Pressure Variation

A typical variation of cavity pressure at the gate and nozzle pressure during an injection molding cycle is given in Figure (III.3.5.1.1.A). In all experimental conditions, the nozzle pressure rises very fast and then remains roughly constant until filling and packing are completed.

Both cavity and nozzle pressure values drop finally to atmospheric levels at the end of cooling; however, the cavity pressure drop is slower than that at the nozzle; this is a result of the retraction of the screw after the gate is sealed and the dominance of cooling in cavity pressure control. The variation of the cavity pressure at the gate during filling is more specifically given in Figure (III.3.5.1.1.B).

(III.3.5.2) Progression of the Melt Front

The progression of the melt front into the cavity in both cases can be observed indirectly by monitoring the response of the thermocouples. Typical results are shown in Figure (III.3.5.2.1). The effect of melt temperature on the melt progression speed and filling time can also be seen in Figure (III.3.5.2.1). As expected, higher melt temperature results in faster filling due to the corresponding lower viscosities.

(III.3.5.3) Shape of the Advancing Front

A number of short shot experiments was performed in order to determine the evolution and shape of the melt front during filling. Figures (III.3.5.3.1) and (III.3.5.3.2) show short shots obtained for various injection times. The melt temperature was 200° C and the speed valve opening 5/12. Initially, a nearly semicircular filling pattern is observed. This becomes only slightly curved as the melt front reaches the middle part of the cavity. The shape of the free surface becomes more complex as the melt closes behind the obstacle, becoming flat near the end of filling. Figure (III.3.5.3.3) shows short shots that illustrate the detailed evolution of the shape of the melt front as it closes behind the obstacle and the formation of a

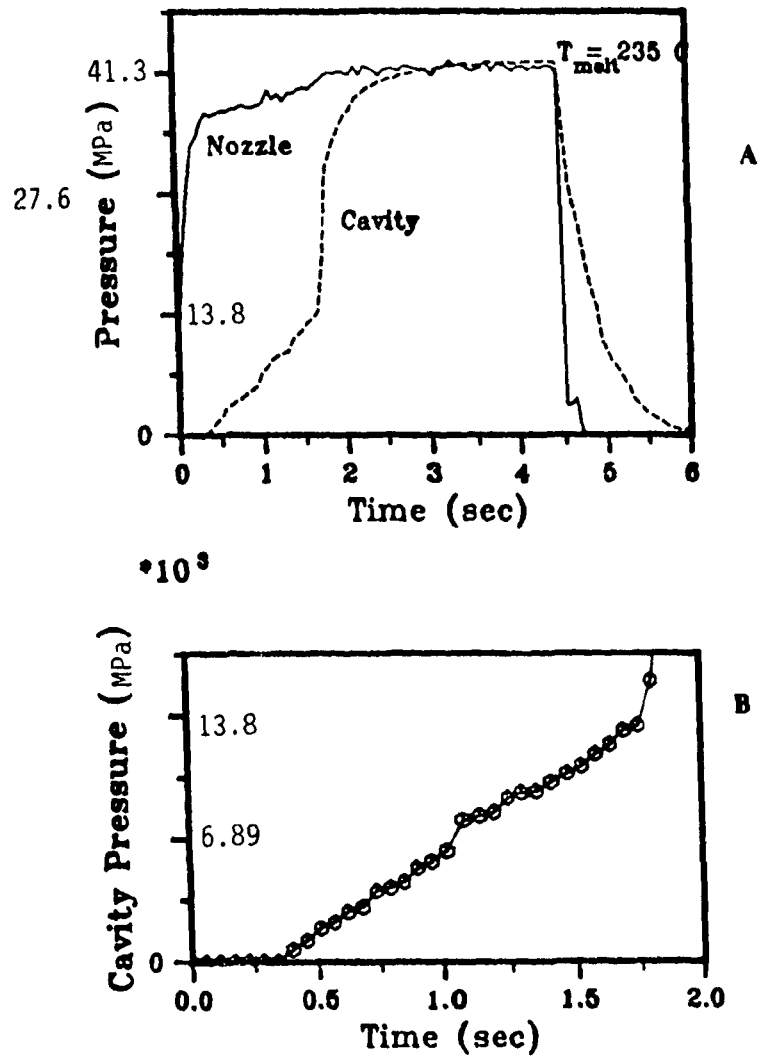


Figure (III.3.5.1.1): (A) Typical variation of cavity and nozzle pressure during an injection molding cycle; (B) Typical variation of cavity pressure at the gate (cavity CR1).

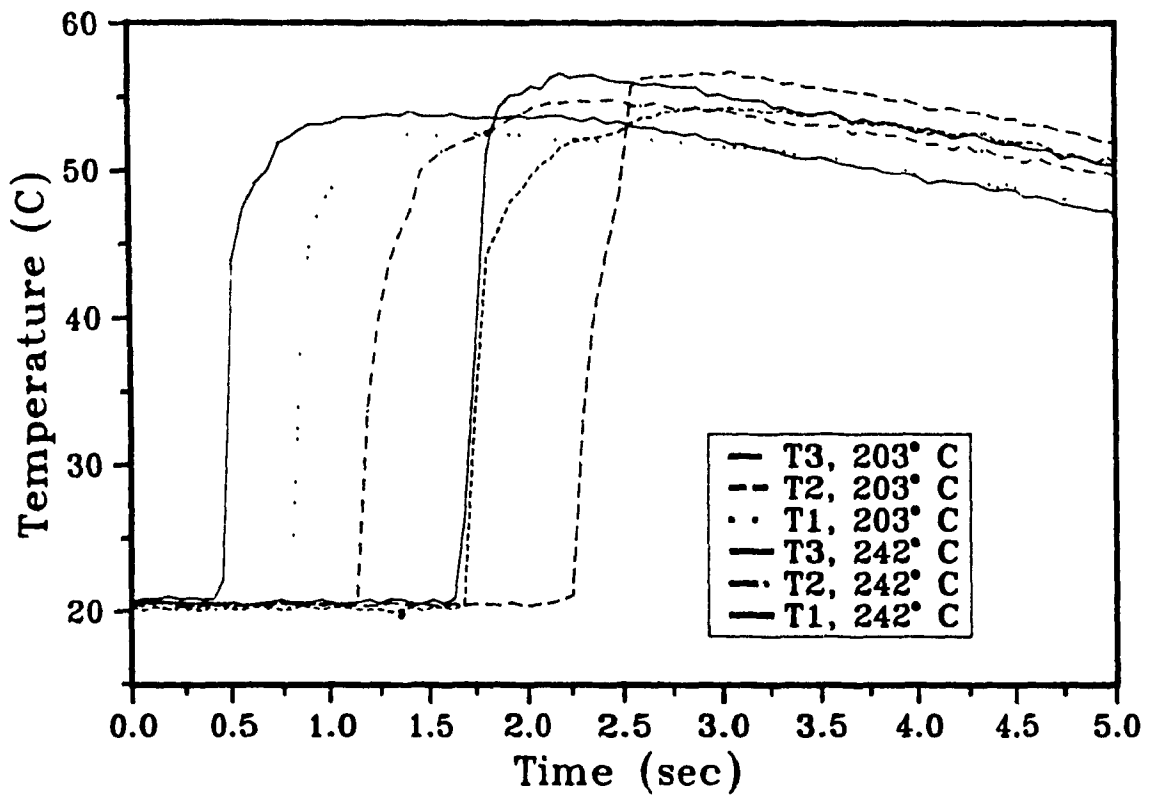


Figure (III.3.5.2.1): Response of the surface cavity thermocouples during an injection molding cycle at two temperatures showing the effect of melt temperature on melt progression speed and filling times; experimental.

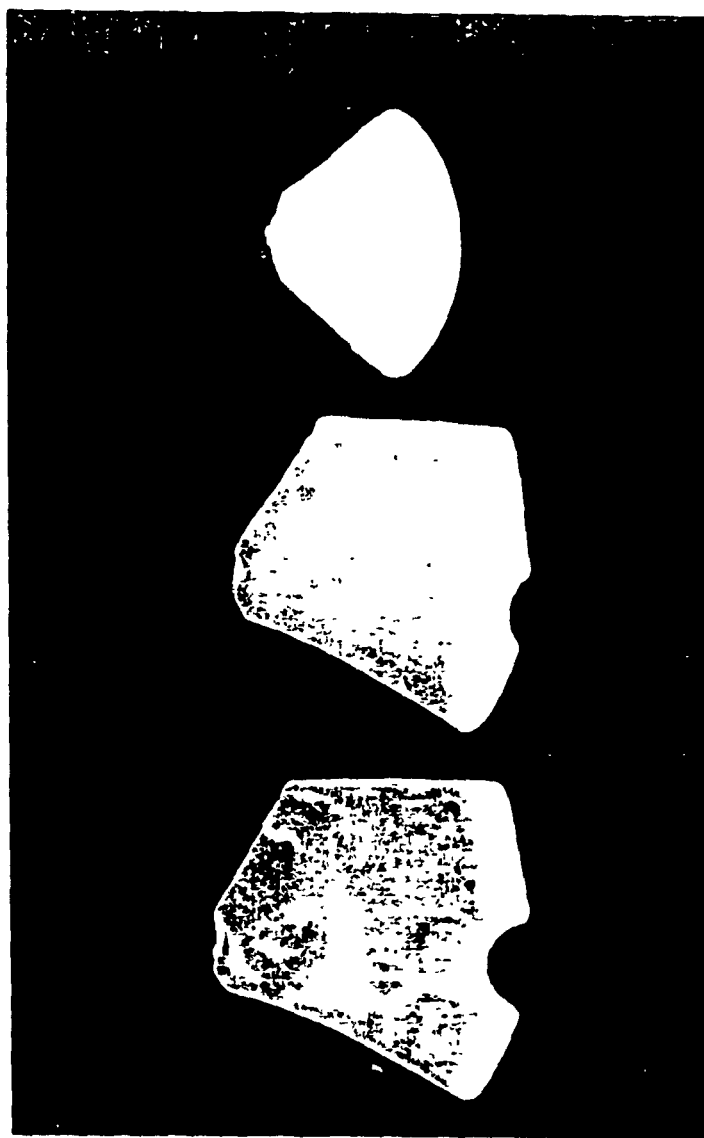


Figure (III.3.5.3.1): Experimental short shots showing the evolution of the shape and location of the free surface during filling.

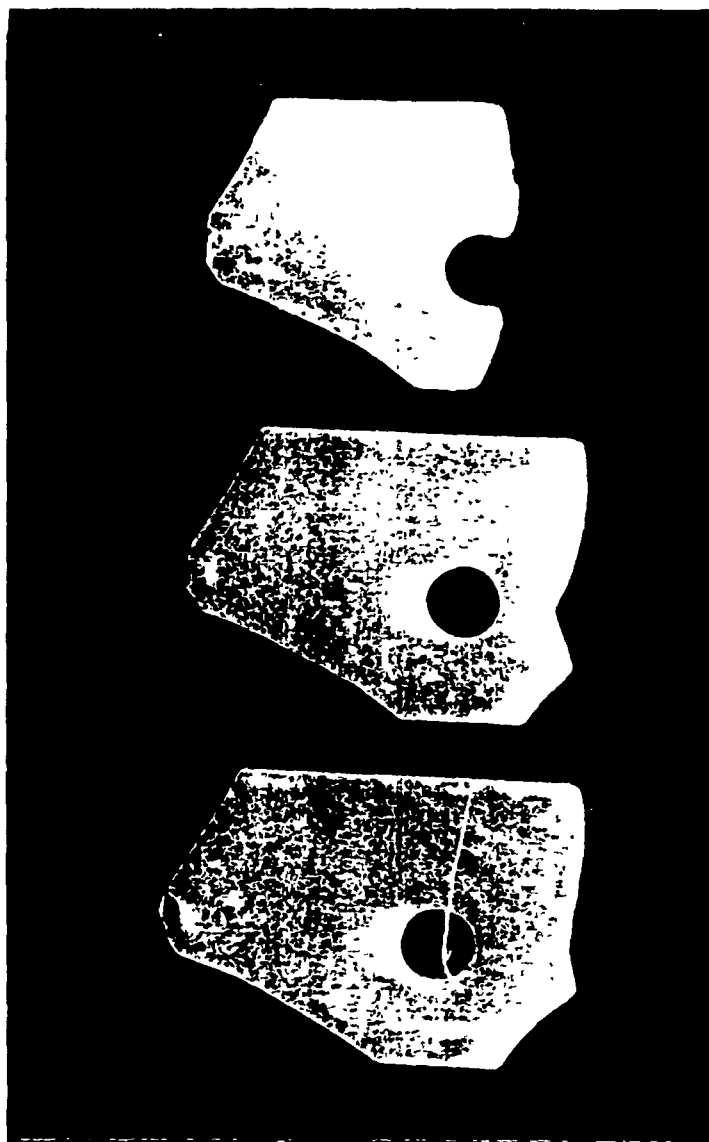


Figure (III.3.5.3.2): Experimental short shots showing the evolution of the shape and location of the free surface during filling.

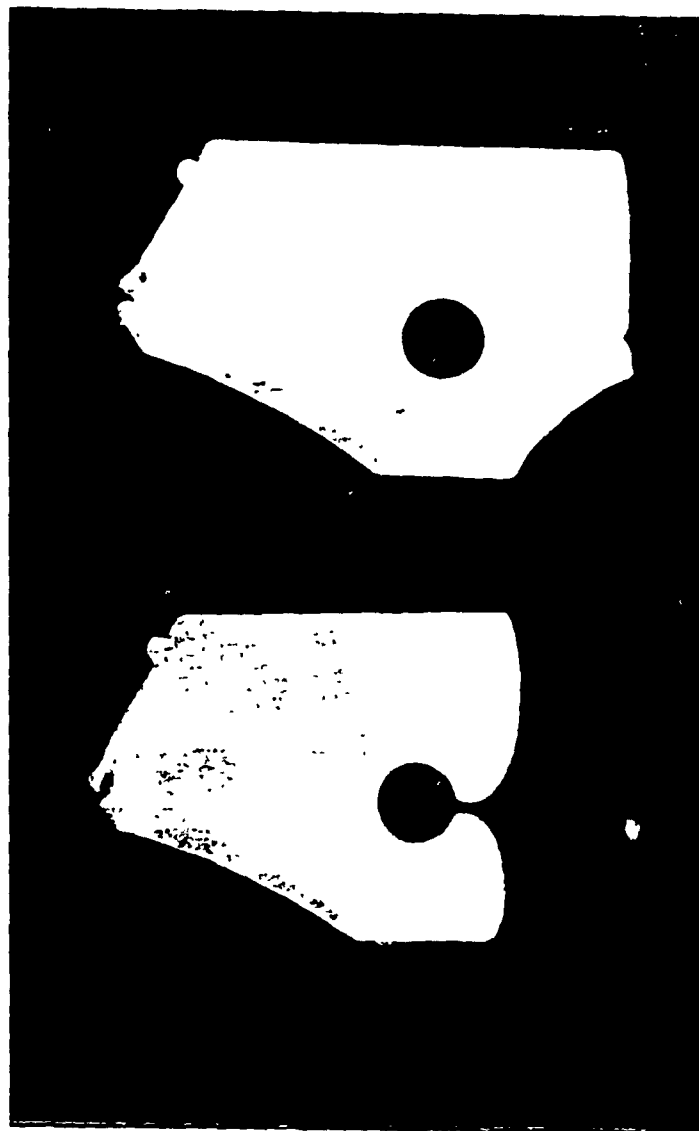


Figure (III.3.5.3.3): Experimental short shots showing the evolution of the shape of the free surface behind the obstacle and the formation of weld line.

weld line.

(III.4) SIMULATION RESULTS

The objective of the following section is to identify, through computer simulation, the spatial and temporal variation of key process parameters such as pressure, temperature, filling patterns, velocity and stresses during the filling stage. Comparison of such predictions with experimental data will be performed in the next section. A 21*21 grid was used in all these simulations. Validation of the model predictions using successive grid refinements has not been done in this section, mainly due to computer time limitations. However, the core subroutines of the computer code (kinematics, geometrical transformations and QUICK upwinding for the stresses) have been tested with extensive grid refinement in part (II) of this Thesis. The accuracy of the Laplacian solver, critical in the calculation of pressure, has been tested against analytical solutions in part (I). These, along with the reasonable agreement between simulations and experiment (see next section) have convinced the author that the proposed model is numerically correct.

(III.4.1) Progression of the Melt Front

The computational treatment and tracking of the free surface have been dealt with in Appendix A.4 (section A.4.7). Predicted filling patterns in the complex-shaped cavity are given in Figure (III.4.1.1). It can be concluded, with reference to the experimentally observed filling patterns (section (III.3.5.2)), that the computer program is able to simulate the movement and the shape of the free surface with success. It was found that the filling pattern was independent of the parameters of the process, such as the injection speed and the melt flowrate, at least for the range of variables that was studied. The shape of the free surface was mainly determined by the geometry of the mold. For comparison, predicted filling patterns in a simple rectangular cavity are shown in Figure (III.4.1.2).

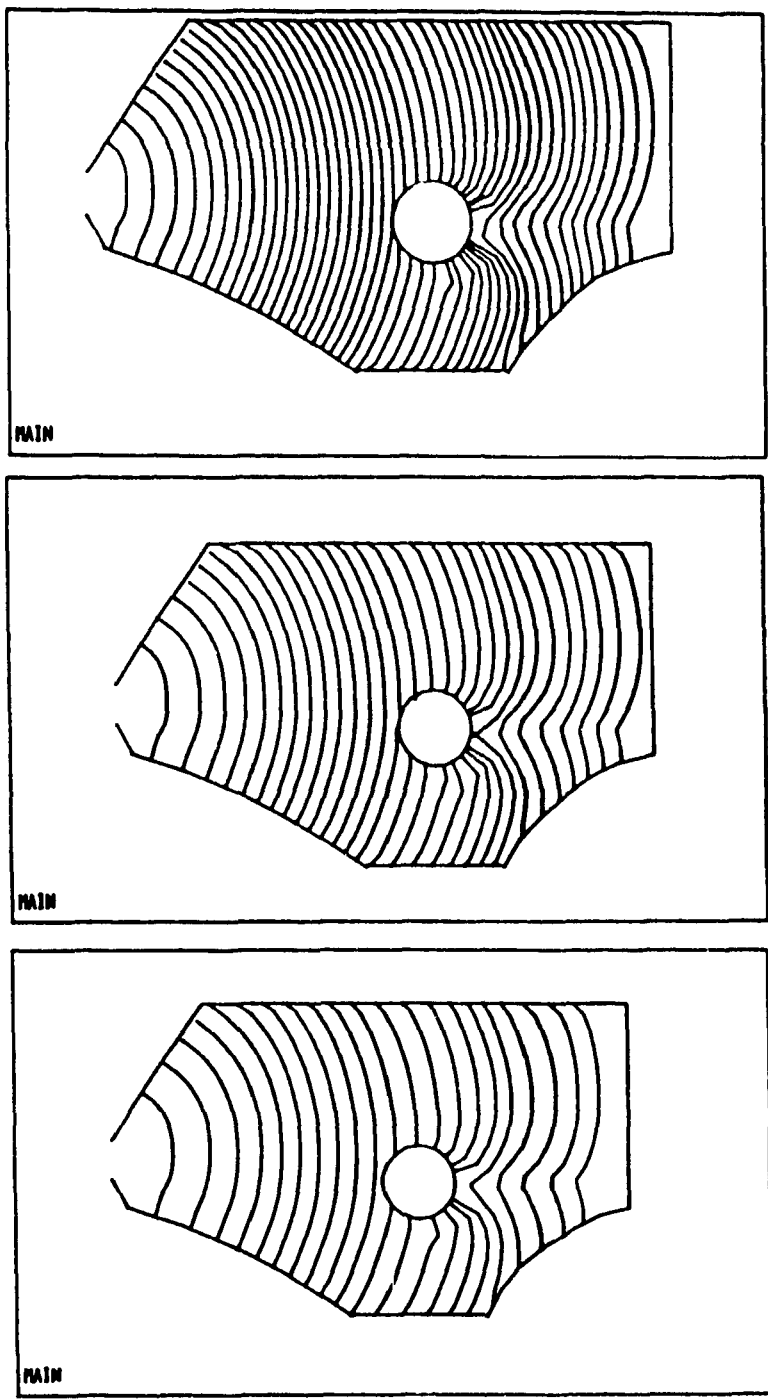


Figure (III.4.1.1): Predicted filling patterns for the complex cavity TE9 (Table (III.4.2.2.1)) at various melt flowrates. $\Delta t = 0.044$.

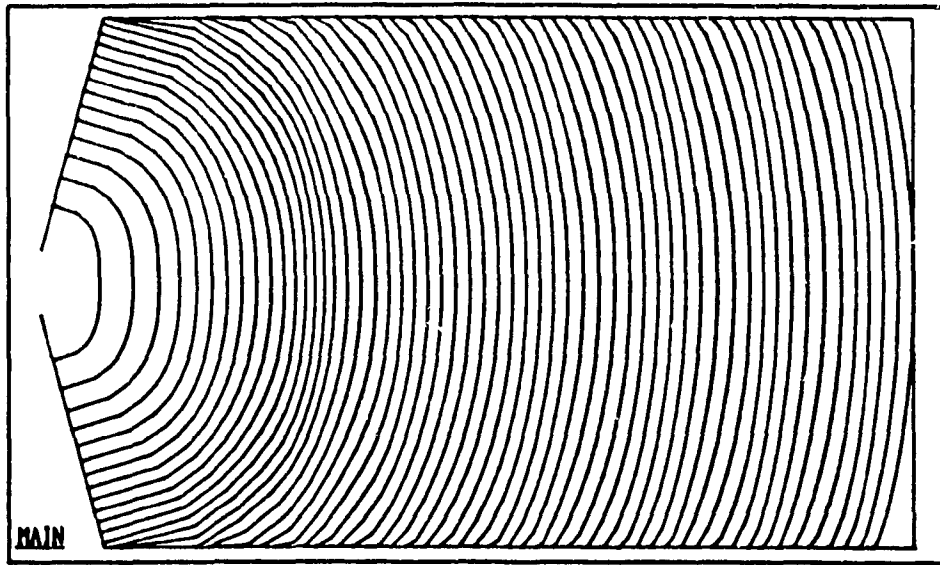


Figure (III.4.1.2): Predicted filling patterns in a rectangular cavity of constant thickness. $\Delta t = 0.044$

The continuous generation of a computational grid at every time step following the advancement of the free surface is a key issue in the present numerical simulation of the filling stage. Figures (III.4.1.3) and (III.4.1.4) show computational grids constructed at various instances during the filling of the complex shaped cavity. The computer program was able to automatically generate suitable computational grids following the advancement of the free surface with no need for interruptions and/or adjustments.

(III.4.2) Variation of Cavity Pressure with Time

(III.4.2.1) Effect of Ram Velocity

Figure (III.4.2.1) gives the predicted pressure-time profile at two locations in the cavity, for two values of the ram velocity (or, equivalently, the melt flowrate). In these runs, an average heat transfer coefficient of 68 Btu/ft²/F/hr (386 W/m²K) was assumed, uniform along each face of the mold. Cavity CR1 was used in these simulations. It can be seen that increased ram velocity results in shorter filling times and significantly higher pressures.

(III.4.2.2) Effect of the Geometry of the Cavity

Figure (III.4.2.2) shows the computed pressure-time history at the location of pressure transducers P1 and P2 at three geometrical configurations of the cavity, designated here as TE2, TE9 and TE15. All configurations have the same planar shape as cavity CR1. Table (III.4.2.2.1) lists the thickness distributions of these cavities. The two groups of curves in Figure (III.4.2.2) correspond to the predicted response of pressure transducers P1 and P2. Clearly, the geometry TE15 with the smallest thickness is associated with larger pressures. A cavity of uniform thickness is associated with the smallest pressure and the smoothest pressure-time profiles. Figure (III.4.2.2) allows for an evaluation of variations in the thickness of the cavity

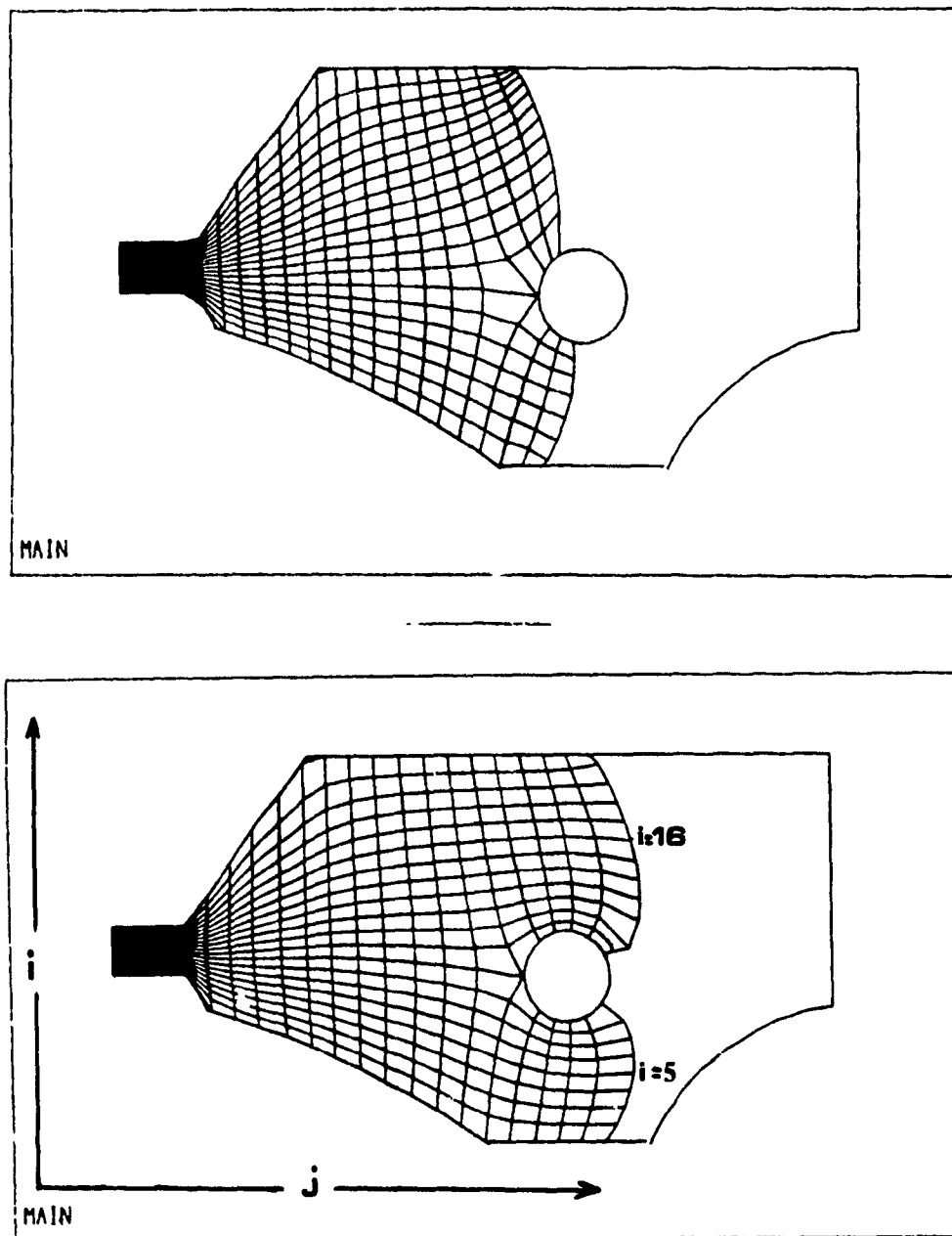


Figure (III.4.1.3): Computational grids constructed automatically at various instances during filling of mold CR1, along with mesh indexing.

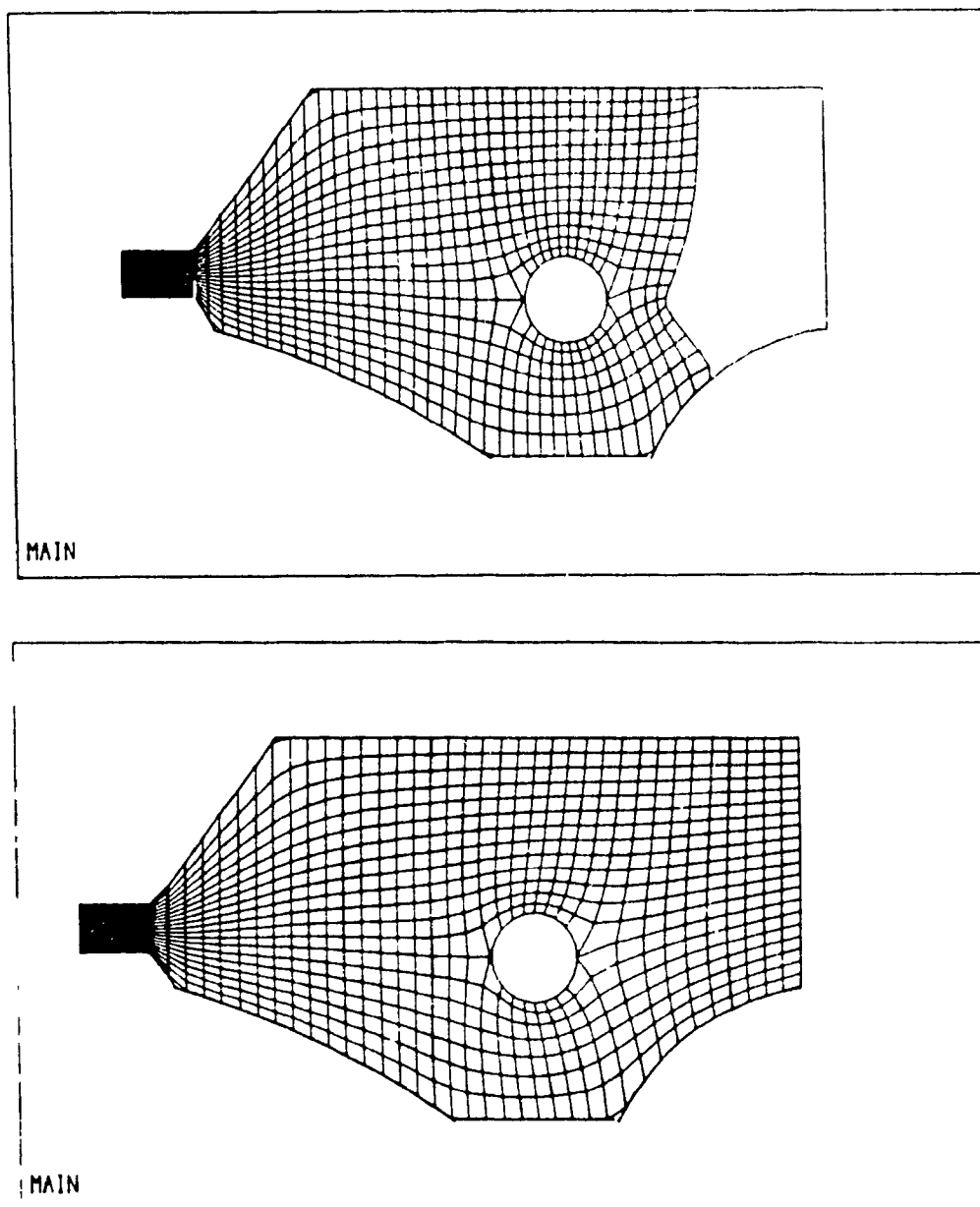


Figure (III.4.1.4): Computational grids constructed automatically at various instances during filling of mold CR1.

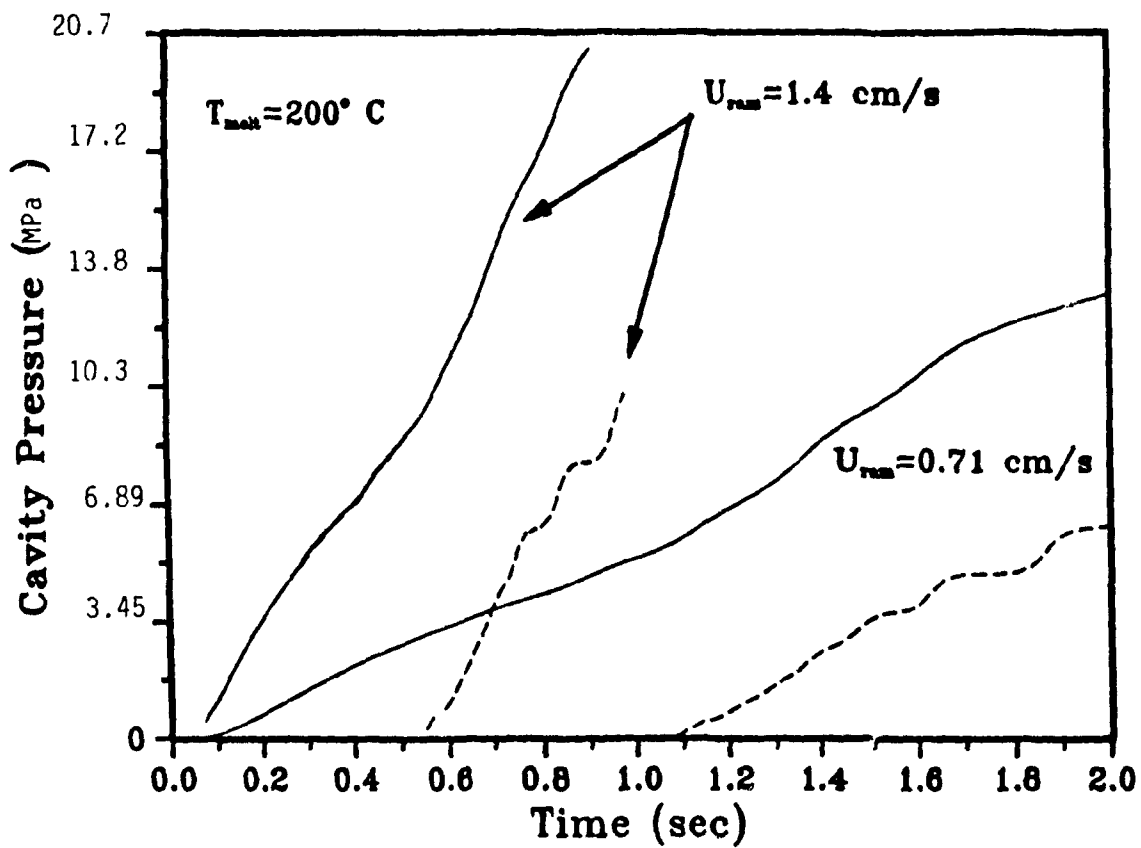


Figure (III.4.2.1): Effect of ram velocity on pressure-time profiles at two locations in the cavity CR1 (corresponding to the locations of transducers P1 and P2). $T_{max} = 200^\circ$ C.

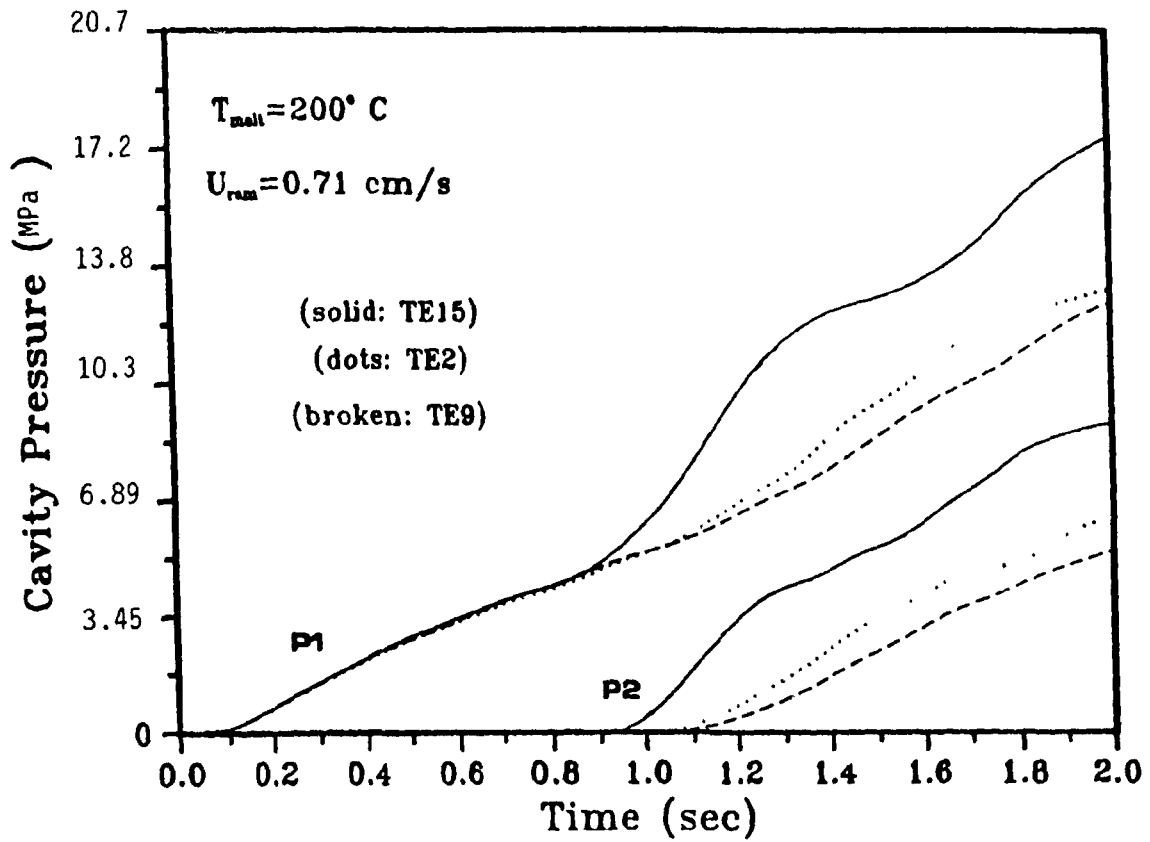
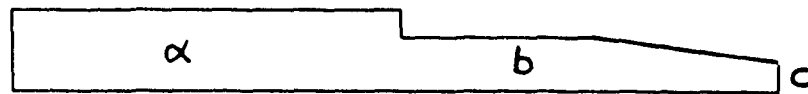


Figure (III.4.2.2): Effect of the geometry of the mold on pressure-time profiles at two locations in the cavity (corresponding to the locations of transducers P1 and P2). $T_{\text{mold}} = 200^{\circ} \text{C}$.



cavity	dimensions (cm)		
	(a)	(b)	(c)
TE2	0.32	0.26	0.20
TE9	0.32	0.32	0.32
TE15	0.32	0.127	0.05

Table (III.4.2.2.1): Dimensions of cavities used in simulation studies.

on the pressure-time profiles.

(III.4.2.3) Effect of Melt Temperature at the Gate

The temperature at which the melt enters the cavity is another important process parameter. Its effect on the computed pressure history at two locations in the cavity is given in Figure (III.4.2.3), for two melt temperatures (200° and 235° C). In Figure (III.4.2.3) P1 and P2 indicate predicted pressures at locations corresponding to those of pressure transducers P1 and P2. Higher melt temperature at the gate results in lower gate pressures; this is expected, since higher melt temperatures correspond to lower melt viscosities. The cavity considered in these simulations is cavity TE9.

(III.4.2.4) Effect of Material Properties

Figure (III.4.2.4) gives predicted variation of pressure in cavity CR1 at a location corresponding to that of the gate transducer (P1). Curve (A) is obtained using the power law parameters reported by Lafleur (1983). In curve (B) the power law parameters are as reported in section (III.3.2.1) of this Thesis. The variation of ram velocity with time in this simulation is represented by three linear parts: for $0 < t < 0.55s$, $1.1 \text{ cm/s} < U_{ram} < 1.25 \text{ cm/s}$; for $0.55s < t < 1.3s$, $0.7 \text{ cm/s} < U_{ram} < 1.1 \text{ cm/s}$; for $1.3s < t < 2.01s$, $0.375 \text{ cm/s} < U_{ram} < 0.7 \text{ cm/s}$. Use of higher power law constant (0.822 in (A) compared to 0.755 in (B)) results in higher gate pressures. The qualitative form of the pressure-time profile, which reflects changes in the geometry of the mold, remains unaffected by the specific values of the material properties.

(III.4.3) Pressure Drop in the Cavity During Filling

(III.4.3.1) Effect of Ram Velocity

The pressure drop at two instances during filling of the complex cavity CR1 is shown

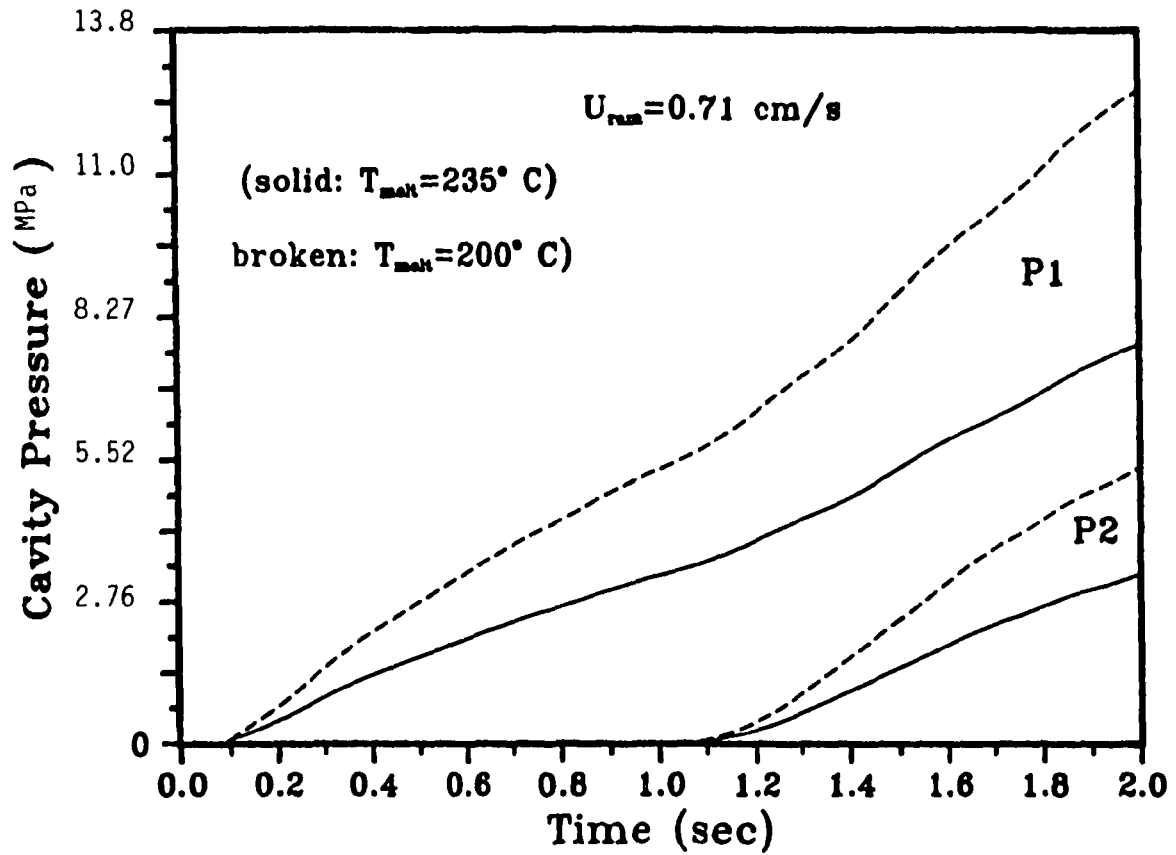


Figure (III.4.2.3): Effect of the melt temperature at the gate (T_{melt}) on pressure-time profiles at two locations in the cavity TE9 (corresponding to the locations of transducers P1 and P2).

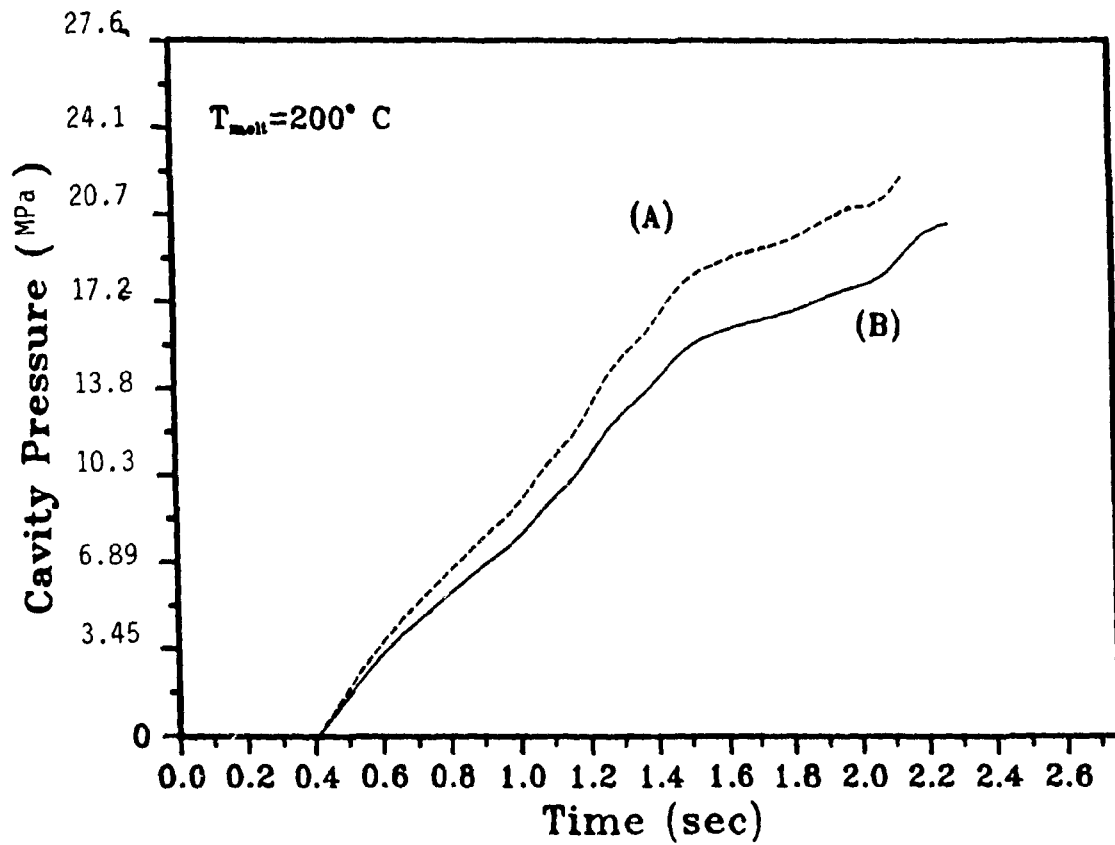


Figure (III.4.2.4): Effect of power law parameters on the pressure-time profile at the gate; (A) parameters as reported by Lafleur (1983), (B) parameters determined in this study. Cavity CR1.

in Figure (III.4.3.1) for two values of the ram velocity. These profiles are obtained along the $i=5$ (lower part of the cavity) and $i=16$ (upper part of the cavity) grid lines. With reference to Figure (III.4.1.3), these are horizontal (left -to-right) coordinate lines emanating from the gate and terminating at the free surface. Notice the slight differences in the pressure drops along these lines. Even though these differences are numerically very small, they appear consistently in all simulations. This leads to the conclusion that they are manifestations of the non symmetric nature of the flow rather than numerical artifacts. It can also be observed that higher melt flowrate results in larger pressure drop in the cavity.

(III.4.3.2) Effect of the Geometry of the Cavity.

The effect of geometry on the pressure drop in the cavity is given in Figure (III.4.3.2). Clearly, the cavity of the smallest thickness (solid line) shows the largest pressure gradients. Because of the smaller cavity volume, the melt front travels faster in the cavity TE15 (compare the intercept of the solid and broken lines (corresponding to cavities TE15 and TE9 respectively) with the x-axis).

(III.4.3.3) Effect of Melt Temperature

The effect of melt temperature at the gate on the pressure drop along the line $i=16$ (upper part of the cavity) is given in Figure (III.4.3.3). Lower melt temperatures result in higher pressure drops due to the increased viscosity of the melt. In these runs, cavity TE9 was used.

(III.4.3.4) Effect of Material Properties

Figure (III.4.3.4) gives predicted pressure drops in the cavity along the $i=16$ coordinate line at $t=1.34$ s. Curves (A) and (B) correspond to the material properties and processing conditions discussed in section (III.4.2.4). Use of the material

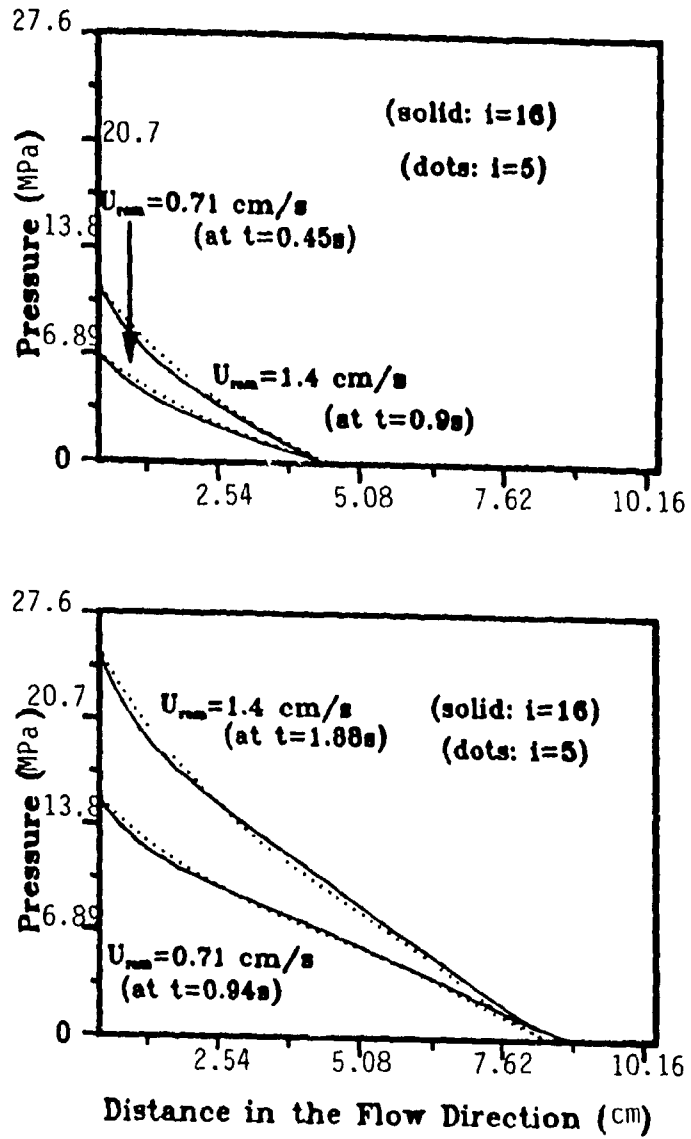


Figure (III.4.3.1): Effect of ram velocity on pressure drop in the cavity CR1 at two instances during filling. $T_{melt} = 200^\circ \text{ C}$.

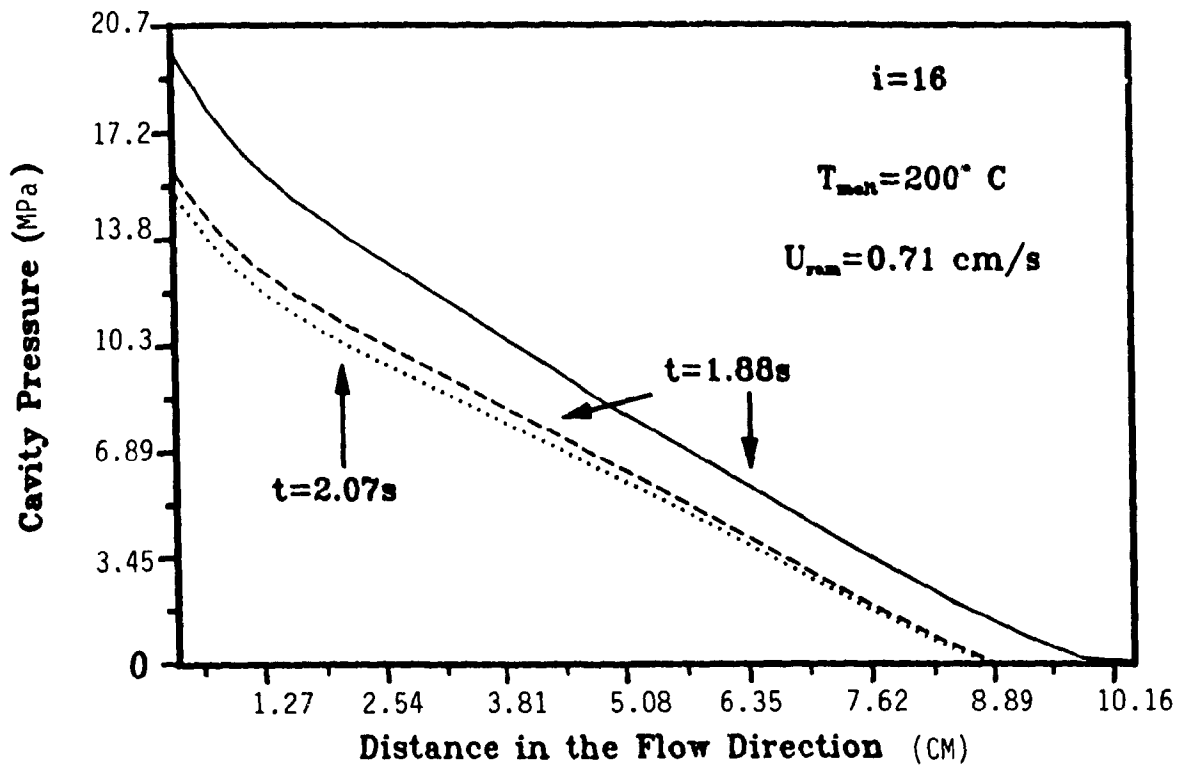


Figure (III.4.3.2): Effect of mold geometry on pressure drop at an instant during filling. $T_{\text{melt}}=200^{\circ}\text{C}$. Solid line: cavity TE15; dotted: TE2, and broken line TE9 (refer to Table (III.4.2.2.1)).

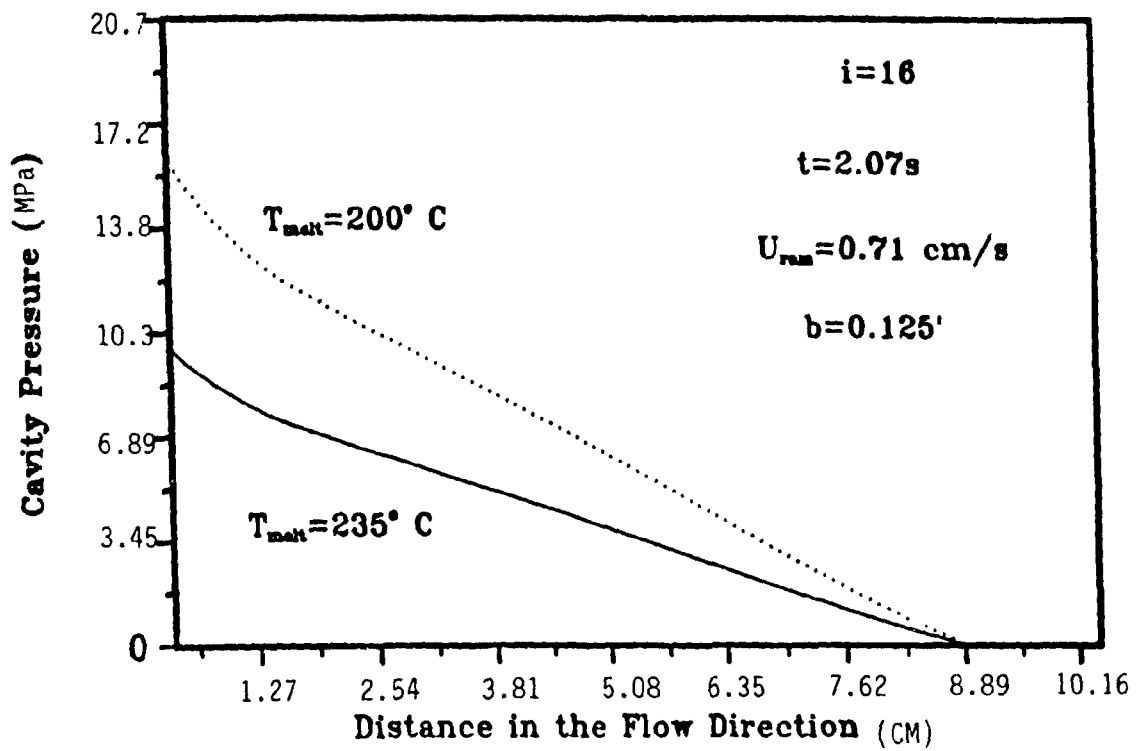


Figure (III.4.3.3): Effect of melt temperature at the gate on pressure drop in the cavity TE9 at an instant (t) during filling, along the $i=16$ coordinate line.

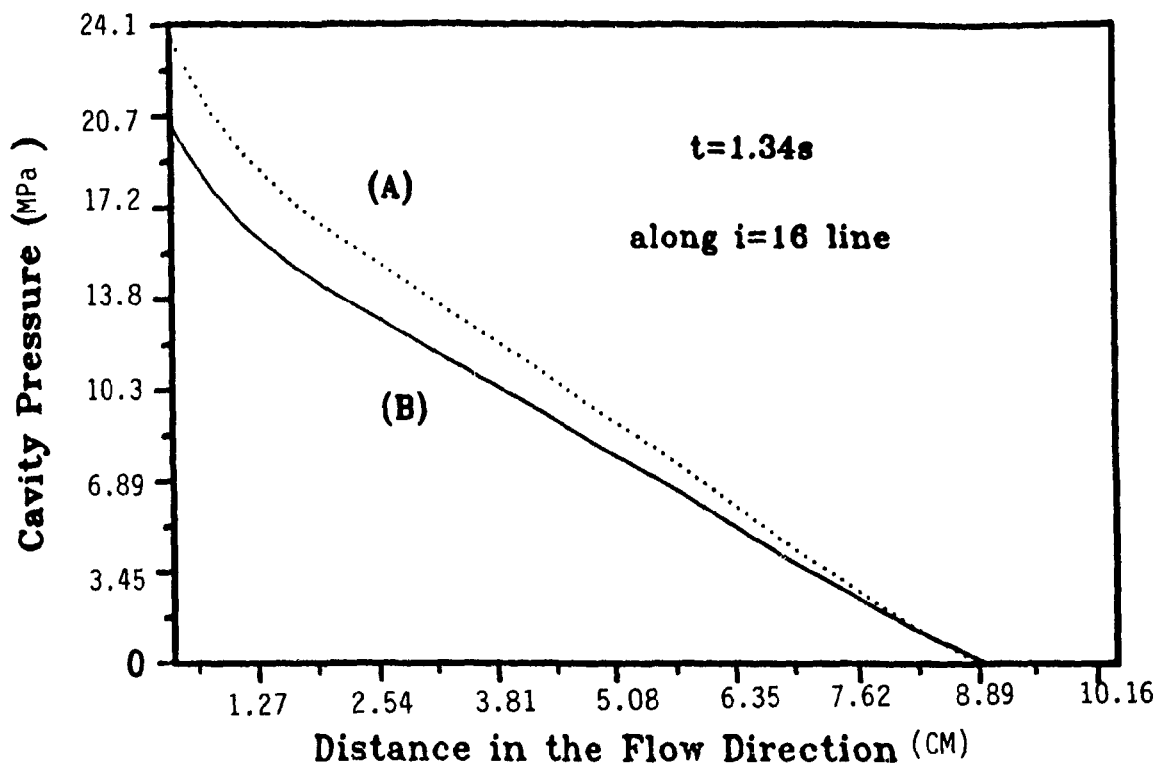


Figure (III.4.3.4): Effect of power law parameters on the pressure drop in the cavity CR1 at $t=1.34s$; (A) parameters as reported by Lafleur (1983), (B) parameters determined in this study.

parameters reported by Lafleur (1983) results in a higher pressure drop in the cavity.

(III.4.4) Temperature Drops in the Cavity During Filling

(III.4.4.1) Effect of Ram Velocity

Figure (III.4.4.1) shows the temperature profiles along the same coordinates lines as in Figures (III.4.3.1), for two instances during filling at two values of the ram velocity. These are gap-averaged temperatures. At some distance from the gate, the lower part of the cavity (solid lines, $i=5$) becomes progressively cooler than the upper part ($i=16$). Simulation has revealed that, in this particular cavity, the material flows faster in the upper part, supplying more hot material from the gate. Viscous heating is also stronger there, and this accounts for the higher temperatures in the upper half of the cavity. These temperature differentials are small in this geometry, but can be significant in other geometric configurations and/or molding conditions. Simulation can help balance these temperature differences by judicious choice of the design of the cooling channels. From Figure (III.4.4.1) it becomes evident that higher ram velocity results in smaller temperature drops in the cavity. This is a result of the combined effect of shorter residence times and higher viscous heating associated with higher melt flowrates. For the case with the higher melt flowrate ($U_{ram}=1.4$ cm/s), the temperature drop is less than half the temperature drop corresponding to the case with half the ram velocity ($U_{ram}=0.7$ cm/s).

(III.4.4.2) Effect of Geometry

Figure (III.4.4.2) gives the effect of the shape of the cavity in the thickness direction on the temperature profiles along the line $i=16$. At the front section of the cavity, which is the same in all configurations TE2, TE9 and TE15, the temperatures are identical. Significant differences occur however in the rest of the cavity as the geometrical configuration changes. In cavity TE15 the temperature passes through

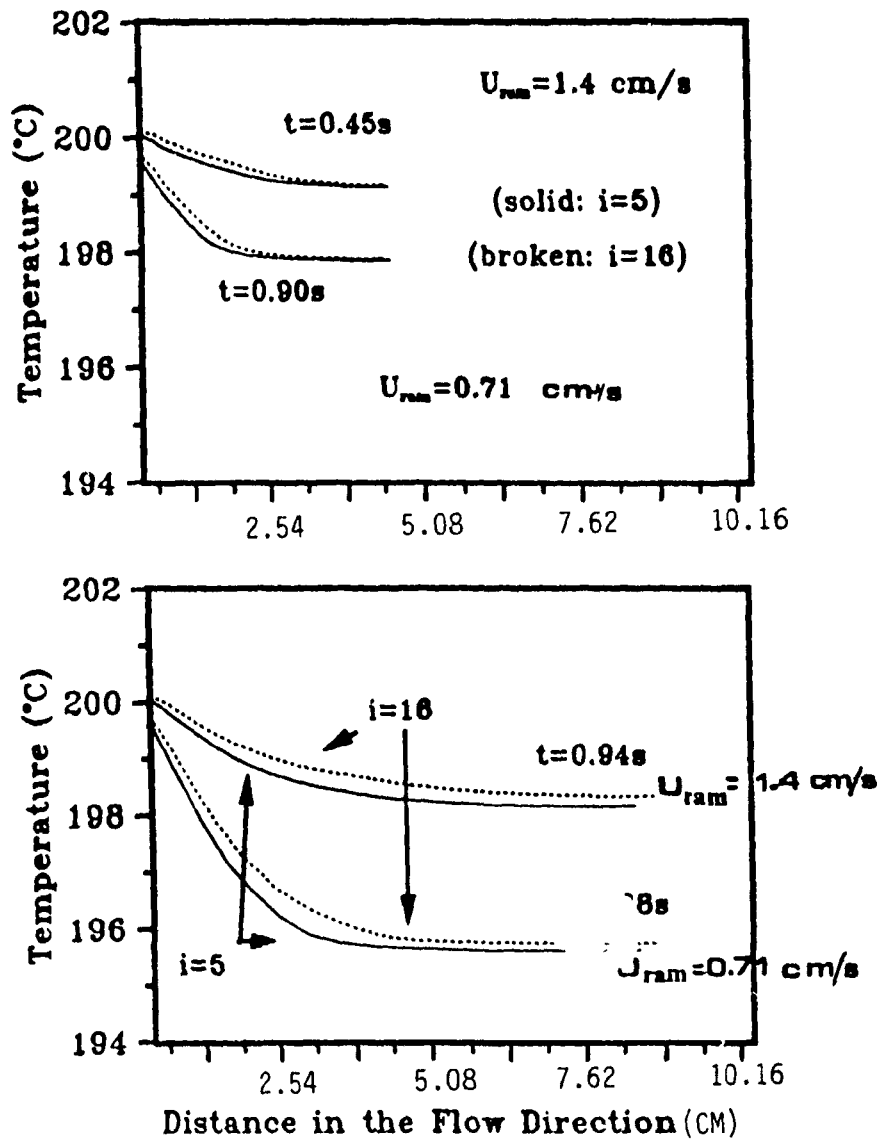


Figure (III.4.4.1): Effect of ram velocity on temperature drop in the cavity CR1 at two instances during filling. $T_{inlet} = 200^\circ \text{ C}$.

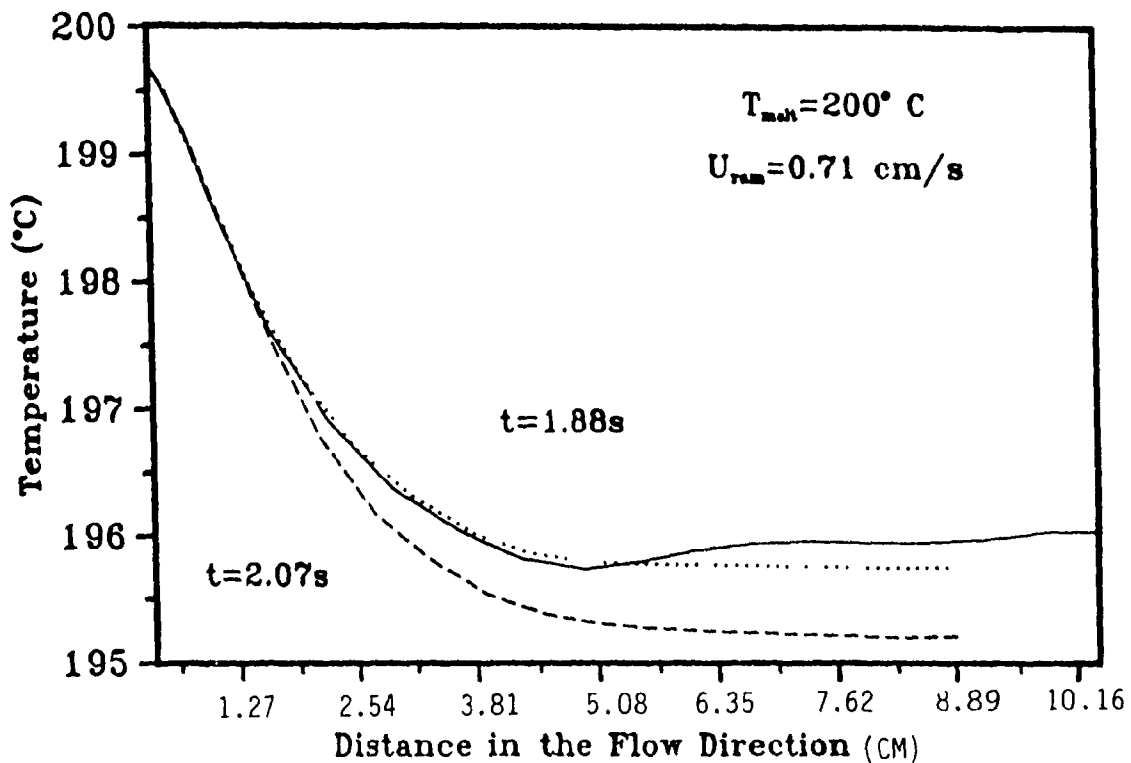


Figure (III.4.4.2): Effect of the mold geometry on temperature drops at various instances during filling, along the line $i=16$. Solid line: cavity TE15; dotted: TE2, and broken line TE9 (refer to Table (III.4.2.2.1)).

a minimum at the end of the thick front section; after that, due to the higher viscous heating and smaller residence times associated with the thinner section, the temperature increases. The constant thickness cavity TE9 shows the lowest temperatures along $i=16$. This is probably due to the longer residence times, with some possible effect of the reduced viscous heating associated with that cavity, since in all three cases the conditions, including the cooling rate, are the same.

(III.4.4.3) Effect of Material Properties

Figure (III.4.4.3) gives predicted temperature profiles in the cavity along the $i=16$ coordinate line at $t=1.34$ s and $t=0.91$ s. Curves (A) and (B) correspond to the material properties and processing conditions discussed in section (III.4.2.4). Use of the material parameters reported by Lafleur (1983) results in slightly higher temperatures in the cavity.

(III.4.5) Spatial Variation of Certain Characteristic Parameters

Appendix (A.5) gives predicted variation of key process characteristics such as stresses, velocities in the two plane directions, viscosities and deformation rates at three instances during filling. Mold TE9 was used in all the results of Appendix A.5. The cooling rate was $85 \text{ Btu/ft}^2\text{/F/hr}$ ($482 \text{ W/m}^2\text{K}$), the melt temperature at the gate 235°C and the ram speed 1.0 cm/s . Certain results will be presented and discussed in this section.

Figure (III.4.5.1) gives predicted temperature contours at $t=1.6$ s in both cavities TE9 and CR1(variable thickness). These are gap-averaged temperatures. In both cases, the temperature gradients are strong only near the gate, the rest of the cavity being essentially isothermal - in a gap-averaged sense. The upper part of the cavity is warmer than the lower part, and this is largely due to the shape of the mold in the X-Y plane, which induces a preferential flow of melt in the upper part of the cavity.

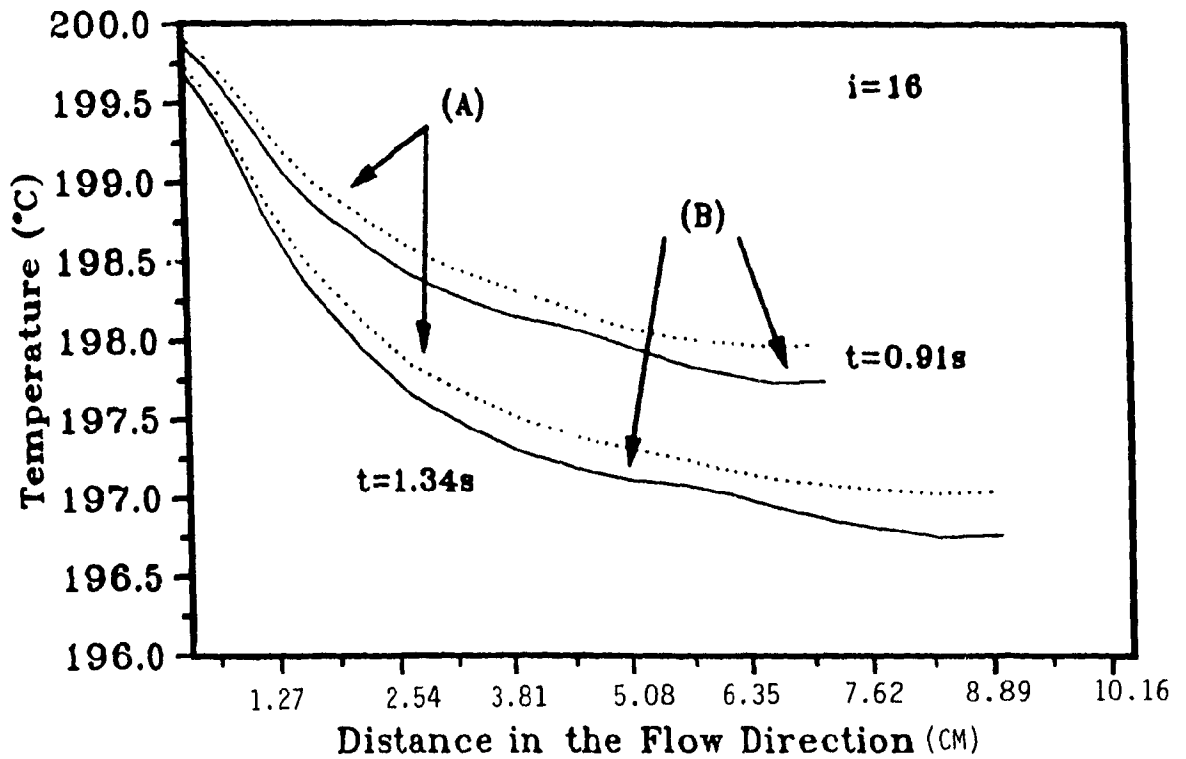


Figure (III.4.4.3): Effect of power law parameters on the temperature profile in the cavity CR1 at $t=1.34\text{s}$ and $t=0.91\text{s}$; (A) parameters as reported by Lafleur (1983), (B) parameters determined in this study.

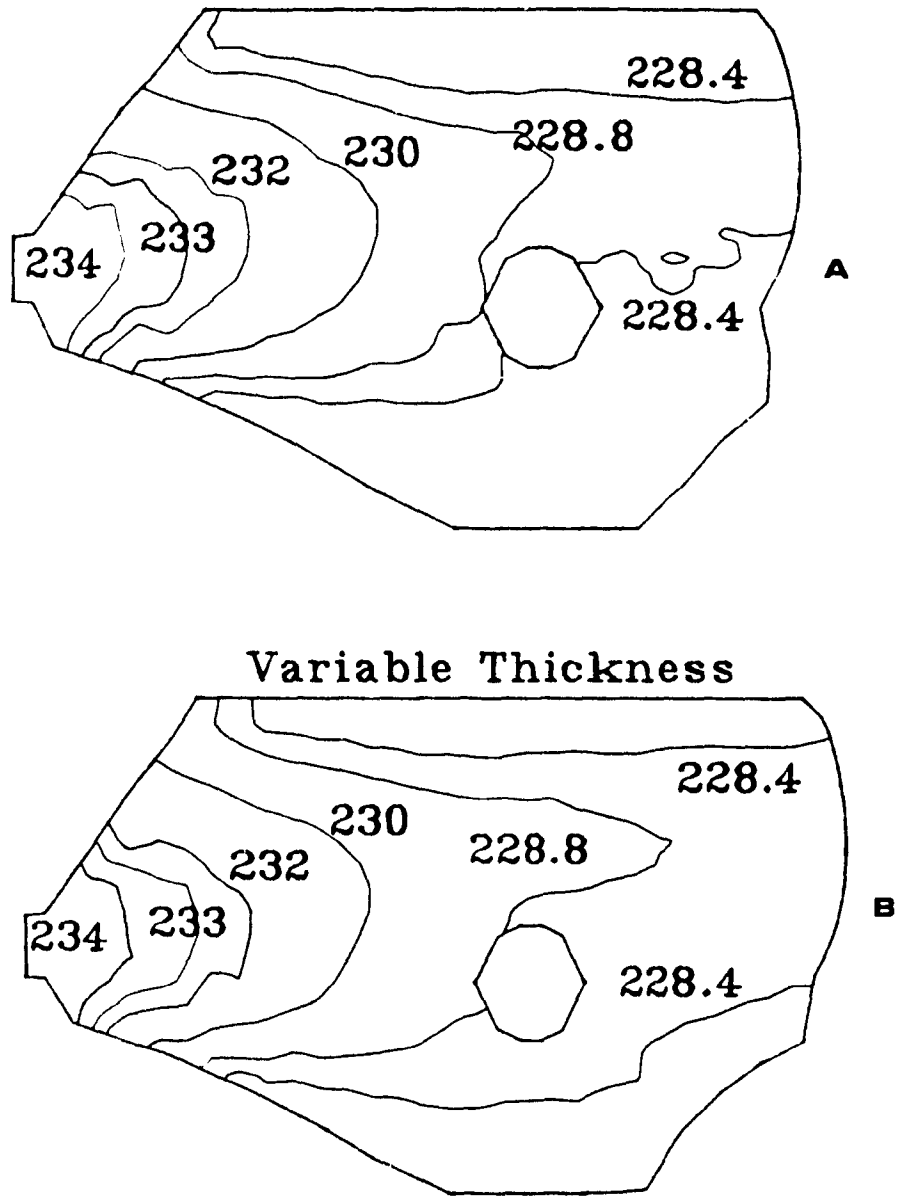


Figure (III.4.5.1): Spatial variation of temperature at an instant towards the end of filling ($t=1.6s$). Heat transfer Coefficient: $482 \text{ W/m}^2\text{K}$; Ram velocity 1.0 cm/s ; $T_{\text{mold}}=235^\circ \text{ C}$. Mold TE9(A) and CR1 (B).

Comparing parts (A) and (B) in Figure (III.4.5.1), it becomes clear that a variation in cavity thickness results in slightly higher melt temperatures at the corresponding part of the cavity.

Figure (III.4.5.2) gives the spatial variation of viscosity and rate of deformation (the second invariant (II) of the rate of deformation tensor is defined by equation III.40) in cavity CR1. Comparison with the corresponding Figure (A.5.7) in Appendix A.5 obtained for cavity TE9, it becomes clear that reduced thickness results in higher deformation rates and slightly reduced viscosities in this part of the cavity.

Figure (III.4.5.3) gives the shear stresses T_{xy} and T_{yz} in cavity CR1 for the same filling conditions. It can be seen by comparing with Figure (III.4.5.5.A) that the gap-averaged shear stresses in the thickness direction are substantially higher (about 10 times) than the XX -stress in the X - Y plane. Figure (III.4.5.4) shows the distribution of the longitudinal (U) and transverse (V) velocities in cavity TE9. This figure confirms that the geometrical configuration of this specific cavity results in faster melt flow in the upper part of the cavity; this is in agreement with the slightly higher temperatures predicted for that part. Finally, Figure (III.4.5.5) gives the xx -normal stress and the longitudinal velocity in cavity CR1. Reducing the thickness of the forward part of the cavity results in higher xx -stress and longitudinal velocities as compared to the constant thickness cavity TE9.

(III.4.6) Three-Dimensional Thermal Analysis

(III.4.6.1) Rectangular Cavity - Thermal Profiles

In this section, results regarding a three-dimensional solution of the energy equation (Equation (III.15)) during the computational analysis of the filling of a simple rectangular cavity of constant thickness are presented. From the coordinate transformation point of view, the curvilinear grid constructed on the x - y plane at each

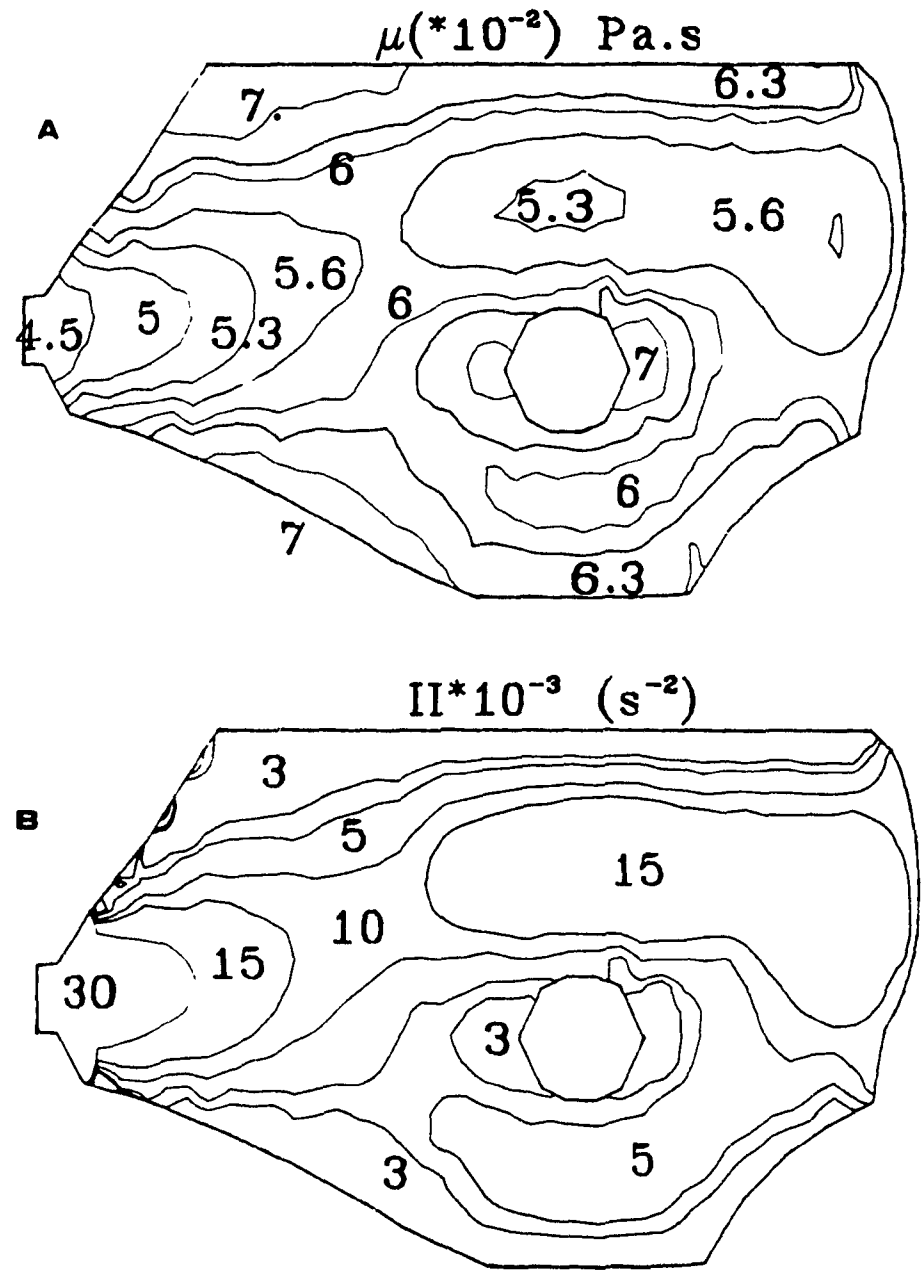


Figure (III.4.5.2): Spatial variation of viscosity (A) and rate of deformation (expressed by $\dot{\gamma}$, (B)) in cavity CR1. Heat transfer Coefficient: 482 W/m 2 K; Ram velocity 1.0 cm/s; $T_{melt} = 235^\circ$ C.

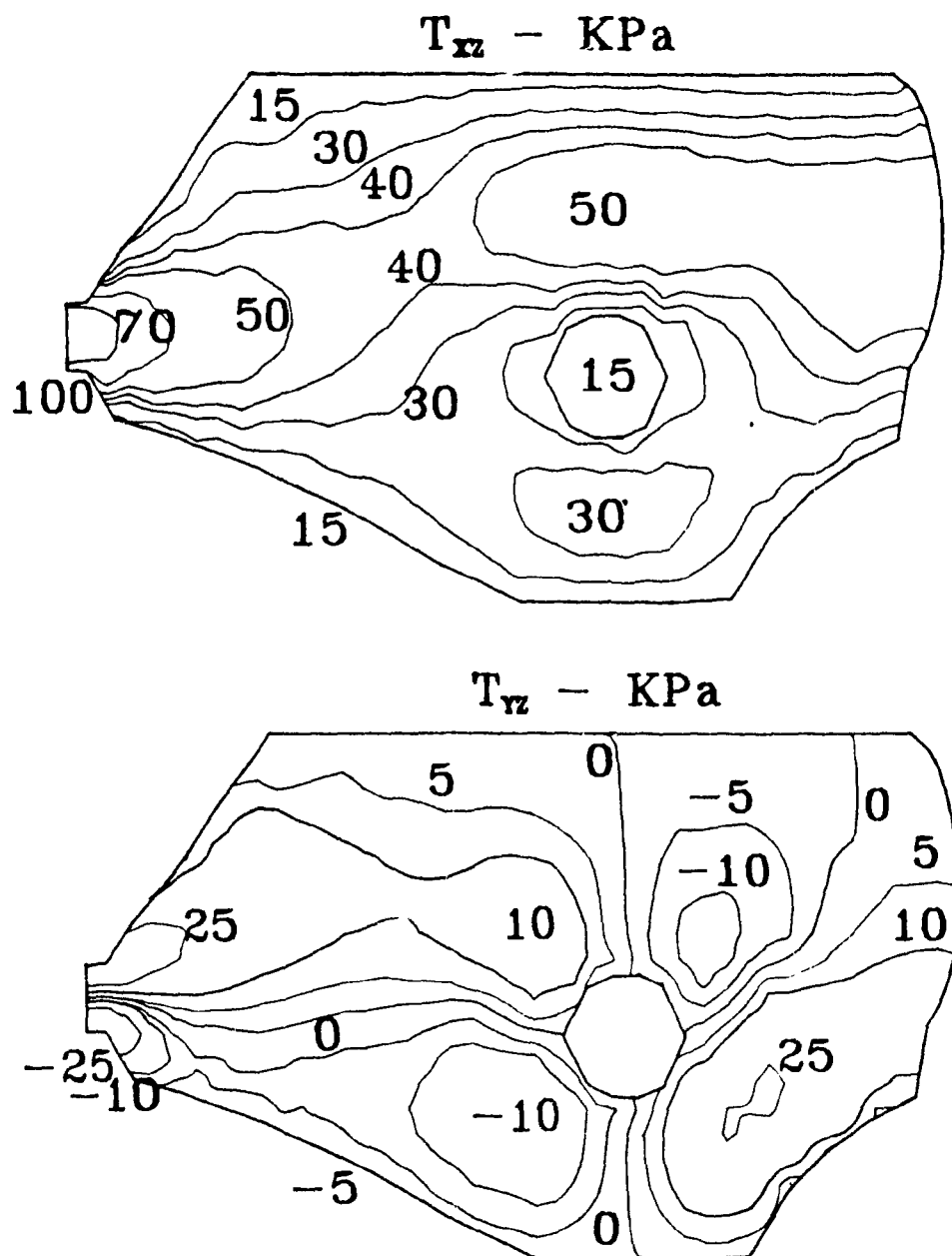


Figure (III.4.5.3): Predicted spatial variation of shear stresses in the thickness direction (T^x and T^y). Cavity CR1. Heat transfer Coefficient: $482 \text{ W/m}^2\text{K}$; Ram velocity 1.0 cm/s ; $T_{\text{in}} = 235^\circ \text{ C}$.

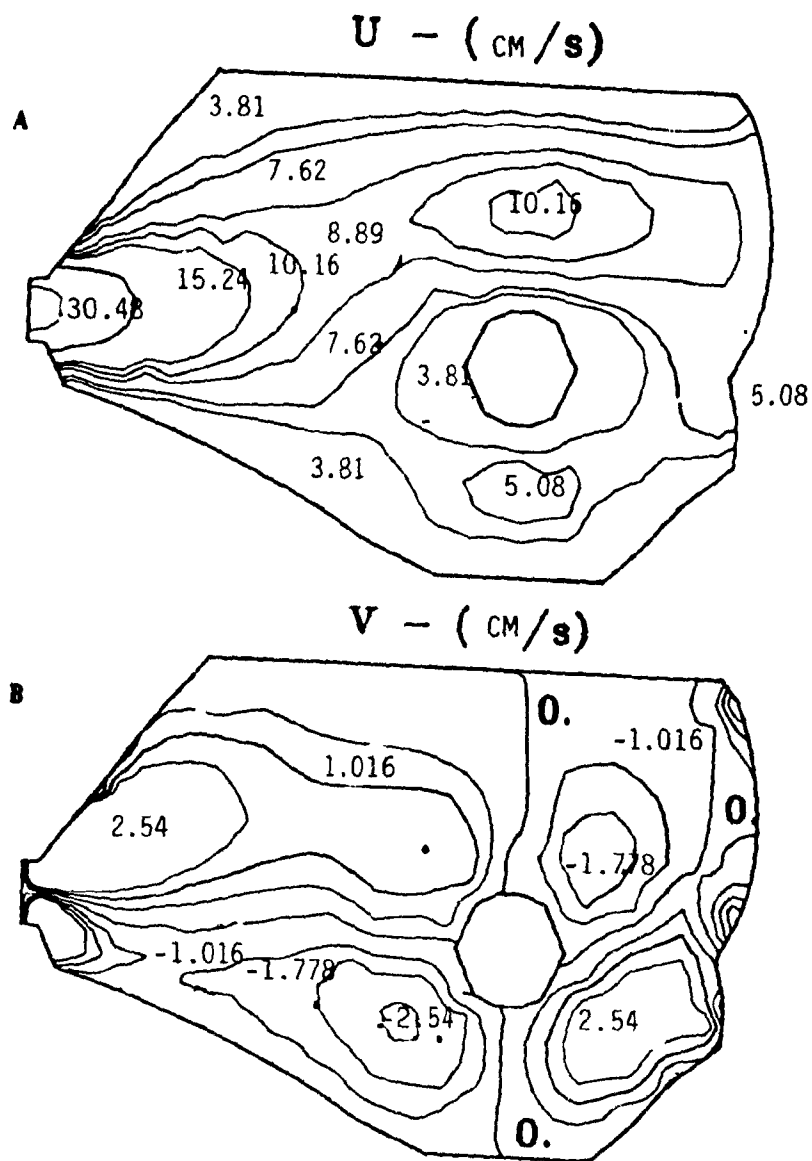


Figure (III.4.5.4): Predicted planar distribution of longitudinal (A) and transverse (B) velocities in cavity TE9. Heat transfer Coefficient: 482 W/m^2K ; Ram velocity 1.0 cm/s; $T_{\infty} = 235^{\circ}C$.

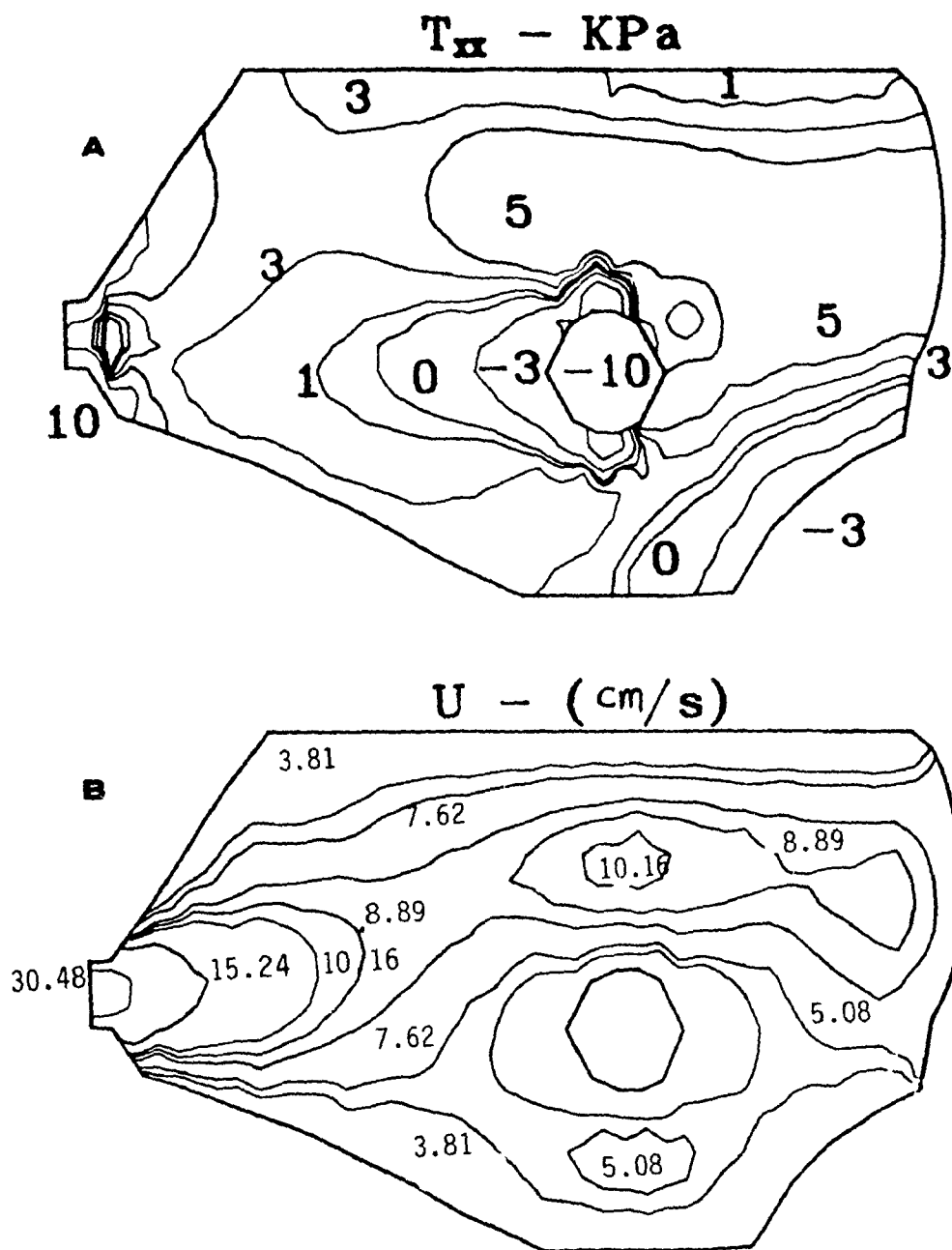


Figure (III.4.5.5): Predicted distribution of T_{xx} (A) and longitudinal velocity U (B) in cavity CR1. Heat transfer Coefficient: $482 \text{ W/m}^2\text{K}$; Ram velocity 1.0 cm/s ; $T_{\infty} = 235^\circ \text{C}$.

point during mold filling was expanded in the thickness direction so that the vertical cartesian coordinate (z) and the vertical curvilinear coordinate coincided. A $21 \times 21 \times 10$ grid was used, with 10 nodal points in the thickness direction. The temperature boundary condition at the faces of the mold was taken to be Equation (A.4.29), whereas the sides (edges) of the mold were considered adiabatic. The edges of the cavity, as points of melt/metal contact are also potential areas of heat exchange. However, in the particular mold used in the experimental part of this Thesis, the cooling channels run parallel to the faces of the mold, and this is the area where previous measurements of heat transfer coefficient have been made (Gao, (1989), Mutel, (1990)). The melt flow is also much slower in the vicinity of the perimeter of the cavity, as compared to more central locations. It was therefore decided that it is more realistic to treat the edges of the mold as adiabatic rather than assign to them the same heat transfer coefficient that was used for the rest of the cavity - or any other arbitrary value. This adiabatic condition along the edges of the cavity has also been used in the 2D simulations of the previous section. The lower temperatures usually occurring near the edges of the cavity are not due to cooling through the edges but mainly a result of the longer residence times of the melt in that region and the limited heat convection. The heat transfer coefficient was taken to be $284 \text{ W/m}^2\text{K}$. The ram velocity was constant during filling and equal to 1.0 cm/s , the cavity thickness 0.32 cm and the melt temperature at the gate was 235° C . Figures (III.4.6.1) and (III.4.6.2) show the spatial variation of temperature towards the end of filling at 4 planes parallel to the walls of the mold. The distance DZ in each figure indicates the distance from the wall. The lower part of Figure (III.4.6.2) corresponds to the centerplane of the cavity. Clearly, the strongest temperature gradients occur at the plane nearest to the wall. As the centerplane is approached, the cavity becomes more and more isothermal, with the most uniform temperature distribution at the centerplane (where the maximum temperature difference is about 1° C). Near the walls of the mold, the spatial variation of temperature is strongly non-uniform. The central part of the cavity is at higher temperature, due to heat supplied by the hot melt at the gate and the small thermal conductivity of the melt. These results show

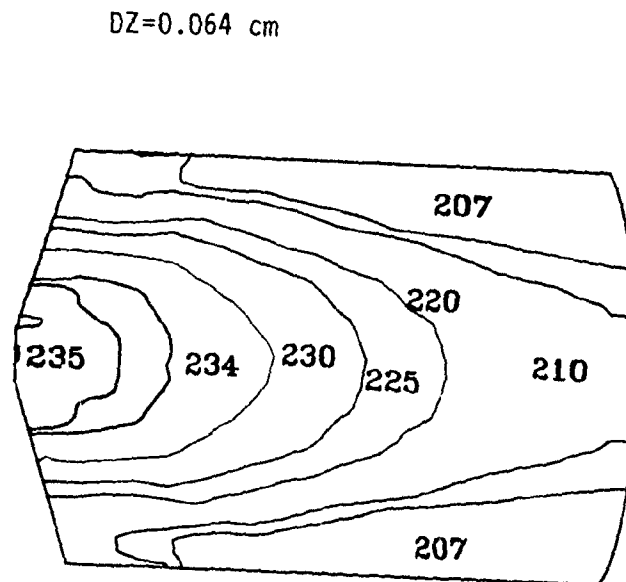
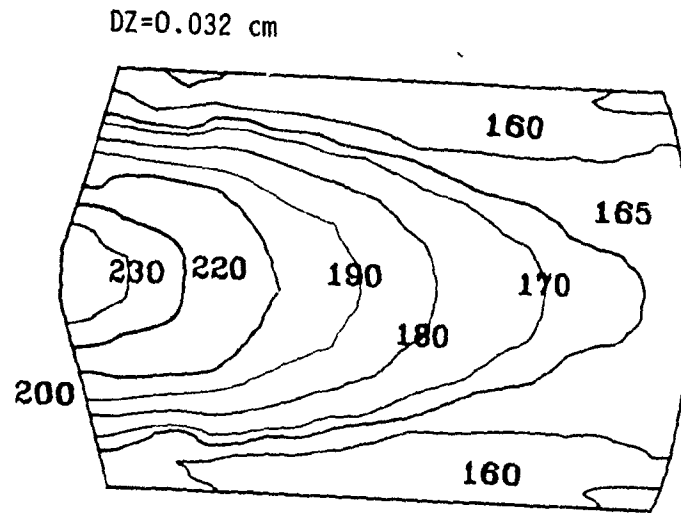


Figure (III.4.6.1): Predicted distribution of temperature at the end of filling of a rectangular cavity, at two planes in distance DZ from the wall of the mold.

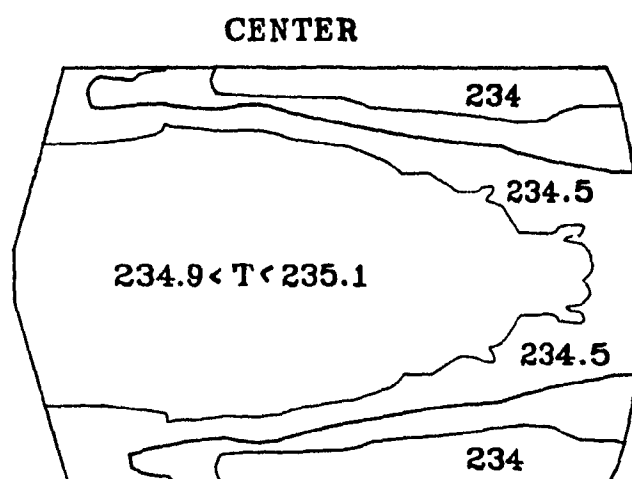
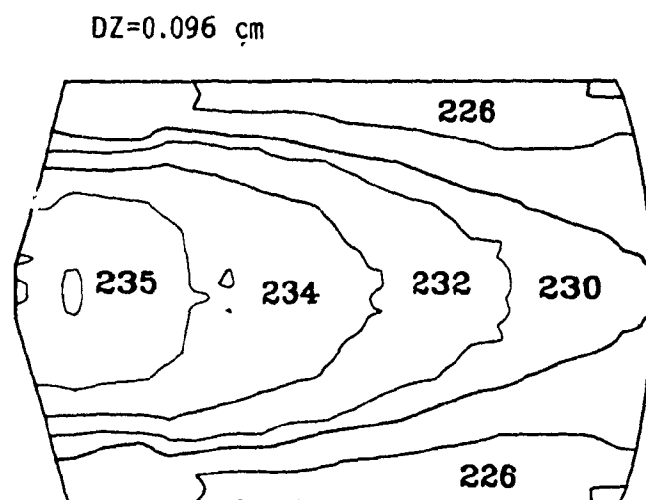


Figure (III.4.6.2): Predicted distribution of temperature at the end of filling of a rectangular cavity, at planes in distance $DZ=0.0378$ inches from the wall of the mold and along the centerplane of the mold.

that even in that simple geometrical configuration, a complete thermal analysis in both planar and thickness directions is essential for a meaningful understanding of the thermal history of the material during filling, including the formation and growth of a layer of solidified polymer at the cold mold walls. In the graphs of figures (III.4.6.1) and (III.4.6.2) the $y=0$ line is an axis of symmetry. Small discrepancies from that symmetry are due to the contour generation by the graphics package and reflect the irregular spacing of the grid points.

Figures (III.4.6.3) to (III.4.6.5) show the temperature profiles across the thickness of the cavity, along three grid lines starting from the gate and terminating at the free surface. Line $i=2$ is the one closest to the edge of the mold, whereas line $i=6$ is between the edge and the centerline (the notation is similar to that of section III.4.3.1). For the purpose of illustration, the thickness of the cavity has been multiplied by 10 in these figures. Again, the strongest thermal gradients occur along the line $i=2$ (nearest to the edge), while the centerline is characterized by higher temperatures. With reference to Figures (III.4.6.3) to (III.4.6.5), it can be concluded that at the end of filling, and with the conditions described above, no significant solidification has occurred.

(III.4.6.2): Complex Cavity - Microstructure Development During Filling

The three-dimensional thermal analysis outlined in the previous section allows for a detailed evaluation of the development of microstructure in crystalline (or semi-crystalline as is polyethylene) systems during filling. The relevant theory and in particular the analysis of non-isothermal crystallization in terms of data for isothermal crystallization has been developed by Nakamura et.al. (1973). On the assumption of isokinetic condition, the fundamental equation has the form:

$$x_r(t) = (1.0 - \exp(-(\int_0^t K(T) \cdot dt)^n)) \quad (\text{III.4.6.1})$$

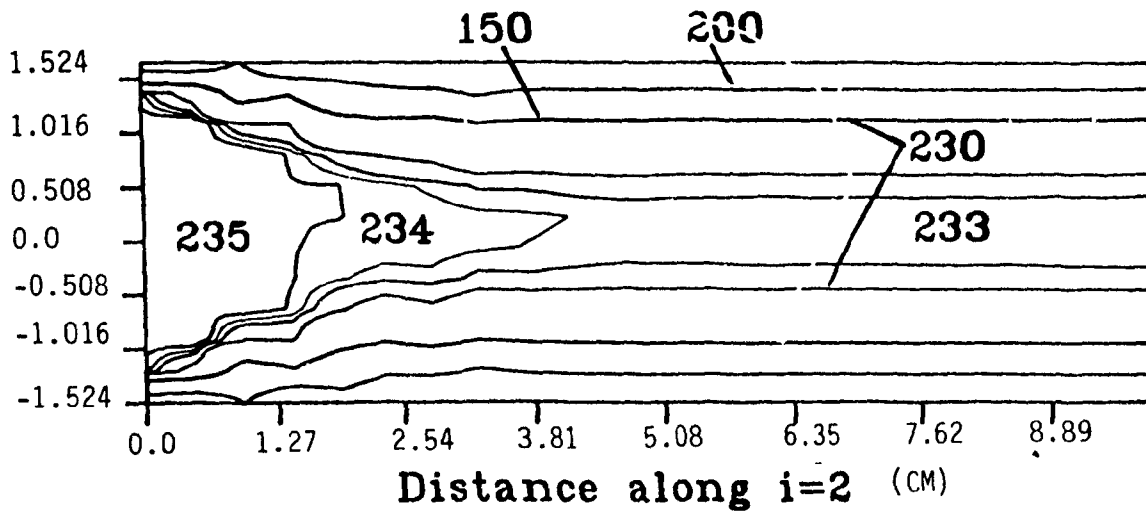


Figure (III.4.6.3): Gap-wise distribution of temperature at the end of filling of a rectangular cavity along the line $i=2$. The thickness of the cavity has been multiplied by 10 for the purpose of illustration.

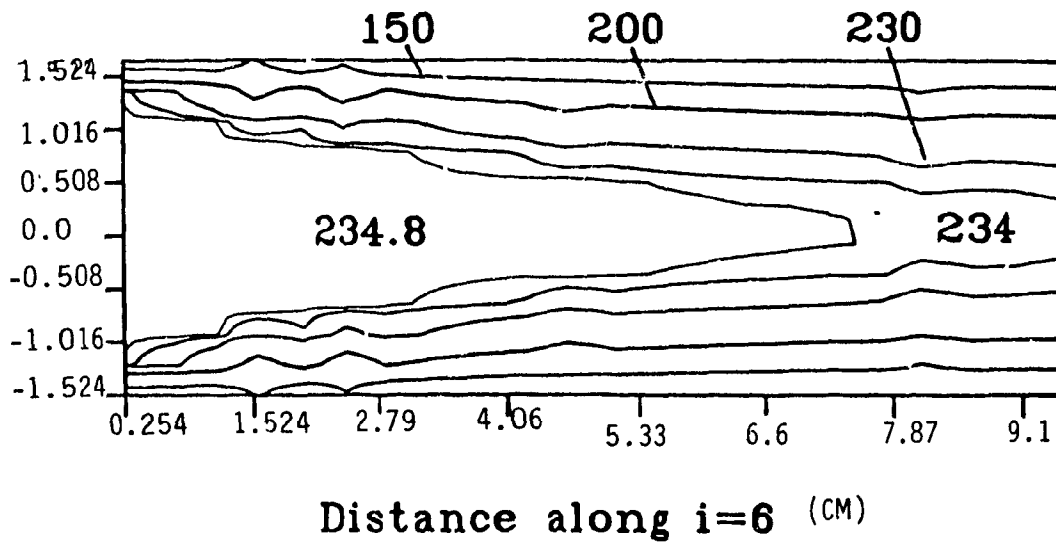


Figure (III.4.6.4): Gap-wise distribution of temperature at the end of filling of a rectangular cavity along the line $i=6$. The thickness of the cavity has been multiplied by 10 for the purpose of illustration.

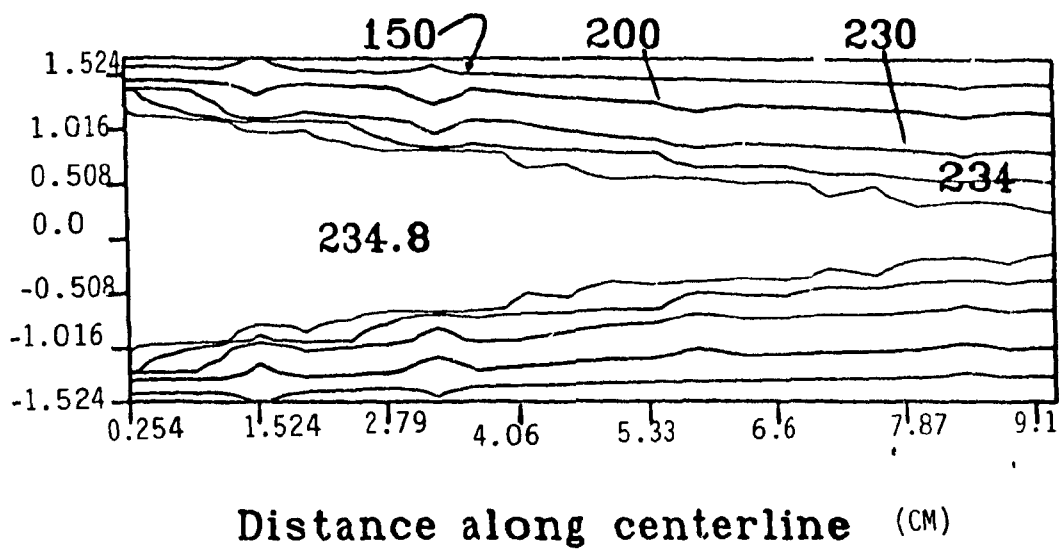


Figure (III.4.6.5): Gap-wise distribution of temperature at the end of filling of a rectangular cavity along the centerline. The thickness of the cavity has been multiplied by 10 for the purpose of illustration.

In the above equation, $x_r(t)$ is the relative degree of crystallinity at time (t), m is the Avrami exponent, and $K(T)$ is related to the isothermal crystallization rate constant ($k(T)$) through the relation $K(T)=(k(T))^{1/m}$.

Regarding the polyethylene used in this study, Lafleur (1983) has reported the following crystallization parameters:

Avrami exponent: $m=2$

Rate constant: $k(t)=\exp(-406.66+2.5981 \cdot T-0.004 \cdot T^2)$, T in K.

The fractional relative crystallinity ($x_r(t)$) is related to the ultimate crystallinity (x_{inf}) through the relationship $x_r(t)=x_c(t)/x_{inf}$. Lafleur (1983) also reports the following empirical relationship for the temperature dependence of x_{inf} , where it is assumed that no crystallinity develops above 121° C.

$$x_{inf}(\%) = A_0 + A_1 \cdot T + A_2 \cdot T^2, \quad T \text{ in C.}$$

with: $A_0=97.81$

For 80 C < T < 114 C

$$A_{-1}=-1.462$$

$$A_2=0.0100$$

and $A_0=2223.20$

For 114 C < T < 121 T

$$A_1=-34.274$$

$$A_2=0.13441$$

The Nakamura non-isothermal crystallization model was used for the calculation of crystallinity development during filling in a "slow filling" simulation run in cavity CR1. The conditions were of the slow filling corresponding to experiment HP7 (see next section). The heat transfer coefficient from the melt to the mold was taken as 538

W/m²K, higher than the experimental value of 356 W/m²K in an effort to produce some observable solidification during filling.

Figures (III.4.6.6) and (III.4.6.7) summarize some results of this simulation regarding the crystallinity development during filling and the associated three-dimensional thermal field. Figure (III.4.6.6) shows the crystallinity (x,y) on a surface that passes through the k=2 (immediately adjacent to the lower mold face) nodal points in the thickness direction. Since the thickness of this mold (CR1) is not constant, the points of figure (III.4.6.6) do not fall on the same physical plane (as is the case in figures (III.4.6.1) and (III.4.6.2)). These points define a "logical plane" with common index (k). The distance of these points from the mold walls is, naturally, smaller in the thinner sections of the cavity. At time 4.82s almost 20% of the cross-sectional area of the mold has been occupied by solidified material - with the exception of a small region near the gate. The crystallinity distribution within this solidified layer is largely uniform for the largest part of the mold, with two weak maxima in the middle section. Crystallization at the forward part of the cavity is favored by lower temperatures. In the mid-section however, longer residence times favor the development of crystallinity, whereas higher temperatures tend to slow it down. Overall, the interplay between these two opposing forces seems to favour the development of higher crystallinity in this section compared to the forward part of the cavity.

Figure (III.4.6.7) shows the temperature profiles along the "logical plane" k=2 and along the logical centerplane. Along the plane k=2 solidification is almost complete. However, the same simulation run confirmed that the solidified layer did not reach the plane k=3. Higher grid refinement in the thickness direction would be a way to capture in greater detail the development of crystallinity within the solidified layer during filling. Use of finer meshes however reached the limits of the computational capacity of the VAX 11/780 computer used in these simulations.

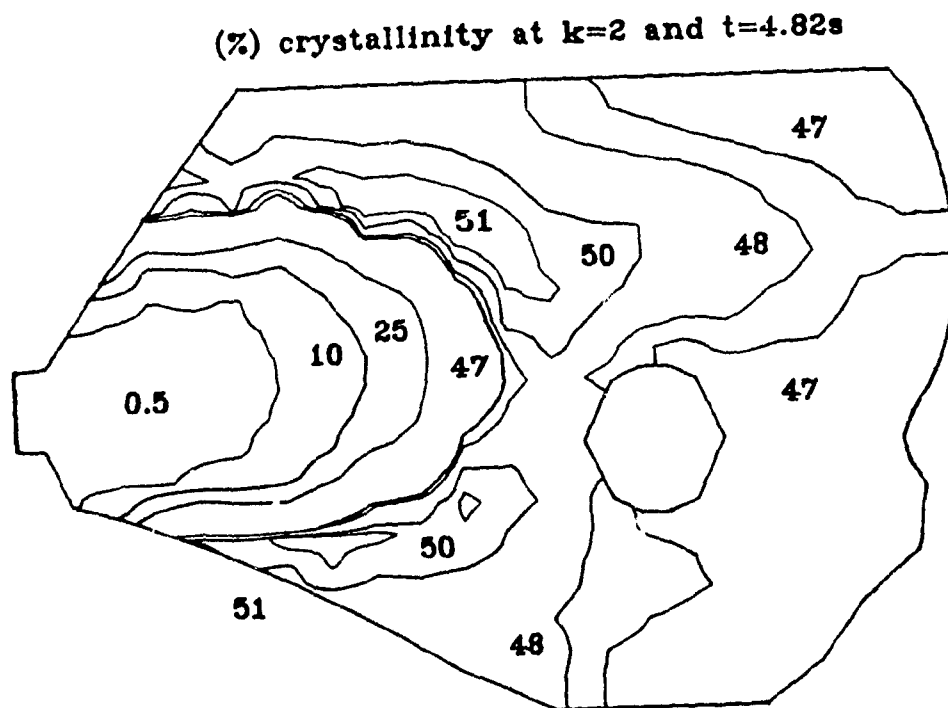


Figure (III.4.6.6): Crystallinity profile along the logical plane $k=2$ towards the end of filling of cavity CR1. Cooling rate based on $h=538 \text{ W/m}^2\text{K}$.

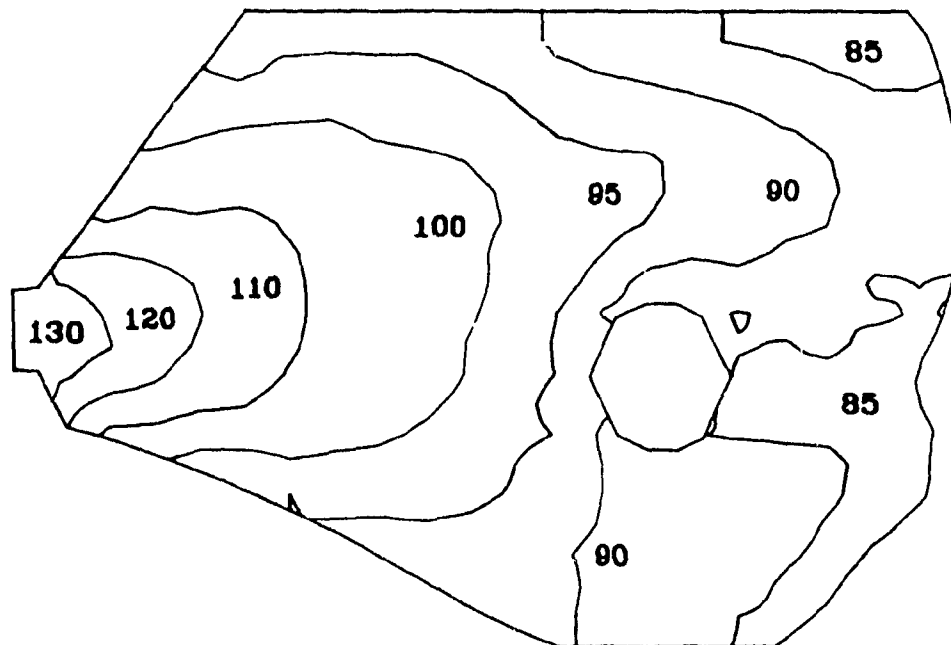
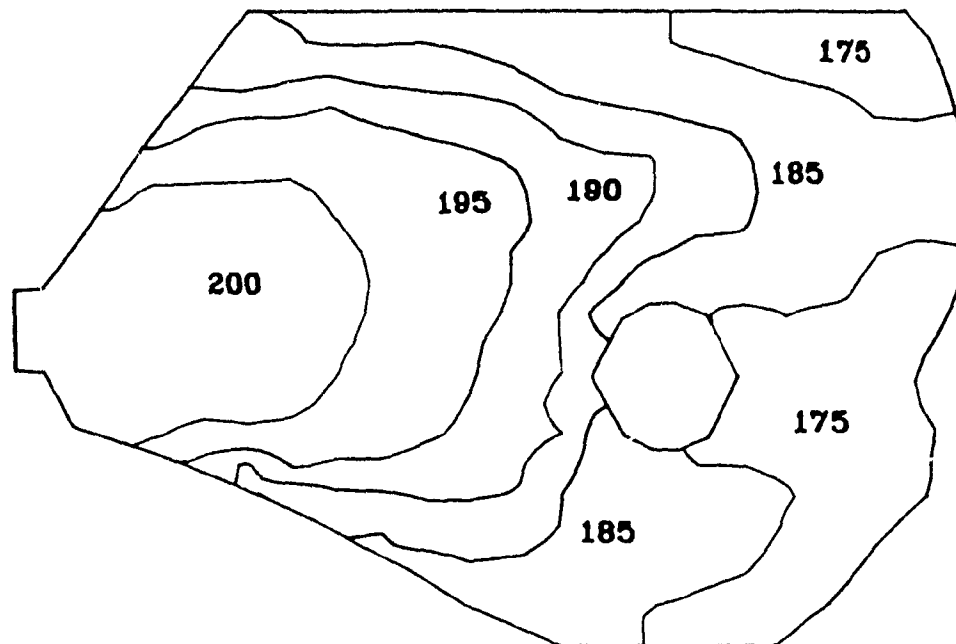
Temperature (C) at $k=2$ and $t=4.82s$ Temperature (C) at centerplane and $t=4.82s$ 

Figure (III.4.6.7): Temperature profiles along the logical plane $k=2$ and on the centerplane ($k=6$), towards the end of filling of cavity CR1. Cooling rate based on $h=538 \text{ W/m}^2\text{K}$.

(III.5) COMPARISONS OF MODEL PREDICTIONS WITH EXPERIMENTAL DATA

The purpose of this section is to compare experimental measurements collected during injection molding experiments of polyethylene Sclair 2908 (section (III.3.2)), carried out on the molding machine described in section (III.3.3) with predictions of the computer program. Data collected during each injection molding run supply information regarding the ram velocity (and indirectly the melt flowrate to the mold), the ram displacement (used along with the ram velocity measurement for validation of the corresponding data), the pressure and surface temperatures at a total of six locations in the cavity. The surface temperature data are used to monitor the advancement of the melt front in the cavity. The response of the pressure transducers can be used for the same purpose but with lower accuracy, given the large area of these transducers whose radius is 0.35cm. The pressure measurement at the gate and the pressure drop within the cavity are the primary data that will be compared to model predictions.

Figure (III.5.1) gives the experimentally measured ram velocity during experiment HP6. This was the entry condition supplied to the computer program. In all experiments, the ram velocity profile exhibits the characteristic shape of Figure (III.5.1). This is because the injection molding machine was operated at a constant hydraulic pressure mode. This resulted in ram speed decreasing as more material is injected into the cavity, since the resistance to the flow increases. Figure (III.5.2) is a comparison between experimental (solid line) and predicted (broken line) pressure variation at a location near the gate (the coordinates of that location are $(x,y)=(1.27\text{cm},0.0\text{cm})$, which coincides with the center of the pressure transducer). The melt temperature at the gate was 200° C.

Figure (III.5.3) is a comparison between predicted and experimental pressure drops

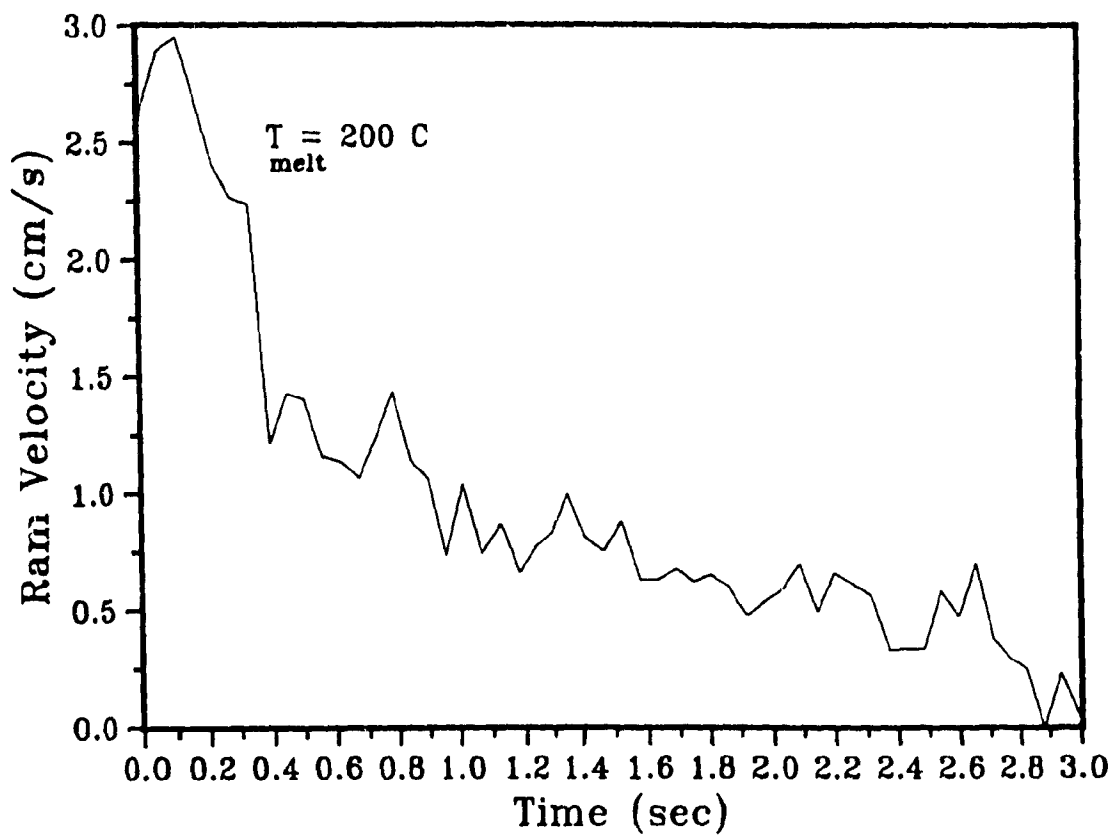


Figure (III.5.1): Experimental ram velocity profile during the filling stage corresponding to experiment HP6.

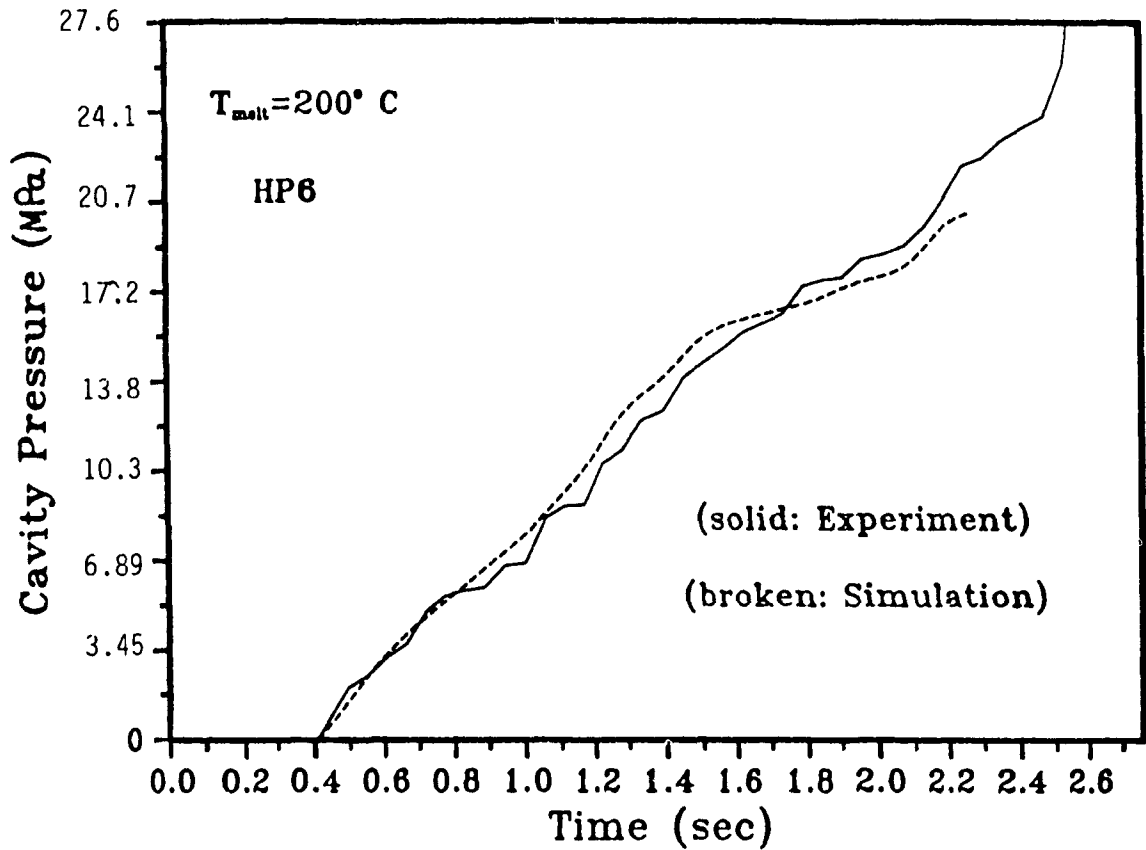


Figure (III.5.2): Comparison between experimental and computed pressure-time profiles. Experiment HP6.

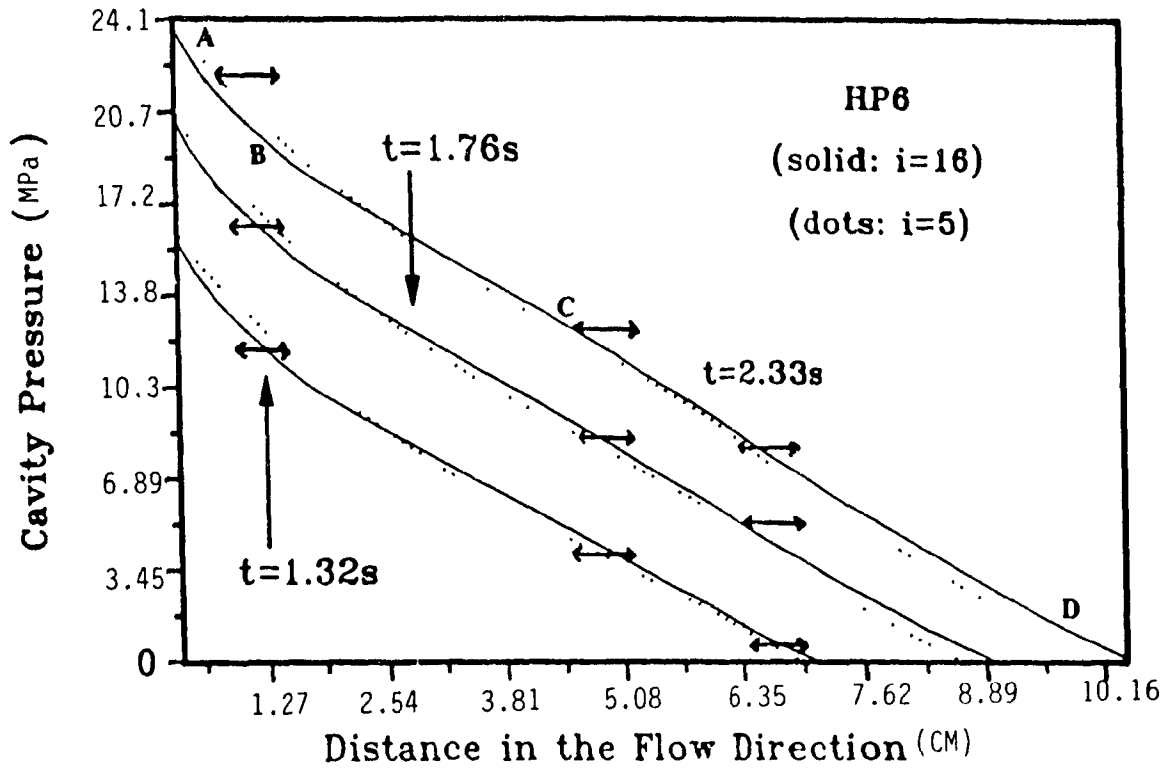


Figure (III.5.3): Comparison between computed (lines) and experimental (bars) pressure drops in the cavity. Experiment IIP6.

in the cavity at various instances during filling. Computationally, these profiles are obtained along the $i=5$ (lower part of the cavity) and $i=16$ (upper part of the cavity) grid lines (Figure (III.4.1.3.)). The horizontal bars in this graph show the corresponding experimental values. It can be concluded, along with Figure (III.5.2) that the agreement is quite satisfactory at all times. The program seems to underpredict the pressure towards the end of filling. The computed pressure drops deviate from the almost linear drops observed in a rectangular cavity of constant thickness (Lafleur, (1983)); this is due to a number of factors, most important of which are the change in the dimensions of the mold along the longitudinal direction and the non-isothermal nature of the flow. The pressure gradient is higher near the gate where the melt velocity is higher (section AB in Figure (III.5.3)). The local pressure gradient (DP/Dx) in the part corresponding to the section of the cavity prior to the area of reduced thickness (BC) is significantly lower. The area corresponding to the thinner part of the cavity (CD) is characterized by a larger local pressure gradient compared to BC but smaller than the pressure gradient near the gate; this can be explained if one considers the smaller melt velocities in the forward part of the cavity.

Figure (III.5.4) shows the temperature profiles along the same coordinates lines as in Figure (III.5.3) and for the conditions of experiment HP6. These are gap-averaged temperatures. The melt enters the cavity at 200° C. In Figure (III.5.4) the three dotted curves correspond to the coordinate line $i=5$, whereas the three solid curves to $i=16$. Several observations can be made with regard to Figure (III.5.4). Firstly, at any location along the lines $i=5$ and $i=16$ (as well as throughout the cavity), the material is cooled with time. This can be seen by observing the relative position of the curves corresponding to $t=1.32s$, $t=1.76s$ and $t=2.33s$. This effect is more pronounced for points away from the gate, since the area near the gate is continuously fed with new hot material. In a small region around the gate, the melt temperature is practically uniform in both the upper ($i=16$) and lower ($i=5$) parts of the cavity. After $0.15'$ ($1'=2.54cm$) from the gate however, the lower part of the

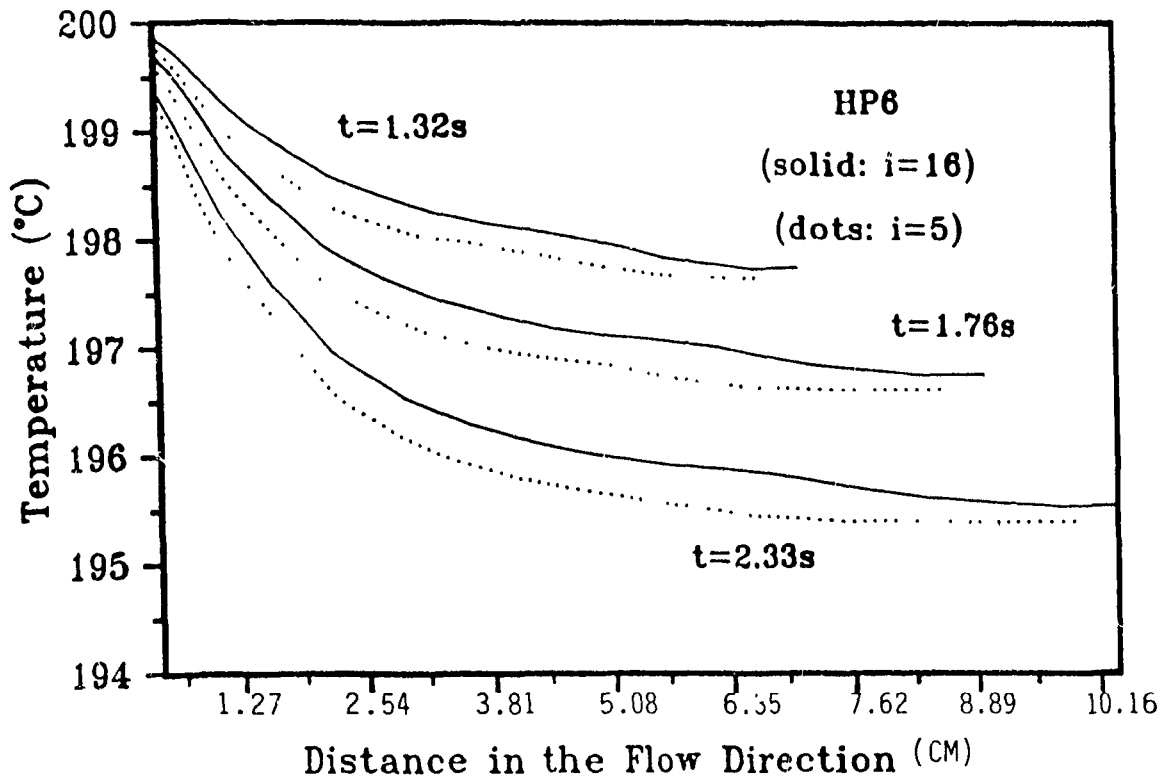


Figure (III.5.4): Computed temperature drops in the cavity CR1 for conditions corresponding to those of experiment HP6.

cavity becomes progressively cooler than the upper part. This can be further seen in Figure (III.4.5.1) which shows contours of temperature at various instances during filling. Simulation has revealed that in this particular cavity and towards the end of filling, the material flows faster in the upper part. Viscous heating is therefore stronger there and residence times are shorter. This, together with the supply of more fresh hot melt compared to the lower part, accounts for the higher temperatures in the upper half of the cavity. These temperature differentials could be minimized by proper design of the cooling system of the mold. Also note in Figure (III.5.4) that near the melt front the temperature differential between the upper and lower part of the cavity decreases.

Table (III.5.2) is a comparison between predicted and measured times at which the melt front reaches each transducer in the cavity, for experiments HP6, HP7, HP8 and HP9. It can be seen that the agreement is quite satisfactory. Such a good agreement is not surprising here, since the experimental melt flowrate is used as the inlet condition in the simulations. However, this agreement confirms that the ram velocity (or displacement) is a good measure of the melt flowrate in the mold (or, equivalently, that compressibility effects in the nozzle are not significantly degrading the quality of that measurement). Furthermore, this good agreement proves that the frequent rearrangement of the free surface nodal points for smooth grid generation purposes (see Appendix A4) does not contaminate the accuracy of the movement of the free surface.

Figure (III.5.5) shows the ram velocities corresponding to experiments HP8 and HP9. Experiment HP9 is a "fast" filling whereas HP8 is a slower filling. The melt temperature in both these runs is 235° C. Figure (III.5.6) gives a comparison between predicted and experimental pressure variations at the gate for these runs. The agreement is fairly good for both cases in the initial and intermediate stages of filling but becomes progressively worse towards the end of filling. The divergence between predictions and experimental data at the last stages of filling is smaller in the faster

	T1	T2	T3	
HP6	0.48	1.33	2.31	Experiment
	0.48	1.32	2.27	Predicted
	-	0.75	1.73	(%) Difference
HP7	0.78	2.99	5.23	Experiment
	0.77	2.94	5.18	Predicted
	1.28	1.67	2.87	(%) Difference
HP8	0.81	2.62	2.35	Experiment
	0.81	2.61	2.32	Predicted
	0.00	0.38	1.28	(%) Difference
HP9	0.37	0.92	1.65	Experiment
	0.37	0.91	1.62	Predicted
	0.00	1.08	1.82	(%) Difference

Table (III.5.2): Comparison between predicted and experimental times required for the melt front to reach the temperature transducers T1, T2 and T3 in cavity CR1.

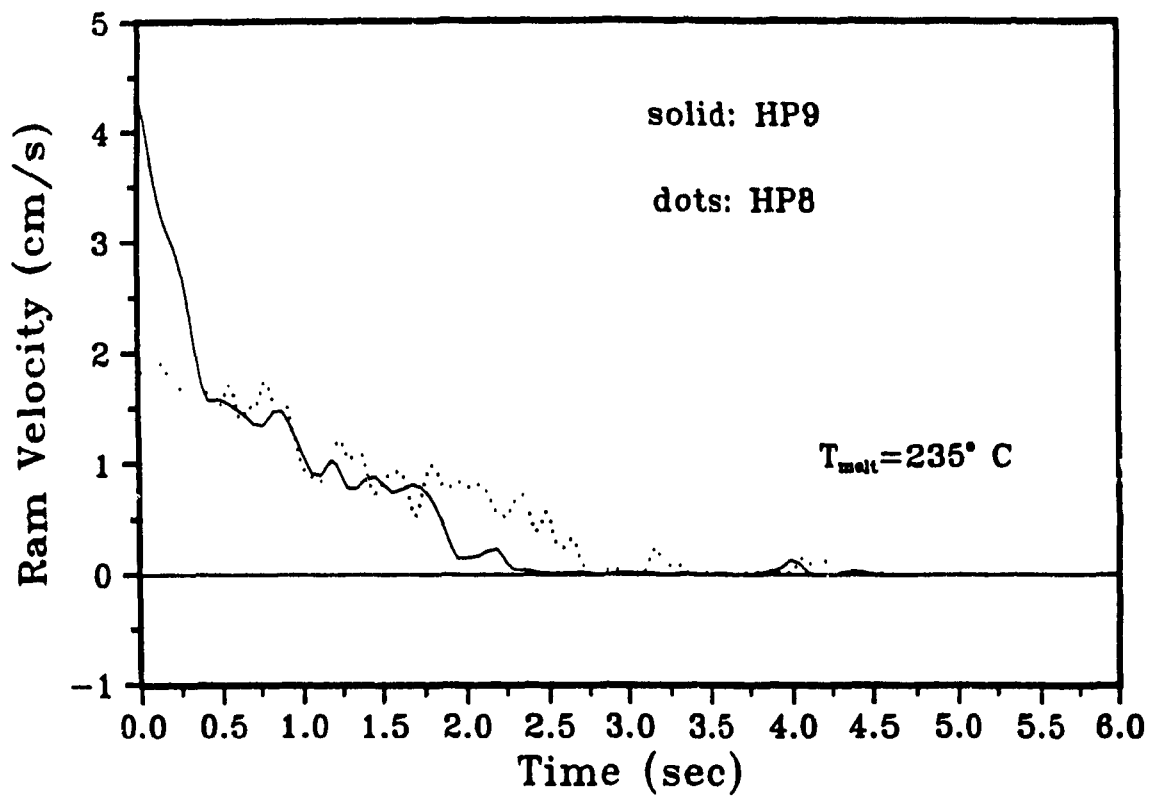


Figure (III.5.5): Experimental ram velocity profile during the filling stage corresponding to experiments HP8 and HP9.

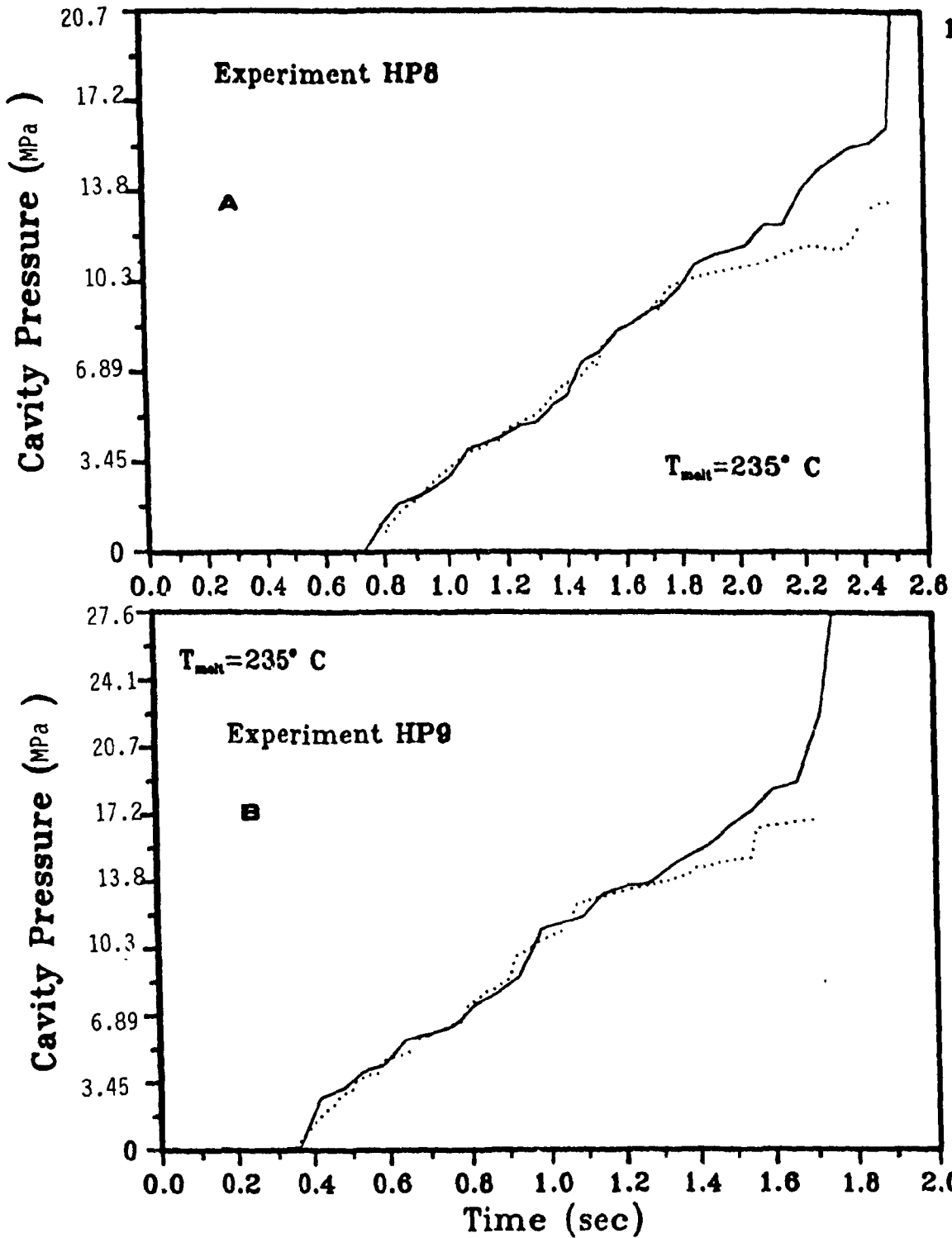


Figure (III.5.6): Comparison between experimental (solid) and computed (dotted lines) pressure-time profiles. (A): Experiment HP8; (B): Experiment HP9.

filling case HP9. This might be due to the smaller solidification associated with shorter filling times. The pressure drops along the cavity at various instances during filling are further shown in Figure (III.5.7). The corresponding temperature profiles are given in Figure (III.5.8). There is a small but interesting qualitative difference in the temperature profiles of Figures (III.5.8.A and (III.5.8.B). The temperature corresponding to the faster run HP9 seems to show a little overshoot at intermediate locations within the cavity; this behaviour is absent from the profiles corresponding to the case HP8. Since all conditions between these experiments are the same but the filling time (or melt flowrate), it is concluded that this is a viscous heating effect. Figure (III.5.9) shows predicted (dotted) and measured (solid lines) pressures at the locations of the three pressure transducers in the cavity. These results correspond to run HP9. Again the agreement is quite satisfactory, especially for the second and third transducers.

Finally, Figures (III.5.10) to (III.5.13) give experimental and simulation results regarding the experiment HP7 which was performed at a very low melt flowrate. The agreement between theory and experiment becomes rather bad towards the end of filling. Upon inspection of Figure (III.5.13), it becomes clear that the gap averaged temperature in the cavity towards the end of filling is relatively low. It was thought that there could be a significant amount of solidification in this experiment which had not been taken into account in the two-dimensional simulation. However, simulations using a three-dimensional thermal analysis code that would take into account the reduction of cross-sectional area of the mold due to solidification, based on a heat transfer coefficient of 68 Btu/ft²/hr/F (386 W/m²K) uniform throughout both faces of the mold, showed that there was no significant solidification - that could be resolved with grids having 10 grid points in the thickness direction. Use of linear temperature interpolations between the mold walls and the adjacent grid points was used to determine, approximately, the thickness of the solidified layer and the consequent reduction in cross-sectional area. This approach resulted in a pressure profile that deviated only slightly from that of a two-dimensional simulation (Figure (III.5.11)).

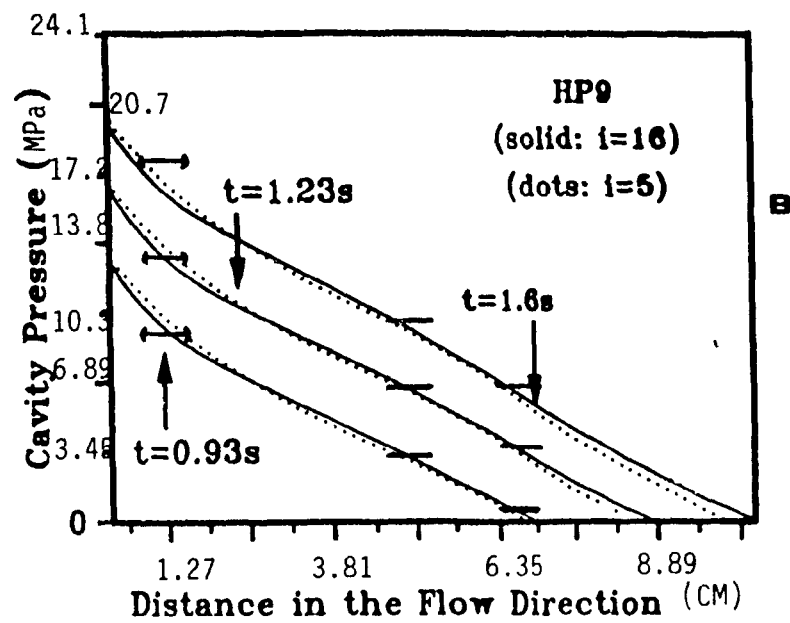
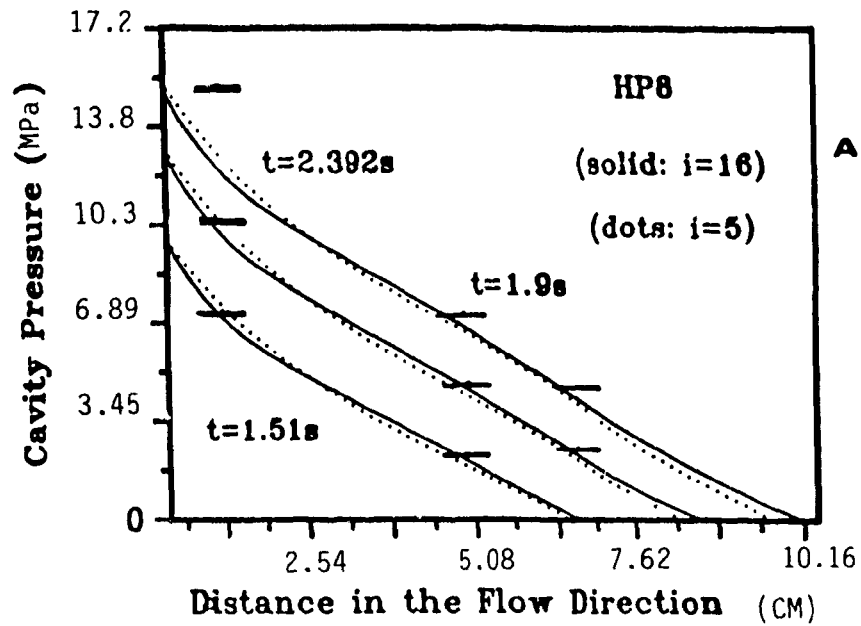


Figure (III.5.7): Comparison between computed (lines) and experimental (bars) pressure drops in the cavity. (A): Experiment HP8; (B): Experiment HP9.

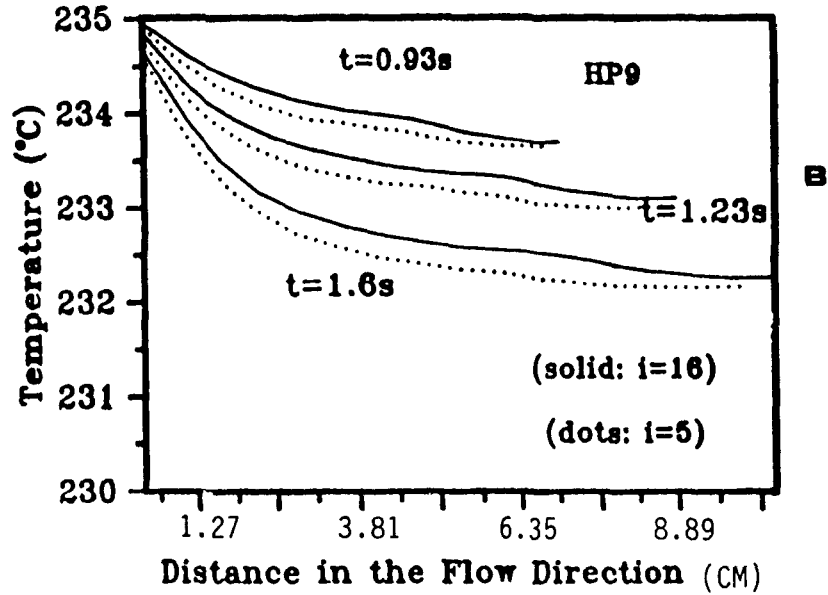
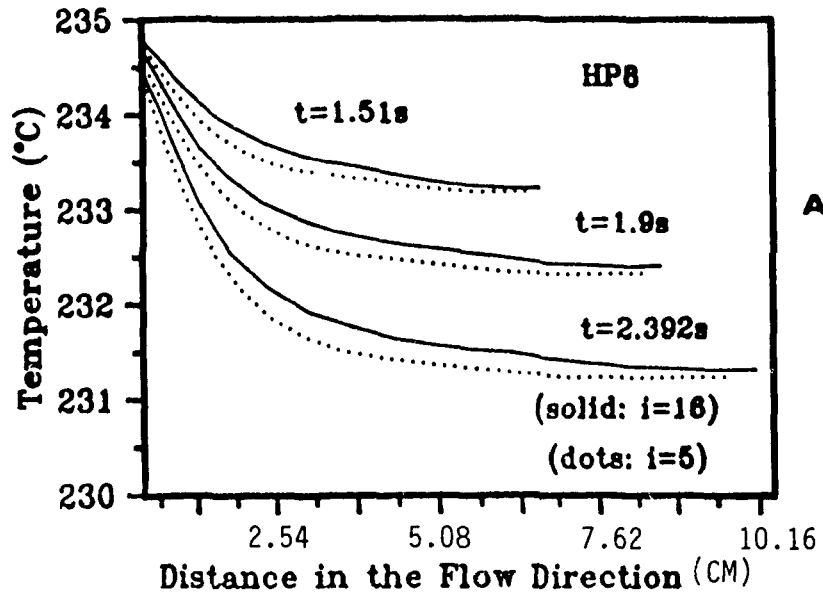


Figure (III.5.8): Computed temperature drops in the cavity CR1 for conditions corresponding to those of (A): Experiment HP8; (B): Experiment HP9.

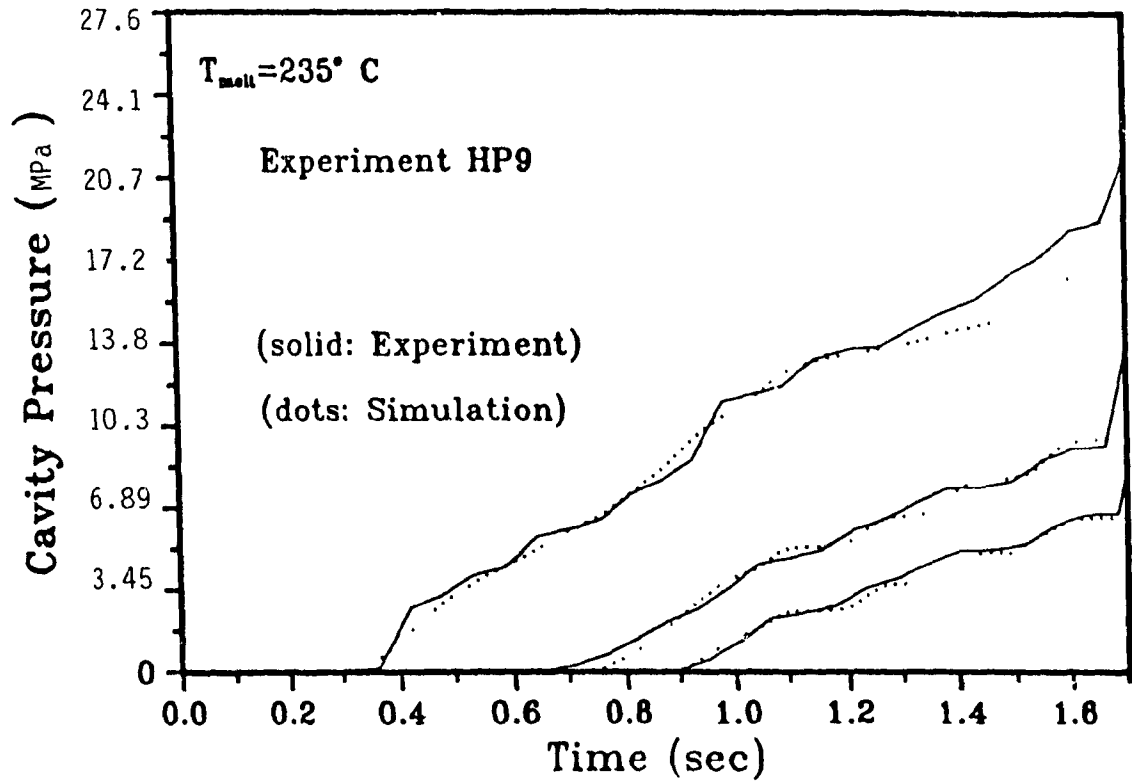


Figure (III.5.9): Comparison between computed and experimental pressure-time profiles at the locations of the three pressure transducers in cavity CR1. Experiment HP9.

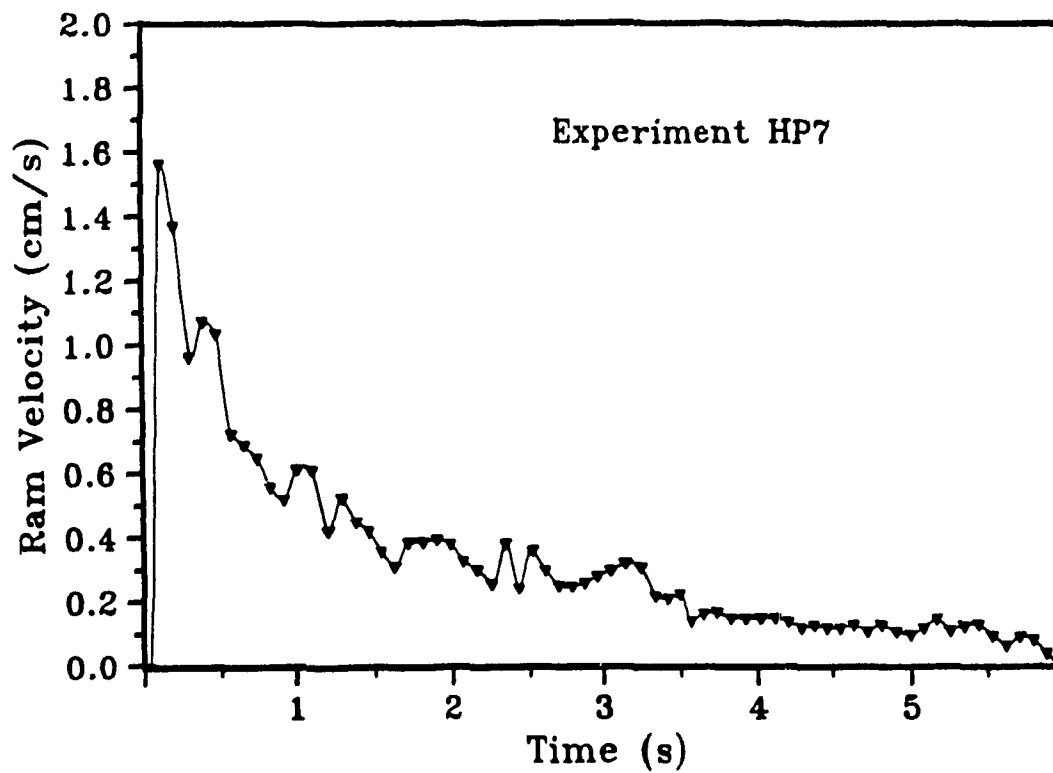


Figure (III.5.10): Experimental ram velocity profile during the filling stage corresponding to experiment HP7.

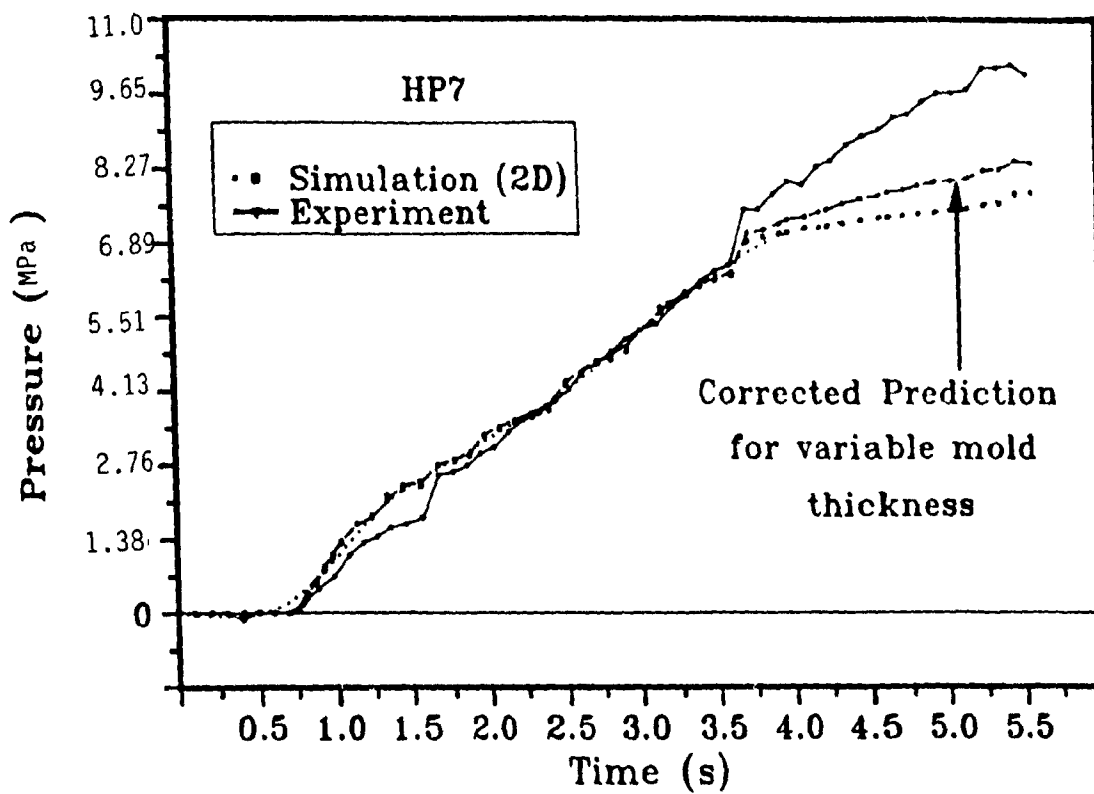


Figure (III.5.11): Comparison between experimental and computed pressure-time profiles. Experiment HP7.

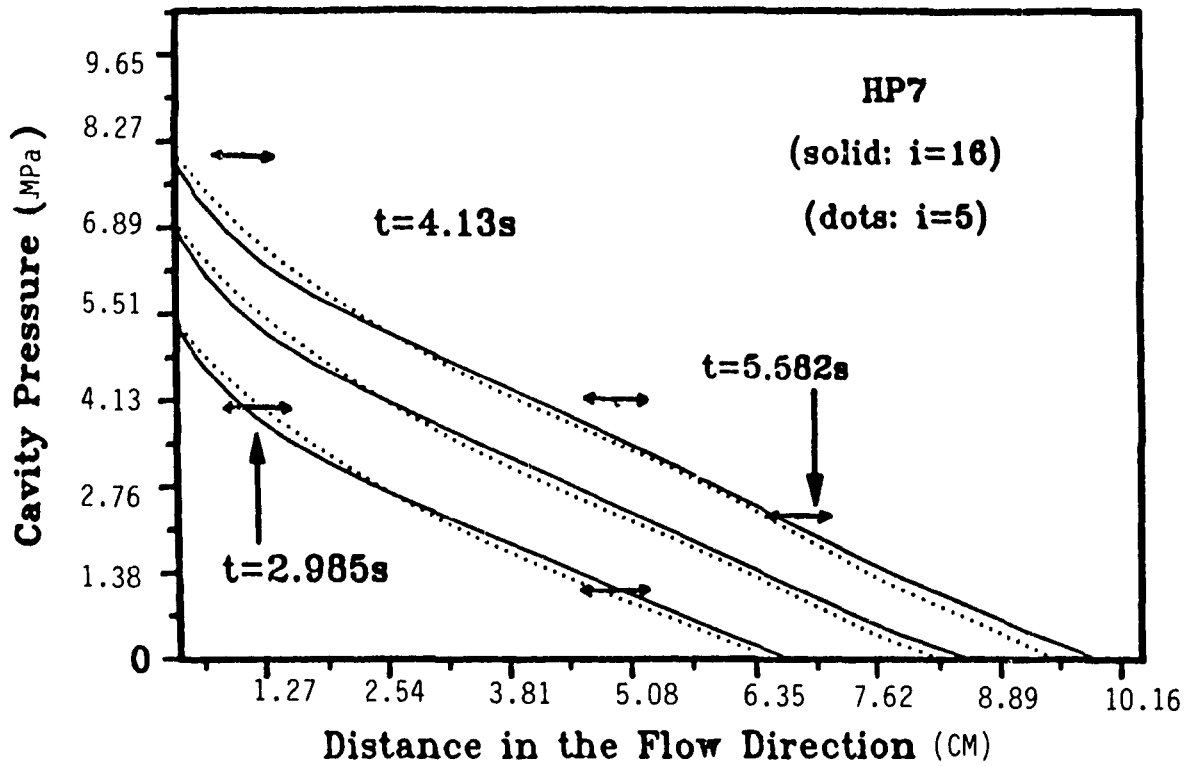


Figure (III.5.12): Comparison between computed(lines) and experimental(bars) pressure drops in the cavity. Experiment HP7.

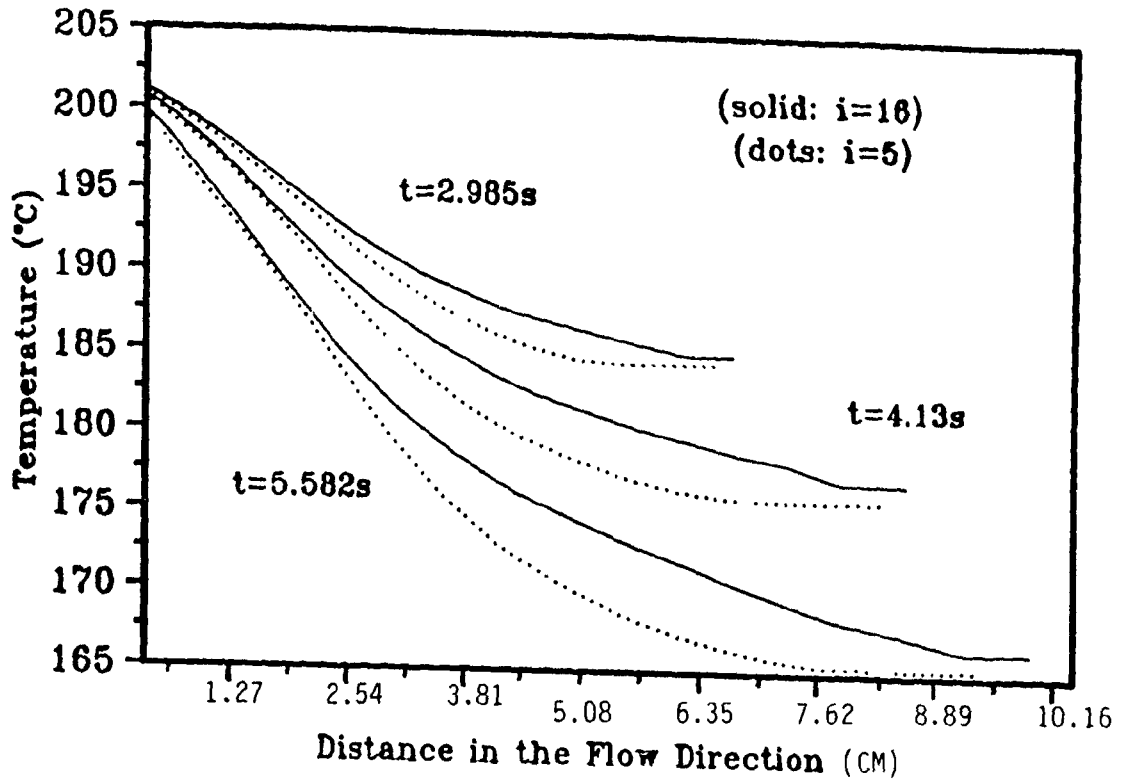


Figure (III.5.13): Computed temperature drops in the cavity CR1 for conditions corresponding to those of experiment HP7.

This points to the direction of reexamining in detail the heat transfer in the mold and in particular the possibility of strong spatial variation of cooling rate along the faces of the mold. More experimental work is needed in this direction.

(III.6) SUMMARY

A model for the simulation of the filling stage in injection molding has been developed. The model considers viscoelastic, non-isothermal, transient flow with an advancing free surface in a cavity of complex shape with an insert. The location of the melt front is determined in the course of the computations; following that, the computer program automatically generates suitable curvilinear computational meshes in the region of the cavity covered by the melt. Based on the above model, parametric studies were performed, which revealed the effects of key process characteristics such as melt flowrate, melt temperature, material properties and mold geometry on the pressure and temperature gradients in the cavity, as well as on the pressure history near the gate. The spatial distribution of velocities, stresses and temperatures was also evaluated at various instances during filling and various geometrical configurations. A three-dimensional analysis of the thermal problem during filling, coupled with two-dimensional kinematics in a rectangular and in a complex shaped cavity, resulted in a detailed description of the temperature field, which is of considerable complexity even in geometrically simple situations. Coupling of the Nakamura non-isothermal crystallization kinetics model allowed for a calculation of the crystallinity development within the solidified polymer layer during filling.

Predictions of the model have been compared to experimental data obtained during the injection molding of high density polyethylene, whose complete rheological characterization was performed, in a cavity of complex shape. The model predicts reasonably well the experimentally measured pressure-time profiles at three locations in the cavity, as well as the progression of the melt front. The model predictions

deviate the most from the experimental data towards the end of filling and for experiments with long filling times; consideration of the reduction in mold cross-sectional area during filling did not improve substantially the predictions of the program. A possible reason for this discrepancy might be inaccuracies in the calculated melt flowrate at the gate toward the end of filling due to noise in the ram velocity signal as well as poorly defined thermal conditions along the mold walls.

(IV) CONCLUSION

(IV.1) Conclusions

This Thesis has presented a finite difference numerical simulation of viscoelastic flows in complex geometries. A number of steady state flows of an upper convected Maxwell fluid have been studied numerically; this study has revealed the effect of elasticity, inertia and geometry on the structure of the stress and flow fields. Vortex growth with elasticity has been predicted in contractions; grid refinement studies have shown that this growth is independent of the size of the computational grid, depending strongly on the geometrical configuration of the channel. In expanding flows, the elasticity of the fluid is found to reduce the size and strength of the secondary flow.

The same numerical techniques with geometry-adaptive remeshing have been used for the simulation of the filling stage of the injection molding process. Non-isothermality, shear thinning viscoelastic behaviour and the presence of an advancing free surface of complex shape are issues that have also been dealt with in this part. In the two-dimensional version, the numerical scheme solves the conservation and constitutive laws on the plane of the flow; however, velocity, thermal and stress gradients in the thickness direction are included in the analysis in a gap-averaged sense. This has allowed for consideration of both planar and gap-averaged stresses in the development of the pressure in the cavity, and, for the first time, for a comparison between the magnitude of planar and gap-averaged stresses in a geometrically complex situation. The latter are predicted to be about ten times larger than the planar stresses - for the cavity and the filling conditions studied.

A completely three-dimensional solution of the energy equation, coupled with the Nakamura model for non-isothermal crystallization kinetics, two-dimensional

kinematics and stresses, has been performed in a rectangular and in a complex-shaped cavity. This analysis allowed for a detailed description of the thermal conditions in the cavity, as well as for the development of microstructure during filling - the later for very slow injections with relatively high cooling rates. The results of the 3D simulation showed that thermal fields can be considerably complex even in a cavity of a simple shape. In the case of the rectangular cavity, this means that treatment of the filling stage as a flow problem between two infinite flat plates is representative of only a small part of the real process. In this sense, the present work on injection molding can be seen as fusing together and expanding the best characteristics of previous research done at the Polymer Processing Group at McGill, and in particular the work of Kuo and Kamal (1976), which modelled the spreading flow in a rectangular cavity using non-isothermal potential flow theory, and the work of Lafleur and Kamal (1983) which modelled in detail the flow of a viscoelastic melt between two infinite flat plates. Furthermore, the use of boundary fitted curvilinear coordinates has allowed for the modelling of the filling stage in a complex cavity which includes an insert; this adds a new dimension in the modelling capabilities of the Group.

Model predictions have been compared to experimental measurements obtained in an injection molding machine. Melt front progression data and pressure data were in reasonably good agreement with model predictions. The material used was an injection molding grade polyethylene; its rheological characterization has been part of this work.

(IV.2) Recommendations

Based on the experience gained during this study, the following recommendations for future work can be made:

- (1) The three-dimensional model produced in this work can be used in

conjunction with existing models for the packing and cooling stages. This way three-dimensional distributions of crystallinity in the final product, thermal stresses and pressure variation during the complete injection molding cycle can be determined.

- (2) Extend the stress calculation in three-dimensions. At a first stage, this can be accomplished by considering fully developed inelastic (power-law) velocity profiles across the gap, therefore ignoring the fountain flow effect. Consideration of completely three-dimensional kinematics in the context of the stream function / vorticity formulation is tedious; it might be advisable to use the velocity/pressure formulation in a three-dimensional simulation.
- (3) Improve the efficiency of the pressure SOR solver by considering techniques such as the method of conjugate gradients.
- (4) Consider alternative viscoelastic models, particularly models that include a retardation time, since their use might improve the stability of the stress iterative solver. Their prediction should however be compared to experimental data in simple flow situations before any effort is made to incorporate them in the model.
- (5) Enhance the physical description of the process by considering stick-slip flow on the mold wall, particularly near points of high stress concentrations. The effect of shear and elongational stresses as well as the effect of pressure on the crystallization kinetics of polyethylene could also be tested experimentally and incorporated in the model. The rheological description of the resin could further be enhanced by considering a spectrum of relaxation times.
- (6) The present model can be modified to include the delivery channels in the analysis. This can be done by changing the flow field so as to include the

delivery channels (which can be of arbitrary planar shape, but not of an axisymmetric shape; in the later case modifications in the core routines will be needed). This is expected to improve considerably the quality of the model predictions, since the nozzle pressure can be used instead of the melt flowrate as a boundary condition.

- (7) At the experimental level, investigate the spatial distribution of the heat transfer coefficient along the faces of the mold. Incorporation of spatially variable cooling might improve the quality of the model predictions, particularly in situations with long filling times.

(IV.3) Novel Contributions

- (1) Part (II) of this work presents the first application of the method of boundary fitted curvilinear coordinates for the finite difference simulation of viscoelastic flows in complex geometries. All previous work in complex geometries has been done in the context of finite elements, with finite difference solutions confined to geometrically simple situations.
- (2) The QUICK upwinding scheme has not been previously used in the modelling of viscoelastic flows.
- (3) Certain cases studied in part (II) of this Thesis, such as the flow in contractions with a rounded or non-symmetric corner have either not been analyzed before or have attracted only limited attention.
- (4) It is the first time that both planar (shear and elongational) and gap-averaged (shear only) stresses have been considered in the modelling of the flow of a viscoelastic material in injection mold filling. Consequently, this is the first time that the relative magnitudes of planar and gap averaged stresses that

development in a viscoelastic material during filling have been quantified.

- (5) This is maybe the second application of the method of boundary fitted curvilinear coordinates with adaptive remeshing in the modelling of transient free surface flows during injection mold filling (Subbiah et al. (1989)), and the first that utilizes a viscoelastic model. To the Author's best knowledge, it is the first study that, in the context of BFCCs and injection molding, tackles the problem of an insert and the first work that couples a filling analysis of a complex mold with three-dimensional crystallization kinetics. Even though the amount of crystallinity (and solidification) that develops during filling is very small, it can be very important in the final properties of the finished article.
- (6) All data reported in this Thesis (in rheological characterization and injection molding) and all computer programs used in the simulations are original contributions.

(V) LIST OF SYMBOLS

a_t	Time-temperature superposition shift factor
a_{ij}	Components of the velocity gradient tensor(Eqn.III.21)
A	Viscosity Coefficient (Eqn. III.41)
$A(T)$	Model dependent tensor (Eqn. II.9)
A_1	Coefficient introduced by Equation II.16
A_2	Coefficient introduced by Equation II.17
A_3	Coefficient introduced by Equation II.18
b	Thickness of the cavity
B	Coefficient introduced in Equation II.19
C	Coefficient introduced in Equation II.20
C_p	Heat capacity
D	Coefficient defined in equation II.66
D	Diagonal matrix
D_1	Coefficient defined by equation II.68
D_2	Coefficient defined by equation II.69
D_3	Coefficient defined by equation II.70
D_4	Coefficient defined by equation II.71
$D(S)$	Non-Newtonian source function (Eqn. II.3)
d, D	Rate of deformation tensor (Eqn. III.22)
d_{ij}	Components of the tensor D (Eqn. III.22)
D/Dt	Material time derivative (Eqn. II.10.c)
De	Deborah number ($De=\lambda \cdot \dot{\gamma}_{max}$)
E	Matrix defined by Equation II.79
F	Coefficient defined by Equation (II.67)
F	Matrix defined by Equation II.79
F_1	Coefficient introduced by Equation II.2
F_2	Coefficient introduced by Equation II.22
F_3	Coefficient introduced by Equation II.23
f_R, f_L	Functional values at mid-cell locations
G'	Storage Modulus
G''	Loss Modulus
G_1	Coefficient introduced by Equation II.27
G_2	Coefficient introduced by Equation II.28
G_3	Coefficient introduced by Equation II.29

h	Grid spacing (Equation II.34)
i,j	Indices in finite difference discretization
II	Second invariant of D (Eqn. III.40)
J	Jacobian of the coordinate transformation (Eqn. I.8)
k(T)	Isothermal crystallization rate
K(T)	Consistency index (Eqn. III.41)
L	Characteristic length
L	Lower-triangular matrix(Eqn. II.77)
L₁	Coefficient defined by Equation (II.72)
L₂	Coefficient defined by Equation (II.73)
L₃	Coefficient defined by Equation (II.74)
L₄	Coefficient defined by Equation (II.75)
L₅	Coefficient defined by Equation (II.76)
NORM	Norm of iterative corrections in SR algorithm
n	Power law index ($n=1/s$)
N₁	First normal stress difference($T^{xx}-T^{yy}$)
P	Control function (Eqn. I.1) and Pressure
Q	Control Function (Eqn. I.2)
R	Gas law constant
Re	Reynolds number ($Re=\rho UL/\mu$)
r	Position vector
s	Inverse of power law index
S=(S^{xx},S^{yy},S^{xy})	Elastic stress tensor
T=(T^{xx},T^{yy},T^{xy})	Total stress tensor
T⁽¹⁾	Upper convected derivative(Eqn. II.10.a)
T₍₁₎	Lower convected derivative (Eqn. II.10.b)
T	Temperature(K)
T_i(x)	Truncation error (Equation II.54)
t	Time(s)
u,v,w	Velocities in the x,y and z directions(cm/s)
<u>,<v>	Gap-averaged velocities(Eqn.III.28 & III.29)
U	Characteristic velocity
U	Upper-triangular matrix
We	Weissenberg number ($We=\lambda U/L$)
x,y	Cartesian coordinates

Greek Letters

α	Transformation coefficient (Eqn. I.5)
β	Transformation coefficient (Eqn. I.6)
γ	Transformation coefficient (Eqn. I.7)
$\delta/\delta t$	Objective time derivative (Eqn. II.10)
ΔE	Activation energy (Eqn. III.41)
η	Curvilinear coordinate
ξ	Curvilinear coordinate
κ	Thermal conductivity(W/mK)
λ	Relaxation time(s)
μ	Viscosity(Pa.s)
ρ	Density(Kg/m ³)
ρ_1	Grid cell Reynolds number
ϕ_m	Lagrange polynomial (Eqn. I.13)
Φ	Viscous dissipation (Eqn. III.16)
ψ	Stream function
ω	Vorticity

REFERENCES

1. Ahrens M., Yoo Y.J., and Joseph D.D., *Journal of Non Newtonian Fluid Mechanics*, **24**, 67, (1987).
2. Aldhouse S.T.E., Mackley M.R., and Moore I.P.T., *Journal of Non Newtonian Fluid Mechanics*, **21**, 359, (1986).
3. Apelian M.R., Armstrong R.C., Brown R.A., *Journal of Non Newtonian Fluid Mechanics*, **27**, 299, (1988).
4. Armstrong R.C., Brown R.A., Berris A.N., Lawler J.V., and Muller S.J., *Viscoelasticity and Rheology*, (1985).
5. Asaithambi N.S., *Journal of Computational Physics*, **73**, 380, (1987).
6. Ascoli E.P., Dandy D.S., Leal L.G., *Journal of Computational Physics*, **72**, 513, (1987).
7. Aubert X., Deville M., *Journal of Computational Physics*, **49**, 490, (1983).
8. Baba N., Miyata H., *Journal of Computational Physics*, **69**, 362, (1987).
9. Bell J.B., Shubin G.R., Stephens A.B., *Journal of Computational Physics*, **47**, 463, (1982).
10. Bird R.B., Armstrong R.C and Hassager O., "Dynamics of Polymeric Liquids, Volume I", second edition, John Wiley & Sons, (1987).
11. Boger D.V., Hur D.U., and Binnington R.J., *Journal of Non-Newtonian Fluid Mechanics*, **20**, 31, (1986).
12. Burton T.E. and Rezayat M., in "Applications of CAE in Injection Molding", Hanser Publishers, (1987).
13. Cable P.J., and Boger D.V., *AIChE Journal*, **24**(5), 869, (1978).
14. Choi H.C., Song J.H., and Yoo J.Y., *Journal of Non-Newtonian Fluid Mechanics*, **29**, 347, (1988).
15. Chikhiwala E.D., and Yortsos Y.C., *Journal of Computational Physics*, **57**, 391, (1985).
16. Collatz L., "The Numerical Treatment of Differential Equations", Third edition, Springer Verlag, (1966).
17. Cochrane T., Walters K., and Webster M.F., *Journal of Non-Newtonian Fluid Mechanics*, **10**, 95, (1982).
18. Cochrane T., Walters K., and Webster M.F., *Phil.Trans.R.Soc.Lon. A* **301**, 163, (1981).
19. Crochet M.J., Davies A.R., Walters K., "Numerical Simulation of Non-Newtonian Flow", Elsevier, (1984).
20. Crochet M.J. and Walters K., in *Computational Analysis of Polymer Processing*, Pearson J.R.A., and Richardson S.M., Eds. (1983).
21. Davies C.W., *Journal of Computational Physics*, **39**, 164, (1981).
22. Davies A.R., *Journal of Non-Newtonian Fluid Mechanics*, **16**, 195, (1984).
23. Davies A.R., Lee S.J., and Webster M.F., *Journal of Non-Newtonian Fluid Mechanics*, **16**, 117, (1984).
24. Debbaut B., and Crochet M.J., *Journal of Non-Newtonian Fluid Mechanics*, **20**, 173, (1986).
25. Debbaut B., Marshall J.M. and Crochet M.J., *Journal of Non-Newtonian Fluid Mechanics*, **29**, 119, (1988).
26. Deiber J.A. and Schowalter W.R.; *AIChE Journal*, **27**, 912, (1981).
27. de Boor C., "A practical guide to splines", Springer Verlag, NY, (1978).
28. Duppret F., Marshal J.M., and Crochet M.J., *Journal of Non-Newtonian Fluid Mechanics*, **18**, 173, (1985).
29. Dvinsky A.S., Popel A.S., *Journal of Computational Physics*, **67**, 73, (1986).
30. Eiseman P.R., *Journal of Computational Physics*, **47**, 352, (1982).

- 31 Eiseman P.R., *Journal of Computational Physics*, **47**, 331, (1982).
- 32 Eiseman P.R., *Annual review of Fluid Mechanics*, **17**, 487, (1985).
- 33 Eiseman P.R., *International Journal for Numerical Methods in Fluids*, **8**, 1165, (1988).
- 34 Evans R.E., and Walters K., *Journal of Non-Newtonian Fluid Mechanics*, **20**, 11, (1986).
- 35 Ferziger J.H., *Journal of Computational Physics*, **69**, 1, (1987).
- 36 Floryan J.M., *Journal of Computational Physics*, **62**, 221, (1986).
- 37 Floryan J.M., *Journal of Computational Physics*, **58**, 229, (1985).
- 38 Fodemski T.R., Voke P.R., Collins M.W., *International Journal for Numerical Methods in Fluids*, **7**, 277, (1987).
- 39 Gao, F., MSc Thesis, Department of Chemical Engineering, McGill University, (1989).
- 40 Garg V.K., Maji P.K., *International Journal for Numerical Methods in Fluids*, **8**, 579, (1988).
- 41 Gatski T.B., and Ramley, J.L.: *Journal of Computational Physics*, **27**, 42, (1978).
- 42 Gatski T.B., and Ramley, J.L.: *Journal of Fluid Mechanics*, **86**, 623, (1978).
- 43 Gentry, R.A., Martin R.E., and Daly, B.J.: *Journal of Computational Physics*, **1**, 87, (1966).
- 44 Gilmore S.D., and Guceri S.I., *Numerical Heat Transfer*, **14**, 165, (1988).
- 45 Glakpe E.K., Watkins C.B., Kurien B., *International Journal for Numerical Methods in Fluids*, **7**, 155, (1987).
- 46 Glekas J., Bergeles G., Athanassiadis N., *International Journal for Numerical Methods in Fluids*, **7**, 319, (1987).
- 47 Gupta, M.M and Mahonar R.P., *Journal of Computational Physics*, **31**, 265, (1984).
- 48 Haussling H.J., Coleman R.M., *Journal of Computational Physics*, **43**, 373, (1981).
- 49 Hausser J., Paap H.G., Eppel D., and Sengupta S., *International Journal for Numerical Methods in Fluids*, **6**, 507, (1986).
- 50 -----; *International Journal for Numerical Methods in Fluids*, **6**, 554, (1986).
- 51 Hieber C.A., "Injection and Compression Moulding Fundamentals", Ed. A.I.Isayev, Marcel Dekker, New York, (1987).
- 52 Hieber C.A., Shen S.F., *Journal of Non-Newtonian Fluid Mechanics*, **7**, 1, (1980).
- 53 Hung T.K., and Brown T.D., *Journal of Computational Physics*, **23**, 343, (1977).
- 54 Hsu C.C., Tu C.G., *Journal of Computational Physics*, **7**, 567, (1987).
- 55 Inoue K., *Journal of Computational Physics*, **52**, 130, (1983).
- 56 Inoue K., *Journal of Computational Physics*, **58**, 146, (1985).
- 57 Jensen, V.G., *Proc. Roy. Society London*, **A249**, 346, (1959).
- 58 Josse S.L., and Finlayson A., *Journal of Non-Newtonian Fluid Mechanics*, **16**, 13, (1984).
- 59 Joseph D.D., Renardy M., and Saut J.C., *Arch. Ration. Mech. Anal.*, **87**(3), 213, (1985).
- 60 Kamal M.R., in "applications of CAE in injection molding", Hanser Publishers, (1987).
- 61 kamal M.R., and Lafleur P.G., *Polymer Engineering and Science*, **26**, 103, (1986).
- 62 Kamal M.R., and Bata G.L., in "Polymer Processing and Properties", Astarita and Nicolais (eds.), **1**, (1983).

- 63 Kamal M.R., Kuo Y., and Doan P.H., *Polymer Engineering and Science*, **15**, 863, (1975).
- 64 Kamal M.R., Goyal S.K., and Chu E., *AIChE Journal*, **34**, 94, (1988).
- 65 Kamal M.R., and Kenig S., *Polymer Engineering and Science*, **12**, 294, (1972).
- 66 -----, *Polymer Engineering and Science*, **12**, 305, (1972).
- 67 Kamal M.R., and Lafleur P.G., *Polymer Engineering and Science*, **22**, 1066, (1982).
- 68 Kawaguti M., *The Physics of Fluids* s.II, 1969, (101-104).
- 69 Keunings R., in "Fundamentals of Computer Modelling for Polymer Processing", Carl Hanser Verlag, (1987).
- 70 Keunings R., *Journal of Non-Newtonian Fluid Mechanics*, **20**, 209, (1986).
- 71 Kim H.J. and Thompson J., *AIAA 26th Aerospace Sciences Meeting*, Reno, Nevada, (1988).
- 72 King R.C., Apelian M.R., Armstrong R.C., and Brown R.A., *Proceedings to the fifth Workshop on Numerical Methods in non-Newtonian Fluid Mechanics*, (1988).
- 73 Kuo Y., and Kamal M.R., "Proc. Intl. Conference on Polymer Processing, N.P. Suh and N.H.Sung (eds.), MIT, (1977).
- 74 Kuo Y., and Kamal M.R., *AIChE Journal*, **22**, 661, (1976).
- 75 Lafleur P.G., and Kamal M.R., *Polymer Engineering and Science*, **26**, 92, (1986).
- 76 Lafleur, P.G., "Computer Simulation of the Injection Molding of Viscoelastic Crystalline Thermoplastics", PhD Thesis, McGill University, (1983).
- 77 Lapidus L. and Pinder G.F., "Numerical Solution of Partial Differential Equations", John Willey & Sons, (1982).
- 78 Leonard B.P., *Comp.Meth.Appl.Mech.Engg.*, **19**, 59-98, (1979).
- 79 Lipscomb G.G., Keunings R., and Denn M.M., *Journal of Non-Newtonian Fluid Mechanics*, **24**, 85, (1987).
- 80 Li B., Lu Y., *International Journal for Numerical Methods in Fluids*, **7**, 1343, (1987).
- 81 Liou R.J., Clark M.E., Robertson J.M and Cheng L-C., *Journal of Engineering Mechanics*, **110**, (11), (1984).
- 82 Loeffler A.L., *International Journal for Numerical Methods in Fluids*, **8**, 463, (1988).
- 83 Manero, O. and Mena B.; *Journal of Non-Newtonian fluid Mechanics*, **9**, 379, (1981).
- 84 Marshal J.M. and Crochet M.J., *Journal of Non-Newtonian Fluid Mechanics*, **26**, 77, (1987).
- 85 Marshall G., Eiseman P., Kuo J.T., *Journal of Computational Physics*, **62**, 180, (1986).
- 86 Mavridis H., Hrymak A.N and Vlachopoulos J., *AIChE Journal*, **34**(3), 403, (1988).
- 87 Mendelson M.A., Yeh P.W., Brown R.A., and Armstrong R.C., *Journal of Non-Newtonian Fluid Mechanics*, **10**, 31, (1982).
- 88 Middleman, S.: "Fundamentals of Polymer Processing", McGraw Hill, (1979).
- 89 Miki K. and Takagi T., *Journal of Computational Physics*, **67**, 352 (1986).
- 90 Miyata H., Nishimura S., *Journal of Computational Physics*, **60**, 391, (1985).
- 91 Mobley C.D., and Stewart R.J., *Journal of Computational Physics*, **34**, 124, (1980).

- 92 Mutel, T., private communication, (1990).
- 93 Nakamura K., Watanabe T., Katayama K. and Amano T., *Journal of Applied Polymer Science*, **16**, 1077, (1972).
- 94 Nakamura K., Katayama K. and Amano T., *Journal of Applied Polymer Science*, **17**, 1031, (1973).
- 95 Ogawa S., Ishiguro T., *Journal of Computational Physics*, **69**, 49, (1987).
- 96 Ohring S., *Journal of Computational Physics*, **50**, 307, (1983).
- 97 Olling C.R., Dulikravich G.S., *International Journal for Numerical Methods in Fluids*, **7**, 103, (1987).
- 98 Papathanasiou T.D., and Kamal M.R., ANTEC'89, (1979).
- 99 Paris J. and Whitaker S., *AIChE Journal*, **11**(6), 1033, (1965).
- 100 Perera M.G.N., and Walters K., *Journal of Non-Newtonian Fluid Mechanics*, **2**, 191, (1977).
- 101 Perera M.G.N., and Walters K., *Journal of Non-Newtonian Fluid Mechanics*, **2**, 49-81(1977).
- 102 Pilate G., and Crochet M.J., *Journal of Non-Newtonian Fluid Mechanics*, **1**, 247, (1976).
- 103 Pope S.B., *Journal of Computational Physics*, **26**, 197, (1978).
- 104 Potter D.E., and Tuttle G.H., *Journal of Computational Physics*, **13**, 483, (1973).
- 105 Ramanathan S., and Kumar R., *Numerical Heat Transfer*, **14**, 187, (1988).
- 106 Rangwalla A.A., Munson B.R., *Journal of Computational Physics*, **70**, 373, (1987).
- 107 Rapley C.W., *International Journal for Numerical Methods in Fluids*, **8**, 305, (1988).
- 108 Roache P.J., "Computational Fluid Dynamics", Hermosa Publishers, (1972).
- 109 Rosenberg J.R. and Keurings R., *Journal of Non-Newtonian Fluid Mechanics*, **29**, 295, (1988).
- 110 Ryan M.E., and Chung T.S., *Polymer Engineering and Science*, **20**, 642, (1980).
- 111 Ryskin G., and Leal L.G., *Journal of Computational Physics*, **50**, 71, (1983).
- 112 Saltzman J., *Journal of Computational Physics*, **63**, 1, 91986).
- 113 Shen S-F., *International Journal for Numerical Methods in Fluids*, **4**, 171, (1984).
- 114 Shyy W., *International Journal for Numerical Methods in Fluids*, **8**, 475, (1988).
- 115 Shyy W., Braaten M.E., *International Journal for Numerical Methods in Fluids*, **6**, 861, (1986).
- 116 Song J.H., and Yoo J.Y., *Journal of Non-Newtonian Fluid Mechanics*, **24**, 221, (1987).
- 117 Spalding, D.B., *International Journal for Numerical Methods in Engineering*, **4**, 551-559, (1972).
- 118 Sparis P.D., *Journal of Computational Physics*, **61**, 445, (1985).
- 119 Steinhoff J., *Journal of Computational Physics*, **65**, 370, (1986).
- 120 Subbiah S., Trafford D.L and Guceri S.I., *International Journal of Heat and Mass Transfer*, **32**(3), 415, (1989).
- 121 Tadmor Z., and Gogos C.G., "Principles of Polymer Processing", John Wiley & Sons, 1979.
- 122 Takagi T., Miki K., Chen B.C.J., Sha W.T., *Journal of Computational Physics*, **58**, 67, (1985).
- 123 Tanner R.I., "Engineering Rheology", Clarendon Press, (1985).

- 124 Tanner R.I., in *Computational Analysis of Polymer Processing*, Pearson J.R.A., and Richardson S.M., Eds. (1983).
- 125 Thompson J.F., *Computer Methods in Applied Mechanics and Engineering*, **64**, 377, (1987).
- 126 Thompson, J.F., Warsi, Z.U.A: *Journal of Computational Physics*, **47**, 1, (1982)
- 127 Thames F.C., Thompson J.F., Mastin C.W., Walker R.L., *Journal of Computational Physics*, **24**, 245, (1977).
- 128 Thompson J.F., Thames F.C., Mastin C.W., *Journal of Computational Physics*, **15**, 299, (1974).
- 129 Thompson J.F., Warsi Z.U.A., Mastin C.W., North-Holland Publishers, (1985).
- 130 Tiefenbruck, G., and Leal, L.G.: *Journal of Non-Newtonian Fluid Mechanics*, **10**, 115-155, (1982).
- 131 Tzaribas G., Dimas A., Loukakis T., *Journal of Computational Physics*, **6**, 789, (1986).
- 132 Walters K., and Webster M.F., *Philos.Trans.Roy.Soc.London Ser. A* **308**, 199-218, (1982).
- 133 Wang V. and Hieber C., ANTEC '88, 290, (1988).
- 134 Wang K.K., Shen S.F., Cohen C., Hieber C.A., Progress Report #13, College of Engineering, Cornell University, (1987).
- 135 White J.L., in "CAE for injection molding", Hanser Publishers, (1983).
- 136 White J.L., and Dietz W., *Polymer Engineering and Science*, **9**, 1081, (1979).
- 137 White S.A., Gotsis A.D., and Baird D.G., *Journal of Non-Newtonian Fluid Mechanics*, **24**, 121, (1987).
- 138 Woods, L.C., *Aeronaut. Q.*, *Journal of Computational Physics*, **5**, 176, (1954).
- 139 Yang S.L., Shih T.I-P., *International Journal for Numerical Methods in Fluids*, **6**, 291, (1986).
- 140 Yang H., Camarero R., *International Journal for Numerical Methods in Fluids*, **6**, 35, (1986).
- 141 Yoo J.Y., and Joseph D.D., *Journal of Non-Newtonian Fluid Mechanics*, **19**, 15, (1985).

(A.1) Numerical Implementation of Elliptic Grid Generator

For the numerical solution of the grid generating equations ((I.3) and (I.4)), the derivatives of the spatial coordinates (x,y) with respect to the curvilinear coordinates are discretized using central differences in the interior of the flow domain and one-sided, second order accurate differences on the boundaries.

$$(x_s)_{ij} = (x_{i+1j} - x_{i-1j})/2h \quad (\text{A.1.1})$$

$$(x_\eta)_{ij} = (x_{ij+1} - x_{ij-1})/2h \quad (\text{A.1.2})$$

$$(y_s)_{ij} = (y_{i+1j} - y_{i-1j})/2h \quad (\text{A.1.3})$$

$$(y_\eta)_{ij} = (y_{ij+1} - y_{ij-1})/2h \quad (\text{A.1.4})$$

$$(\partial^2 x / \partial \xi^2)_{ij} = (x_{i+1j} - 2x_{ij} + x_{i-1j})/h^2 \quad (\text{A.1.5})$$

$$(\partial^2 x / \partial \eta^2)_{ij} = (x_{ij+1} - 2x_{ij} + x_{ij-1})/h^2 \quad (\text{A.1.6})$$

$$(\partial^2 x / \partial \xi \partial \eta)_{ij} = (x_{i+1j+1} - x_{i-1j+1} - x_{i+1j-1} + x_{i-1j-1})/4h^2 \quad (\text{A.1.7})$$

$$(\partial^2 y / \partial \xi^2)_{ij} = (y_{i+1j} - 2y_{ij} + y_{i-1j})/h^2 \quad (\text{A.1.8})$$

$$(\partial^2 y / \partial \eta^2)_{ij} = (y_{ij+1} - 2y_{ij} + y_{ij-1})/h^2 \quad (\text{A.1.9})$$

$$(\partial^2 y / \partial \xi \partial \eta)_{ij} = (y_{i+1j+1} - y_{i-1j+1} - y_{i+1j-1} + y_{i-1j-1})/4h^2 \quad (\text{A.1.10})$$

Since the boundary correspondence is given, the generating equations need to be solved only in the interior of the domain of interest. Therefore, in this case, there is

no need for the use of special difference expressions at the boundaries.

The discretized form of the generating equations was solved using an iterative successive relaxation algorithm. Iterative changes were smoothed by means of a factor (w) as follows:

$$f_{ij}^{(n)} = w \cdot f_{ij}^{(n)} + (1-w) \cdot f_{ij}^{(n-1)} \quad (\text{A.1.11})$$

where the superscript (n) indicates functional values at the n th iteration. The convergence of the iterative solution was usually rapid without stability problems. The only problems were encountered when improper values for the coefficients e, c, b, d in the equations defining the control function P and Q were being selected. For example, if attraction to an η -line (say η_{ref}) was desired, too high a value of (e_i) would impose a very strong attraction on the nearby coordinate lines. This would lead to some of the η -lines crossing the η_{ref} line, resulting in numerical instabilities and an unacceptable grid. Similarly, a very small value of the decay coefficient (c) would result in attraction even to distant η -lines, and usually in an unacceptable grid. Figure (A.1.1) shows some of the problems associated with unreasonable values for the distortion functions.

The concentration of coordinate lines in areas of interest can, besides a proper choice of P and Q , be controlled by a proper distribution of the boundary nodes. Figure (II.5.1.1) shows parts of three grids used in the study of flow in a 4:1 contraction. Grid (II.5.1.1.a) was constructed with $P=Q=0$ and a fairly uniform distribution of the boundary nodes. In grid (II.5.1.1.b) P and Q were calculated so as to give a higher concentration of coordinate lines near the upper boundary. Finally, Grid (II.5.1.1.c) was constructed with $P=Q=0$ and a higher density of boundary nodes near the reentrant corner.

(A.1.1) Grid Orthogonality at the Boundary

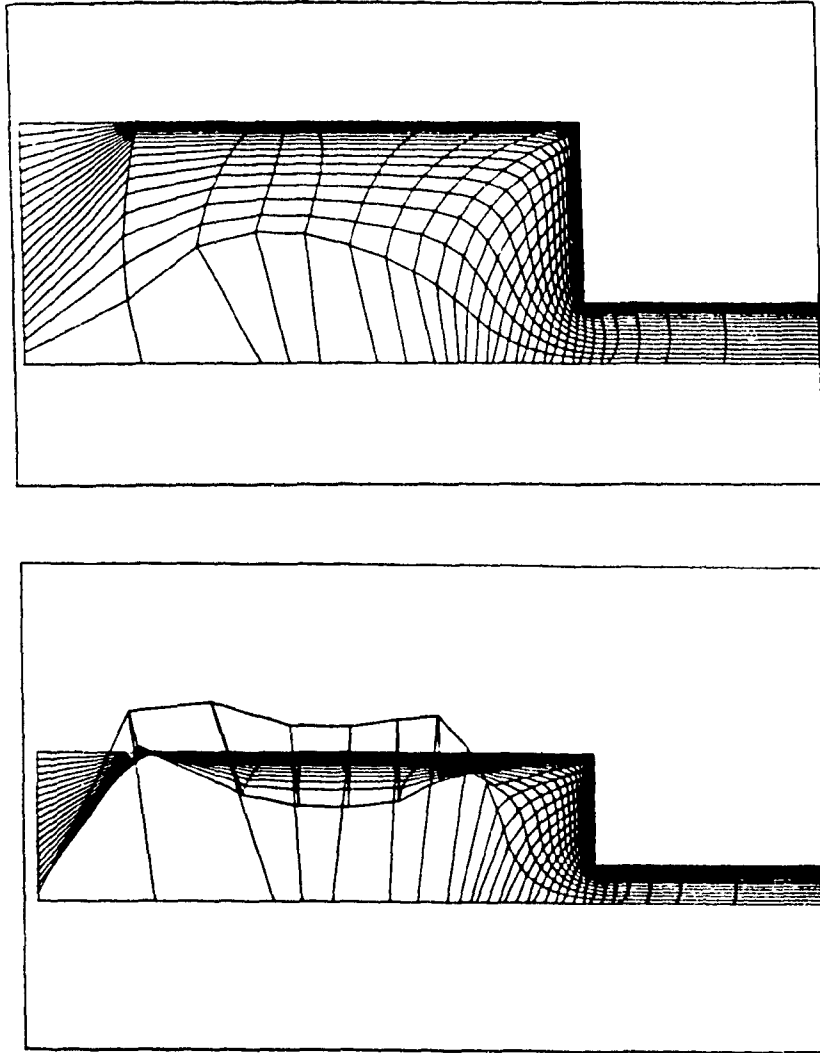


Figure (A.1.1): Some of the problems associated with unreasonable values of the distortion functions in Poisson-type elliptic grid generation.

When Neumann boundary conditions are to be used, as is the case in the solution of the pressure equation in the modelling of the filling stage in injection molding, it is desirable to have a grid that is normal to the boundary. In the context of second order elliptic generating systems, this can be accomplished in two ways:

- (a) Keep the boundary points constant and place the interior nodes in a manner that assures orthogonality. This can be accomplished by proper selection of the control functions. (Thompson et al. (1985))
- (b) Move the boundary points so that the coordinate lines intersect the boundary at right angles.

In this work method (b) was followed. Its application was facilitated by the fact that the boundary of the flow channel consisted of lines with explicitly known parametric equations. Therefore the location of the boundary points for orthogonality could be easily determined by geometrical considerations.

(A.2) Coordinate Invariance of Partial Differential Equations

The objective of this section is to prove the following theorem:(Lapidus & Pinder, 1982).

Theorem: The sign of the discriminant of a second order partial differential equation (p.d.e) in two independent variables is invariant under non-singular transformation of coordinates.

This proposition is fundamental in the theory of partial differential equations. It guarantees, that an elliptic, for example, equation will remain elliptic after a non-singular transformation of coordinates, even though the transformed form might include additional terms not present in the original equation. In this work we are particularly interested in the transformation of the Laplace operator appearing in the Poisson equations for the vorticity and the stream function. In curvilinear coordinates (ξ, η) , the transformed form of the Laplacian operator of a scalar (u) is:

$$\nabla^2 u = [\alpha \cdot u_{\xi\xi} - 2 \cdot \beta \cdot u_{\eta\xi} + \gamma \cdot u_{\eta\eta}] / J^2 + (\nabla^2 \xi) \cdot u_{\xi} + (\nabla^2 \eta) \cdot u_{\eta} \quad (\text{A.2.1})$$

where the coefficients are functions of the coordinate transformation. The general second order partial differential equation of the form

$$a \cdot u_{xx} + 2b \cdot u_{xy} + c \cdot u_{yy} + d \cdot u_x + e \cdot u_y + f \cdot u + g = 0 \quad (\text{A.2.2})$$

defined in ω , can be elliptic, hyperbolic or parabolic, depending on whether the discriminant

$$\Delta = b^2 - a \cdot c \quad (\text{A.2.3})$$

is negative, positive or zero respectively. If the sign of the discriminant changes in ω ,

then the equation is of the mixed type. In the theory of partial differential equations there is a fundamental distinction between those of elliptic, parabolic and hyperbolic type. Each type has different requirements as to the boundary or initial data required to assure existence, uniqueness and continuous dependence on initial data; that is for the problem to be well posed. These requirements are well known for each of the above types of equations, and many analytical and numerical techniques have been developed for solving the various types of equations, including non-linear equations, subject to suitable boundary conditions. However, for the equations of mixed type much less is known and it is usually difficult to know even what the proper boundary conditions are. It becomes therefore apparent that it is crucial to establish that the type of a general partial differential equation of the form of Equation (A.2.2) is coordinate system invariant.

Let the new coordinates (ξ, η) be related to the old (x, y) coordinates by:

$$\xi = \xi(x, y) \quad \eta = \eta(x, y) \quad (\text{A.2.4})$$

The Jacobian of this transformation will be non-zero, since we are interested in non-singular transformations

$$J = \partial(\xi, \eta) / \partial(x, y) = \xi_x \cdot \eta_y - \xi_y \cdot \eta_x \quad (\text{A.2.5})$$

Because of this, the inverse relations also hold

$$x = x(\xi, \eta) \quad y = y(\xi, \eta) \quad (\text{A.2.6})$$

Using the chain rule, one can calculate the derivatives of the function (u) appearing in (A.2.2). Substituting in (A.2.2), one can get the transformed equation in the new coordinate system. This will be

A2.3

$$A \cdot u_{\xi\xi} + 2B \cdot u_{\xi\eta} + C \cdot u_{\eta\eta} + \dots = 0 \quad (\text{A.2.7})$$

where the derivatives of order less than two were dropped since their coefficients do not affect the sign of the discriminant. It can now be proved that the discriminant of equation (A.2.7) is

$$\Delta' = B^2 - A \cdot C = \Delta \cdot J^2 \quad (\text{A.2.8})$$

This results shows that the sign of the discriminant remains indeed unaffected by the coordinate transformation.

(A.3) Review of Transformation Relations

A complete presentation of the relations involved in the transformation of derivative and integral operators from one curvilinear system to another can be found in Thompson et al. (1985). Such expressions for the basic derivative operators of fluid mechanics are given in this section for the sake of completeness. Both conservative and non-conservative forms are included.

(A.3.1) Conservative Relations

$$\text{Divergence: } \nabla \cdot \mathbf{f} = J^{-1} \Sigma (\mathbf{J} \mathbf{a}^i \cdot \mathbf{f})_i \quad (\text{A.3.1})$$

$$\text{Gradient: } \nabla f = J^{-1} \Sigma (\mathbf{J} \mathbf{a}^i f)_{,i} \quad (\text{A.3.2})$$

$$\text{Curl: } \nabla \times \mathbf{f} = J^{-1} \Sigma (\mathbf{J} \mathbf{a}^i \times \mathbf{f})_{,i} \quad (\text{A.3.3})$$

$$\text{Laplacian: } \nabla^2 f = \Sigma [a^i \cdot (\mathbf{J} \mathbf{a}^i f)_{,i}]_{,i} \quad (\text{A.3.4})$$

(A.3.2) Non-conservative Relations

$$\text{Divergence: } \nabla \cdot \mathbf{f} = \Sigma \mathbf{a}^i \cdot \mathbf{f}_{,i} \quad (\text{A.3.5})$$

$$\text{Gradient: } \nabla f = \Sigma \mathbf{a}^i f_{,i} \quad (\text{A.3.6})$$

in view of (A.3.6), the (∇) operator can be written, in general curvilinear coordinates, as:

$$\nabla = \Sigma \mathbf{a}^i (\partial / \partial x^i) \quad (\text{A.3.7})$$

$$\text{Curl: } \nabla \times \mathbf{f} = \sum a^i \times \mathbf{f}_i \quad (\text{A.3.8})$$

$$\text{Laplacian: } \nabla^2 f = \sum \sum a^i \cdot a^j f_{ij} + \sum \sum a^i \cdot (a^j)_i f_j \quad (\text{A.3.9})$$

In the equations (A.3.1) to (A.3.9), x^i , $i=1,2,3$ are general curvilinear coordinates, whereas a^i , $i=1,2,3$ are the contravariant base vectors corresponding to these curvilinear coordinates. The contravariant base vectors are defined as:

$$\mathbf{a}^i = \nabla x^i, \quad i=1,2,3 \quad (\text{A.3.10})$$

In equations (A.3.1) to (A.3.10) bold letters indicate vectors, non-bold letters are scalar quantities and all the summations are over $i=1,2,3$ and/or $j=1,2,3$.

(A.3.3) Transformation of Temporal Derivatives

Equations (A.3.1) to (A.3.10) refer to spatial discretization. With moving grids and time dependent equations however, as is the case during the modelling of the filling stage of injection molding, the time derivatives need to be considered as well. For the first time derivative, the transformation relation is:

$$(\dot{f})_t = (\dot{f})_x + \nabla f \cdot (\mathbf{x})_t \quad (\text{A.3.11})$$

where the subscripts outside the parentheses indicate the spatial variable being held constant in the time differentiation. The term \mathbf{x}_t is the grid point speed. With the time derivatives transformed as in Equation (A.3.11), only time derivatives at fixed points in the logical space will appear in the equations and, therefore, all computations can still be done on a fixed uniform mesh without interpolation, even though the grid points are in motion in the physical space.

(A.4) The Boundary Conditions

(A.4.1) Preliminaries

The importance of the boundary conditions in computational fluid dynamics cannot be overstated. Besides affecting the accuracy and stability of computational algorithms, the type of boundary conditions is an important factor that will determine the predicted flow patterns. After all, all the fantastic flow phenomena in gases and liquids are solutions of the same set of partial differential equations, namely the Navier Stokes equations and it is the difference in initial/boundary conditions and flow parameters such as the Reynolds number that create the great variety of observable flow patterns. In the solution of the coupled viscoelastic problem, the type of boundary conditions can greatly affect the results and the stability of a computational algorithm.

(A.4.2) Boundary Conditions for the Stream Function and Vorticity

The boundary conditions for the stream function are of the Dirichlet type. Since solid boundaries and axes of symmetry are streamlines, the stream function is defined as follows:

$$\psi_{\text{inlet}} = \text{constant} \quad \psi_{\text{outlet}} = \text{constant} \quad (\text{A.4.1})$$

In the inlet of a flow channel, (ψ) and (ω) can be determined by integration and differentiation respectively of the inlet velocity profile. In general, it will be:

$$\psi_{\text{inlet}}(y) = \int u_{\text{inlet}}(y) dy, \quad \omega_{\text{inlet}} = -\partial u_{\text{inlet}} / \partial y \quad (\text{A.4.2})$$

The evaluation of $(\psi, \text{ and } \omega)$ at outflow boundaries is not as straightforward and has been the subject of considerable research (Roache, (1976)). Use of improper outflow boundary conditions has been shown to result in catastrophic instabilities that propagate upstream from the outflow boundary and destroy the solution.

When the length of the outflow section is sufficiently large, it is reasonable to assume a fully developed profile and extract (ψ) and (ω) in a similar fashion as in the inlet. However, it has been shown (Paris and Whitaker, (1965)) that the less restrictive condition

$$v = \partial\psi/\partial x = 0 \quad \text{and} \quad \partial\omega/\partial x = 0 \quad (\text{A.4.3})$$

allows greater accuracy for comparable computational meshes. This outflow condition has been used in this work.

(A.4.2.1) Evaluation of Vorticity on Solid Boundaries

The evaluation of vorticity on solid walls is maybe the most important and sensitive computational boundary condition. One possible way to obtain boundary values for vorticity is by expanding (ψ) in Taylor series from its wall value (ψ_{wall}) :

$$\psi_{w+1} = \psi_w + \Delta y \cdot (\partial\psi/\partial y)_w + 0.5 \cdot (\Delta y)^2 \cdot (\partial^2\psi/\partial y^2)_w + \text{HOT} \quad (\text{A.4.4})$$

where HOT stands for higher order terms that are neglected in the following analysis and the subscript (w) indicates wall values. Assuming non-slip conditions on the walls, and using the equations defining (ψ) and (ω) , one obtains

$$\omega_w = -2(\psi_{w+1} - \psi_w)/h^2 \quad (\text{A.4.5})$$

where the subscript (w+1) indicates the point closest to the wall, and (h) is the

normal distance between points (w) and ($w+1$). Equation (A.4.5) is a first order approximation of the wall vorticity. This form has been reported by Thom as early as 1928, and has been widely and successfully used since then. It has been found to give results that essentially equal to those of higher order forms (Roache, (1976)), when first order accurate discretization of the derivatives of (ψ) and (ω) is used. However, when second order central differences are used, application of equation (A.4.5) has been found to undermine the accuracy of the global scheme (Gupta and Manohar, (1979)). Second order approximations for the wall vorticity have therefore been proposed. Two of these forms, introduced by Jensen (1959) and Woods (1954) respectively are:

$$\omega_w = -(\psi_{w+2}/2 + 4\psi_{w+1} - 7\psi_w/2)/h^2 \quad (\text{A.4.6})$$

$$\omega_w = -3(\psi_{w+1} - \psi_w)/h^2 + \omega_{w+1}/2 \quad (\text{A.4.7})$$

Discussions on the relative merits of first and second order formulae for the evaluation of the wall vorticity can be found in Crochet et al.(1984) and Roache (1976), each with numerous references supporting each side. It has been said (Crochet et al. (1984)) that in the case of viscoelastic flow, the introduction of the non-Newtonian source function (term $D(S)$ in equation (II.2)) which is first order accurate because of the backward differences usually used in the discretization of the stress derivatives in the constitutive equation, removes most of the merits of using a second order accurate formula for the wall vorticity - unless the Weissenberg number is very small, in which case the problem is essentially a Newtonian one. In the light of possible instabilities induced by second order formulae, it has been suggested (Crochet et al. (1984)) to use the more reliable, even though less accurate, equation (A.4.5). However, use of the higher order accurate QUICK scheme in the discretization of the stress equations makes the application of second order vorticity approximations a meaningful alternative. In the context of this work, both first and second order boundary approximations have been used with success.

All the previous formulae for wall vorticity are based on straight walls that are parallel to either the x- or the y-axis. Roache (1976) shows how approximations for wall vorticity on a solid boundary that forms an angle with the axis of the flow can be derived. However, that method is not of general use on curved boundaries. In the context of this work, the wall vorticity on general curved solid boundaries has been evaluated by the following defining expression:

$$\omega_w = -(\nabla^2 \psi)_w \quad (\text{A.4.8})$$

In general curvilinear coordinates, (ξ, η) the RHS of equation (A.4.8) can be written as:

$$(\nabla^2 \psi)_w = (\gamma \cdot \psi_{\eta\eta} + \alpha \cdot \psi_{\xi\xi} - 2\beta \cdot \psi_{\eta\xi})/J^2 + (\nabla^2 \xi) \cdot \psi_{\eta} + (\nabla^2 \eta) \cdot \psi_{\xi} \quad (\text{A.4.9})$$

where all derivatives are defined on the wall (w) of the flow channel and α, β, γ are given by equations (I.5) to (I.7)). Since (ψ) is constant along the wall, equation (A.4.9) reduces to:

$$(\nabla^2 \psi)_w = \alpha \cdot \psi_{\xi\xi}/J^2 + (\nabla^2 \eta) \cdot \psi_{\xi} \quad (\text{A.4.10})$$

It can further be shown that on solid no-slip walls it will always be $(\partial\psi/\partial\xi) = 0$. Therefore, equation (A.4.8) simplifies to:

$$-\omega_w = (\nabla^2 \psi)_w = J^2 \cdot ((x_{\eta})^2 + (y_{\eta})^2) \cdot \psi_{\xi\xi} \quad (\text{A.4.10.a})$$

A similar boundary condition has been used by Liou et. al. (1984) for the evaluation of the wall vorticity in a bent with curved walls. When a first order approximation for the derivative $(\partial^2 \psi / \partial \xi^2)$ is used, it can be shown that for a boundary parallel to the x (or y) axis, equation (A.4.10.a) reduces to equation (A.4.5). Both first and second order one-sided approximations for the partial derivative in (A.4.10.a) were used,

resulting in two different formulae for the wall vorticity. The second order formula is (Collatz (1966)):

$$(\psi_{\xi\xi})_w = (2\psi_w - 5\psi_{w+1} + 4\psi_{w+2} - \psi_{w+3})/h^2 \quad (\text{A.4.10.b})$$

Use of a first order expression for the second derivative $(\psi_{\xi\xi})_w$ results in the following wall vorticity approximation:

$$\omega_w = -2J^2 \cdot ((x_\eta)^2 + (y_\eta)^2) \cdot (\psi_{w+1} - \psi_w)/h^2 \quad (\text{A.4.10.c})$$

The second order expression (equation (A.4.10.b)) was found to be less stable than the first order formula (A.4.10.c). However, both methods worked well in geometries that did not involve boundary discontinuities such as a reentrant corner. Smoothing of iterative changes based on equation (A.1.11) with relaxation parameter (w) determined by trial-and-error was necessary in certain cases with the second order formula but not with equation (A.4.10.c). Both methods gave essentially the same results in smooth geometries.

At a point of boundary discontinuity, the directional derivatives (x_η) and (y_η) are undefined. In such a corner, the vorticity was calculated using the well-known Kawaguti method.

(A.4.3) Boundary Conditions for the Stress Equations

The boundary conditions for the total stress will be derived from the constitutive model by proper selection of (u) , (v) and their gradients. On solid, no-slip walls, $u=v=0$ and the upper convected Maxwell model reduces to a set of algebraic equations which, upon solution, yields the following expressions for T^x , T^y , T^z .

$$T^x = 2 \cdot (u_x + We \cdot (u_y \cdot v_x + 2 \cdot (u_x)^2 + (u_y)^2)) / (1 - 4 \cdot \alpha^2 \cdot \lambda^2) \quad (\text{A.4.11})$$

$$T^y = (u_y + v_x + 2 \cdot We \cdot (u_y \cdot v_y + u_x \cdot v_x)) / (1 - 4 \cdot \alpha^2 \cdot \lambda^2) \quad (\text{A.4.12})$$

$$T^z = 2 \cdot (-u_x + We \cdot (u_y \cdot v_x + 2 \cdot (u_x)^2 + (v_x)^2)) / (1 - 4 \cdot \alpha^2 \cdot \lambda^2) \quad (\text{A.4.13})$$

where $\alpha^2 = (u_x)^2 + v_x \cdot u_y$, and the subscripts denote partial differentiation.

These expressions are valid on any non-slip boundary. On boundaries parallel to the x-axis, the above equations further simplify to:

$$T^x = 2We \cdot (u_y)^2 \quad (\text{A.4.14})$$

$$T^y = We \cdot (u_x)^2 \quad (\text{A.4.15})$$

$$\text{and } T^z = T^x = T^y = 0 \quad (\text{A.4.16})$$

On boundaries parallel to the y-axis, we get:

$$T^y = 2We \cdot (v_x)^2 \quad (\text{A.4.17})$$

$$T^z = We \cdot (v_x)^2 \quad (\text{A.4.18})$$

$$\text{and } T^x = T^y = T^z = 0 \quad (\text{A.4.19})$$

On axes of symmetry the constitutive model simplifies to the following set of ordinary differential equations:

$$\lambda \cdot u \cdot (dT^x/dx) + (1 - 2 \cdot \lambda \cdot u_x) \cdot T_{xx} = 2\mu \cdot u_x \quad (\text{A.4.20})$$

$$\lambda \cdot u \cdot (dT^y/dx) + (1 - 2 \cdot \lambda \cdot v_y) \cdot T_{yy} = 2\mu \cdot v_y \quad (\text{A.4.21})$$

with $T^y = 0$, indicating that an axis of symmetry is a shear-free line.

(A.4.4) Boundary Conditions for Pressure

The boundary condition for the Poisson equation of pressure along the edges of the cavity is the following Neumann condition:

$$\partial P / \partial n = L_p \quad (\text{A.4.22})$$

where the term L_p in (A.4.22) is calculated from the momentum equations. The approximation $\partial P / \partial n \approx 0$ is also frequently used. This is a mild approximation, since the constant pressure region is confined to the very vicinity of the solid boundary. The existence of Neumann condition requires transformation of the normal derivative to the curvilinear coordinate system. In a general, non-orthogonal system, this leads to a boundary condition of the form:

$$s(x,y) \cdot (\partial P / \partial \xi) + h(x,y) \cdot (\partial P / \partial \eta) = 0 \quad (\text{A.4.23})$$

This type of boundary condition will feedback in the iterative algorithm and possibly destabilize its convergence. Initial experience in this respect confirmed that possibility. However, in the context of a coordinate system that is normal to the boundary, either $s(x,y)$ or $h(x,y)$ will disappear and the boundary condition will retain its simple functional form. For this reason, it was decided that in the analysis of the injection molding normal-to-the-boundary curvilinear coordinate systems were used. Their construction has been discussed in APPENDIX (A.1).

At the inlet of the cavity the pressure gradient can be obtained by simply considering fully developed one dimensional flow between two flat plates with distance equal to

the thickness of the cavity at the gate. The resulting pressure drop will then be:

$$P_r = [2Q(s+2)/b^2W]^{(1/s)} \cdot (2k/b) \quad (\text{A.4.23})$$

In A.4.23, k is the consistency index of the polymer and Q is the melt flowrate at the gate. (b) is the thickness and (W) the width of the cavity at the gate. In A.4.23, $s=1/n$.

(A.4.5) Boundary Conditions at the Free Surface

At the filling stage of injection molding particular attention should be placed on the description of the free surface. A local force balance provides the following boundary condition on a free surface:

$$\mathbf{n} \cdot \mathbf{T} = (2 \cdot H/Ca)\mathbf{n} - P_a \mathbf{n} \quad (\text{A.4.24})$$

where (\mathbf{n}) is the outward unit vector normal to the surface, $2H$ is the surface curvature and P_a the ambient pressure, usually taken as zero. Ca is the capillary number, defined as the ratio of viscous to surface tension forces ($Ca = \mu \cdot u/\lambda$). Since in molten polymers the viscous forces are dominant, $1/Ca \sim 0$, and equation (A.4.24) simplifies to the no-traction condition:

$$\mathbf{n} \cdot \mathbf{T} = - P_a \mathbf{n} \quad (\text{A.4.25})$$

In the case that the curvature of the free surface is small and the stresses follow some power law expression, that is when elasticity effects on the shape of the free surface are ignored, the boundary conditions at the surface can be written as (Lafleur, 1983):

$$P = P_a + 2\mu \cdot (u_r) \quad (\text{A.4.26})$$

$$\mu \cdot (u_y + v_x) = 0 \quad (\text{A.4.27})$$

Application of the boundary conditions (A.4.26) and (A.4.27) is relatively straightforward in the context of a (u,v,P) solution. However, in the context of an (ψ,ω) solution, there exists a difficulty in formulating the boundary conditions at the free surface in forms that can be used computationally without affecting the stability of the numerical scheme. Tanner (1983) states that no successful application of the (ψ,ω) solution in free surface flows is known. In this work the values of the stream function at the free surface were obtained as in an inflow/outflow boundary by integrating the appropriate velocity profile, in a manner similar to the one used by Subbiah et al. (1989). At each time step, the velocities used in these forms were obtained by differentiation of the ψ -field at the previous time level. Comparison of computational results for the shape of the free surface with experimental profiles obtained with short shots shows a very good agreement. This verifies that in injection molding, with the associated very high flow rates, the shape of the free surface is determined mainly by the geometry of the cavity and the overall kinematics of the flow, rather than by conditions prevailing at the vicinity of the free surface.

(A.4.6) Boundary Conditions for Temperature

At the inlet of the cavity the melt temperature is assumed to be uniform:

$$T_{x=0}(y) = T_{\text{melt}} \quad (\text{A.4.28})$$

On the faces of the mold, the following condition is used:

$$k_m(T_x)_n = h(T_o - T) \quad (\text{A.4.29})$$

where k_m is the thermal conductivity of the melt, T_o is a reference temperature and

h is the overall heat transfer coefficient. Again, the subscript (w) indicates wall values.

(A.4.7) Computational Treatment of the Free Surface

For a successful continuous marching solution of the model equations during filling, it is essential to be able to generate a proper computational grid at each time step. Besides orthogonality at the mold walls, which will ensure accurate representation of the pressure boundary conditions, a proper grid should have a relatively uniform distribution of nodes. In general, we wish to avoid uncontrollably large or small concentrations of grid nodes; a relatively uniform distribution is a good, if not optimal, compromise. It is fairly simple to generate automatically an equidistant distribution of boundary nodes on the mold walls, but not so simple on the free surface. The difficulty lies in that the location of the melt front is not known a-priori, and therefore, no parametric expression is available. This problem was solved by providing for the generation, at each time step, of a suitable interpolant for the sequence, say $\{x,y\}$, of the surface points. Then the grid nodes were rearranged at equal intervals on this interpolant. With equally spaced nodes on all 4 boundaries of the physical domain, a Laplace generating system always produces a smooth and uniform mesh. Amongst the many available interpolants (such as least squares polynomials, piecewise polynomials, cubic splines and general B-splines of k_{th} order), it was found that the B-splines were the most consistent and accurate in preserving the shape of the interpolated data.

By consistent, it is meant that the interpolant should perform well - that is, represent the shape of the melt front with minimum distortion - at any location into the cavity (from almost semicircular near the gate to slightly curved in the middle of the cavity and more complicated at the wake of the obstacle). The question of accuracy is a more subtle one. In least squares polynomial approximations we can always determine a measure of deviation of the interpolant from the interpolated data, usually in the form of summation of squares of deviations. However, general

conditions are not known for the exact behaviour of spline interpolants (de Boor, (1978)). Therefore, the various interpolants were assessed by observing plotted results before and after interpolation.

A B-spline is specified by supplying its breakpoint sequence and its order. The spline interpolant will then satisfy:

$$y_i = \sum \alpha_j B_j(x_i) \quad (\text{A.4.30})$$

where α_j are the spline coefficients and B_j denotes the j -th B-spline of the desired order with respect to the specified knot sequence. More details on splines and specifically B-splines can be found in de Boor (1978). To avoid wiggles in the shape of the melt front, low (second) order splines were used.

The reason for the necessity of rearranging the surface grid points can be understood with reference to Figure (A.4.1). The kinematic condition at the free surface is:

$$dx/dt = u \quad (\text{A.4.31})$$

where \mathbf{x} and \mathbf{u} are position and velocity vectors respectively. Because of the curvature of the free surface and the existence of fountain flow, the surface points will regularly tend to move outwards (Figure (A.4.1.a)). When this happens at each time step, many grid points tend to concentrate near the contact point and fewer near the center. Ultimately, the grid becomes unsuitable for computations. In the case that the contact point is not moving (Figure (A.4.1.b)) as the result of a no-slip boundary condition, at some instant one grid point will collapse to the wall, defining a new contact point. In this case the surface nodes have to be rearranged in order to continue the computations. Another possible case is shown in Figure (A.4.1.c). Encountering a change in the curvature of the mold wall, some intermediate surface points might touch the wall first. Again, an automatic rearrangement of the surface

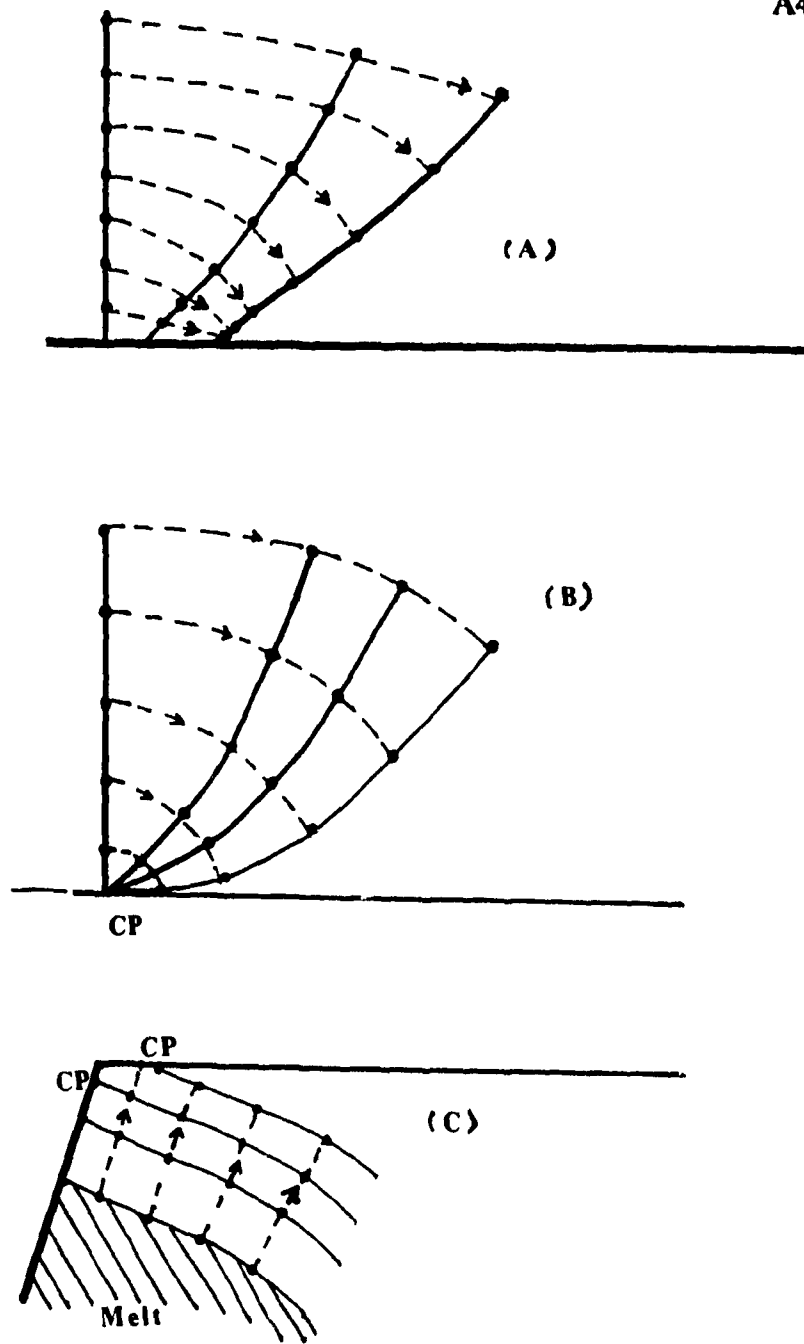


Figure (A.4.1): Situations arising during mold filling that necessitate rearrangement of free surface nodes for successful continuation of the computations.

points might touch the wall first. Again, an automatic rearrangement of the surface nodes is necessary for successful continuation of the computations. Other cases where rearrangement of surface nodes is required is shown in Figure (A.4.2.a) and (A.4.2.b).

Application of the no-slip boundary condition at the contact point results, macroscopically, in an apparent rolling of the free surface on the mold walls (Mavridis et al. (1988)). This representation of the motion of the free surface gave results that compare very well with experimental evidence. Figure (A.4.3) is a detail of the computational advancement of a free surface in the case of flow between two parallel planes. The free surface is 'rolling' on the walls with no need for artificial slip to be imposed at the contact point. The alternative determination of the contact point as the point where the free surface intersects normally the mold wall (Shen (1984), Subbiah et al. (1989)), gives melt front shapes that can be highly unrealistic.

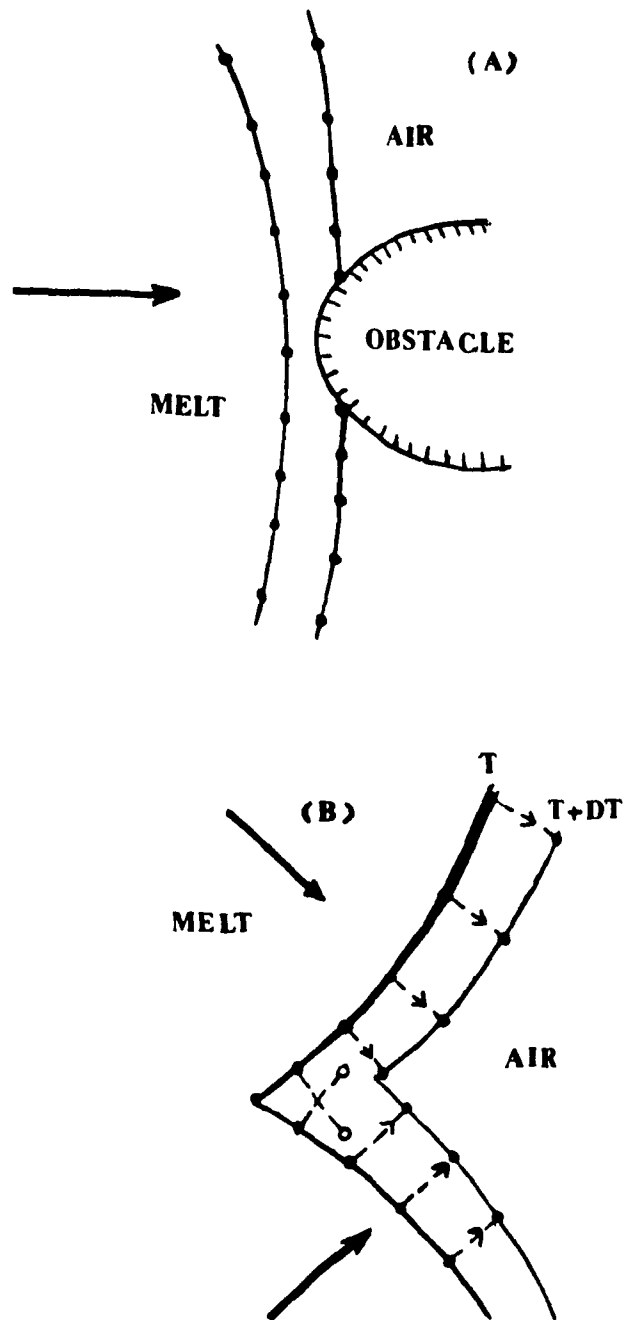


Figure (A.4.2): Other situations where rearrangement of the grid nodes on the free surface might be necessary.

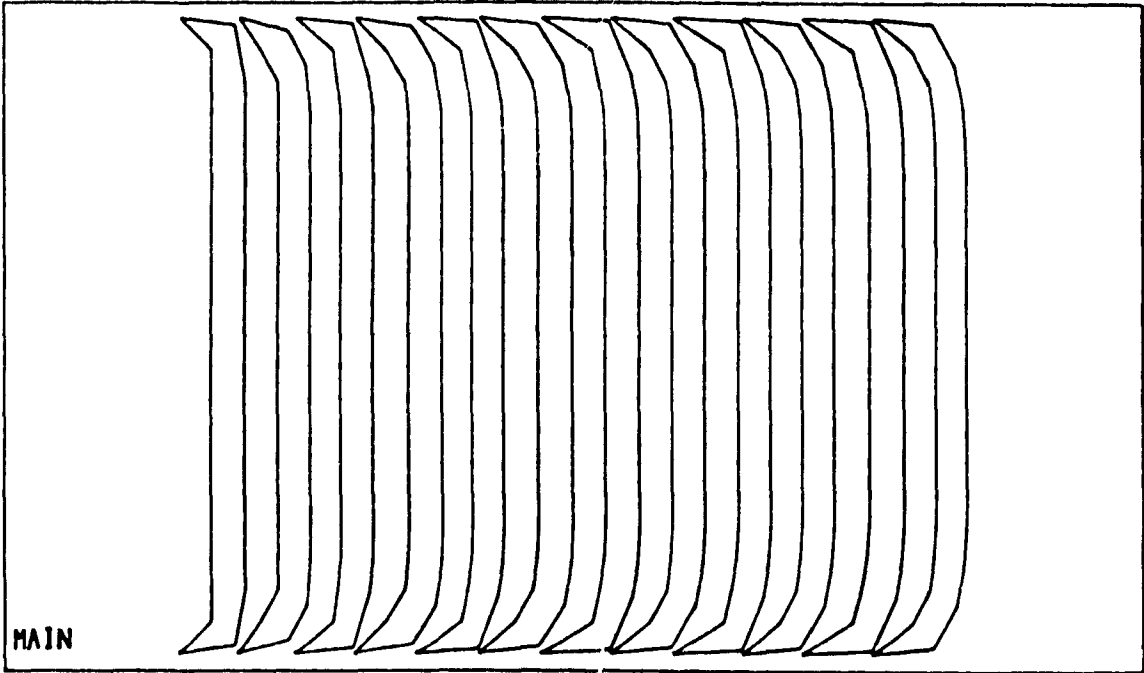


Figure (A.4.3): Computational advancement of the free surface in the case of flow between two parallel planes, displaying the rolling motion of the free surface. No-slip conditions are imposed on the walls.

(A.5) Further results on the spatial variation of key process parameters during injection mold filling.

The purpose of this section is to present, in Figures (A.5.1) to (A.5.10) further results on the spatial and temporal variation of key process characteristics during filling of the mold CR1. For more details on the conditions during these runs refer to section III.4.5. These results illustrate the capabilities of the computer program produced in this work to give a large amount of information regarding temperature, viscosity and shear rate variations, stress distributions etc. at every instant during filling. The three instances chosen to be presented here show some of the characteristics of the almost radial flow at early stages of filling ($t=0.8s$), the flow around the obstacle ($t=1.2s$) and the flow towards the end of filling ($t=1.6s$). $85 \text{ Btu/ft}^2\text{/F/hr} = 482 \text{ W/m}^2\text{/K}$.

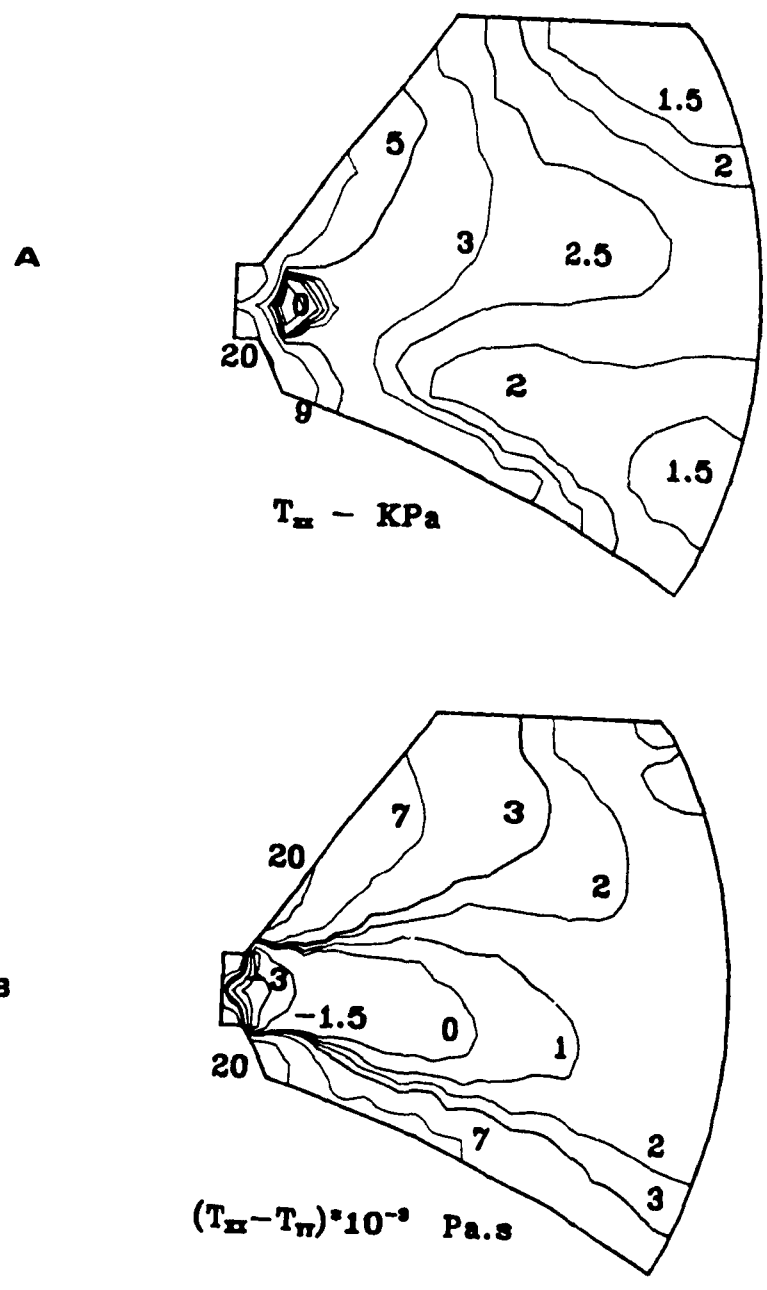


Figure (A.5.1): Spatial variation of T_m and $(T_m - T_w)$ at $t=0.8s$. Heat transfer Coefficient: $482 \text{ W/m}^2\text{K}$; Ram velocity 1.0 cm/s ; $T_m = 235^\circ \text{ C}$. Mold TE9.

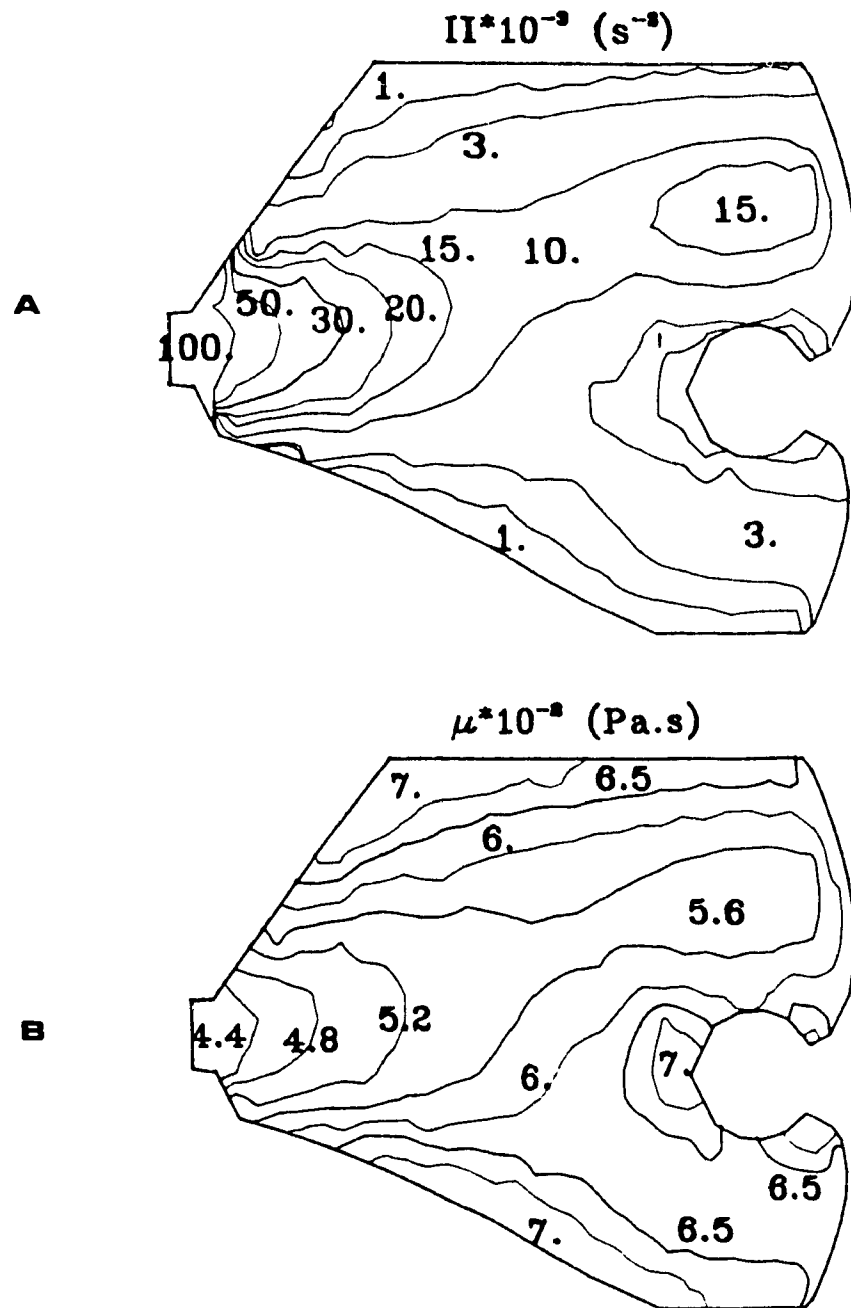


Figure (A.5.2): Spatial variation of the second invariant of the rate of deformation tensor (A) and of viscosity (B) during the filling of cavity TE9 at $t=1.2\text{s}$. Predicted values. Heat transfer Coefficient: $482 \text{ W/m}^2\text{K}$; Ram velocity 1.0 cm/s ; $T_{\text{amb}}=235^\circ \text{ C}$.

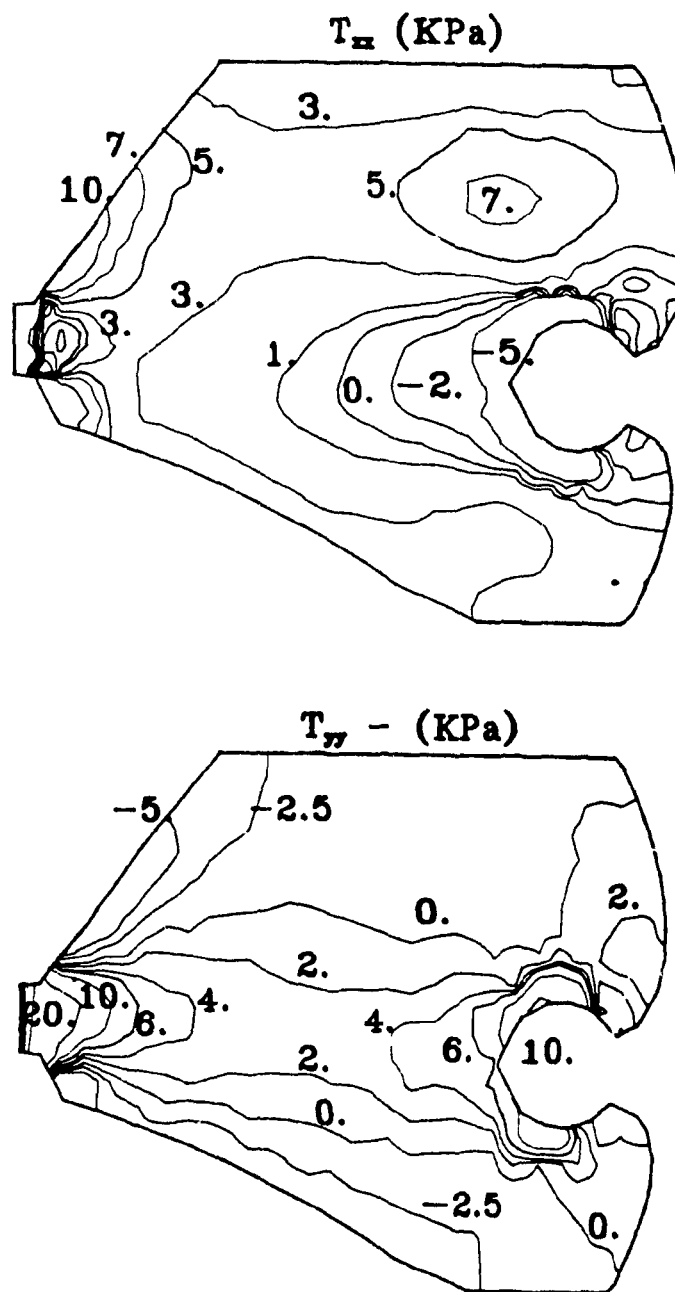


Figure (A.5.3):

Spatial variation of T_{xx} and T_{yy} stresses during the filling of cavity TE9 at $t=1.2s$. Predicted values; Heat transfer Coefficient: $482 \text{ W/m}^2\text{K}$; Ram velocity 1.0 cm/s ; $T_{\text{in}}=235^\circ \text{ C}$.

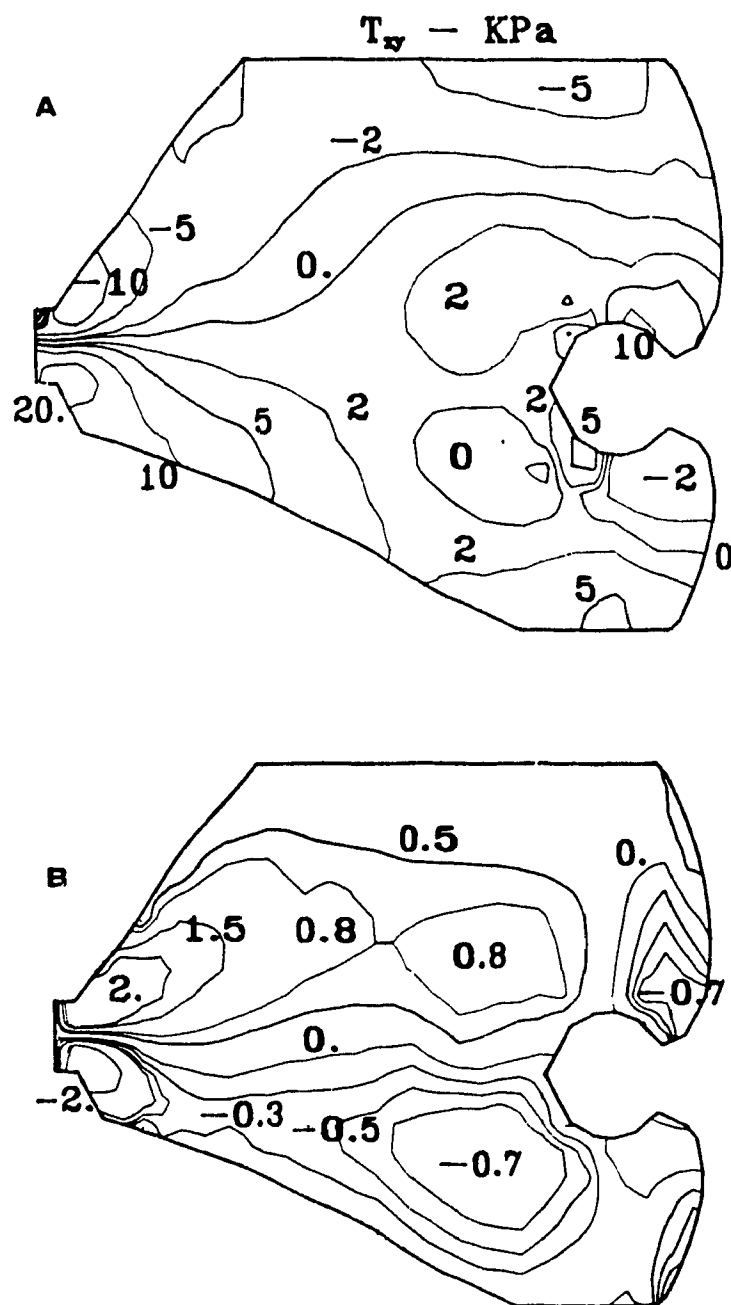


Figure (A.5.4): Spatial variation of T_v (A) and transverse planar velocity (B, in in/s) during the filling of cavity TE9 at $t = 1.2$ s. Predicted values. Heat transfer Coefficient: $482 \text{ W/m}^2\text{K}$; Ram velocity 1.0 cm/s ; $T_{\text{in}} = 235^\circ \text{ C}$.

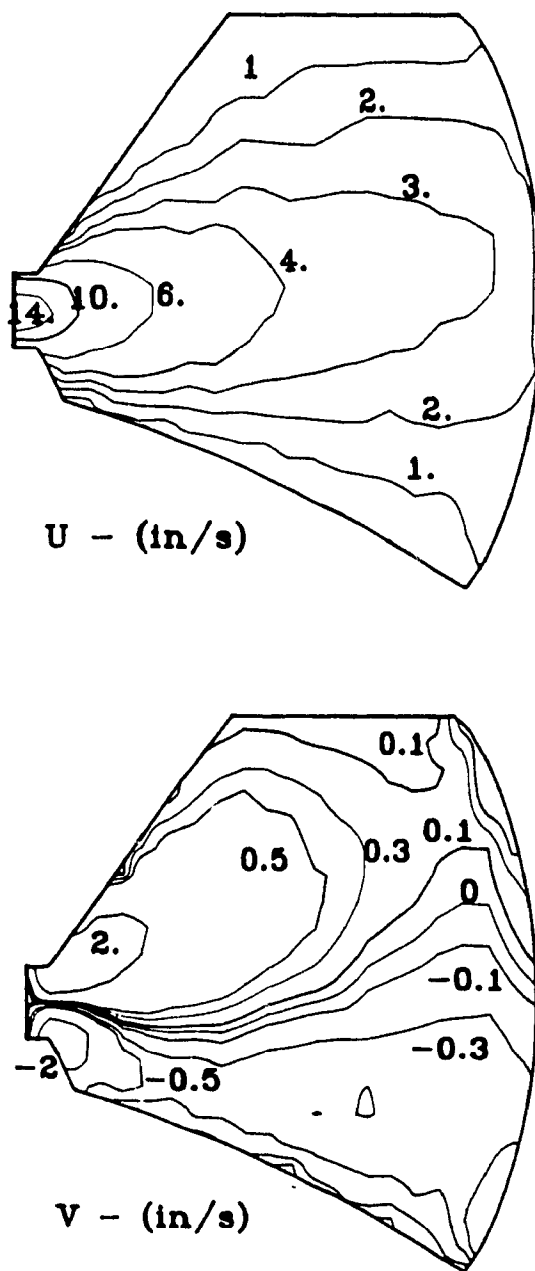


Figure (A.5.5):

Spatial variation of longitudinal (U) and transverse (V) planar velocities at $t=0.8s$. Cavity TE9. Heat transfer Coefficient: 482 W/m^2K ; Ram velocity 1.0 cm/s; $T_{\infty}=235^{\circ}C$.

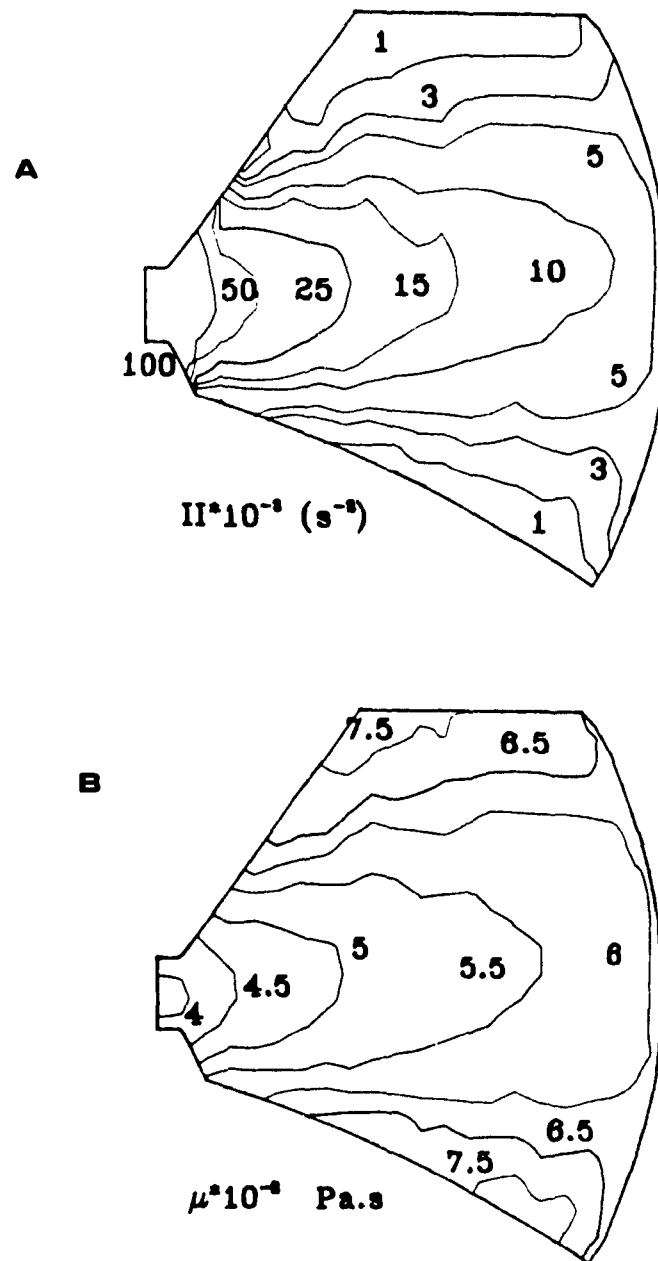


Figure (A.5.6):

Spatial variation of the second invariant of the rate of deformation tensor (A) and of viscosity (B) during the filling of cavity TE9 at $t=0.8\text{s}$. Predicted values. Heat transfer Coefficient: $482 \text{ W/m}^2\text{K}$; Ram velocity 1.0 cm/s ; $T_{\text{wall}}=235^\circ \text{ C}$.

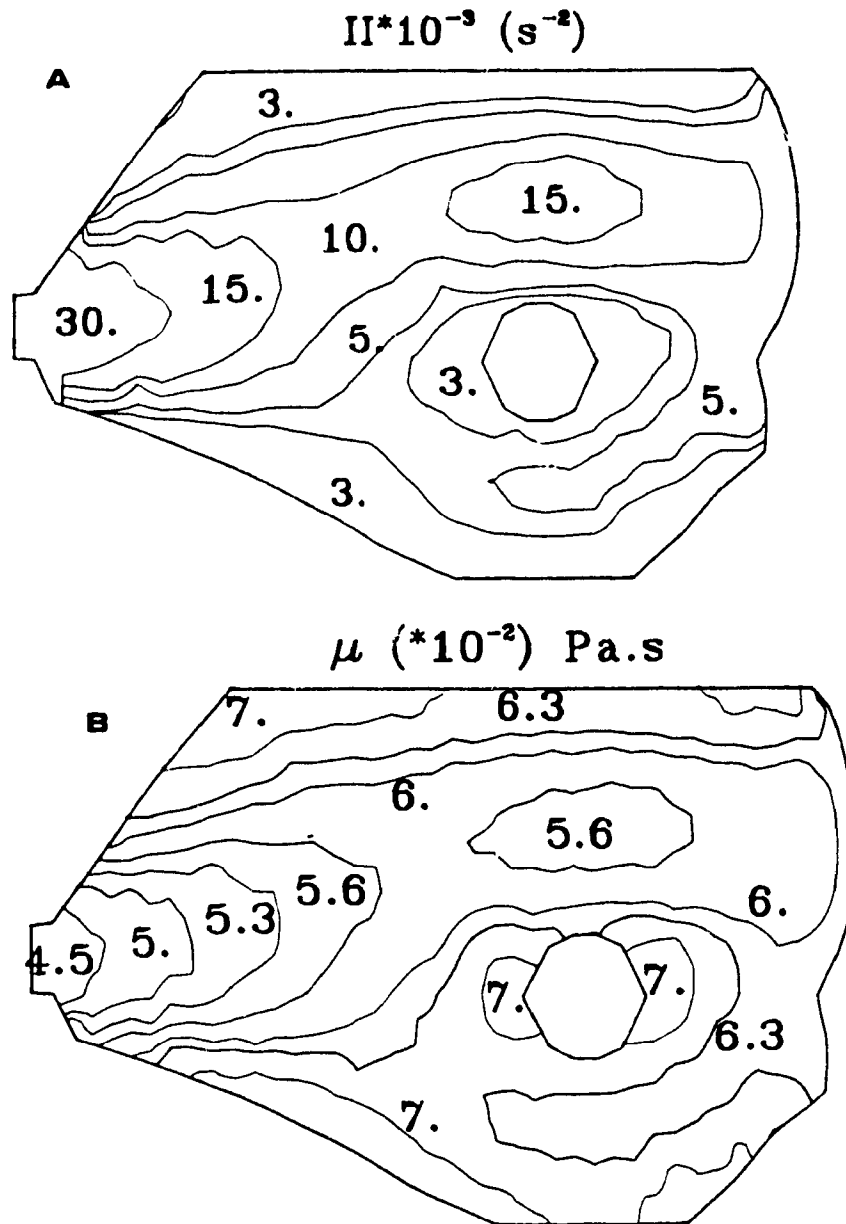


Figure (A.5.7): Spatial variations of the second invariant of the rate of deformation tensor (A), and of viscosity (B) at $t=1.6\text{s}$ during filling of mold TE9. Heat transfer Coefficient: $482 \text{ W/m}^2\text{K}$; Ram velocity 1.0 cm/s ; $T_{\text{m}}=235^\circ \text{ C}$.

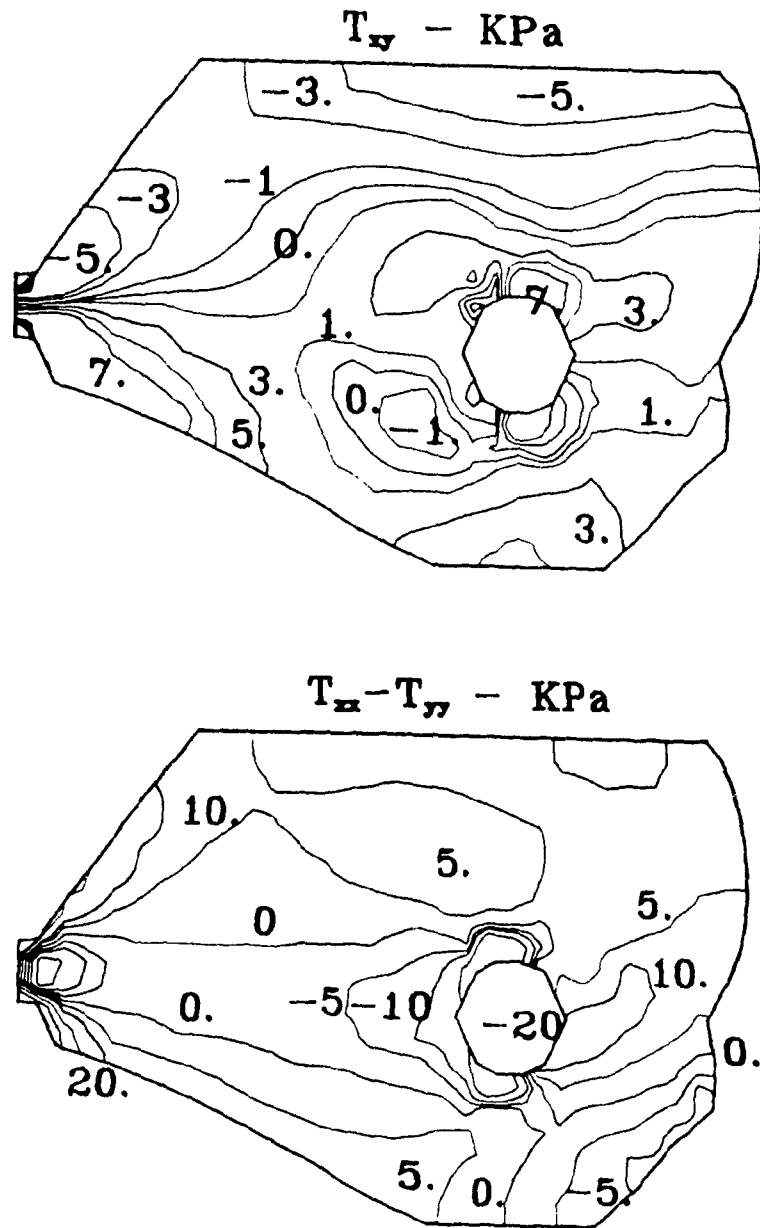


Figure (A.5.8): Spatial variation of T^m and $(T^m - T^w)$ at $t=1.6s$ during the filling of mold TE9. Heat transfer Coefficient: $482 \text{ W/m}^2\text{K}$; Ram velocity 1.0 cm/s ; $T_{\text{in}}=235^\circ \text{ C}$.

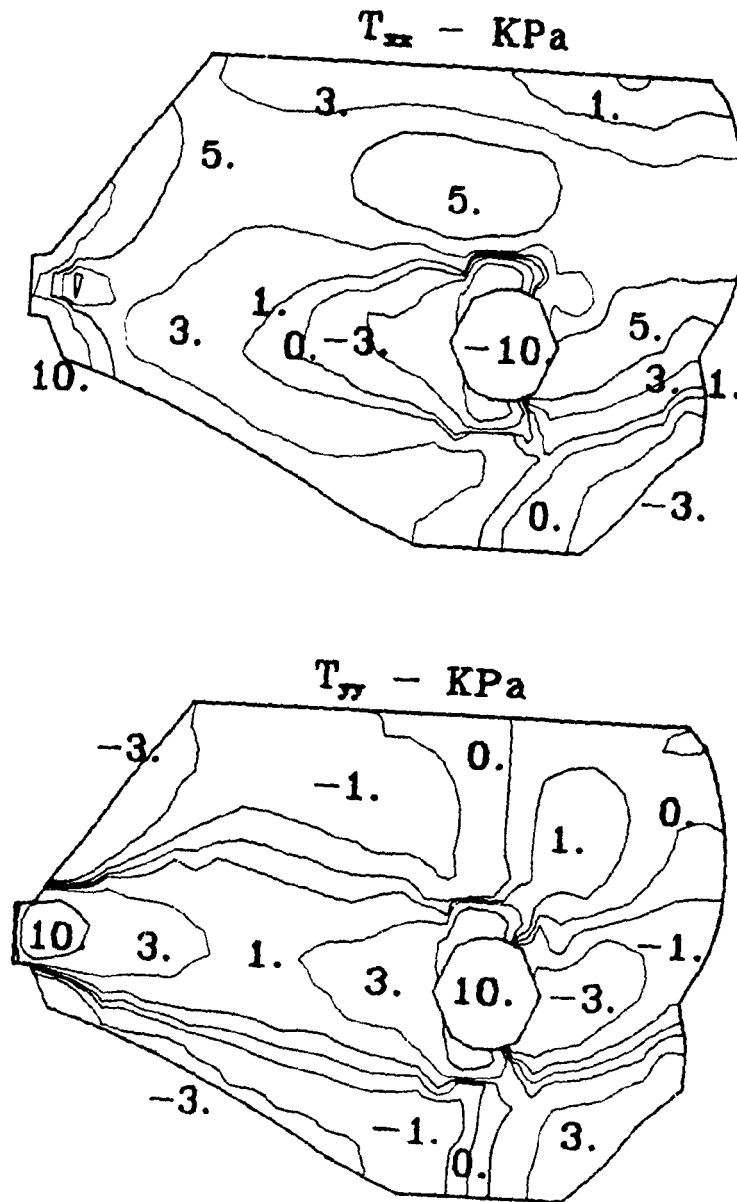


Figure (A.5.9): Spatial variation of T_{xx} and T_{yy} stresses during the filling of cavity TE9 at $t=1.6\text{s}$. Predicted values. Heat transfer Coefficient: $482 \text{ W/m}^2\text{K}$; Ram velocity 1.0 cm/s ; $T_{\text{amb}}=235^\circ \text{ C}$.

(A6): Dimensions of the Complex Cavity Used in Injection Molding

With reference to figure (III.3.1.1), the following part contains the cartesian coordinates of the points which define the perimeter of the cavity CR1. The thickness dimensions have been given in part (III).

- (a): (0.0, -0.397)
- (b): (0.317, -0.9525)
- (c): (5.08, -3.175)
- (d): (7.78, -3.175)
- (e): (10.795, -0.9525)
- (f): (10.795, 3.175)
- (g): (1.905, 3.175)
- (h): (0.0, 0.397)

Obstacle: Centre at (6.43, 0.476), radius=0.749
Part bc: Arc with centre at (-4.29, -16.83), radius=16.51
part de: Arc with centre at (11.43, -4.92), radius=3.97

All dimensions in (cm).

(A7): Boundary conditions in injection mold filling

The following table summarizes the boundary conditions used in the modelling of the filling stage of injection molding. "Edges" indicate the side walls of the cavity that form its perimeter in the x-y plane. Walls are the two faces of the mold through which most of the heat transfer takes place.

Variable	Entrance	Edges	Walls	Free Surface
Stream Function	A.4.2	A.4.1	-	A.4.3
Vorticity	A.4.2	A.4.10.a	-	A.4.3
Stresses (T)	From proper velocity profile	$(\partial T/\partial n)=0$	-	$(\partial T/\partial n)=0$
Temperature (T)	A.4.28	Adiabatic	A.4.29(*)	Adiabatic
Pressure (P)	A.4.23.a	$(\partial P/\partial n)=0$	-	P=0.

(*) This boundary condition is only applicable in the three-dimensional solution. In the 2D solution, a heat flux source term is used instead.